UNIVERSITAT POLITÈCNICA DE CATALUNYA

DOCTORAL THESIS

Entanglement and Bell Correlations in Strongly Correlated Many-Body Quantum Systems

Author:
Angelo PIGA

Supervisor:
Prof. Dr. Maciej LEWENSTEIN

Cosupervisor:
Dr. Shi-Ju RAN

Declaration of Authorship

The thesis relies on the material published in the following papers:

- A. Piga, A. Aloy, M. Lewenstein, I. Frérot, *Bell correlations at Ising quantum critical points* - Physical Review Letters 123, 170604 (2019).
- A. Piga, M. Lewenstein, and J. Q. Quach, *Quantum chaos and entanglement in ergodic and nonergodic systems* - Physical Review E 99, 032213 (2019).
- J. Jünemann, A. Piga, S.-J. Ran, M. Lewenstein, M. Rizzi, and A. Bermudez, *Exploring Interacting Topological Insulators with Ultracold Atoms: The Synthetic Creutz-Hubbard Model* - Physical Review X 7, 031057 (2017).
- S.-J. Ran, A. Piga, C. Peng, G. Su, and M. Lewenstein, *Few-body systems capture many-body physics: Tensor network approach* - Physical Review B 96, 155120 (2017).

0.1 Abstract - English

During the past two decades, thanks to the mutual fertilization of the research in quantum information and condensed matter, new approaches based on purely quantum features without any classical analog turned out to be very useful in the characterization of many-body quantum systems (MBQS). A peculiar role is obviously played by the study of purely quantum correlations, manifesting in the "spooky" properties of entanglement and nonlocality (or Bell correlations), which ultimately discriminate classical from quantum regimes. It is, in fact, such kind of correlations that give rise to the plethora of intriguing emergent behaviors of MBQS, which cannot be reduced to a mere sum of the behaviors of individual components, the most important example being the quantum phase transitions. However, despite being indeed closely related concepts, entanglement and nonlocality are actually two different resources.

With regard to the entanglement, we will use it to characterize several instances of MBQS, to exactly locate and characterize quantum phase transitions in spin-lattices and interacting fermionic systems, to classify different gapped quantum phases according to their topological features and to provide a purely quantum signature of chaos in dynamical systems.

Our approach will be mainly numerical and for simulating the ground states of several one-dimensional lattice systems we draw heavily on the celebrated "density matrix renormalization group" (DMRG) algorithm in the "matrix product state" (MPS) ansatz. A MPS is a one-dimensional tensor network (TN) representation for quantum states and occupies a pivotal position in what we have gained in thinking MBQS from an entanglement perspective. In fact, the success of TNs states mainly relies on their fulfillment, by construction, of the so-called "entanglement area law". This is a feature shared by the ground states of gapped Hamiltonians with short-range interactions among the components and consists of a sub-extensive entanglement entropy, which grows only with the surface of the bipartition. This property translates in a reduced complexity of such systems, allowing affordable simulations, with an exponential reduction of computational costs. Besides the use of already existing TN-based algorithms, an effort will be done to develop a new one suitable for high-dimensional lattices.

While many useful results are available for the entanglement in many different contexts, less is known about the role of nonlocality. Formally, a state of a multi-party system is defined nonlocal if its correlations violate some "Bell inequality" (BI). The derivation of the BIs for systems consisting of many parties is a formidable task and only recently a class of them, relevant for nontrivial states, has been proposed. In an important chapter of the thesis, we apply these BIs to fully characterize the phase transition of a long-range ferromagnetic Ising model, doing a comparison with entanglement-based results and then making one of the first efforts in the study of MBQS from a nonlocality perspective.

0.2 Abstract - Castellano

Durante las dos últimas décadas, gracias al enriquecimiento mutuo entre las investigaciones en información cuántica y materia condensada, se han desarrollado nuevos enfoques que han resultado muy útiles en la caracterización de los sistemas cuánticos de muchos cuerpos (SCMC), basados en características puramente cuánticas sin ningún análogo clásico . El estudio de las correlaciones puramente cuánticas juega obviamente un papel fundamental. Estas correlaciones se manifiestan en las propiedades del entrelazamiento cuántico ("entanglement") y no-localidad (o correlaciones de Bell), que en última instancia discriminan los regímenes clásicos de los regímenes cuánticos. Este tipo de correlaciones son, de hecho, las que dan lugar a la plétora de comportamientos emergentes enigmáticos de los SCMC, que no pueden reducirse a una mera suma de los comportamientos de los componentes individuales, siendo el ejemplo más importante siendo las transiciones de fase cuánticas (TFC). Sin embargo, a pesar de ser conceptos estrechamente relacionados, el entrelazamiento y la no-localidad son en realidad dos recursos diferentes.

Con respecto al entrelazamiento, lo utilizaremos para caracterizar varios ejemplos de SCMC, para localizar y caracterizar exactamente las TFC en retículos de espines y de sistemas de fermiones interactuantes, para clasificar las diferentes fases cuánticas de acuerdo con su topológia y para proporcionar una señal puramente cuántica del caos en los sistemas dinámicos.

Nuestro enfoque será principalmente numérico y para simular los estados fundamentales de varios sistemas unidimensionales nos basamos en gran medida en el célebre algoritmo "density matrix renormalization group" (DMRG), formulado en el ansatz de los "matrix product states" (MPS). Un MPS es un "retículos de tensores" ("tensor networks", TN) unidimensional que representa estados cuánticos y ocupa una posición central entre los mayores logros obtenidos al estudiar los SCMC desde la perspectiva del entrelazamiento cuántico. De hecho, el éxito de los TN depende principalmente de su cumplimiento, por construcción, de una "ley del area" ("area-law") de la entropía de entrelazamiento. Esta es una característica compartida por los estados fundamentales de los Hamiltonianos con interacciones de corto alcance entre los componentes del sistema y con una brecha ("gap") entre el estado fundamental y los niveles excitados, que consiste en una entropía de entrelazamiento subextensiva, que crece sólo con la superficie de la bipartición. Esta propiedad se traduce en una menor complejidad de dichos sistemas, permitiendo simulaciones asequibles, con una reducción exponencial de los costes computacionales. Además del uso de los algoritmos ya existentes basados en TN, se desarrollará uno nuevo adecuado para sistemas en dimensiones altas.

Si bien se dispone de muchos resultados útiles para el entrelazamiento en muchos contextos diferentes, se sabe menos sobre el papel jugado por la no-localidad. Formalmente, un estado de un sistema compuesto de muchas partes, se define como no-local si sus correlaciones violan alguna "desigualdad de Bell"

("Bell inequality", BI). La derivación de dichas desigualdades para sistemas compuestos de muchas partes es un reto y sólo recientemente se ha propuesto una clase de ellas, relevante para estados no triviales. En un capítulo importante de la tesis, aplicamos estas BIs para caracterizar completamente la transición de fase de un modelo de Ising ferromagnético con interacciones de largo alcance, haciendo una comparación con los resultados basados en el entrelazamiento y luego haciendo uno de los primeros esfuerzos en el estudio de los SCMC desde una perspectiva de la no-localidad.

Perhaps this work is just a small step for man and a giant step backward for mankind…
Anyway, it is the moment to dedicate just a few lines to all those that made completing this work possible.
Science and knowledge are a collective endeavor, so I thank the general intellect (by humans and nonhumans).
To my family and its patience. They are always so close to me...even from afar. In a precarious life, having a fixed point that keeps you anchored to your roots, is a privilege.
To the ICFO QOT group, all its members from 2015 to 2020, those who collaborated with me, officially (Shi-Ju, James, Irénée, Albert) and unofficially (Nello, Emanuele, Luca, Jessica, David, Arnau, Daniel, and Alex among others). A special thought is for Maciek, for his support in difficult moments.
To my friends.
To my comrades, another great family that branches out all over the world. To l@s Zapatistas from all over the world and the "ConCiencias por la Humanidad".
A special thanks to the squirrels, companions of many trips.
A nostalgic memory is devoted to the good vibes of Melbourne and the wild side of Australia.
To rebel scientists, the rebellious scientists, the rebels.
Last but not least, to my intellectual and artistic heroes that somehow positively changed my life and also influenced my scientific perspectives, giving me the strength to survive in the jungle of academia. Just to name a few: Paul, Mark, Carl, Tonino, Silvia, Lee, Marcello, Isabelle, Eduardo, Jimmy, Jimi, Jerry, Ott, Ben, David, John, Neil, Miles...and the respective crews.

Contents

1 Introduction

1.1 The puzzle of entanglement and nonlocality in quantum mechanics

Quantum entanglement [Hor+09] has been for a long time a puzzle (and actually it continues to be a puzzle) at the core of the interpretation of quantum mechanics (QM); it is responsible for profound debates bridging physics and philosophy. The *"spooky"* action at a distance between entangled quantum systems brought Einstein, Podolsky and Rosen [EPR35] to force physicists to face two apparent mutually exclusive alternatives, nowadays known as *EPR paradox*: concerning the impossibility of predicting the simultaneous outcomes of two non-commuting observables, they stated that *"either (1) the description of reality given by the wave function in QM is not complete or (2) these two quantities cannot have simultaneous reality"* and consequently *"if (1) is false then (2) is also false"*. Aware of the success of the QM, but not available to abandon the *principle of reality*, the three scientists opted for arguing that QM is not complete. The implications of such a belief is that QM is a statistical approximation of an underlying more general and complete theory, whose predictions are not accessible because of the missing of some inaccessible variables, the so called **local "hidden" variables** (**LHV**).

In the face of the instrumentalist approach to the physics programs, the EPR paradox was soon relegated to be a secondary issue [1]. It was not until 1964 that the seminal works of Bell [Bel64; Bel66] shed new light on the problem. Bell provided a set of inequalities which must be satisfied to certify that a two-party system possesses a *"local hidden variable description"* and whose violation signals

[1] At the epistemological level, the dispute within the physics community can be roughly traced back to the philosophical opposition between *"realism"* and *"instrumentalism"*. By *"instrumentalism"* I mean something more subtle than the trivial *"shut up and calculate!"* [Mer04]. Instead, I refer to that approach in which physical theories are not true descriptions of some existing reality, but a "tool" to organize and predict phenomena [DN91]. Actually, in my opinion, to explain the winning of the instrumentalists, the materialistic approach that takes into account the political and economic context between the 1930s and the 1970s, is unavoidable. Disproportional investments in high energy physics (particle and nuclear physics) were in fact preferred since allowing faster advancements especially in the military technologies during the cold war. On the other hand, the organization of research in high energy physics was the first example and prototype of *"big science"*, where the strict division of tasks and roles among researchers reflected the model production at that time, the *fordism* (see for example Smolin [SH08] - for a point of view internal to the research community and with special attention to the advent and explosion of string theory - and Kaiser [Kai11]).

nonlocality (or **Bell nonlocality**). The EPR state violates such inequalities. **Bell inequalities** (**BIs**) [Bru+14] can be formulated in terms of correlators involving two space-like separated observables (such as, for instance, the famous CHSH BI [Cla+69]) and can be experimentally tested. Several experimental results [AGR81; ADR82; Giu+15; Hen+15] confirmed the QM predictions that nonlocality is manifested by some entangled quantum states and the entanglement was finally "promoted" as a physical measurable property.

The renewed enthusiasm around the foundations of the QM paved the way for a new approach to information theory. From the 1980s, some papers which exploited entanglement as a resource for communication [Her82], cryptography [BB84; WZ82], computation [Deu85] and teleportation [Ben+93] are now considered pionering works for modern *quantum information theory* [NC02].

Entanglement and nonlocality, however, are not equivalent concepts, although the distinction has been blurred for long time. In particular, in a paper of 1991 in memoriam for Bell, Gisin [Gis91] proved that any bipartite entangled *pure* state is nonlocal, whereas Popescu and Rohrlich in 1992 [PR92; GG17] extended this result to an arbitrary number of parties. But Werner in 1989 [Wer89] explicitly constructed a *mixed* state which is entangled and yet admits an LHV description. Hence, entanglement is actually a weaker property *i.e.* only a necessary condition for nonlocality.

Nevertheless, the use of entanglement broadened faster than nonlocality and permeated other branches of QM. Many useful results are available for the entanglement in several contexts, while less is known about BIs, especially in the study of **many-body quantum systems**, a field of particular interest for this dissertation.

1.2 The complexity of Hilbert space

Entanglement is first of all a formal property of states acting on **tensor product** of local Hilbert spaces. Such structures involve a **complexity** with no classical analog.

To assess the differences between classical and quantum complexity, consider a system of N-components. In the quantum picture, each subsystem is associated to a Hilbert space $\mathcal{H}_i$ and the system lives in the tensor product $\mathcal{H} = \bigotimes_{i=1}^{N} \mathcal{H}_i$. In particular, a generic pure quantum state is the superposition state

$$|\psi\rangle = \sum_{\{s_i\}=1}^{d} c_{s_1 s_2 \dots s_N} |s_1\rangle \otimes |s_2\rangle \cdots \otimes |s_N\rangle, \tag{1.1}$$

where d is the local dimension of each Hilbert space (the d's are chosen to be identical, for simplicity) and the sum runs over all the possible configurations $\{s_i\}$. There are therefore $\mathcal{O}(d^N)$ possible configuration-coefficients $c_{s_1 \dots s_N}$ *i.e.* the complexity is exponential in the number of components. In comparison, the classical representation of the same system is the **Cartesian** product of the

subsystem vector-spaces $V = \bigoplus_{i=1}^{N} V_i$, and each classical collective state is *always* a trivial **product state** whose complexity is linear in N. Starting from this consideration, Jozsa [Joz98] argued that the benefit of the quantum computation does not derive from the *quantum superposition*, which is actually mimicable also by classical waves, but from entanglement, which *"allows one to construct exponentially large superpositions* with only linear physical resources *and this cannot be achieved with classical superposition"*. Exploiting such intrinsic quantum complexity lies at the heart of the exponential speed-up of quantum algorithms with respect to the classical ones [Sho94] and motivates the challenge of the universal quantum computer [Fey82].

The downside of such complexity, on the other hand, is: *while waiting for a quantum computer, how can we efficiently simulate composite quantum systems with only classical resources?* This task is far from trivial especially if one has to deal with macroscopic systems of $N = \mathcal{O}(10^{23})$ components. In such case, there is no way to exactly solve the related secular equation, neither to store the information content of Eq. (1.1) with current computers.

1.3 Entanglement and nonlocality in many-body quantum systems

By **many-body quantum systems** (**MBQS**), we mean compounds of many interacting quantum components which show emergent collective phenomena not reducible to a mere sum of the singular component behaviors. An instance of such features occurs at **quantum phase transitions** (**QPTs**) [Sac11; Car10] [2].

Despite being a weaker property than nonlocality, entanglement is a powerful method to study MBQS (see review [Ami+08] and references therein). As an analysis tool, in a number of works entanglement has been proven to be useful in classifying ground states and characterizing quantum critical phenomena, with outstanding results especially for **lattice models** [LSA12; BDZ08]. In the following, a non exhaustive review of the main results relevant for this thesis is given.

- Seminal works in the erlier 2000s focused on pairwise entanglement. In 2002, independently in [ON02] and [Ost+02], it was found that for an Ising chain in a transverse field, pairwise entanglement is nonzero only for neirest- and next-neirest neighbors spins, and divergence of its derivative with respect to the external field occurs at critical point.

[2] Differently than the classical case, where transition is driven by temperature, a QPT takes place at absolute zero, driven by some external parameter or coupling constant. In the case of second order phase transitions, both classical and quantum critical points are characterized by a diverging correlation length, whose shape is described by universal critical exponents, but QPTs have in addition different kinds of correlations without classical counterparts, namely entanglement and nonlocal correlations. In this thesis we essentially do not deal with first order QPTs [Pfl05].

- Later in 2004 the concept of **localizable entanglement** was introduced in [VPC04a], as the maximum amount of entanglement one can concentrate in two spins performing local measurements on the rest of the system. The resulting maximal distance at which two spins can be entangled is the **entanglement length** [VMDC04]. Such new characteristic length is lower bounded by two-points correlation length and therefore also diverges at criticality. Importantly, transition of entanglement (diverging entanglement length but finite correlation length) has been found for spin-1 systems in one-dimension [VMDC04].

- Changing of focus towards **Von Neumann entanglement entropy** (**EE**) of bipartitions of arbitrary size, was a step forward to understand the structure of ground states. For almost all the states, EE grows linearly with the number of particles in the bipartition (*i.e.* is an extensive quantity) but in the ground states of gapped (*i.e.* non-critical) local Hamiltonians EE is sub-extensive, satisfying an **area law** [ECP10], *i.e.* the EE scales only with the surface of the boundary between the two partitions.

- The area law plays a fundamental role in the numerical treatment of MBQS, being the fundamental reason of the success of **tensor networks** (**TN**) approaches [VMC08; Orú14; Ran+19] from 2003. TN provide a special *ansatz* for wave functions and operators on a lattice (consider in particular *matrix product states* (MPS) [FNW92; VPC04b] in one-dimension and *projected entanglement-pair state* (PEPS) [VC04b; VC04a] in higher dimensions); the quantities of interest are expressed as a result of the contraction of a network of small constituent tensors. The success of TN is unquestionable, allowing simulations previously impossible with older techniques (*e.g* exact diagonalization or quantum Monte Carlo). Especially in one-dimensional lattices **density matrix renormalization grup** (**DMRG**) [Whi92] and **time evolving block decimation** (**TEBD**) [Vid04], remain among the most accurate tools for studying low energy properties and time evolution of a pletora of models. In two- and higher-dimensions, in systems with long-range interaction and close to criticality, applications of TN are still relevant but difficulties of several nature emerge. TN are ubiquitous in this thesis, in applications of already existing algorithms as well as in the development of new ones.

- Near to a quantum critical point, divergences of EE frequently occur. Most is known for one-dimensional spin models, where, thanks to an underlying conformal symmetry the system posseses at criticality, **universal logarithmic scalings of EE** emerge [Vid+03; CC09]. Much less is known in two- and higher-dimensions.

- According to the *Landau-Ginzburg* paradigm of the second order QPTs, a non-zero *local order parameter* distiguishes an ordered from the disordered phase: in the ordered phase, the ground state does not satisfy the same

symmetries of the Hamiltonian, that is it experiences a *spontaneous symmetry breaking*. A breakthrough in classification of QPTs has been the discovery of **topological phases**, which elude the above description. Here, the ground state does not break any symmetry. In topological phase transitions the absence of any local order is compensate by some global symmetries which "protect" the phase, leading to the notions of **symmetry protected topological** (**SPT**) **phases** and **topological order** [Wen04], both defined in terms of the kind of entanglent owned by the state. Topology is often associated with the presence of *edge states* (gapless, conducting, state on the boundaries) and is the the theoretical framework for the study of many intriguing, not yet fully understood, phenomena, such as the *fractional quantum Hall effect*. **Entanglement spectrum** [LH08] (*i.e.* the spectrum of the reduced density matrix of a bipartition) shows regular degeneracy throughout a topological phase of matter and the **topological entropy** [KP06; LW06] (a negative correction to the area law), which are strong indicators of topological order in two dimensions. Topological phases are well studied in non interacting systems. Much less is known about their robustness in presence of strong interactions. Some of the tools just mentioned will be applied in this thesis to distinguish between topological and trivial phases in a paradigmatic strongly interacting fermionic system, the *Creutz-Hubbard ladder*.

- Being classical systems supposed to be ultimately quantum, it is of fundamental importance to understand classical phenomena in terms of intrinsic quantum mechanical properties. **Classical chaos** manifests as consequences of non-linear equations of motions. This is in contrast with the linearity of the Schrödinger equation. Nevertheless, **quantum signatures of chaos** [Haa13] are the subject of intense studies since the 1980s. This research direction starts from the consideration that some classical chaotic systems can be seen as the semiclassical limit of a strongly interacting MBQS. The most important research direction includes the characterization of quantum chaos via statistics of quantum energy levels. In systems that have semiclassical chaotic counterpart, different rates of production of EE seems to distinguish between regular and chaotic behaviours of the former [Wan+04]. One chapter of this work is dedicated to the extension of this conjecture to systems not yet studied.

Conversely, less results are available concerning the role of nonlocality in MBQS. Generically, a many-body quantum state of a MBQS, and in particular the ground state, is pure and entangled, it violates some BIs, *i.e.* is nonlocal.

In the modern framework of **device independent quantum information processing** [Ací+07] a Bell scenario is represented with several black boxes (one for each observer, or party) with their relative input and outputs of local measurements. The only relevant quantities characterizing the experiments are the conditional probabilities to obtain a vector of outputs, given the inputs (the measurments choices). It results [Fro81; Pit86] that the sets of classical behaviours

form a bounded convex set, the **Bell polytope**, embedded in the multidimensional space of the probability distributions of outcomes (see Fig. 2.4 in Chap. 2.3 for an explanatory graphic representation): the interior of the polytope contains all the classical correlations (namely, the correlations with an LHV representation), while outside the polytope the nonlocal correlations lie. BIs are the linear inequalities defining the facets of this polytope. In practice, BIs are linear combinations of probabilities, resulting from an experiment involving only local measurements performed on a composite system.

To signal violation of BIs, two parallel and interconnected problems arise, of mathematical as well as experimental nature. On the one hand, since the number of facets increases exponentially with the number of observers, the characterization of the full Bell polytope is an impossible task (an NP-hard o NP-complete problem). On the other hand, concerning the realization of a Bell test in laboratory, many BIs require the measure of high-order correlators (resulting from the product of many local observables), and this is very difficult with state of art experiments.

To overcome these problems, quite recently, in a series of theoretical works [Tur+14; Tur+15b], BIs involving only one- and two-body correlators were formulated. They are experimentally accessible and, surprisingly, they are violated by relevant many-body states, ground states of nontrivial Hamiltonians. These promising results encourage an exploration of new insights BIs can give about quantum phenomena. In fact, another motivation of this work is the study of Bell correlations in the vicinity of a quantum critical point.

1.4 Plan of the thesis

The thesis is organized as follows.

Chapter 2 provides an overview of the theory of the entanglement and nonlocality. This chapter does not contain any original results and focuses on those fundamental concepts recurring in the rest of the dissertation. The formal definitions of entanglement and separability for pure and mixed states are introduced for finite dimensional Hilbert spaces in the bipartite scenario. For pure states, the Von Neumann entanglement entropy (EE) provides a unique measure for the bipartite entanglement. In contrast, in the multipartite case an obvious generalization of the previous definitions is missing and different nonequivalent separability criteria exist: we introduce the notions of "k-separability" and "entanglement depth". A brief section is devoted to the use of entangled states as resource in metrology, where the "squeezing" is a good indicator of the entanglement depth for spin systems.

For many-body quantum system (MBQS), we restrict to the case of spin lattices and to the bipartite case, and introduce the crucial area-law for the EE, for one-dimensional and higher-dimensional systems. We review the relevant

cases in which its violation can occur: long-range interactions systems and critical systems. Since in the former case there are no general results available, we review some partial results present in literature, but a general theory is still missing. For one-dimensional short-range interactions critical systems instead, violations usually consists in a logarithmic divergence of the EE, whose multiplicative factor is a universal signature of the underlying conformal field theory.

In the second part of the chapter, the theory of Bell nonlocality is reviewed in the modern approach of the device independent quantum information processing, where all quantities and relations are expressed only in terms of the conditional probabilities of the experiments. One distinguishes between classical (or local), quantum and non-signaling correlations. In particular, classical correlations lie inside a polytope, in turn embedded in the set of quantum correlations. The facets of the classical polytope, which are the boundaries between quantum and the classical behaviours, define the BIs. A Bell experiment is classified by a triplet (N, m, Δ): the number N of parties, the number m of local observables and the number Δ of outputs of each observable. For the simplest $(2, 2, 2)$ scenario, we show the celebrated CHSH BI. The derivation of all BIs becomes practically impossible when N increases. However, in the $(N, 2, 2)$ scenario a class of nontrivial BIs was proposed. We review in details such BIs. They obey permutational invariance and correspond to the facets of a projected polytope. In turn, their violation is a sufficient but not necessary condition to certified a state as nonlocal. However, we show that relevant many-body states violate the BI. Finally, we show that the level of violation of such many-body BI also provides a criteria to certificate the amount of multipartite entanglement in the state.

In **chapter** 3 the TN approach for the classical simulation of MBQS is reviewed. Also in this case, no original results are presented. Many concrete examples are instead provided. We introduce the TN formalism starting from the way we can represent one-dimensional states: the matrix product state (MPS). We take advantage of a very suitable standard graphical representation to reduce the complexity of the understanding of the formulas. We emphasize the fact that TN by construction satisfy an EE area-law, which is the main reason for its success in simulating the ground states of gapped MBQS in generic dimension. For one-dimensional systems the "canonical representation" of MPS is introduced, which allows for the calculation of the Schmidt coefficients (and then EE and entanglement spectrum) of any bipartition in a very simple way. The way to represent operators is also given. The DMRG, which will be used in chapters 5, 6 and 7 is described in its variational version based on the MPS formulation. The final part of the chapter is devoted to sketching the problems of the contraction of high dimensional TN.

Chapter 4 is based on the original article *Quantum chaos and entanglement in ergodic and nonergodic systems* [PLQ19]. We study EE as a signature of quantum chaos in ergodic and nonergodic systems. In particular we look at the quantum

kicked top and kicked rotor as multi-spin systems and investigate the single-spin EE which characterizes bipartite entanglement of this spin with the rest of the system. Even if the dynamics of these model is not exactly solvable, the symmetries of their Hamiltonian allow to restrict the numerical simulations to a small symmetric sector of the Hilbert space, hence exact diagonalization is sufficient to explore very long-time evolution for many-particle regimes. We study the correspondence of the "Kolmogorov-Sinai entropy" (a measure of classical chaos) of the classical kicked systems with the EE of their quantum counterparts. We find that EE is a signature of chaos in ergodic and nonergodic systems. In particular, we show that EE can be maximized even when systems are highly nonergodic, when the corresponding classical system is locally chaotic. In contrast, we find evidence of a quantum analog of "Kolmogorov-Arnol'd-Moser" theory (a classical theory describing the stability of dynamical systems under perturbations) and we conjecture that entanglement should here play an important role.

Chapter 5 is based on the original article *Exploring interacting topological insulators with ultracold atoms: The synthetic Creutz-Hubbard model* [Jün+17]. We provide a complete analysis of the synthetic Creutz-Hubbard ladder, a concrete interacting quasi-one-dimensional fermionic system where correlated topological phases and standard insulating phase compete, resulting in a rich phase diagram. Entanglement properties of the ground state are studied in different regimes to explore new physics.

The first section of the chapter is an overview on topological insulating materials. The Haldane phase of the Heisenberg model is considered, as a paradigmatic example that eludes any classification based on a local-order parameter. The definitions of "topological order" and "symmetry-protected topological" (SPT) phases are given. Then, a particular focus is devoted to fermionic systems. In the non interacting regime there exists a complete classification of all the possible SPT phases (the AZ classification [AZ97]), based on the symmetries of the Hamiltonian. When interactions are added such classification breaks down, new phases appears and others are destroyed. For one-dimensional systems, a new classification is possible based on the different projective representations of the Hamiltonian symmetries which have a direct relation with the degeneracy of the entanglement spectrum of a bipartition of the ground state. The latter is proven exploiting the properties of the MPSs under symmetry-group transformations.

All these concepts are then applied to the Creutz ladder, in the non-interacting case and then when Hubbard interactions are added. Concerning numerics, with the DMRG algorithm we are able to characterize the ground state of the model in all regimes and to locate exactly its critical lines and the underlying conformal field theories. Wherever possible (namely, in the limit of strong and weak interactions and in the intermediate regime) we compare numerical results with analytical calculations. We give special attention to the competition of correlated topological phases and standard insulating phase. An analysis of

the entanglement spectrum further provided evidence of the presence of an extended topological phase.

Chapter 6 is based on the original article *Bell correlations at Ising quantum critical points* [Pig+19]. Focusing on the Ising model in a transverse-field with power-law ($1/r^\alpha$) ferromagnetic interactions, we show that a certain permutationally invariant Bell inequality based on two-body correlations [Tur+14] is violated in the vicinity of the quantum-critical point. This observation, obtained via analytical spin-wave calculations and numerical DMRG computations, is traced back to the squeezing of collective-spin fluctuations generated by quantum-critical correlations. We observe a maximal violation for infinite-range interactions ($\alpha = 0$), namely when interactions and correlations are themselves permutationally invariant.

Chapter 7 is based on the original article *Few-body systems capture many-body physics: Tensor network approach* [Ran+17]. Here we propose a new TN-based scheme to accurately capture the ground-state properties of infinite MBQS in higher dimensions, directly in the thermodinamic limit. The general idea is to embed a small bulk of the infinite model in an "entanglement bath" so that the many-body effects can be faithfully mimicked. We benchmark the results of the algorithm against other already existing techniques in some simple models, namely spin models on honeycomb and simple cubic lattices, showing that the ground-state properties including quantum phase transitions and the critical behaviors are accurately captured.

The conclusions are finally exposed in **Chapter** 8.

The thesis contains also four appendices.

Appendix A contains explicit calculations for some results used in Chap. 4.

In **Appendix** B and **Appendix** C the matrix product operators representations for, respectively, the imbalanced Creutz-Hubbard ladder treated in Chap. 5 and the long-range Ising model studied Chap. 6, are derived to adapt the original Hamiltonians to the DMRG calculations.

In **Appendix** D some details about the algorithm introduced in Chap. 7 as well as some relations between this algorithm and other existing algorithms are described.

2 Entanglement and nonlocality

In this chapter, we introduce the fundamental theoretical concepts that will be used in rest of the thesis: basic facts about entanglement and entanglement measures; the role of entanglement as a resource in metrology; the entanglement properties of many-body quantum system; Bell correlations and important class of Bell inequalities for many-body systems. Also the Chap. 3 will be devoted to preliminaries, but it will be completely focused on tensor networks numerical methods.

2.1 Entanglement

In this section we overview the entanglement properties of finite-dimensional Hilbert spaces. In Sec. 2.1.1 we introduce the concepts of **separable** and **entangled** states, for bipartite and multipartite systems. The **Von Neumann entanglement entropy** is presented as the entanglement measure for bipartite pure states. The multipartite case is more involved, we underline the differences with respect to the bipartite scenario and the open problems. Entangled states play a crucial role also in **quantum metrology** [Sec. 2.1.4]: we in particular review some fundamental results for spin systems, where the amount of squeezing of a state is related to its degree of multipartite entanglement.

2.1.1 Entanglement in the bipartite scenario

Let us restrict to the finite dimensional case and set $\mathcal{H}_A = \mathbb{C}^m$ and $\mathcal{H}_B = \mathbb{C}^n$, the model system is fully described by the vectors in the tensor product $\mathcal{H} = \mathcal{H}_A \otimes \mathcal{H}_B$.

Pure states case. We call a **pure state** $|\psi_{AB}\rangle \in \mathcal{H}$ **separable** (or **product**) if it can be written as a product state between two vectors $|\psi_A\rangle \in \mathcal{H}_A$ and $|\psi_B\rangle \in \mathcal{H}_B$, *i.e.*

$$|\psi_{AB}\rangle = |\psi_A\rangle \otimes |\psi_B\rangle. \tag{2.1}$$

Otherwise the pure state is **entangled**.

Given a bipartite pure state $|\psi_{AB}\rangle$, the *separability problem*, *i.e.* the problem of knowing if the state is separable or entangled, can be solved thanks to the **Schmidt's theorem**, which states that the following decomposition (**Schmidt decomposition**) holds [1]:

$$|\psi_{AB}\rangle = \sum_{i=1}^{r} a_i |u_i\rangle |v_i\rangle, \tag{2.2}$$

where $\{|u_i\rangle_A\}$ and $\{|v_i\rangle_B\}$ are convenient orthonormal vectors respectively in $\mathcal{H}_A$ and $\mathcal{H}_B$ with $m \leq n$. The numbers $a_i > 0$ $(i = 1, \ldots, r)$ are the **Schmidt numbers** and satisfy the condition $\sum_{i=1}^{r} a_i^2 = 1$ with $r \leq m$. If $r = 1$ the state is separable, otherwise is entangled [2].

An important class of entangled states are the **maximally entangled states** $|\Phi_+^d\rangle = \frac{1}{\sqrt{d}} \sum_{i=1}^{d} |u_i\rangle|v_i\rangle$, where $d = \min\{m, n\}$ (the reason for such name will be clear in Sec. 2.1.3 after the introduction of the entanglement measures.)

Mixed states case. Pure states are not generic and a complete theory of the entanglement must involve **mixed states** [3]. For such states, not only the detection of entanglement is an NP-hard problem [Gur03], but also the definition of separability (even in the simplest bipartite case) is not trivial and has been given only relatively later: according to Werner [Wer89] a **bipartite mixed state** ρ_{AB} is said to be **separable** *iff* it admits the following decomposition:

$$\rho_{AB} = \sum_{i=1}^{K} p_i \rho_i^{(A)} \otimes \rho_i^{(B)}, \tag{2.3}$$

for some integer $K \leq (mn)^2$, where $\rho_i^{(A)} = |\phi_i^{(A)}\rangle\langle\phi_i^{(A)}|$ and $\rho_i^{(B)} = |\chi_i^{(B)}\rangle\langle\chi_i^{(B)}|$, $|\phi_i^{(A)}\rangle$ and $|\chi_i^{(B)}\rangle$ are pure states in $\mathcal{H}_A$ and $\mathcal{H}_B$ respectively and the $0 < p_i < 1$

[1] To sketch the proof, let us first write the state of the bipartite system in a generic form $|\psi_{AB}\rangle = \sum_{i,j} \psi_{ij} |i\rangle_A |j\rangle_B$, where $\{|i\rangle_A\}$ and $\{|j\rangle_B\}$ are orthonormal bases in $\mathcal{H}_B$ and $\mathcal{H}_B$. The complex coefficients ψ_{ij} can be seen as a $m \cdot n$ rectangular matrix $[\Psi]_{ij}$ that can be decomposed by a *singular value decomposition*, obtaining $[\psi]_{ij} = U_{il} D_{ll} V_{lj}^{\dagger}$, where U and $V^{\dagger}$ are unitary matrix and D is a non-negative diagonal matrix whose elements are the Schmidt coefficients. This decomposition will be also important later in Chap. 3: the *matrix product state* representation of the quantum states, is essentially made by repeated singular value decompositions.

[2] In Chap. 5, in the context of the *topological phases of matter*, we will reinterpret the ladder of the Schmidt numbers as the spectrum of an "entanglement Hamiltonian" H_A such that $\rho^{(A)} = e^{-H_A}$, where $\rho^{(A)} = Tr_B \rho_{AB}$ is the trace with respect to the subsystem B of the density matrix $\rho_{AB} = |\psi_{AB}\rangle\langle\psi_{AB}|$. In this different fashion, we will also refer to the Schmidt numbers as *entanglement spectrum*

[3] Actually, every realistic physical system is coupled with other (more or less complex) systems and a perfect isolation is ultimately impossible (even though in some circumstances, theoretical and experimental well motivated approximations allow to describe a system as closed). In these cases the density matrix is the most general object which describes a quantum state: pure states and statistical mixtures.

are probabilities ($\sum_i^K p_i = 1$). In other words, ρ_{AB} is a convex combination of tensor products $\rho_i^{(A)} \otimes \rho_i^{(B)}$.

This definition, in addition to being merely formal, has actually an operational meaning. In fact Eq. (2.3) represent the most general state that can be prepared by means of only **local operations and classical communications** (**LOCC**) [Ben+96] [4]. Alternatively one can say that [PV14] *"entanglement may be defined as the sort of correlations that may not be created by LOCC alone"*. Even if we shall not directly deal with mixed states in this thesis, their importance is hardly underestimable from the theoretical point of view. Definition of separability in [Wer89] was in fact provided with the aim to show an example of mixed entangled bipartite yet admitting a *local hidden variable* description, a situation impossible to encounter in the pure case. This proved the nonequivalence between the concepts entanglement and *nonlocality* (namely, the violation of some Bell inequalities) which, as will be clearer in Sec. 2.3, are different resources for quantum information and communication.

2.1.2 Entanglement in the multipartite scenario

In the multipartite scenario $\mathcal{H} = \mathcal{H}_1 \otimes \mathcal{H}_2 \otimes \cdots \otimes \mathcal{H}_N$, the situation is more involved and the definition of separability admits many different generalizations, since there are many ways of grouping the parties [GT09]. Directly considering the general case of mixed states, we start giving the definition of k-**separability**, which resembles the notion of separability. Let us then label the n parties as $[n] = \{1, \ldots, N\}$ and consider the possible partitions into k nonempty, pairwise disjoint subsets: $A_1, \ldots, A_k \subsetneq [n]$, $A_i \cap A_j = \emptyset$ for $i \neq j$ and $\cup_i^k A_i = [n]$. We call $\mathcal{P}_{sep}^k$ the set of all such possible partitions of $[n]$. Then, a state $\rho \in \mathcal{D}(\mathcal{H})$ is k-**separable** if admits the following convex decomposition:

$$\rho = \sum_{p \in \mathcal{P}_{sep}^k} \lambda_p \sum_i \lambda_i^p \bigotimes_{A_j \in p} \rho_i^{(j)}, \tag{2.4}$$

for $0 < \lambda_p < 1$, $\sum_p \lambda_p = 1$ and $0 < \lambda_i^p < 1$, $\sum_i \lambda_i^p = 1$.

Alternatively, one can classify multipartite entangled states with the notion of k-**producibility** [Tót12; Hyl+12; Alo+19]. The partitions $\mathcal{P}_{prod}^k$ of $[n]$ are now taken in a way that subsystems A_i contain at most k elements. A pure state $|\psi\rangle \in \mathcal{H}$ is k-**producible** with respect to $\mathcal{P}_{prod}^k$ *iff* it can be written as:

$$\rho = \sum_{p \in \mathcal{P}_{prod}^k} \lambda_p \sum_i \lambda_i^p \bigotimes_{A_j \in p} \rho_i^{(j)}, \tag{2.5}$$

[4] As perceivable from the name, in the *local operations and classical communications* (LOCC) paradigm two agents, Alice and Bob, are allowed to perform only *local operation* (unitaries and measurements) on their own subsystems $\mathcal{H}_A$ and $\mathcal{H}_B$ respectively. No nonlocal operations on the whole system are allowed. They can furthermore share (in one- or two-way) *classical information (communication)* (bits) through a classical channel, but they cannot share any quantum state.

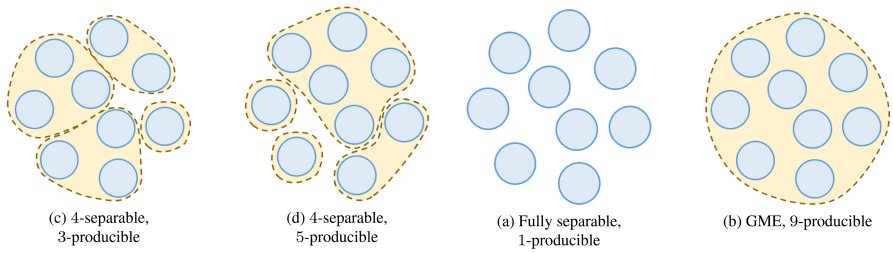

FIGURE 2.1: An illustration of examples of different possible degrees of k-producibility and l-separability for a system of $N = 9$ parties (blue circles). (Reprinted from [Tur+19])

with obvious meaning of notation. A quantum state that cannot be written in the form of Eq. (2.5) is said to have an **entanglement depth** *at least of* $k+1$ or, in other words, that there are at least $k+1$ parties *genuinely entangled* among them. Finally, a state is **genuine multipartite entangled** if it is not $N-1$-producible or, equivalently, if it has an entanglement depth of N. Refer to Fig. 2.1 for a pictorial representation of these definitions.

As we will see in Sec. 2.1.4, k-producibility is related in spin systems to the squeezing of the state. Without any reference to the concrete system, it can be certified by a special class of Bell inequalities which we will introduce Sec. 2.3.

2.1.3 The Von Neumann entanglement entropy

Besides the necessity of distinguishing between entangled and separable states, the *quantification of entanglement* is a fundamental task. Again, in the simplest but important case of bipartite pure state it is possible to show that there exists a *unique* [5] measure of entanglement E, given by the **Von Neumann entropy** S of the bipartition:

$$\begin{aligned} E(|\psi_{AB}\rangle) &= S(\rho_A) = -Tr(\rho_A \log \rho_A) \\ &= S(\rho_B) = -Tr(\rho_B \log \rho_B) = -\sum_i a_i^2 \log a_i^2, \end{aligned} \tag{2.6}$$

where $\rho_{A(B)} = Tr_{B(A)}\rho_{AB}$ is the reduced density matrix for the subsystem $A(B)$. In other words, S is the Shannon entropy of the Schmidt coefficient a_i.

[5] For an axiomatic approach to the entanglement quantification see the review [Hor+09]. Two reasonable constraints that each entanglement measure should satisfy are: (1) *monotonicity under LOCC*: a LOCC operation cannot increase entanglement; (2) entanglement vanishes on separable states. Furthermore, the Von Neumann entropy is the *unique* measure which satisfy the following three formal conditions: (1) *normalization*: it behaves in an "information theoretic way" on maximally entangled states, *i.e.* it counts e-bits $E(|\Phi_+^d\rangle) = \log d$; (2) *asymptotic continuity*: if $\|\rho - \sigma\|_1 \to 0$, $|E(\rho) \to E(\sigma)|$ (ρ and σ states); (3) *additivity*: for several copies of the system, $E(\psi_{AB} \otimes \phi_{AB}) = E(\psi_{AB}) + E(\phi_{AB})$.

This definition makes particularly clear the information contents of entanglement entropy. We also refer to the Von Neumann Entanglement entropy simply as **entanglement entropy** (**EE**). In the rest of this section we mainly focus on the properties of EE to characterize MBQS.

2.1.4 Entanglement and quantum metrology

Quantum metrology [6] is that branch of physics which aims to exploit quantum properties to improve the measurement precision. The precise measurement of a physical quantity is often indirect, inferred by the statistical occurrences of another one, which is the output of the experiment. The paradigmatic framework is an interferometric setting, where the target quantity depends on the precise determination of a phase shift.

Let us consider the case of ν independent measurements where, as input-state ρ_0 we have an N-particle system, whose degrees of freedom are two. In the quantum case we restrict to states of N spin-$1/2$ components. An output μ is measured to have an estimation $\Theta(\mu)$ of the unknown quantity θ. By only using classical states, the statistical precision $\Delta\theta$ in such estimation is bounded by the so-called **Cramér-Rao bound**

$$\Delta\theta \geq \Delta\theta_{CR} = \frac{1}{\sqrt{F_C(\theta)\nu}}. \tag{2.7}$$

$F_C(\theta)$ is the (**classical**) **Fisher information**

$$F(\theta) = \sum_{\mu} \frac{1}{P(\mu|\theta)} \Big(\frac{\partial P(\mu|\theta)}{\partial\theta}\Big)^2, \tag{2.8}$$

where $P(\mu|\theta)$ is the likelihood function, the probability of obtaining μ conditioned by the measurement of θ.

The **quantum Fisher information** $F_Q(\theta)$ is defined as the Fisher information maximized over all the possible quantum measurements. By this extension, the Cramér-Rao bound is improved to the **quantum Cramér-Rao bound**

$$\Delta\theta_{CR} \geq \Delta\theta_{QCR} = \frac{1}{\sqrt{\nu F_Q(\theta)}}, \tag{2.9}$$

since $F_C(\theta) \leq F_Q(\theta)$. The quantum Fisher information is upper bounded: $F_Q \leq N^2$. By considering only separable states one can reach the **standard quantum limit**

$$\Delta\theta_{SQL} = \frac{1}{\sqrt{N\nu}}. \tag{2.10}$$

[6] For a comprehensive review see [Pez+18] and references therein.

To beat this limit, using entangled states as input is a necessary (but not sufficient) condition. In particular, a large Fisher information requires large entanglement depth: for genuine multipartite entanglement F_Q is maximized ($F_Q = N^2$) and the maximum possible sensitivity in phase estimation, the so-called **ultimate Heisenberg limit**, is achieved

$$\Delta\theta_{HL} = \frac{1}{N\sqrt{\nu}}. \tag{2.11}$$

More in general, the quantum Fisher information is a witness for the entanglement depth, in fact if

$$\frac{F_Q}{N} \geq k, \tag{2.12}$$

the state has an entanglement depth of at least $k+1$.

Let us consider spin states and the collective spin operators $J_\gamma = \sum_{i=1}^{N} \frac{\sigma_{\gamma_i}}{2}$ where σ_{γ_i} are Pauli matrices, $\gamma = x, y, z$. Let $\vec{J} = \{\sigma_x, \sigma_y, \sigma_z\}$ and $\hat{n} \cdot \vec{J} = \vec{J}_n$ the projection of $\vec{J}$ within the direction $\hat{n}$. $F_Q(\theta) \leq 4(\Delta\vec{J}_n)^2 \leq (2J)^2 \leq N^2$, where $\sqrt{J(J+1)}$ is the spin length. Therefore the most sensitive spin states are those with maximum spin $J = N/2$, which are symmetric for exchange of particles.

Among those entangled states useful in metrology, an important position is occupied by the **spin-squeezed states**, which are states with squeezed variance along a direction at the expense of an antisqueezing along an orthogonal direction (in order to satisfy the Heisenberg principle). To characterize them, suppose to rotate the multi-spin state around an axis $\hat{n}$ perpendicular to the mean spin direction $\hat{s}$, a **spin squeezing parameter** is introduced:

$$\zeta^2 = \frac{N(\Delta\vec{J}_\perp)^2}{\langle\vec{J}_s\rangle^2}, \tag{2.13}$$

where $\perp$ is a third directions orthogonal to both s and $\hat{n}$. If $\zeta^2 < 1$, the state is spin-squeezed along $\perp$ [KU93]. Importantly, optimal spin-squeezed states saturate the Heisenberg inequality $(\Delta\vec{J}_\perp)^2(\Delta\vec{J}_n)^2 \geq |\langle\vec{J}_s\rangle|^2/4$, whereas a lower bound for the squeezing parameter is $\zeta_a^2 \geq 2/(N+2)$.

A fundamental relation between spin-squeezing and Fisher information is useful to detect k-particle entanglement in spin systems. In fact from Eqs. (2.12)-(2.13) it follows that if

$$\zeta^{-2} \geq k, \tag{2.14}$$

the state has an entanglement depth of at least $k+1$.

2.2 Many-body quantum systems: area law for the entanglement entropy

Quantum information theory paves the way for an alternative approach to the study of the **many-body quantum systems** (**MBQS**) [Ami+08]. From a fundamental point of view, it is interesting to characterize ground states and critical phenomena of MBQS by involving only exclusively quantum quantities. To this purpose, we focus here on the so-called **area law for the EE** and its violations. We limit the review to the context of **MBQS on lattices**, where many rigorous theoretical results are available and experimental implementations are very sophisticated (in particular *ultracold atoms in optical lattices* [BDZ08; LSA12] and *trapped ions* [PC04] are widely used thanks to their scalability and tunability).

Taking a bipartition of $\mathcal{H}$ and randomly picking a state from one block, the resulting block EE is nearly maximal and, just as in the classical case, is an *extensive* thermodynamic quantity [7]. We refer to this behavior as a *volume law* scaling of EE. However, this quite generic property fails in a very special but yet important case: the ground states of gapped-local Hamiltonians. For these states, an **area law** for the EE holds [ECP10], *i.e.* the EE grows proportionally the surface of the blocks of the bipartition [Fig. 2.2]. Formally, let R be a subsystem of a lattice, consisting of contiguous sites, ρ_R its reduced density matrix and ∂R its boundary, having an area law means that

$$S(\rho_R) = \mathcal{O}(\partial R). \tag{2.15}$$

Concrete versions of bound (2.15) depend on the particular geometry of the system taken into account (dimensionality, topology of bipartition, etc.). Well established results are available mostly for one-dimensional systems. Here, for spin-Hamiltonians with short-range interactions, a logarithmic violation of the area law is characteristic of criticality [Sec. 2.2.2]. Less clear is the situation in higher dimensions [Sec. 2.2.3] where, although area law is fulfilled for non-critical systems and several forms of the bound (2.15) have been calculated, there are not clear violations of the bound at criticality. Long-range interactions Hamiltonians [Sec. 2.2.4] deserve a separate discussion since there is still a lack of general results: for example, violations of the area law may occur even for gapped systems, but weaker versions of the theorem are restored if interactions decay fast. Finally, let us note that the area law lies behind the reason for the success of **tensor networks numerical methods** we will introduce in Chap. 3.

[7] Sen proved [Sen96] that randomly piking up a state from a Hilbert space of dimension nm, the average entropy of a subsystem of dimension m with $m \leq n$ is $\langle S(\rho_A)\rangle = \left(\sum_{k=n+1}^{nm} 1/k\right) - \frac{m-1}{2n}$. Asymptotically for $1 \ll m \leq n$ the formula reduces to $\langle S(\rho_A)\rangle \simeq \log m - \frac{m}{2n}$, where $\log m$ is just the maximum entropy the subsystem can have (maximally entangled state).

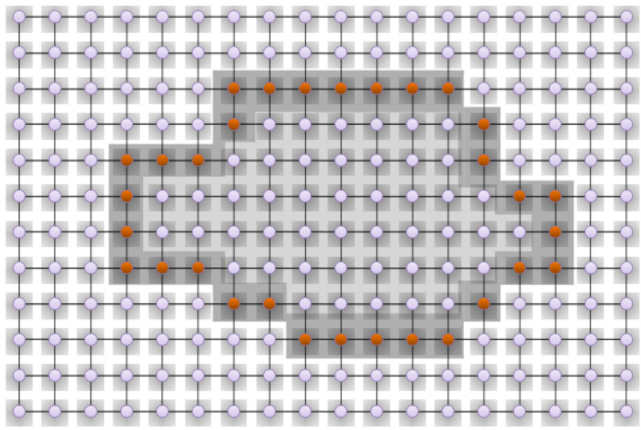

FIGURE 2.2: A bidimensional lattice L is bipartite in two regions R (shaded-grey) and $L \setminus R$: if the area law [Eq. (2.15)] holds, the Von Neumann entanglement entropy scales as the length of the boundary of bipartition (the number of red sites). (Reprinted from [Tur+15a])

2.2.1 Area law in one-dimensional non-critical systems

For one dimensional ($1D$) lattice systems a general result was provided by Hastings [Has07]. Let $L = \{1, \dots, N\}$ be a N-sites lattice, with arbitrary local dimension d and take as sub-region R the block of spins $R = \{1, \dots, n\}$, $n < N$. Consider an Hamiltonian with only nearest-neighbors interactions [8]:

$$H = \sum_{i,i+1} H_{i,i+1}, \tag{2.16}$$

where each element $H_{i,i+1}$ has support on sites i and $i+1$. Another requirement is that interactions are bounded by a constant: $\|H_{i,i+1}\| \leq J$. Finally, let the Hamiltonian be *gapped* with an unique ground state, *i.e.* there must be a finite energy gap ΔE between the ground state and the first excited state (the system is not critical). Under these assumption the Hastings' theorem states that

$$S(\rho_R) \leq 6c_0\xi' \log(\xi') \log(d) 2^{\xi' \log(d)}, \tag{2.17}$$

for some numerical constant c_0 of order of unity and $\xi' = \max\{2v/\Delta E, \xi_C\}$. v is the velocity of sound and ξ_C another constant of the order of unity. The last two quantities appear as consequence of the *Lieb-Robinson bound* which in words expresses a causality principle: there exists a causality cone for the spread

[8] Without loss of generality any local short-range-interactions Hamiltonian can be viewed as a nearest-neighbors one, grouping more sites in a single site.

of correlations in a lattice, *i.e.* a bound for the velocity (and then the time) the information can propagate [9].

Finally, note that bound (2.17) is independent of R because in $1D$ the boundary of the set R of contiguous spins is simply just one or two spins (depending on the chain has respectively open or periodic boundary conditions). Hence in $1D$ EE is always upper bounded by a constant, a crucial property behind the success of the DMRG [Sec. 3.3].

2.2.2 One-dimensional critical systems: logarithmic corrections to area law

A general feature of quantum phase transitions is that approaching the critical point the gap gets closed. Therefore a violation of the area law is expected. However, for continuous phase transitions (second and topological phase transitions) the criticality is also accompanied by a diverging correlation length and because of that the system is invariant under global dilatation of the length scale $l \to \lambda l$. In such a case a theorem of Polyakov holds (see [Mus10], Chap. 10, for a discussion): *a physical system with local interactions that is invariant under translations, rotations, and a global dilatation, is also automatically invariant under the larger class of conformal transformations*. Namely, those transformations that preserve the angles.

Studying criticality with the conformal group of symmetries [Vid+03; CC09] allowed one to prove that block EE scales logarithmically with the number of components of the bipartition, with a universal prefactor that is the **central charge** of the specific **conformal symmetry** the system possesses at criticality. For a spin chain of length N with open boundary conditions, one has [CC04]

$$S(l) = \frac{c}{6} \log \left[\frac{N}{\pi a} \sin \left(\frac{\pi}{N} n \right) \right] + c_1, \tag{2.19}$$

where c is the central charge, n is the length of the bipartition (the formula is symmetric for $n \to N - n$), a is the lattice spacing and c_1 is a non universal constant. As examples, $c = 1/2$ for the Ising model and $c = 1$ for XX and XXZ chains [Vid+03].

[9] The Lieb-Robinson theorem [LR72] states that on a lattice and for local Hamiltonians with bounded interaction strength, there exists a velocity v and length scale ξ_C such that for any two operators A and B with support on sets X and Y respectively,

$$\|[A(t), B]\| \leq c\|A\|\|B\| \exp\{-\xi_C \text{dist}(X, Y)\}, \tag{2.18}$$

for $|t| \leq 1/v$, where $A(t) = \exp\{iHt\} A \exp\{-iHt\}$ and where the distance between sets X and Y is given by $\text{dist}(X, Y) = \min_{i \in X, j \in Y}(|i - j|)$.

2.2.3 Area law in higher dimensions

For higher D-dimensional lattices a number of results for concrete systems (fermionic and bosonic) suggest that an area law still holds (see [ECP10] for a review). On the other side, logarithmic violations at criticality do not seem to hold.

In $D > 1$, technical difficulties arise especially because in high dimension the block surface can be a nontrivial object. However, for gapped phases, Masanes could prove in [Mas09] that an area law with logarithmic corrections holds for the low energy eigenstates (ground state and first excited states):

$$S(\rho_R) \leq c|\partial R| \log(|R|)^k, \tag{2.20}$$

where $|R|$ is of order of the number of lattice sites in R, c is a system-dependent constant ad k is an integer ($k = 1$ for connected cubic regions, $k = D$ for arbitrary regions). Exact forms of bound (2.20) can be found in the original paper [Mas09] for different underlying hypothesis generally more restrictive with respect to the $1D$ case. In fact, besides requiring gapped-local Hamiltonian and bounded interactions (the Lieb-Robinson theorem is still part of the proof), some constraints have to be added on the decay of the correlations. Finally, note that logarithmic correction in (2.20) does not compromise the behavior of the EE being still a true area low, at least in the asymptotic limit, because $|\partial R| \log(|R|)^k/|R| \to 0$ for $|R| \to \infty$ with $k > 0$.

2.2.4 Area law in systems with long-range interactions

Systems with long-range interactions are not an anomaly in nature [Cam+14]. In effect, short-range interactions are often only a very good approximation of very fast decaying couplings. For instance, in bosonic ultra-cold quantum gases, besides van der Waals interactions, approximated with a contact potential, long-range *dipolar-dipolar interactions* are responsible for many intriguing effects [Lah+09]. For lattice spin systems, violations of the area law have been numerically observed also in gapped phases. As a typical example, let us consider spin-1/2 models with polynomial $J(\alpha) \propto 1/r^\alpha$ decays of coupling strength. Violation of the area law are found, often depending on α (reasonably one can expect that for large α the interactions behave as short-range). In [KLT12] for anti-ferromagnetic interactions, clear logarithmic violations appear for $\alpha \lesssim 1$ deep inside the paramagnetic phase. In [Vod+15] the latter system and also a long-range Kitaev chain have been proven break the conformal symmetry at criticality for $\alpha \lesssim 1$, with an anomalous big values of the central charge. Quite general results for lattice spin Hamiltonian of arbitrary dimension D and power-law decay of correlations $1/r^\alpha$ was presented in [Gon+17], where it was proved that for $\alpha > 2D + 2$ the area law is satisfied if the ground state can be adiabatically connected to another satisfying the area law. In conclusion, previous results show that short-range correlations are not strictly necessary to have an area law of the EE.

From an experimental point of view, exponentially or power-law decaying long-range interactions are now possible to be realized for the $1D$ case, see for example [Ric+14] or [Dou+15] for an experimental proposal.

2.3 Nonlocality

Quantum mechanics can give rise to a kind of correlations which, according to the terminology in the EPR paper [EPR35], are not compatible with the paradigm of *local realism*. In the modern terminology, are called **nonlocal** (or **EPR correlations**), those correlations among the results of local measurements which do not admit a description in terms of **local hidden-variable** models [Bel64; Boh51; Bel66; Bel04; Bru+14]. From an operational point of view, the latter definition applies to correlations violating some **Bell inequalities** (**BIs**). These are inequalities formulated in terms of linear combinations of conditional probabilities, resulting from an experiment involving only local measurements performed on a composite system.

As already pointed out in the introduction (Chap. 1), the concept of **nonlocality** is strictly related, although nonequivalent, to that of **entanglement**. On the one hand, it has been proven that any entangled pure state is nonlocal [Gis91; PR92; GG17], but it is possible to construct entangled mixed states which do not violate any BI [Wer89]. On the other hand, this nonequivalence manifests also in somehow counterintuitive behaviors when characterizing quantum states: for example, it is known that, in many cases, violation of BIs is larger for partially entangled states than for maximally entangled states [MS06], with nontrivial consequences in the use of entanglement and nonlocality as resources in quantum information protocols.

These differences, proven in few-body systems, may have fundamental impacts in many-body systems, where the role of nonlocality is fairly unexplored, although much is know about entanglement. One reason for such difficulty lies in the extreme difficulty in deriving BIs when the number of parties of a Bell experiment increases. In fact, as we shall see, the number of BIs necessary to fully characterize the set of local behaviors of a many-body system grows exponentially with the number of parties.

Besides computational complexity, there are also experimental difficulties. A many-body Bell experiment, in fact, requires the measurement of a product of as many observables as the number of parties but at the state of art experimental techniques this is extremely difficult (although in principle possible [Bak+09; She+10]).

In this section, we review the main concepts related to nonlocality and Bell experiments in the general framework of the **device-independent quantum information processing** [Sec. 2.3.1], where all the relevant quantities characterizing the experiments are the conditional probabilities to obtain a vector of outputs, given the inputs [Ací+07]. In Sec. 2.3.2 the definitions of **local correlations**

and **nonsignaling correlations** are given, with the corresponding characterization in terms of **polytopes** in the probability spaces. **Quantum correlations** are also defined but they do not form a polytope. In the same section, we also show that in the case of dichotomic local measurements (two outputs) conditional probabilities have a useful interpretation in terms of expectation values. In Sec. 2.3.3 a formal definition of BIs is provided. Finally, in Sec. 2.3.4 we face the many-body case. The recent results of Tura *et al.* in [Tur+14; Tur+15b] are illustrated: they found a class of analytic **permutationally invariant BIs involving only one- and two-body correlators**, which are violated by relevant many-body states and can be experimentally tested. The amount of violation of these BIs provides also a certification of the entanglement depth, in alternative to the squeezing measurements.

2.3.1 Device-independent formulation of Bell inequalities

In order to have a theory robust against experimental imperfections and the derivation of BIs independent of any concrete experimental realization, we will work in the modern framework of **device-independent quantum information processing** (**DIQIP**) [Ací+07]. In the DIQIP approach, each party is imagined as a *black box*, where an agent is able to locally select an *input* (namely a button; there is one button for each possible local *measurement setting*) in order to get an *output* (the local *measurement outcome*) [Fig. 2.3]. No assumptions are made about the contents of the boxes.

A **Bell experiment** (or **scenario**) is described by a triplet of numbers (N, m, Δ). N is the number of parties (boxes); each party is labeled by an index i. In a run of the experiment, the i-th party performs the measurement $\mathcal{M}_{x_i}^{(i)}$, where $x_i \in \{1, \dots, m\}$. Each measurement x_i has Δ outcomes $a_i \in a_1^{x_i}, \dots, a_\Delta^{x_i}$ [10]. The simplest Bell experiment is $(2, 2, 2)$ and the celebrated *Clauser-Horne-Shimony-Holt* (CHSH) inequality [Cla+69] is an example.

In the DIQIP approach, one considers probability distributions of results as the only relevant quantities. After many repetitions of the experiment, one obtains the **joint conditional probabilities** or **correlations**

$$P(\vec{a}|\vec{x}) := P(a_1, a_2, \dots, a_N|x_1, x_2, \dots, x_N) \geq 0, \tag{2.21}$$

denoting the probability to get the outputs $a_1, a_2 \dots a_N$ once the measurements $x_1, x_2, \dots x_N$ are performed. To get a valid probability distribution, each $P(\vec{a}|\vec{x})$ must be *non-negative*. There are $\Delta^N m^N$ possible combinations of inputs and outputs $\vec{a}|\vec{x}$. The available information is the collection $\{P(\vec{a}|\vec{x})\}$ of these probabilities, giving the required probability distribution. From a geometric perspective, one can imagine conditional probabilities $P(\vec{a}|\vec{x})$ as vectors $\vec{P} \in \mathbb{R}^D$, with

[10] For the sake of clarity and since we will concern with situations that are symmetric under permutation of the parties, we limit to the case where the number Δ and m of I/O are the same for any box. Furthermore, continuous outputs or/and input can be considered (see [Bru+14] for references).

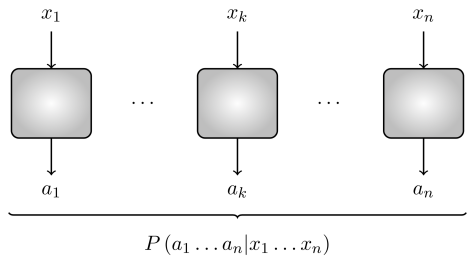

FIGURE 2.3: Schematic picture of the Bell experiment in the DIQIP approach. Each party is a black box, where an agent locally selects a measurement setting or input x_i to get an output (the local measurement outcome). The results of a repetition of the experiments are collected in vectors of conditional probabilities. (Reprinted from [Tur+15a])

$D = (\Delta m)^N$. Actually, components of $\vec{P}$ are not independent but satisfy some linear constraints. First of all, a **normalization condition** is required:

$$\sum_{a_1,\dots,a_N=1}^{\Delta} P(a_1, a_2, \dots, a_N | x_1, x_2, \dots x_N) = 1. \tag{2.22}$$

Thanks to non-negativity and normalization, the set of conditional probabilities (2.21) is an affine subspace of $\mathbb{R}^D$ of dimension $d = (\Delta - 1)^N m^N$, the **probability space** $\mathcal{P}$. $\mathcal{P}$ is a **polytope** [Pit86] (a bounded polyhedron), *i.e.* a convex hull fully described by a finite list V of extreme points, its *vertices* $v \in V$. The number of vertices of $\mathcal{P}$ is D [11]. We will encounter two more polytopes in next section, both contained in $\mathcal{P}$: one is the set $\mathcal{NS}$ of *no-signaling* behaviors, the other one is the set $\mathcal{L}$ of *local* behaviors, whose vertices have the important physical interpretation of *deterministic* local behaviors, while its facets are the Bell inequalities.

2.3.2 No-signaling, local and quantum correlations

No-signaling constraint. Besides normalization, it is physically reasonable to impose $P(\vec{a}|\vec{x})$ also a **no-signaling constraint**, which expresses causality when parties are spacelike separated, *i.e.* the impossibility of a party to instantaneously influence the others by its measurement choices. Mathematically, this requires

[11] Thanks to convexity, each vector $\vec{P}$ of the polytope $\mathcal{P}$ can be always expressed as the convex sum

$$\vec{P} = \sum_{v \in V} P_v v, \tag{2.23}$$

for $0 \leq P_v \leq 1$, $\sum_{v \in V} P_v = 1$

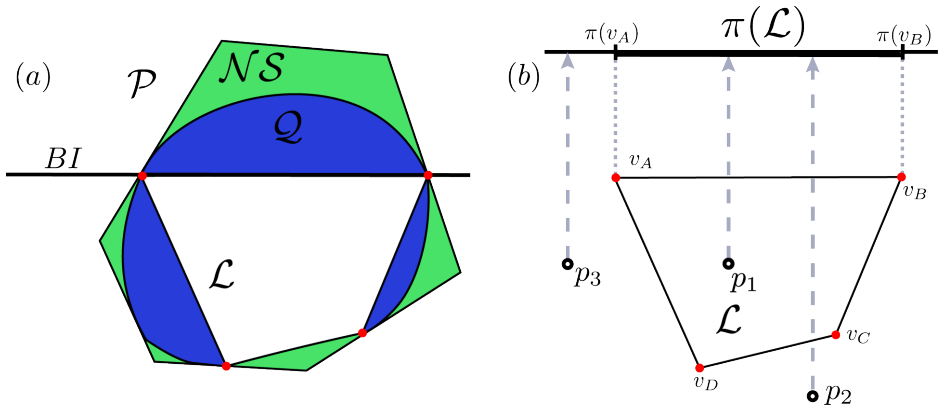

FIGURE 2.4: (a) Graphical representation of the chain of inclusions in Eq. 2.35: $\mathcal{L} \subsetneq \mathcal{Q} \subsetneq \mathcal{NS} \subsetneq \mathcal{P}$. Local polytope $\mathcal{L}$ is strictly contained in the set $\mathcal{Q}$ of quantum correlations (which is not a polytope), in turn strictly contained in the no-signaling polytope $\mathcal{NS}$. Each facet of $\mathcal{L}$ is a BI. Red dots v_i are the vertices of $\mathcal{L}$. (b) Polytope $\mathcal{L}$ is projected in a lower dimensional one $\pi(\mathcal{L})$ (by considering only low-order correlators). Vertices are projected into vertices, but some of them will fall in the interior of $\pi(\mathcal{L})$ (in general external points of $\mathcal{L}$ are projected in external points of $\pi(\mathcal{L})$, this is the case for v_A and v_B). Projection does not come for free: whereas local behaviors still remain local (point p_1), there are some nonlocal behaviors which are not correctly evaluated (for example point p_2). Importantly, if a violation of PIBI is found, the corresponding point is nonlocal also in the general case (this is the case for point p_3).

that *marginal probability distributions* among all parties except the k-th, are independent of x_k:

$$\begin{aligned} &\sum_{a_k=1}^{\Delta} P(a_1, a_2, \ldots, a_k, \ldots, a_N | x_1, x_2, \ldots, x_k, \ldots, x_N) \\ &= P(a_1, a_2, \ldots, a_{k-1}, a_{k+1}, \ldots, a_N | x_1, x_2, \ldots, x_{k-1}, x_{k+1}, \ldots, x_N), \end{aligned} \tag{2.24}$$

requiring the existence of well defined conditional probabilities $P(a_i|x_i)$ for each box. The subset $\mathcal{NS}$ of $\mathcal{P}$ of no-signaling correlations is also a polytope of dimension $\dim \mathcal{NS} = (m(\Delta^N - 1) + 1)^N - 1$.

Local (or classical) correlations. In terms of conditional probabilities we can now formalize the central notion of **locality**. In general, correlations (2.21) could be not factorizable, *i.e.* $P(a_1, \ldots, a_N | x_1, \ldots, x_N) \neq \prod_{i=1}^{N} P(a_i|x_i)$, denoting *statistical dependence* among local measurements. There is nothing strange in such

dependence, which does not mean there is any influence at distance among the parties: in a local theory, statistical dependence takes place if the subsystems have interacted in the past. In fact, conditional probabilities factorize if we are able to exactly reconstruct the full story of the parties (and the interactions among them), encoded in a **local hidden-variable** (**LHV**) λ:

$$P(a_1, a_2, \ldots, a_N|x_1, x_2, \ldots, x_N) = P(a_1|x_1, \lambda)P(a_2|x_2, \lambda)\cdots P(a_N|x_N, \lambda), \tag{2.25}$$

meaning that in the experiment, the probability of obtaining each a_i depends only on the local measurement x_i and on λ, but not on other measurements and outcomes. λ is called "hidden" because in practice it could be not accessible. In general, λ may also vary along the experimental runs and it is substituted by a probability distribution $q(\lambda)$:

$$\begin{aligned} &P(a_1, a_2, \ldots, a_N|x_1, x_2, \ldots, x_N) \\ &= \int_\Lambda d\lambda q(\lambda) P(a_1|x_1, \lambda)P(a_2|x_2, \lambda)\cdots P(a_N|x_N, \lambda), \end{aligned} \tag{2.26}$$

where $\lambda \in \Lambda$, $q(\lambda) \geq 0$ and $\int_\Lambda d\lambda q(\lambda) = 1$. Such a factorization formally expresses the condition of locality in Bell experiments, meaning the capability of simulate the experiment with a **local hidden-variable model**.

Joint probability correlations can equivalently factorize in terms of **deterministic LHV model**. In a deterministic model, given x_i, the outcome of a box is completely determined by the local variable λ; the deterministic conditional probabilities $D(a_i|x_i, \lambda)$ can assume only two values: 1 for the fixed (deterministic) outcome of the measure and 0 otherwise, *i.e.* $D(a_i|x_i, \lambda) = \delta(a_i - a_i^{x_i})$. Eq. (2.26) now reads:

$$\begin{aligned} &P(a_1, a_2, \ldots, a_N|x_1, x_2, \ldots, x_N) \\ &= \sum_\Lambda q_\lambda D(a_1|x_1, \lambda)D(a_2|x_2, \lambda)\cdots D(a_N|x_N, \lambda). \end{aligned} \tag{2.27}$$

The set of local (deterministic) strategies is a *convex polytope*, the important **Bell polytope** $\mathcal{L}$ [Fro81; Pit86], whose $(\Delta m)^N$ vertices are just the local deterministic behaviors $D(a_i|x_i, \lambda)$. Since deterministic strategies satisfy no-signaling constraint, $\mathcal{L} \subset \mathcal{NS}$ [12].

[12]The no-signaling property of deterministic strategies are proven as follows:

$$\begin{aligned} &\sum_{a_k=1}^{\Delta} P(a_1, \ldots, a_k, \ldots, a_N|x_1, \ldots, x_k, \ldots, x_N) \\ &= \sum_\Lambda q_\lambda D(a_1|x_1, \lambda)\cdots \sum_{a_k=1}^{\Delta} D(a_k|x_k, \lambda)\cdots, D(a_N|x_N, \lambda) \\ &= P(a_1, \ldots, a_{k-1}, a_{k+1}, \ldots, a_N|x_1, \ldots, x_{k-1}, x_{k+1}, \ldots, x_N). \end{aligned} \tag{2.28}$$

It is worth noting that no assumptions about the underlying theory have been done so far, in particular no mention about classicality: (formal notion of) locality [Eqs. (2.26, 2.27)] is the only assumption behind the definition of the local polytope. However, being classical physics local, the local polytope is commonly interpreted as **classical polytope** while the related probability distributions (2.26, 2.27) correspond to our understanding of *classical correlations between local independent measures*.

Quantum correlations. When the system is in a quantum state and quantum observables are involved, the vectors $\vec{P}$ of **quantum conditional probabilities** are predicted via the Born's rule:

$$P(a_1, a_2, \dots, a_N|x_1, x_2, \dots x_N) = Tr(\rho \Pi_{x_1}^{a_1} \otimes \Pi_{x_2}^{a_2} \cdots \otimes \Pi_{x_N}^{a_N}). \tag{2.29}$$

$\rho \in \mathcal{H} = \bigotimes_{i=1}^{N} \mathcal{H}_i$ and $\Pi_{x_i}^{a_i}$ are measurement operators acting on $\mathcal{H}_i$ [13]. Set $\mathcal{Q}$ of quantum correlations is convex but is not a polytope [Pit86]. Using similar arguments as in footnote 12, one proves that quantum correlations satisfy no-signaling constraint, *i.e.* $\mathcal{Q} \subset \mathcal{NS}$.

Dichotomic observables. The above definitions have a convenient interpretation in the $\Delta = 2$ scenario $(N, m, 2)$, which is particularly relevant for this dissertation. For dichotomic measurements, one can, in fact, work with **expectation values** or **correlators** [14], instead of probability vectors (2.21). Provided the redefinition of the outcomes from $\{0, 1\}$ to $\{-1, +1\}$, the relation between the two representations is, for one-body expectation values:

$$\langle \mathcal{M}_{x_i}^{(i)} \rangle = P(a_i = 1|x_i) - P(a_i = -1|x_i), \tag{2.30}$$

For two-body correlators:

$$\langle \mathcal{M}_{x_j}^{(j)} \mathcal{M}_{x_i}^{(i)} \rangle = P(a_i = a_j|x_i) - P(a_i \neq a_j|x_i). \tag{2.31}$$

Similar relations hold for higher order correlators:

$$\begin{aligned} &\langle \mathcal{M}_{x_{j_1}}^{(j_1)} \cdots \mathcal{M}_{x_{j_k}}^{(j_k)} \rangle \\ &= \sum_{a_{j_1} \cdots a_{j_k}} (-1)^{a_{j_1} \oplus a_{j_2} \oplus \cdots \oplus a_{j_k}} P(a_{j_1}, \dots, a_{j_k}|x_{j_1}, \dots, x_{j_k}), \end{aligned} \tag{2.32}$$

with $j_1 < j_2 < \ldots < j_k = 1, \dots, n$, $k = 1, \dots, N$ and $\oplus$ indicates the sum modulo 2. In particular, for quantum observable $\mathcal{M}_{x_i}^{(i)} = \Pi_{x_i}^{(+1)} - \Pi_{x_i}^{(-1)}$. Deterministic

[13] Measurement operators are called also *positive operator-value measures* (POVM). They are positive semi-definite $\Pi_{a_i}^{x_i} \geq 0$ for any a_i and x_i and sum the identity $\sum_{a_i} \Pi_{a_i}^{x_i} = \mathbb{1}$. If dimensions D_i of local Hilbert spaces $\mathcal{H}_i = \mathbb{C}^{D_i}$ are not bounded, we can always assume $\Pi_{a_i}^{x_i}$ to be standard projective *"Von Neumann"* measurements [NC02].

[14] Do not confuse the terminology: for *"correlators"* we mean expectation values or correlation functions, which are different from *"correlations"* that is the conditional probabilities (2.21).

behaviors defining the vertices of $\mathcal{L}$ are those correlators that factorize as:

$$\langle \mathcal{M}_{x_{j_1}}^{(j_1)} \mathcal{M}_{x_{j_2}}^{(j_2)} \cdots \mathcal{M}_{x_{j_k}}^{(j_k)} \rangle_{(det)} = \langle \mathcal{M}_{x_{j_1}}^{(j_1)} \rangle \langle \mathcal{M}_{x_{j_2}}^{(j_2)} \rangle \cdots \langle \mathcal{M}_{x_{j_k}}^{(j_k)} \rangle. \tag{2.33}$$

Relation (2.32) can be inverted to provide the combination of correlators necessary to obtain a given conditional probability vector:

$$\begin{aligned} &P(a_1, a_2, \ldots, a_N | x_1, x_2, \ldots, x_N) \\ &= \frac{1}{2^N} \Big(1 + \sum_{k=1}^{N} \sum_{1 \le j_1 < \cdots < j_k \le N} a_{j_1} \cdot \ldots \cdot a_{j_k} \langle \mathcal{M}_{x_{j_1}}^{(j_1)} \cdots \mathcal{M}_{x_{j_k}}^{(j_k)} \rangle \Big). \end{aligned} \tag{2.34}$$

2.3.3 Bell inequalities

So far in the DIQIP approach, we have defined a series of requirements the probabilities distributions of outcomes from a Bell experiment must satisfy in order to: (1) be true probabilities (normalization condition (2.22)); (2) respect causality (no-signaling constraint (2.3.2)); (3) be local [Eqs. (2.26) and 2.27)]. We also stated that the sets $\mathcal{P}$, $\mathcal{NS}$ and $\mathcal{L}$ are convex polytopes, whereas $\mathcal{Q}$ is convex but is not a polytope.

Importantly, we found the following inclusion-relations among these sets hold: both local and quantum joint conditional probabilities satisfy no-signaling principle, *i.e.* $\mathcal{L} \subset \mathcal{NS}$ and $\mathcal{Q} \subset \mathcal{NS}$ and they are strictly contained in $\mathcal{P}$. In addition, we know that $\mathcal{L} \subset \mathcal{Q}$ because all correlations belonging to $\mathcal{L}$ can be realized with separable (factorizable) states. Thanks to Bell's theorem [Bel64], we know there are quantum states which are nonlocal, therefore $\mathcal{Q} \neq \mathcal{L}$. Finally it is possible to find no-signaling correlations which are not quantum [PR92], hence also $\mathcal{Q} \neq \mathcal{NS}$. In summary, the following chain of inclusions holds [Fig. 2.4(a)]:

$$\mathcal{L} \subsetneq \mathcal{Q} \subsetneq \mathcal{NS} \subsetneq \mathcal{P}. \tag{2.35}$$

Once the local polytope $\mathcal{L}$ has been introduced, it is natural to define the BIs as its facets [Fig. 2.4(a)] [Fro81; Pit86]. In fact, alternatively to the vertex-description (deterministic outcomes), the *Farkas–Minkowski–Weyl theorem* assures that a polytope embedded in a space of dimension D can be described as the intersection of finitely many half-spaces, each one defined by points $\vec{p}$ satisfying a linear inequality of the form $\vec{h} \cdot \vec{p} \geq h_0$, for suitable $(\vec{h}, h_0) \in \mathbb{R}^{D+1}$. Hence, the generic form of a BI is:

$$I := \sum_{\vec{a}_i, \vec{x}_i} T_{\vec{a}_i, \vec{x}_i} P(\vec{a}_i | \vec{x}_i) \geq -\beta_C, \tag{2.36}$$

where $T_{\vec{a}_i, \vec{x}_i}$ are real coefficients and $\beta_C = -\min_{\vec{p} \in \mathcal{P}}(I)$ is the **classical bound of the Bell inequality**. If the inequality is satisfied, $\vec{P}$ is guaranteed to belong to

$\mathcal{L}$, *i.e.* the conditional probabilities resulting from a Bell experiment can have an interpretation in terms of a local hidden variable model.

In the particular $(N, m, 2)$ scenario, one can completely characterize $\mathcal{L}$ from the knowledge of *all* the correlators [15]

$$\langle \mathcal{M}_{x_{j_1}}^{(j_1)} \rangle,\ \langle \mathcal{M}_{x_{j_1}}^{(j_1)} \mathcal{M}_{x_{j_2}}^{(i_2)} \rangle,\ \ldots,\ \langle \mathcal{M}_{x_{j_1}}^{(j_1)} \mathcal{M}_{x_{j_2}}^{(i_2)} \cdots \mathcal{M}_{x_{j_N}}^{(j_N)} \rangle. \tag{2.37}$$

Combining Eq. (2.36) and Eqs. (2.30-2.32), the most general BI for the $(N, m, 2)$ scenario in terms of expectation values is

$$\sum_{k=1}^{N} \sum_{1 \le j_1 < \cdots < j_k \le N} \sum_{j_i \in \{1,\ldots,m\}} \alpha_{x_{j_1},\ldots,x_{j_k}}^{(j_1,\ldots,j_k)} \langle \mathcal{M}_{x_{j_1}}^{(j_1)} \cdots \mathcal{M}_{x_{j_k}}^{(j_k)} \rangle + \beta_C \ge 0 \tag{2.38}$$

with $\alpha_{x_{j_1},\ldots,x_{j_k}}^{(j_1,\ldots,j_k)} \in \mathbb{R}$.

CHSH inequality. To give an example, let us return to the simplest Bell scenario $(2, 2, 2)$ where the CHSH inequality [Cla+69] is the only nontrivial BI [Fin82]. In this case the Bell polytope has 16 vertices and the inequality reads:

$$\begin{aligned} &P(00|00) - P(01|00) - P(10|00) + P(11|00) \\ &+P(00|01) - P(01|01) - P(10|01) + P(11|01) \\ &+P(00|10) - P(01|10) - P(10|10) + P(11|10) \\ &-P(00|11) + P(01|11) + P(10|11) - P(11|11) \le 2. \end{aligned} \tag{2.39}$$

According to Eq. (2.31), it can be rewritten in the "usual" form, involving only two-body correlators:

$$|\langle \mathcal{M}_1^{(1)} \mathcal{M}_1^{(2)} \rangle + \langle \mathcal{M}_1^{(1)} \mathcal{M}_2^{(2)} \rangle + \langle \mathcal{M}_2^{(1)} \mathcal{M}_1^{(2)} \rangle - \langle \mathcal{M}_2^{(1)} \mathcal{M}_2^{(2)} \rangle| \le 2. \tag{2.40}$$

CHSH is violated by entangled states. The maximal violation allowed to quantum states is $2\sqrt{2}$, also known as *Tsirelson bound* [Cir80].

2.3.4 Detecting nonlocality in many-body systems with two-body correlators

As discussed, the full characterization of local polytope becomes practically impossible in the generic case for bigger N, m and Δ, since the number of facets/vertices grows exponentially with N. What is necessary is the knowledge of all correlation functions, whereas in the dichotomic measurements scenario

[15] Note the difference between correlators (expectation values of product of operators) and joint conditional probabilities, crucial in the construction of the local polytope, clearly expressed in Eq. (2.34). In fact, it should be stressed that to get the full conditional probability vector $\vec{P} = P(\vec{a}|\vec{x})$, the full-body correlator $\langle \mathcal{M}_{x_1}^{(1)} \cdots \mathcal{M}_{x_N}^{(N)} \rangle$ *alone* is not enough. Instead, one needs *all* the k-body correlators: one-, two- and so on, until the N-body correlator.

$\Delta = 2$ one can alternatively require the knowledge of all k-body correlators (2.37). Furthermore, in experiments, one typically accesses to only few-body correlators, typically one- and two-body correlators. However, even if, intuitively, most of the information about correlations is contained in high-order correlators, BIs involving all-but-one parties have been proven useful to detect nonlocality [Wür+12; WNZ12; Kas+08]. These results motivate the detection of nonlocality with the minimum amount of available information, which is incorporated in the one- and two-body correlators. To attack this problem in the $(N, 2, 2)$ scenario, in [Tur+14; Tur+15b] Tura *et al.* projected the local polytope $\mathcal{L}$ onto a subspace of lower dimension, by taking into account only **one- and two-body correlators**. Furthermore they focused only on **permutationally invariant BIs**.

By reducing to only one- and two-body correlators and $m = 2$, one has

$$\begin{aligned} &\sum_{i=1}^{N} \left(\alpha_i \mathcal{M}_0^{(i)} + \beta_i \mathcal{M}_1^{(i)}\right) + \sum_{1\leq i<j}^{N} \gamma_{ij} \left\langle \mathcal{M}_0^{(i)} \mathcal{M}_0^{(j)} \right\rangle \\ &+ \sum_{1\leq i\neq j}^{N} \delta_{ij} \left\langle \mathcal{M}_0^{(i)} \mathcal{M}_1^{(j)} \right\rangle + \sum_{1\leq i<j}^{N} \epsilon_{ij} \left\langle \mathcal{M}_1^{(i)} \mathcal{M}_1^{(j)} \right\rangle + \beta_C \geq 0, \end{aligned} \tag{2.41}$$

with α_i, β_i, γ_{ij}, δ_{ij} and ϵ_{ij} real parameters. This simplification corresponds to a **projection** of the full local polytope in a smaller one, dubbed $\mathcal{L}_2$. Projection procedure strongly reduces the dimension of the polytope, from $\dim \mathcal{L} = 3^N - 1$ to $\dim \mathcal{L}_2 = 2N^2$ [16]. Although reduced, this dimension still grows quickly with N while keeping the number of vertices unchanged $D = (\Delta m)^N$ [17]. To further reducing complexity, in [Tur+14] (in the spirit of [BGP10]) permutational symmetry is imposed to BIs. This implies that in Eq. (2.38) expectation values $\langle \mathcal{M}_k^{(i)} \rangle$ and $\langle \mathcal{M}_k^{(i)} \mathcal{M}_l^{(j)} \rangle$ now take the same coefficients $\alpha_i = \alpha$, $\beta_i = \beta$, $\gamma_{ij} = \gamma$, $\delta_{ij} = \delta$, $\epsilon_{ij} = \epsilon$, when $k = l$ and for $i \neq j$. One obtains the following general form of **permutationally invariant BI with one- and two-body correlators** (**PIBI**):

$$I := \alpha \mathcal{S}_0 + \beta \mathcal{S}_1 + \frac{\gamma}{2} \mathcal{S}_{00} + \delta \mathcal{S}_{01} + \frac{\epsilon}{2} \mathcal{S}_{11} + \beta_C \geq 0, \tag{2.43}$$

[16] We saw that $\dim \mathcal{L} = (m(\Delta-1)+1)^N - 1$, which equals $3^N - 1$ in the $(N, 2, 2)$ scenario. This can be also understood by considering that for each party there are three possible measurement choices (two observables or not measure anything) to the power N. The 1 must be subtracted because if no measures are performed in each party, the result is trivial. After projecting $\mathcal{L}$ in the space of correlators up to order K, dimension of $\mathcal{L}_K$ is [Tur+15b]

$$\dim \mathcal{L}_k = \sum_{k=1}^{K} \binom{N}{k} m^k (\Delta - 1)^k, \tag{2.42}$$

Which equates $(m(\Delta - 1) + 1)^N - 1$ for $k = N$

[17] Vertices are projected in vertices, but some vertices can be projected within the interior o $\mathcal{L}_2$, see Fig. 2.4(b).

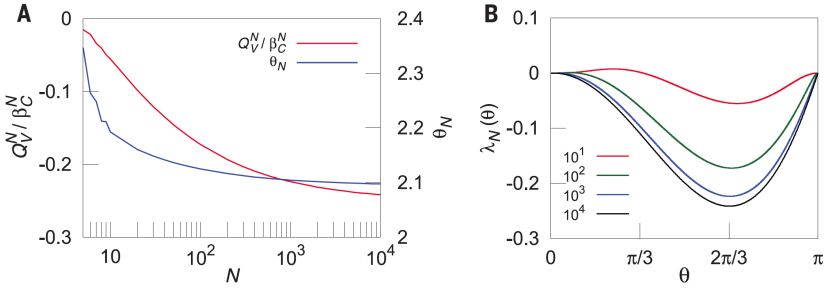

FIGURE 2.5: From [Tur+14], quantum violation of (2.45), scaling with N. The chosen local operators are $\mathcal{M}_0^{(i)} = \mathcal{M}_0 = \sigma_z$ and $\mathcal{M}_1^{(i)} = \mathcal{M}_1 = \cos\theta\sigma_z + \sin\theta\sigma_x$ (only one angle θ to optimize). In (A) Maximal relative quantum violation $Q_V^N/2N$ of the Bell operator $\mathfrak{B}(\theta)$ (red line) and corresponding optimal angle θ_N (blue line). In (B)The violation as function of θ. Increasing N, also violation grows, meaning robusteness against misalignement of the measurements. (Reprinted from [Tur+14])

where

$$\mathcal{S}_k := \sum_{i=1}^{N} \langle \mathcal{M}_k^{(i)} \rangle \qquad \mathcal{S}_{kl} := \sum_{\substack{i,j=1 \\ i \neq j}}^{N} \langle \mathcal{M}_k^{(i)} \mathcal{M}_l^{(j)} \rangle. \tag{2.44}$$

Elements of the symmetric polytope $\mathcal{L}_2^s$ are now five-tuples $(\mathcal{S}_0, \mathcal{S}_1, \mathcal{S}_{00}, \mathcal{S}_{01}, \mathcal{S}_{11})$, hence $\dim \mathcal{L}_2^s = 5$ independently on N. It can be proven that the number of vertices (and of BIs) of $\mathcal{L}_2^s$ is $2N^2 + 1$, that is still hardly tractable and the characterization of all the PIBI is still nontrivial. Nevertheless, a three-parameter class of PIBI was found in [Tur+14], of which an important representative is:

$$-2\mathcal{S}_0 + \frac{1}{2}\mathcal{S}_{00} - \mathcal{S}_{01} + \frac{1}{2}\mathcal{S}_{11} + 2N \geq 0. \tag{2.45}$$

Finally, let us point out that projection does not come for free. In Fig. 2.4(b) its consequences are depicted: whereas local behaviors still remain local (point p_1), there are some nonlocal behaviors which are not correctly evaluated (point p_2). Importantly, if a violation of PIBI is found, the corresponding point (p_3 in Fig. 2.4) is nonlocal *also* in the general case.

Quantum violations. In the context of detection of nonlocality for concrete many-body ground states, inequality (2.45) will play a crucial role for its simplicity.

For this purpose, we now characterize a Bell experiment specifying local quantum observables. For the $(N, 2, 2)$ scenario, one can always obtain maximal violations restricting to local Hilbert spaces of dimension $D_i = 2$ [TV06] and

projective measurements (see footnote 13). As local observables one can chooses linear combination of Pauli operators: $\mathcal{M}_{x_i}^{(i)} = \hat{n} \cdot \vec{\sigma}$, where $\hat{n} = (x, y, z)$, $|\hat{n}| = 1$, $\vec{\sigma} = (\sigma_x, \sigma_y, \sigma_z)$. When restricting to real observables

$$\mathcal{M}_{x_i}^{(i)} = \cos\theta_{x_i}^{(i)}\sigma_z^{(i)} + \sin\theta_{x_i}^{(i)}\sigma_x^{(i)}, \tag{2.46}$$

for $\theta_{x_i}^{(i)} \in [0, 2\pi)$. Since there are two observables per site, notation can be simplified with $\theta_{x_1}^{(i)} := \theta^{(i)}$ and $\theta_{x_2}^{(i)} := \phi^{(i)}$. By means of this specific choice of measurements, one can associate a quantum operator $\mathfrak{B}(\theta^{(i)}, \phi^{(i)})$ (the so-called **Bell operator**) to the left hand side of Eq. (2.45). By diagonalizing $\mathfrak{B}(\theta^{(i)}, \phi^{(i)})$ the many-body states violating the PIBI are found, the corresponding eigenvalues representing the violation. In [Tur+14], the further simplification of measuring the same pair of observable for each party (the angles $\phi^{(i)} = \phi$, $\theta^{(i)} = \theta$) was considered, justified by the numerical evidences that this choice preserves optimality. In fact, they found that states that maximally violate $\mathfrak{B}(\theta^{(i)}, \phi^{(i)})$ are symmetric for exchange of particles [18]. Restriction to symmetric sector of the Hilbert space, allowed reaching very big size ($N = 10^4$ parties) with exact diagonalization routines. Results from [Tur+14] are shown in Fig. 2.5.

As a further remarkable result from the same work, another PIBI has been found, violated by Dicke states $|D_N^k\rangle$ in spin-$\frac{1}{2}$ N-particle systems, which are symmetric N-qubit states we shall encounter also in Chap. 4 as initial states that we let evolve under the kicked dynamic of quantum kicked top and rotor:

$$|D_N^k\rangle = \sqrt{\frac{(N-n)!n!}{N!}} \sum_{\mathcal{P}} \mathcal{P}(|+\frac{1}{2}\rangle^{\otimes N-k}|-\frac{1}{2}\rangle^{\otimes k}), \tag{2.47}$$

that is a symmetric linear combination of permutations of product states with $N-k$ qubits in the state $|+\frac{1}{2}\rangle$ and k qbits in the state $|-\frac{1}{2}\rangle$. Dicke states are relevant states for concrete MBQS, emerging as ground state of the *Lipkin-Meshkov-Glick* Hamiltonian [LMG65]:

$$H_{LMG} = -\frac{\lambda}{N}\sum_{\substack{i,j=1 \\ i\neq j}}^{N}\left(\sigma_x^{(i)}\sigma_x^{(j)} + \sigma_y^{(i)}\sigma_y^{(j)}\right) - h\sum_{i=1}^{N}\sigma_z^{(i)}. \tag{2.48}$$

Importantly, the amount of violation of the PIBI (2.45) is related to the multipartite entanglement (Sec. 2.1.2): in recent works [Alo+19; Tur+19] it was proven – in a device-independent scenario – that k-producible states cannot violate the PIBI by more than a certain relative quantum violation $\beta(k)$, which is (in the

[18] Importantly, although the intuition may bring one to associate the symmetry of BI with the symmetry of nonlocal states (in this case, a permutational symmetry) no theoretical reasons justify the generalization of the statement. Derivation of BIs is in fact independent of any theory (only the no-signaling and locality hypothesis are necessary to construct the local polytope).

asymptotic limit, for large n and k):

$$\beta(k) \approx \frac{1}{4} + \frac{e^{-1/(8s)}}{2} + \frac{1}{2k}\Big(6s - e^{-1/(8s)} - \frac{1}{8n}\Big), \tag{2.49}$$

where $s = \sqrt{\frac{k+1}{48}}$. Therefore, observing a violation exceeding $\beta(k)$ certifies an entanglement depth of at least $k+1$. Note that, in comparison with the spin-squeezing criteria [Eq. (2.14)], BIs witness less multipartite entanglement [Tur+19; Alo+19], but the key advantage is that they certified it in a device-independent way.

Finally let us note that in the symmetric measurement scenario, where all the parties measure the same observables, the violation can be estimated by collective measures. Collective measures were experimentally performed in [Sch+16] in a Bose-Einstein condensate of entangled states of two-level atoms, violating inequality (2.45). In this scenario, in Chap. 6, PIBI (2.45) will be used to detect nonlocality in a long-range Ising model.

3 Tensor networks approach to many-body quantum systems

In Chap. 2 we reviewed the concepts of entanglement [Sec. 2.1] and nonlocality [Sec. 2.3]. Being purely quantum properties without any classical counterpart, their study and application in different contexts is an essential part of the understanding of nature. We payed special attention to their declinations in many-body systems. In particular, we saw that entanglement plays a crucial role in characterizing ground states and quantum phase transitions. A problem of practical interest remained still untouched: having at our disposal only classical resources, how to overcome the difficulties derived from the extreme complexity of the Hilbert space, in order to explicitly simulate extended quantum systems? This chapter is devoted to tensor networks (TNs), a modern numerical and theoretical method to efficiently simulate many-body systems on a lattice. In the next section, we briefly review pros and cons of the main numerical tools available for many-body quantum systems. In Sec. 3.2 TN states are introduced, with explicit examples in one-dimension, where they are called matrix product states. It is shown that TN states satisfy by construction an area law for the entanglement entropy. In Sec. 3.2.3 an analog representation for operators (matrix product operators) is given, for short-range interactions Hamiltonian, where the representation is exact as well as for the long-range case, where some approximations might be necessary. Sec. 3.3 is devoted to the density-matrix renormalization group (DMRG), which is the most important and used TN based algorithm to simulate ground states for one-dimensional lattices. In Sec. 3.4 the view is broadened towards high-dimensional systems and the problem of the contraction of TNs.

3.1 Numerical methods for many-body quantum systems

Many-body quantum systems (**MBQS**) are notoriously hard to simulate by classical computers due to the exponential increase of the complexity of their wave function with the number of their constituents (see Introduction, Sec. 1.2).

Solving the full eigenvalue problem becomes *de facto* intractable already for moderate values of N. When constituents are weakly interacting, single particle approximations work typically well: this is, for example, the case of various versions of the *mean field theory*, which describe efficiently such diverse systems as *Bose-Einstein condensates* [GSS96] or *Bardeen-Cooper-Schrieffer superconductors* [FW12]. However, in many cases strong interactions and strong correlations have to be taken in consideration, since they are source of many exotic phenomena, such as *superfluid-Mott insulator transition* [Mot49; Fis+89], *BEC-BCS crossover* [SR06; GR07], *Fractional Quantum Hall Effect* [Lau83], *High-Temperature Super-Conductivity* [Kei+15] or *quark confinement* [Cre83; MM97], to name a few.

For strongly interacting MBQS, exact analytical results are available only in a very restricted number of cases (for one-dimensional ($1D$) models see for instance [Tak05]). For non-integrable systems analytical approximations often dramatically fail, and numerical approaches are then necessary.

For small enough MBQS (up to few tens of constituents) we can still exactly solve the Schrödinger's equation by means of an **exact diagonalization** [NM05; Rav+17], and try to extrapolate our understanding to larger systems, employing finite-size analysis and scaling.

Nevertheless, the true collective emergent phenomena appear only in thermodynamic limit; in practice, they require to consider MBQS with hundreds of constituents. So far, several algorithms have been developed for attacking this problem.

Quantum Monte Carlo methods (**QMC**) [Fou+01] handle very large systems of the order of thousands of particles in arbitrary dimension, with a precision that scale statistically with the number of the sampling in the wave-function configuration space. Nevertheless, the well-known *"negative-sign" problem* [Whi+89; TW05] hinders the applicability of QMC to fermionic and frustrated spin systems, even if *variational approaches* [Umr+07] may overcome this obstacle with impressive results.

Tensor networks (**TNs**) [VMC08; Orú14; Sch11; Eis13; Ran+19] are a special *ansatz* for wave functions and operators on a lattice, where the quantities of interest are expressed as a result of the contraction of a network of small constituent tensors [1]. TN algorithms [Orú14; Eis13] basically try to reduce the computational cost *from exponential to polynomial* in the number of particles. TN representation is suitable for simulating low entangled states, in particular non-critical ground states of MBQS, in fact TNs satisfy by construction the entanglement area law (Sec. 2.2). They can be easily formulated in a variational way to circumvent the negative-sign problem. For example, in $1D$, looking for the ground state, the energy should be regarded as a *cost functional*, which is supposed to be minimized over the set of wave functions, expressed in the

[1] Indeed, also QMC-based method have been developed that provide an ansatz for the wave function, often integrated with other methods. Among others, here we mention the *Resonating valence-bond wave functions* [Cap+01], the *entangled-plaquette-state* [Mez+09] and the *neural-networks* (NN) ansatz proposed in [CT17], where the NN parameters are optimized ("trained", in the language of NN) with variational or time-dependent variational QMC.

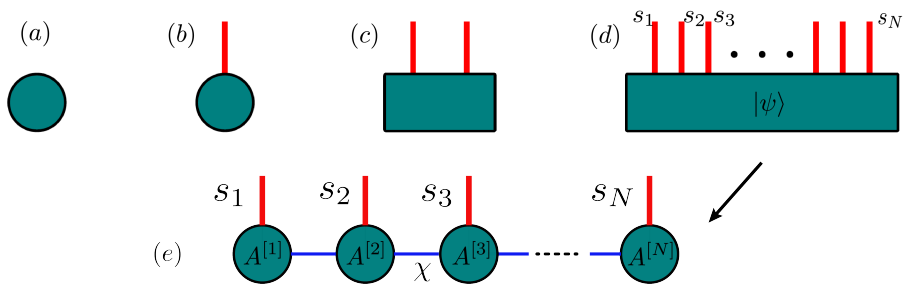

FIGURE 3.1: Pictorial representation of TN. (a) Scalar. (b) Vector. (c) Rectangular matrix. (d) A multi-index tensor representing a many-body quantum state ψ with local dimensions $s_1, \ldots, s_N$ as in Eq. (3.1). (e) the MPS representation of (d) for open boundary conditions. The pictorial representation of TN is usually exploited to make the calculations simpler and clearly shows the contractions relations.

form of a $1D$ TN, or **matrix product state** (**MPS**) [Sch11]. TNs have been proposed as the best candidates for the numerical simulation of static and dynamic properties for both fermionic and bosonic non-critical systems. Especially in $1D$, the success of TN is unquestionable: **density matrix renormalization group** (**DMRG**) [Whi92] (and its modern adaptations), **time-evolving block decimation**(**TEBD**) [Vid04; Vid07a] and the **time-dependent variational principle** (**TDVP**) [Hae+11] to name a few, remain among the most accurate tools (with an error of the order of the machine precision) for studying low energy properties and time evolution of lattice systems with or without translation invariance, for open as well as periodic boundary conditions [VPC04b], for pure and mixed states [ZV04], for short- and long-range interactions [CDV08; FND10a], for both bosonic and fermionic models [Sch+98; WS99; GC+02; Riz+05; She+08; DCLS11; YHW11]. For critical systems adaptation of TN have been proposed: the **multiscale entanglement renormalization ansatz** (**MERA**) [Vid07b; Vid08] is an example.

3.2 Tensor networks states and operators

Let us consider the general many-body quantum state already encountered in the introduction [Eq. (1.1)] and here rewritten for the sake of convenience:

$$|\psi\rangle = \sum_{\{s_i\}=1}^{d} c_{s_1 s_2 \ldots s_N} |s_1\rangle \otimes |s_2\rangle \cdots \otimes |s_N\rangle. \tag{3.1}$$

The TN way to handle this wave function is by interpreting the set of coefficients $c_{s_1 \ldots s_N}$ as a tensor of N indices and in turn decomposing it in a *network* of N

smaller connected tensors. The paradigmatic example is given in $1D$ by the **matrix product states** (**MPSs**). Many different yet similar ways are available to write down an MPS. For *periodic boundary conditions* we may have for example:

$$|\psi[A]\rangle = \sum_{\{s_i\}=1}^{d} Tr\left[A^{s_1}_{\alpha\beta} A^{s_2}_{\beta\gamma} \cdots A^{s_N}_{\mu\alpha}\right] |s_1 \dots s_N\rangle. \tag{3.2}$$

Notation $|\psi[A]\rangle$ means the state now depends on tensors $A^{s_i}_{\delta\kappa}$. Each $A^{[i]} := A^{s_i}_{\delta\kappa}$ has three indices [2] and dimension $\chi \times d \times \chi$: s_i are let free (uncontracted) and corresponds to physical indices (the local Hilbert space) of dimension d, already present in the original tensor $c_{s_1 \dots s_N}$; remaining indices $\alpha, \beta \cdots \nu$ have dimensions χ and are contracted. χ is called **bond dimension** and we shall see it is related to the entanglement of the state. The number of parameters required in the representation is now $\mathcal{O}(Nd\chi^2)$, therefore linear in N. In Fig. 3.1 a graphical representation of the decomposition is shown, which makes the formalism transparent. Actually, many calculations involved TN can be directly done in a very simple way through the graphical representation.

A physical way to interpret the tensor decomposition (3.2) is by using the **valence bond picture** (**VBP**) [FNW92; VPC04b; PG+06].

In VBP every tensor $A^{[i]}$ can be obtained assigning two virtual spins to each lattice site, in a way the right one of them is maximally entangled with the left one in the following site [Fig. 3.2(b)] and then projecting the state on the physical space:

$$A^{[i]} = \sum_{s_i=1}^{d} \sum_{\delta,\kappa=1}^{\chi} A^{s_i}_{\delta\kappa} |s_i\rangle\langle\delta,\kappa|. \tag{3.3}$$

Thanks to VBP, is easy to show how MPSs automatically satisfy an entanglement area law: taking a bipartition of length l (cutting the ring in two virtual bonds) one has $S(\rho_l) \leq 2\log(\chi)$ [3]. VBP can be straightforward generalizable in higher dimensions, where the TN *ansatz* for states, takes the name of **projected entanglement pair state** (**PEPS**) [VC04b] [Fig. 3.2(c)].

3.2.1 States efficiently represented by MPS

Decomposition (3.2) is just a different representation of (3.1). In practice, only those states satisfying an entanglement area law can be *efficiently* put in this form. For high entangled states, the MPS representation is not efficient, requiring the bond dimension growing exponentially. However, there exist also important states with an *exact* MPS representation: this is the case of *e.g* the

[2] From now on, we denote as $A^{[i]}$ the i-th tensor $A^{s_i}_{\delta\kappa}$, if it is not necessary to explicitly indicate its indices.

[3] the coefficient 2 is because of the double cutting; for infinite chain one has 1 (one cut). In general the coefficient expresses the size of the boundary surface, *i.e.* the number of cut virtual bonds. For example, in $2D$, for a square bipartition of side L, $S(\rho_L) \leq 4L\log(\chi)$.

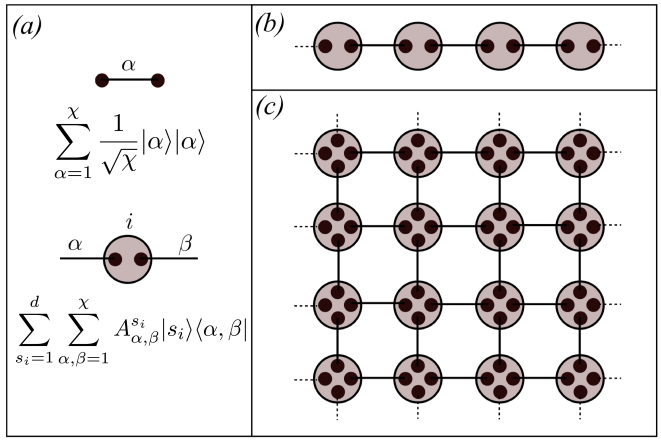

FIGURE 3.2: (a) The MPS representantion of a many body quantum state. The valence bond representation for (b) an MPS and (c) a $2D$ PEPS. (Reprinted from [Tur+15a]).

Greenberger-Horne-Zeilinger (**GHZ**) and **W** states [GHZ89] and the **Affleck-Kennedy-Lieb-Tasaki** (**AKLT**) state [Aff+04].

AKLT state deserves particular attention. It is the ground state of the spin $S = 1$ Hamiltonian (local-physical dimension $d = 3$):

$$H_{AKTL} = \sum_i \vec{S}_i \vec{S}_{i+1} + \frac{1}{3}(\vec{S}_i \vec{S}_{i+1})^2. \tag{3.4}$$

This Hamiltonian resembles the antiferromagnetic Heisenberg model $H_H = \sum_i \vec{S}_i \vec{S}_{i+1}$ and in fact there is no phase transition between the ground state of the AKLT Hamiltonian and the ground state of the Heisenberg chain as long as the coefficient of the biquadratic term varies between 0 and $1/3$. The AKLT state results then very useful to indirectly study the Heisenberg model and in particular to verify the *Haldane conjecture* [Hal83], which states that the integer-spin anti-ferromagnetic Heisenberg chains are gapped. For periodic boundary conditions, the MPS representation [Eq. (3.2)] of the AKLT state requires a bond dimension $\chi = 2$ (then it is nontrivially entangled) with tensor-matrices [Sch11]:

$$A^1 = \begin{pmatrix} 0 & \sqrt{\frac{2}{3}} \\ 0 & 0 \end{pmatrix}; \qquad A^2 = \begin{pmatrix} -\sqrt{\frac{1}{3}} & 0 \\ 0 & \sqrt{\frac{2}{3}} \end{pmatrix}; \qquad A^3 = \begin{pmatrix} 1 & 0 \\ -\sqrt{\frac{2}{3}} & 0 \end{pmatrix}.$$

The AKLT state is a completely dimerized state with short-range entanglement only between nearest-neighbour spins, which arrange in singlets (valence bonds,

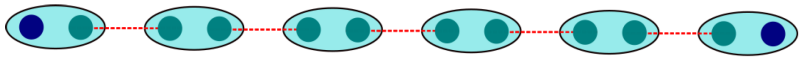

FIGURE 3.3: Pictorial representation of the AKLT state with open boundary conditions (ground state of Hamiltonian (3.4)). It is a completely dimerized state with short-range entanglement only between nearest-neighbour spins, which arrange in singlets (dashed lines). Two spin-1/2 (the left- and rightmost spins) remain uncoupled, forming two "edge states". (Reprinted from [Ran+19]).

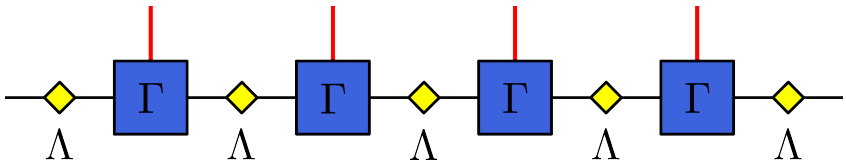

FIGURE 3.4: Canonical representation of an MPS. Tensors Λ^{s_i} are diagonal matrices whose elements are the Schmidt coefficient of the bipartition $1, \ldots, k$ versus $k+1, \ldots N$.

see Fig. 3.3). For infinite chains or periodic boundary condition all spins-1 participate in two valence bonds. For open chains, two spin-1/2 (the left- and rightmost spins) remain instead uncoupled, forming two *"edge states"*, which give the ground state of (3.4) a fourfold degeneracy. We will encounter again the AKLT state in Sec. 5.1.1 as an example of *simmetry protected topological phase* [GW09].

3.2.2 Canonical representation of MPS

To understand how MPS representation works in practice and the special role played by the bond dimension in approximating a generic state, it is useful to introduce in detail another special representation, proposed by Vidal in [Vid03], the so called **canonical representation of MPS** [Fig. 3.4]:

$$|\psi[\Gamma,\Lambda]\rangle = \sum_{\{s_i\}} \Gamma^{s_1}_{a_1}\Lambda^{[1]}_{a_1}\Gamma^{s_2}_{a_1 a_2}\Lambda^{[2]}_{a_2}\Gamma^{s_3}_{a_2 a_3}\cdots\Lambda^{[N-1]}_{a_{N-1}}\Gamma^{s_N}_{a_N}|s_1,\ldots,s_N\rangle \tag{3.5}$$

Tensors $\Gamma^{s_i}_{a_{i-1}a_i}$ lie on each physical site, whereas the tensors Λ_{a_i}, directly accessible on the bonds, are diagonal matrices whose elements are the Schmidt coefficients (the entanglement spectrum) with respect to the bipartition $[1,\cdots,k],[k+1,\cdots,N]$. That is, the reduced density matrices read $\rho^{[1,\cdots,k]} = \rho^{[k+1,\cdots,N]} = (\Lambda^{[k]})^2$. The procedure to bring any state (3.5) in the from (3.1) consists in practice in a concatenation of *reshapes* and *singular value decompositions* (SVD, see also

the footnote 1) of tensor $c_{s_1 s_2 s_3 \dots s_N}$:

$$
\begin{aligned}
c_{s_1 s_2 \dots s_N} &= \Psi_{s_1 (s_2 \dots s_N)} \quad \text{(reshape } c \text{ in a two-index vector } \Psi) \\
&= \sum_{a_1} A^{s_1}_{a_1} \underbrace{\Lambda^{[1]}_{a_1} (V^\dagger)_{a_1 (s_2 \dots s_N)}} \quad \text{(do an SVD and contract } \Lambda \text{ with } V^\dagger) \\
&= \sum_{a_1} \Gamma^{s_1}_{a_1} \Psi_{(a_1 s_2)(s_3 \dots s_N)} \quad \text{(reshape } \Psi) \\
&= \sum_{a_1 a_2} \Gamma^{s_1}_{a_1} A^{s_2}_{a_1 a_2} \underbrace{\Lambda^{[2]}_{a_2} (V^\dagger)_{a_2, (s_3, \dots s_N)}} \quad \text{(do an SVD and contract } \Lambda \text{ with } V^\dagger) \\
&= \sum_{a_1 a_2} \Gamma^{s_1}_{a_1} \overbrace{\Lambda^{[1]}_{a_1} \Gamma^{s_2}_{a_1 a_2}} \Psi_{(a_2 s_3)(s_4 \dots s_N)} \quad \text{(contract } \Lambda \text{ with } V^\dagger \text{ and } A^{s_2}_{a_1 a_2} = \Lambda_{a_1} \Gamma^{s_2}_{a_1 a_2}) \\
&= \dots \quad \text{(iterate the decomposition of } \Psi_{(a_2 s_3)(s_4 \dots s_N)})
\end{aligned}
\tag{3.6}
$$

The crucial step in previous derivation is that when making an SVD, the smallest singular values of Λ_{a_k} can be discarded, storing only the largest $\chi \ll \chi_k = d^{\min(k, N-k)}$, so setting the bond dimension of the MPS. The total error in such approximation is given by the sum of the squares of the neglected singular values: $err = \| |\psi\rangle - |\psi\rangle_{mps} \|^2 \leq \sum_{k=1}^{N-1} \sum_{i=\chi+1}^{\chi_k} \lambda_i(k)$. For non-critical systems, the goodness of this approximation is supported by the general behaviour of the entanglement spectrum coefficients, which scale rapidly to zero as $\lambda_i \approx \exp(-i)$ [Vid03]. A canonical form can be derived also for infinite chains [OV08], where the matrices Γ and Λ satisfy the *canonical conditions*[4]

$$
\sum_i \Gamma^{s_i} \Lambda^2 \Gamma^{s_i \dagger} = \sum_i \Gamma^{s_i \dagger} \Lambda^2 \Gamma^{s_i} = \mathbb{1}. \tag{3.7}
$$

It turns out that the *transfer matrix* [Fig. 3.5]

$$
T_{aa';bb'} = \sum_{s_i} \Gamma^{s_i}_{aa'} \left(\Gamma^{s_i}_{bb'} \right)^* \Lambda_{b'} \Lambda_{a'} \tag{3.8}
$$

has a right eigenvector $\delta_{a'b'}$ with eigenvalue $\lambda = 1$ (an analogous relation holds for the left eigenvector). Furthermore, $\delta_{a'b'}$ is the *only* eigenvector with $|\lambda| = 1$ iff the state is pure. Recently, a unified version of canonicalization, for different lattices and dimensions has been provided in [Eve18].

We conclude noting that MPSs are by construction *finitely correlated*: given two local (on-site) operators $\hat{O}$ and $\hat{Q}$, one can prove that correlation functions behave as

$$
C(r) \equiv \langle \hat{O}_i \hat{Q}_{i+r} \rangle - \langle \hat{O}_i \rangle \langle \hat{Q}_{i+r} \rangle \simeq e^{-r/\xi}, \tag{3.9}
$$

[4] To be more precise, the canonicalization in Eq. (3.6) has been illustrate for a finite-non-translational invariant MPS (for the sake of simplicity) giving a new MPS in a *left*-canonical form, *i.e.* satisfying only $\sum_i \Gamma^{s_i} \Lambda^2 \Gamma^{s_i \dagger} = \mathbb{1}$ [Fig. 3.5(a)]. For a translational invariant MPS, both *left*- and *right*-canonical conditions hold as in Eq. (3.7).

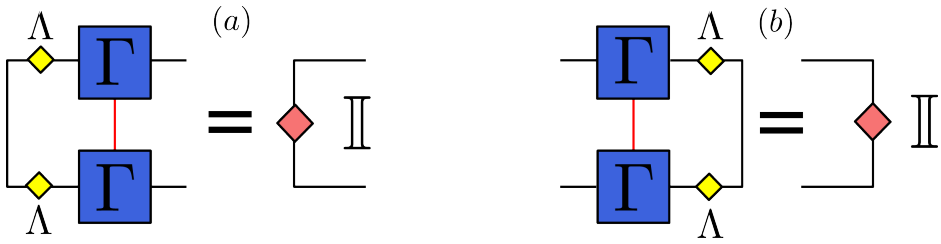

FIGURE 3.5: Transfer matrix of an MPS in canonical representation. (a) left canonical condition; (b) right canonical condition.

with $\xi = -1/\log|\lambda_2/\lambda_1|$ a constant (the correlation length) and $\lambda_{1,2}$ the first and second eigenvalues of the transfer matrix (for canonical MPSs, $\lambda_1 = 1$ and λ_2 directly provides the correlation length).

3.2.3 Matrix product operators

Not only pure states can be decomposed as TN, but also density matrices and Hamiltonians [VGRC04; Pir+10]. They are called **matrix product operators** (**MPO**) in $1D$ and **projected entanglement pair operators** (**PEPO**) in higher dimensions. The explicit form of an MPO in $1D$ for periodic boundary conditions is

$$\hat{O} = \sum_{\{s_i\}=1}^{d} \sum_{\{a_i\}=1}^{K} \left[W_{a_1 a_2}^{s_1 s_1'} W_{a_2 a_3}^{s_2 s_2'} \cdots W_{a_N a_1}^{s_N s_N'}\right] |s_1 \ldots s_N\rangle\langle s_1' \ldots s_N'|. \tag{3.10}$$

This expression is similar to the MPS in Eq. (3.2), unless that for the presence of two physical indices for each local tensor $W^{[i]}$ [Fig. 3.6]. K is the MPO bond dimension, which is different from χ and depends, in the case of Hamiltonians, on the interaction range.

At least when dealing with short-range Hamiltonians, an MPO can be easily constructed without any approximation. Let us start by constructing a general MPO where tensors $W^{[i]}$ are upper-triangular matrices

$$W^{[i]} = \begin{pmatrix} A^{[i]} & B^{[i]} \\ 0 & C^{[i]} \end{pmatrix}, \tag{3.11}$$

where $A^{[i]}$, $B^{[i]}$ and $C^{[i]}$ are square $d \times d$ matrices (d the local physical dimension) and $K = 2 \times d$. Putting the W^i in the MPO decomposition (3.10), one obtains

$$\hat{O} = \sum_{n=1}^{N} A^{[1]} \otimes \cdots A^{[n-1]} B^{[n]} \otimes C^{[n+1]} \otimes \cdots C^{[N]}. \tag{3.12}$$

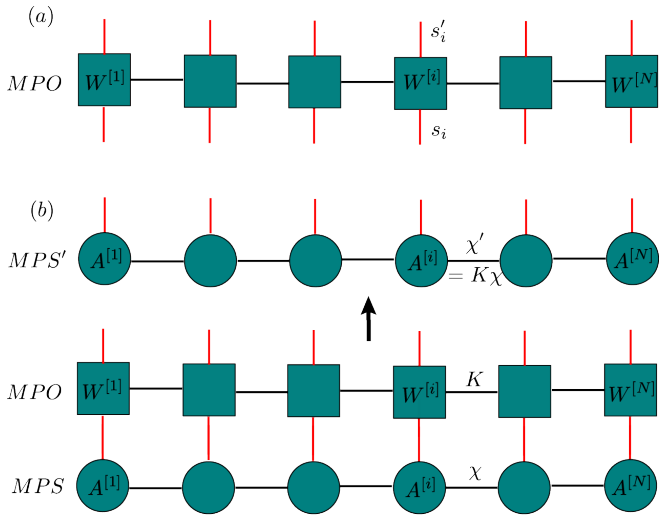

FIGURE 3.6: (a) An MPO. The horizontal indices, a_is in Eq. (3.10), are contracted. Each matrix $W^{[i]}$ can act on the local physical space with the free indices s_i and s_i', respectively to the Hilbert space and its dual. (b) An MPO of bond dimension K acts on an MPS of bond dimension χ via the contraction of the physical indices. The resulting MPS′ has a bond dimension $\chi' = \chi K$.

For a simple local Hamiltonian $H = h\sum_{i=1}^{N}\sigma_i^\mu$, $A^{[i]} = C^{[i]} = \mathbb{1}$, $B^{[i]} = h\sigma^\mu$. For an Ising chain in a transverse field $H = \sum_{i=1}\sigma_i^\nu\sigma_{i+1}^\nu + h\sigma_i^\mu$, where two-body nearest-neighbour interactions are added, one generalizes $W^{[i]}$ as

$$W^{[i]} = \begin{pmatrix} A^{[i]} & B^{[i]} & C^{[i]} \\ 0 & 0 & D^{[i]} \\ 0 & 0 & E^{[i]} \end{pmatrix}, \tag{3.13}$$

with $A^{[i]} = E^{[i]} = \mathbb{1}$, $B^{[i]} = D^{[i]} = \sigma^\nu$ and $C^{[i]} = h\sigma^\mu$. For open boundary conditions, the first and the last tensors of the MPO are (for the last example):

$$W^{[1]} = \begin{pmatrix} A^{[i]} & B^{[i]} & C^{[i]} \end{pmatrix}; \qquad W^{[N]} = \begin{pmatrix} C^{[i]} \\ D^{[i]} \\ E^{[i]} \end{pmatrix}. \tag{3.14}$$

A more general, albeit less intuitive, method to write down an MPO from a generic Hamiltonian was proposed in [CB08], based on a parallelism between tensor networks and **finite-states automata**. This approach is suitable to treat

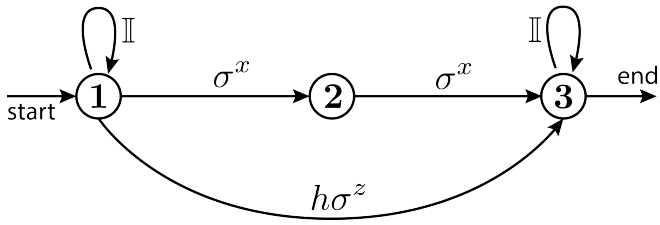

FIGURE 3.7: Scheme of the finite states automaton for an Ising chain in a transverse field.

and efficiently simulate long-range interactions (with exponential and power-law decaying, see *e.g.* [FND10a; CDV08]) and it will result very useful especially in Chap. 6. The Hamiltonian is imagined as constructed by a machine (automaton) having as many internal states as the possible interactions every site of the chain can have. To be concrete, let us focus on the above-written Ising Hamiltonian and, for concreteness, let us set $\nu = x$ and $\mu = z$. The scheme representing this automaton is depicted in Fig. 3.7 and described in the following. One starts from the automaton-state 1 (no-interactions) and therefore has three possibilities: (i) adding an interaction σ^x, passing to the next site of the chain and then changing the automaton-state to the internal-state 3 (completing the interactions); (ii) adding a local transverse field $h\sigma^z$, which brought the automaton in the internal-state 3 or (iii) adding another identity operator (remaining in the same internal state 1). If the internal state is 3, the only possible completion is by adding another interaction σ^x to and changing the state in 2. Finally, being in the internal state 2 there are two possibilities: adding the identity operators (staying in state 2) or exiting from the automaton. Once the automaton is constructed, to put it in MPO form, one has to fill a square matrix $W^{[i]}$ of dimension K equal to the number of internal states (in this case $K = 3$). Rows of $W^{[i]}$ correspond to ingoing internal states (the state in which the automaton is), columns are the outgoing internal states. For example, being in the state 1 (first row) one will have the identity in the first column, σ^x in the second (state 2) and $h\sigma^z$ in the last columns, finally obtaining, in line with (3.13):

$$W^{[i]} = \begin{pmatrix} \mathbb{1} & \sigma^x & h\sigma^z \\ 0 & 0 & \sigma^x \\ 0 & 0 & \mathbb{1}. \end{pmatrix} \tag{3.15}$$

3.3 The density matrix renormalization group

Density matrix renormalization group (**DMRG**) [Whi92] was inspired by the *real-space quantum renormalization group* (RG) [Wil75], a coarse-graining procedure to find the ground state of strongly interacting MBQS on a lattice. The success of the RG is however limited to few cases and White and Noack argued

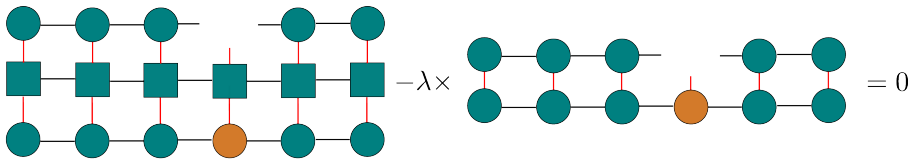

FIGURE 3.8: Graphical representation of the reduced eigenvalue problem at each step of a DMRG [Eq. (3.17)].

in [WN92] that its main lack lies in not properly taking into account the correlations (or boundary effects) existing between each block and the rest of the lattice during the decimation procedure. White's breakthrough was to reformulate the coarse-graining as a variational method involving the reduced density matrices instead of the Hamiltonian. The original formulation of DMRG is quite heuristic, though very powerful, and during the early years after its release it was not very clear the deep theoretical reason for its success. In 1995 Östlund and Rommer [ÖR95] pointed out that ground states found by the DMRG are MPS. From 2004, with the seminal works of Cirac, Latorre, Verstraete, Vidal and coworkers, the previous results were reinterpreted from a quantum information perspective, open the way for a full developing of TN as a theoretical framework for the study of MBQS as well as a numerical tool at the basis of many algorithms.

Since DMRG is ubiquitous in this work, we give here a sketch of the algorithm in its modern MPS formulation. To find the ground state of the Hamiltonian $\hat{H}$, the cost functional to minimize is

$$\min_{\{A\}} \big(\langle\psi[A]|\hat{H}|\psi[A]\rangle - \lambda\langle\psi[A]|\psi[A]\rangle\big). \tag{3.16}$$

This problem is quadratic in each $A^{[i]}$. Instead of minimizing the full Hamiltonian, the DMRG procedure proposes to diagonalize and optimize each small *local* tensor $A^{[i]}$ at a time, keeping the algorithm *globally optimal*, with a computational cost scaling as $\mathcal{O}(\chi^3)$. In practice at each step of the algorithm, one fixes all the tensors A^{s_i} but one, which is the target, and solves the reduced eigenvalue problem (which is computationally affordable with an exact diagonalization)

$$\min_{A^{[i]}}(A^{[i]\dagger}H_{eff}A^{[i]} - \lambda A^{[i]\dagger}N_{eff}A^{[i]}\big), \tag{3.17}$$

where: H_{eff} and N_{eff} depend on all the tensors but $A^{[i]}$ as shown in Fig. 3.8. The algorithm is iterated until convergence (which is guaranteed, see [VPC04b]).

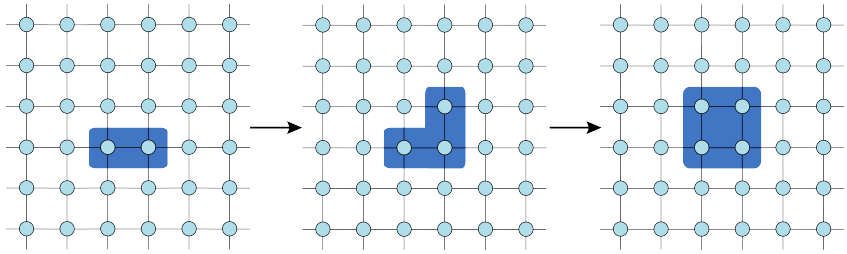

FIGURE 3.9: Example of contraction of a $2D$ TN. If starting from contracting an arbitrary bond between two sites, a tensor with six bonds will be obtain. Then contract the new tensor with a neighbouring one and so on. At each step the number of bonds increases linearly with the boundary of the contracted area ∂ and the memory needed increase exponentially as $\mathcal{O}(\chi^{\partial})$ (χ the bond dimension), making the procedure de facto intractable. (Reprinted from [Ran+19])

3.4 Contraction of tensor networks

We already encountered in the previous section the problem of contracting a TN to calculate quantities of interest. For example, to calculate the expectation value $\langle\psi|\hat{H}|\psi\rangle$ one may start from the contraction of an MPS and an MPO as in Fig. 3.6 and then contracting the resulting MPS' again with the MPS. In the first step the bond dimension increases from χ to $\chi' = \chi K$ but such growth is limited and acceptable. In $1D$ one typically faces manageable contractions, but the $2D$ case may be much more complicated, often intractable, as shown in Fig. 3.9. Maybe, the simplest and instructive example of non exactly contractible $2D$ TN emerges from the time (real or imaginary) evolution of a $1D$ MPS under a **time evolving block decimation** (**TEBD**) algorithm [Vid04; Vid07a]. Under the action of a time-independent Hamiltonian $\hat{H}$ the state $|\psi[A]\rangle$ evolves following the Schrödinger's equation

$$i\partial_t|\psi[A(t)]\rangle = \hat{H}|\psi[A(t)]\rangle. \tag{3.18}$$

In the TEBD one directly starts from the generic solution of (3.18) in exponential form

$$|\psi[A(t)]\rangle = e^{-i\hat{H}t}|\psi[A(0)]\rangle. \tag{3.19}$$

Time t is discretized in small steps τ, $t = n\tau$, with $\tau \to 0$ and $n \to \infty$. For nearest-neighbour interactions $\hat{H} = \sum_{\langle i,j\rangle} H_{ij}$. Each step τ of the evolution is approximated by the operator

$$e^{-i\hat{H}\tau} = e^{i\hat{H}_{12}}e^{i\hat{H}_{23}}e^{i\hat{H}_{34}}\cdots e^{i\hat{H}_{N-1N}} + \mathcal{O}(\tau^2), \tag{3.20}$$

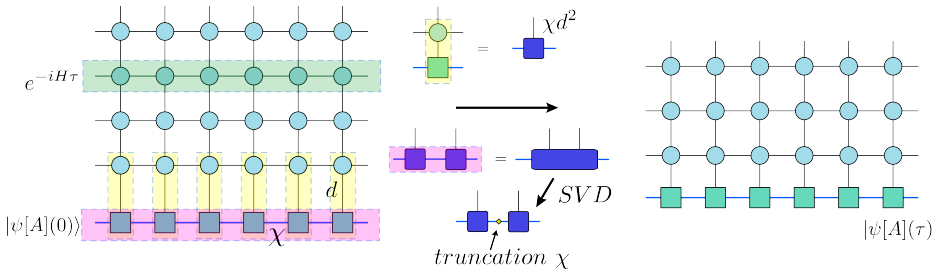

FIGURE 3.10: The basic steps of the TEBD: the initial MPS at time $t = 0$ is contracted with a row of tensors, expressing one step τ of the (real or imaginary) time evolution [Eq (3.20)]. After each contraction, a truncation is implemented exploiting an SVD, retaining only the first χ bigger singular values, in order to keep the bond dimension unchanged and at the same time minimizing the distance of the MPS before and after the truncation.

where the error comes from the (first-order) Trotter-Suzuki decomposition [SI87], necessary because of the non-commutativity of two-sites operators in the Hamiltonian $[\hat{H}_{i,i+1}, \hat{H}_{i+1,i+2}] \neq 0$. The operator in (3.20) can be expressed in MPO form and the full-time evolution operator (3.19) is the contraction of $n \to \infty$ of such MPOs and the initial MPS $|\psi[A](0)\rangle$. At each step τ, the bond dimension of $|\psi[A](t+\tau)\rangle$ increase from $\chi(t) \to \chi(t)d^2$. This exponential growth must be truncated at each step, to limit the bonds to the preset cutoff χ and to save computational costs and memory. This truncation is usually performed by an SVD [5] (refer to Fig. 3.10 for a graphical representation of the TEBD).

There are also exactly contractible $2D$ TN. This is, for example, the case of networks with no *loops*, as the *tree tensor networks* (TTN) [SDV06; TEV09] [Fig. 3.11(a)], which yet can simulate only states with a bounded amount of entanglement. In some algorithms, TTN *ansatz* provides a *mean-field approximation*, very useful for having a first guess of the ground-state energy. The *multiscale entanglement renormalization ansatz* (MERA) [Vid07b; Vid08] [Fig. 3.11(b)] captures the properties of systems at criticality and is contractible, although it contains loops [Fig. 3.11(b)]. In the generic case in $D > 1$ dimension, a contraction-truncation scheme is often unavoidable. In $D = 2$ variational schemes in the spirit of the DMRG [VMC08] or high-dimensional imaginary-time TEBD [Jor+08]

[5] Note in particular that the truncation is in contrast with the Lieb-Robinson theorem which implies that, in many cases of interest, the EE grows linearly with time. Hence, TEBD may not simulate long time regimes with a good accuracy. Furthermore, Trotter decomposition makes the TEBD not simply adaptable to long range Hamiltonian (in general to no translation invariant Hamiltonian) and the bond truncation can spoil some conservation laws and symmetries (for a discussion see [Hae11] pages 118-120). A different approach to the time evolution in $1D$ is the *time dependent variational principle for quantum lattices* [Hae+11] which is based on the geometrical properties of the MPS manifold. It does not require any Trotter decomposition and is suitable for short as long as long range interactions.

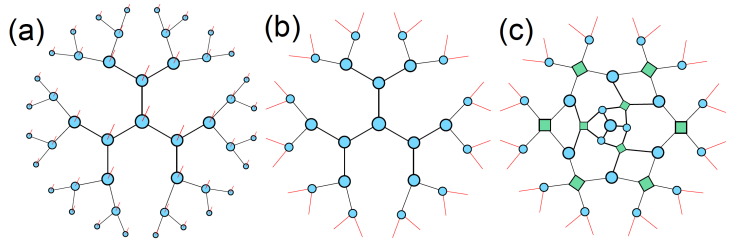

FIGURE 3.11: In (a) and (b) two different tree tensor networks states. In (c) a MERA. (Reprinted from [Ran+19]).

can serve to simulate the ground states of lattice systems. We refer to [Ran+19] for a recent and comprehensive review of the techniques to contract TN in arbitrary dimensions. In Chap. 7 a new algorithm for infinite systems in arbitrary dimensions is proposed, which reduces the full many-body problem to the simulation of a few-body one embedded in an "entanglement bath". This bath "mimics" the degrees of freedom of the extended system and the infinite TN contraction problem is encoded in a simpler set of eigenvalue equations.

4 Entanglement and quantum chaos

In the current chapter we show how entanglement can be used as an intrinsically quantum property capable to characterize the emergence of chaos in classical systems. We tackle this problem by studying in detail two simple but paradigmatic dynamical systems, the quantum kicked top and the quantum kicked rotor, which both have chaotic behaviour in their classical version. In order to directly compare the quantum kicked top and the quantum kicked rotor, we study the latter as a special limit of the former, exploiting the formulation given by Haake and Shepelyansky in [HS88]. Even if the dynamics of these model is not exactly solvable, the symmetries of their Hamiltonian allow to restrict the numerical simulations to a small symmetric sector of the Hilbert space, hence exact diagonalization is sufficient to explore very long-time evolution for many-particle regimes.

In Sec. 4.1 we give a historical overview of the entanglement approach to chaos and discuss more in detail the problems we want to attack in the rest of the chapter. In Sec. 4.2 we review the classical and the quantum kicked top. In Sec. 4.3 we look at the classical and quantum kicked rotor and we derive the kicked rotor as a limiting case of the kicked top. We show that bipartite entanglement entropy is a good signature of quantum chaos in this non-ergodic system. In Sec. 4.4 we discuss properties of our quantum system that are reminiscent of Kolmogorov-Arnol'd-Moser theory.

4.1 Quantum chaos and entanglement

Sketched in the 17th century by Newton and others, the deterministic laws of classical mechanics quickly ran into difficulties. Foremost was the fact that equations of Newtonian gravitation resisted analytic solutions for three or more bodies. The struggles of the unsolvability of many classical mechanical equations was further exacerbated when Poincairé proved that perturbation to known integrable solutions in general leads to non-integrability or chaos. This was in contrast to observation, which saw nature as substantially regular, from the periodic movements of planets to the sounds of a piano. This paradox was resolved in the form of **Kolmogorov-Arnol'd-Moser** (**KAM**) **theory** [Arn13] which formally explains the persistence of quasi-periodic behaviors in chaotic systems.

Chaos in classical physics is characterised by a hypersensitivity of the time evolution of the system to even small changes in the initial conditions. Classically this is well understood in terms of the hypersensitive dependence of the phase space trajectories. **Quantum chaos**, in contrast, cannot be defined in the same terms, largely due to the fact that there is no general quantum analogue of classical phase space trajectories. To put this into context, the unitary evolution of an initial quantum state $\psi_a(0)$ is

$$\psi_a(t) = U\psi_a(0) \,, \tag{4.1}$$

where $U = e^{-iHt/\hbar}$ is the unitary time-evolution operator for a system with Hamiltonian H. Similarly, starting from a nearby initial state ψ_b yields $\psi_b(t) = U\psi_b(0)$. The scalar product of these states is constant for all time,

$$\langle \psi_a(t), \psi_b(t) \rangle = \langle \psi_a(0), \psi_b(0) \rangle \,. \tag{4.2}$$

Therefore, due to the linearity of the Schrödinger equation, differences in initial conditions cannot grow, in stark contrast to the exponential divergence of trajectories of chaotic classical systems. As underlying all classical systems are quantum mechanical ones, the confounding question is: *how does chaos arise from quantum systems?* This question motivates the search for quantum signatures of chaos.

Approaches to quantum signatures of chaos fall into two categories. One involves investigating quantum variables that distinguish between quantum systems whose classical counterparts are integrable and nonintegrable. These approaches typically look at energy spectra properties [Rei13; Haa13; Gut90; Tab89; Zyc90]. A second class of approaches seeks *intrinsic* quantum definitions of quantum chaos. Examples of these include quantum parallels of the Lyapunov exponents and entropy measures [FMR91; SC96a; SŻ94; SC96a; SC96b; ZP94; ZP95; nK04]. There have also been attempts to develop a quantum analogue of KAM theory [Eva04; HTT84; BCK15; GRR86]. In this chapter we will look at the entanglement entropy (EE) as a signature of quantum chaos.

The connection between EE and chaos was first proposed by Zurek and Paz [ZP94]. Here they studied a classical inverted harmonic oscillator (an unstable but not properly chaotic system) and conjectured that in the corresponding quantum system, weakly coupled to a high temperature bath, the rate of production of the von Neumann entropy equals the sum of the positive **Lyapunov exponents**. Importantly, this sum is equivalent to the **Kolmogorov-Sinai entropy** (**KSE**) [Pes77]. Even though the conjecture is not directly generalizable to less trivial systems [MS98], Zarum and Sarkar [ZS98] showed a significant correspondence between the entropy contours of the phase space of the **classical kicked rotator** (**CKR**) and the **quantum kicked rotator** (**QKR**) embedded in a dissipative environment. Subsequent to the Zurek-Paz conjecture, and perhaps motivated by it, Furuya, Nemes, and Pellegrino numerically showed that classical chaos could be related to high EE and classical regular dynamics to low EE

in the context of the Jaynes-Cummings model [FNP98]. This result stimulated further studies of the EE as a direct signature of chaos.

More recently bipartite EE as a signature of chaos was studied in the **quantum kicked top** (**QKT**) modelled as a *multi-qubit system* [Wan+04; Gho+08; RLP17; KG18a; KG18b], without the need for an external environment. In comparison with the Zurek and Paz model, one side of the bipartite system would serve as the harmonic oscillator, whilst the rest of the system as the bath. A significant difference however is that in the Zurek and Paz model, the coupling to the bath was weak, whereas in the later works the coupling to the effective bath is strong. In this strong coupling regime, the system decoheres almost instantaneously. These works found that high EE corresponds to chaos in quasi-ergodic systems. Remarkably, it was experimentally observed in a three superconducting qubit system [Nei+16]. The correspondence between EE and chaos has been argued to not be universal: Lombardi and Matzkin offer a counter-example in the Rydberg molecule [LM11; LM15]. However, their claims are controversial, and have been questioned by others [Mad15; RLP17]. Recently, Kumari and Ghose [KG18b] propose that the conflict arises because Lombardi and Matzkin work deep in the quantum regime, where the correspondence is known to break down.

The correspondence between chaos and EE can be *intuited* when one considers the **linear entanglement entropy** (**EE**) measure

$$S = 1 - \mathrm{tr}\rho_A^2, \tag{4.3}$$

where, following the notation in Sec. 2.1 ρ_A is the reduced density matrix of the bipartition of the Hilbert space $\mathcal{H} = \mathcal{H}_A \otimes \mathcal{H}_B$ (ρ is the density matrix of the whole Hilbert space). When ρ_A is a maximally mixed state, S is maximised (see Appendix A.1 for proof). For a maximally mixed state, further bipartition of ρ would still result in maximally mixed state, and hence the S would still be maximized. For maximally mixed states, all the states accessible to the reduced system share the same probability of occurrence. This situation is reminiscent of the state of a system that corresponds to the canonical ensemble at infinite temperature in which all micro-states of this system occur with the same probabilities. Since we deal here with kicked dynamics, we heuristically expect that energy is periodically delivered to and accumulated in these systems, therefore we expect that in the long-time limit these systems should be described well by the ensemble distribution corresponding to infinite-temperature canonical ensemble. In this sense in the long-time limit, these systems achieve **ergodicity**, that is the time-average of physical observables became equal to the ensemble average with respect to infinite-temperature canonical-ensemble.

In classical systems, one may have chaos even in non-ergodic, or not fully ergodic systems. In the CKR for example, in the presence of **KAM tori** [Arn13] the system is far from ergodic, yet *local chaos* exists, in the sense that trajectories are non-regular but they are restricted to sectors of the phase space (bounded by KAM-tori). Taking this to the quantum regime, it is not immediately obvious

that S can be maximised for an analogous non-ergodic ρ. We would like to ask: *can bipartite EE be a signature of quantum chaos in non-ergodic systems?*

We tackle this problem by studying in detail both the top and rotor in the classical and quantum regimes. These prototypical systems have the main advantage that they exhibit the most important features of chaotic dynamics and a rich phase space, despite their relative simplicity. In order to directly compare the QKT and the QKR, we study the latter as a special limit of the former, exploiting the formulation given by Haake and Shepelyansky in [HS88]. In light of the experimental accessibility of the multi-qubit system, this approach has the further convenience that it allows one to describe the QKT and QKR in the same closed multi-qubit system. Using this system as a case-study, we will show that EE is a signature of quantum chaos even in highly non-ergodic systems. Specifically, in Sec. 4.2 we review the CKT and QKT. We calculate the KSE of the CKT and the EE of the QKT. In Sec. 4.3 we look at the CKR, the QKR and we derive the kicked rotor as a limiting case of the kicked top. We show that bipartite EE is a good signature of quantum chaos in this non-ergodic system. In Sec. 4.4 we discuss properties of our quantum system that are reminiscent of KAM theory.

4.2 Quantum kicked top

The Hamiltonian of the QKT [HKS87] is

$$H_T = \alpha J_x + \frac{\beta}{2j} J_z^2 \sum_{n=-\infty}^{\infty} \delta(t-n) \tag{4.4}$$

where $\boldsymbol{J}$ is the angular momentum vector that obeys the commutation relations

$$[J_i, J_j] = i\varepsilon_{ijk} J_k \ . \tag{4.5}$$

The magnitude $\boldsymbol{J}^2 = j(j+1)\hbar^2$ is a conserved quantity. The first term in Eq. (4.4) describes a precession around the x-axis with angular frequency α. The second term represents a periodic kick. Each kick is an impulsive rotation around the z-axis by an angle proportional to J_z. For convenience we work in natural units where $\hbar = 1$, whereas the time is counted with the number of kicks. The proportionality factor involves dimensionless coupling constant β/j, where β is known as the torsion strength.

The angular momentum operators at each kick can be obtained from the discrete time evolution of the operators in the Heisenberg picture,

$$\boldsymbol{J}_{n+1} = U_T^\dagger \boldsymbol{J}_n U_T, \tag{4.6}$$

where U_T is the **Floquet operator** describing the unitary evolution from kick to kick,

$$U_T = \exp(-i\frac{\beta}{2j} J_z^2) \exp(-i\alpha J_x) \ . \tag{4.7}$$

In the spirit of [Wan+04] (and several following works), modelling the system as a N-spin system, the angular momentum operators can be expressed in terms of Pauli operators,

$$J_\gamma = \sum_{i=1}^{N} \frac{\sigma_{\gamma_i}}{2}, \tag{4.8}$$

where $\gamma = x, y, z$.

We choose the initial pure state to be symmetric under the exchange of any spin, so that the state vector at an later time is also symmetric. Thus we can write the state of our N-spin system in terms of **Dicke states** $|j, m\rangle$ (see also Eq. (2.47) and related discussion), where $m = -j, -j+1, \cdots, j$, with $j = N/2$. To connect the quantum and classical dynamics of the kicked top, we choose the initial state to be the **spin coherent state**

$$|\Phi, \Theta\rangle = \exp\{i\Theta[J_x \sin\Phi - J_y \cos\Phi]\}|j, j\rangle \ . \tag{4.9}$$

The state of the system after $n+1$ kicks is

$$|\psi\rangle_{n+1} = U_T|\psi\rangle_n, \tag{4.10}$$

where $|\psi\rangle_0 = |\Phi, \Theta\rangle$.

4.2.1 Classical kicked top

The classical phase space of the kicked top can be given in the form of a **Poincaré map**, representing the stroboscopic evolution of the classical angular momentum.

As well known in the literature (see e.g. [HKS87]), one can obtain this classical map from the quantum evolution in Eq. (4.6). We firstly introduce the normalised angular momentum vector $\boldsymbol{X} = \langle \boldsymbol{J} \rangle / j$ and take $j \to \infty$ (this is equivalent to taking the thermodynamic limit $N \to \infty$). Its kicked evolution is $\boldsymbol{X}_{n+1} = f(\boldsymbol{X}_n)$ and is obtained substituting $\boldsymbol{X}$ into Eq. (4.6), giving finally the classical map

$$\begin{aligned}
X_{n+1} &= X_n \cos[\beta(Y_n \sin\alpha + Z_n \cos\alpha)] \\
&\quad - (Y_n \cos\alpha - Z_n \sin\alpha) \sin[\beta(Y_n \sin\alpha + Z_n \cos\alpha)] \ , \\
Y_{n+1} &= X_n \sin[\beta(Y_n \sin\alpha + Z_n \cos\alpha)] \\
&\quad + (Y_n \cos\alpha - Z_n \sin\alpha) \cos[\beta(Y_n \sin\alpha + Z_n \cos\alpha)] \ , \\
Z_{n+1} &= Y_n \sin\alpha + Z_n \cos\alpha \ .
\end{aligned} \tag{4.11}$$

The normalised angular momentum vector can be parameterised in polar coordinates, $\boldsymbol{X} = (\sin\Theta\cos\Phi, \sin\Theta\sin\Phi, \cos\Theta)$, to give a two-dimensional classical phase space, in the form of a Poincaré map. Fig. 4.1(a) maps the Poincaré map for $\alpha = \pi/2, \beta = 3$.

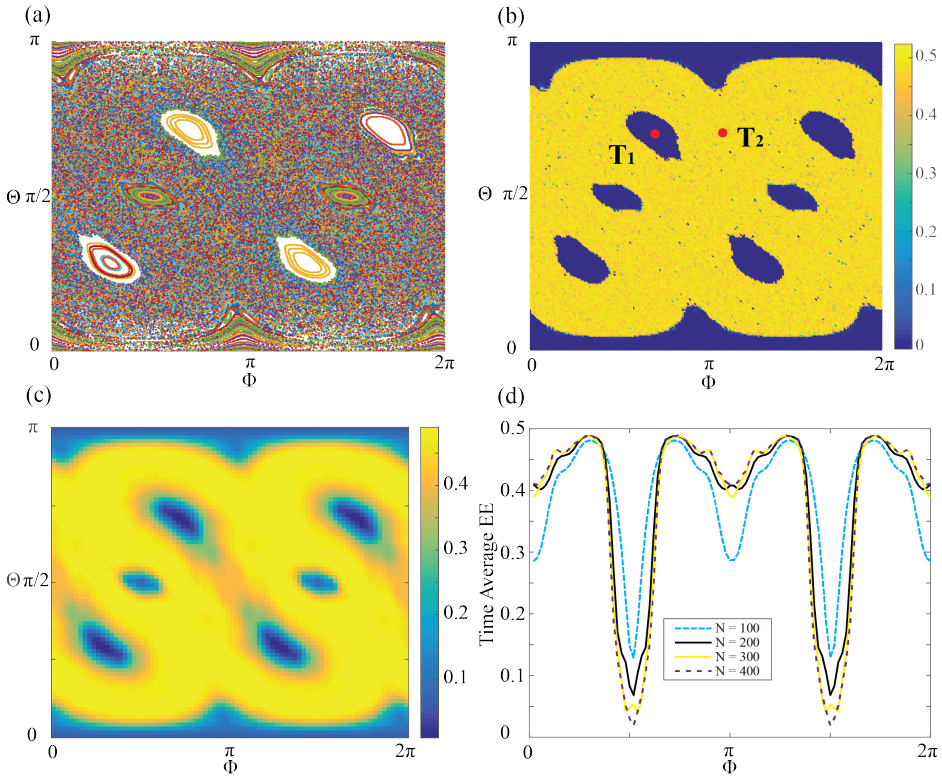

FIGURE 4.1: (a) The classical phase space of the CKT, with 500 random initial conditions for a duration of 500 kicks. (b) The KSE of the CKT, calculated on a grid of 200×200 initial conditions, iterating the linear map for 10^4 steps. KSE > 0 corresponds to chaotic behavior, whereas KSE = 0 indicates regular behavior. Point T_1, T_2 marks $(\Phi, \Theta) = (2.20, 2.25)$ and $(3.57, 2.25)$ respectively. (c) The time-averaged EE of the QKT, calculating for a system of $N = 300$ spins and averaged over $T = 300$ kicks. A comparison of (b) and (c) shows a remarkable correspondence between chaotic (regular) classical behavior and high (low) EE. However, in the classical case there is a well defined demarcation between chaotic and regular regions, whereas in the quantum case the transition from regions of low to high EE is smooth. (d) plots the time-averaged EE at $\Theta = \pi/2$ for different numbers of spins N. The transition from regions of low EE to high EE becomes starker with increasing number of spins, marking the transition to quantum chaos more abruptly, in a similar fashion to classical behavior; $\alpha = \pi/2, \beta = 3$.

4.2.2 Kolmogorov-Sinai entropy of kicked top

The Poincaré map provides a pictorial representation of the phase space, through which one can visually distinguish between regular and chaotic regions. However, to have a proper quantitative measure of the degree of chaoticity, we make use of the KSE. The KSE is the rate of change with time of the coarse-grained Gibbs entropy [Kol58; Kol59] and is calculated as [Pes77]

$$h_{\mathrm{KS}} = \lim_{t\to\infty} \frac{1}{t} \sum_{n=1}^{t} \log_2 l_n \tag{4.12}$$

where $l_n = \sqrt{(\delta X_n)^2 + (\delta Y_n)^2 + (\delta Z_n)^2}$ is the distance in the phase space between two initially close points after n kicks. Importantly, Pesin [Pes77] showed that the KSE is equal to the sum of the positive Lyapunov exponents. As the Lyapunov exponents give the rate of separation of two infinitesimally close trajectories, the KSE $= 0$ for regular regions, and the KSE > 0 for chaotic ones, for times large enough. The KSE therefore is a quantitative measure of the level of chaos. Fig. 4.1(b) plots h_{KS} of the CKT for $\alpha = \pi/2, \beta = 3$. $h_{\mathrm{KS}} = 0$ for regularly regions. For chaotic regions, $h_{\mathrm{KS}} > 0$, as here the trajectories are divergent.

The procedure to obtain the KSE is as follows. The generalised iterative map $\boldsymbol{x}_{n+1} = f(\boldsymbol{x}_n)$ is linearised to give its associated tangent map $\delta\boldsymbol{x}_{n+1} = f(\boldsymbol{x}_n + \delta\boldsymbol{x}_n) - f(\boldsymbol{x}_n)$. The tangent map is rescaled, $\delta\boldsymbol{x}_n \to \delta\boldsymbol{x}_n/l_n$, before being fed back at each iteration. The tangent map reads:

$$\begin{aligned}
\delta X_{n+1} &= \delta X_n \cos\gamma_n \\
&\quad + \delta Y_n\big[- X_n\beta \sin\alpha \sin\gamma_n - Y_n\beta \sin\alpha \cos\alpha \cos\gamma_n \\
&\quad + Z_n\beta \sin^2\alpha \cos\gamma_n - \cos\alpha \sin\gamma_n\big] \\
&\quad + \delta Z_n\big[- X_n\beta \cos\alpha \sin\gamma_n - Y_n\beta \cos^2\alpha \cos\gamma_n \\
&\quad + Z_n\beta \cos\alpha \sin\alpha \cos\gamma_n + \sin\alpha \sin\gamma_n\big], \\
\delta Y_{n+1} &= \delta X_n \sin\gamma_n \\
&\quad + \delta Y_n\big[X_n\beta \sin\alpha \cos\gamma_n - Y_n\beta \sin\alpha \cos\alpha \sin\gamma_n \\
&\quad + Z_n\beta \sin^2\alpha \sin\gamma_n + \cos\alpha \cos\gamma_n\big] \\
&\quad + \delta Z_n\big[X_n\beta \cos\alpha \cos\gamma_n - Y_n\beta \cos^2\alpha \sin\gamma_n \\
&\quad + Z_n\beta \cos\alpha \sin\alpha \sin\gamma_n + \cos\alpha \cos\gamma_n\big], \\
\delta Z_{n+1} &= \delta Y_n \sin\alpha + \delta Z_n \cos\alpha,
\end{aligned} \tag{4.13}$$

where $\gamma_n \equiv Y_n\beta \sin\alpha + Z_n\beta \cos\alpha$. In Appendix A.2 a detailed calculation of the KSE is provided. At the best of our knowledge, this is the first time the KSE has been calculated for the CKT.

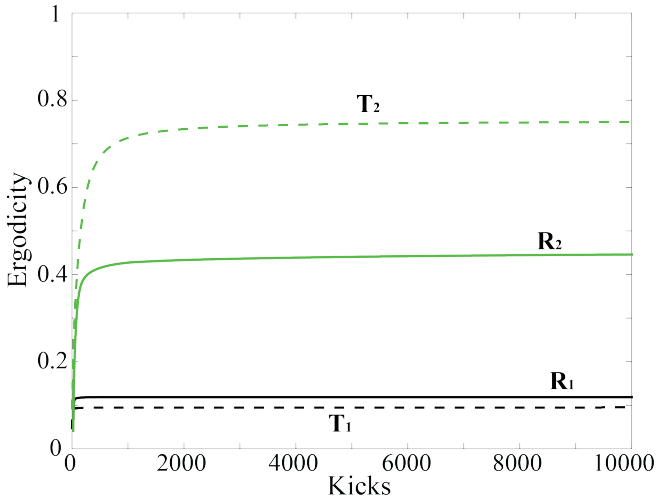

FIGURE 4.2: Time evolution of the ergodicity for the QKT (dashed lines) and the QKR-limit for $j = 9$ (solid lines) in a regular region (black) and chaotic regions (green/grey). Points T_1, T_2 are marked in Fig. 4.1 and R_1, R_2 are marked in Fig. 4.4. The chaotic region (corresponding to the initial point T_2) in the QKT can be termed as quasi-ergodic, since our ergodicity measure is close to 1 (about 0.8). In contrast, the chaotic region (corresponding to the initial point R_2) in the QKR-limit hardly shows any signature of ergodicity. We attribute this fact to the persistent presences of the KAM tori, bounding the classical chaotic regions in the CKR. The number of spins is $N = 500$.

4.2.3 Top ergodicity

Ergodic systems are dynamical systems in which time averages of the observables are provided by a suitable ensemble averages:

$$\langle O \rangle_{\text{time}} = \langle O \rangle_{\text{ensemble}} \, . \tag{4.14}$$

In a very special situation, in which the dynamics is such that the energy is delivered to and accumulated in the system, one expects that the time averages of observables in the long-time limit correspond to ensemble averages calculate with respect to the canonical Gibbs-Boltzmann ensemble $\rho_G(T)$ at infinite-temperature:

$$\rho_\infty = \lim_{T\to\infty} \rho_G(T) = \lim_{T\to\infty} \sum_n \exp^{-\frac{H_T}{k_B T}} |\psi\rangle_n \langle\psi|_n, \tag{4.15}$$

where T is the temperature and k_B is the Boltzmann constant. In this situation the system uniformly explores all states over time, such that an observable O averaged over time equals the same observable averaged over all states.

The full QKT system is in a pure state, therefore its EE, defined in Eq. (4.19), is always zero if we do not take any bipartition of the system. This is not so with its ergodicity. We measure the ergodicity as the *fidelity* [Joz94]

$$F(\rho, \rho_\infty) = \text{tr}\sqrt{\sqrt{\rho_\infty}\bar{\rho}\sqrt{\rho_\infty}} \tag{4.16}$$

where $\bar{\rho}$ is the time averaged density matrix of the full system. As all states are equally probable in the infinite-temperature Gibbs-Boltzmann canonical ensemble, $\rho_\infty = \frac{1}{N+1}\mathbb{1}$ is (proportional to) a unit matrix of the same dimension as ρ. The closer F is to 1, the closer our system is to ergodic behavior, *i.e.* time averages are equal to state-space averages. It is worth noting that at time n, $\rho_n = |\psi\rangle_n\langle\psi|_n$ is density matrix of a pure state, but here we are taking the density matrix averaged over time n, $\bar{\rho} = \sum_i^n \rho_i/n$. Another important point it is necessary to clarify here is that the concept of canonical ensemble is valid only for systems interacting and exchanging energy with the heat-bath; indeed, the classical and quantum kicked top are explicitly time-dependent and are not of this category. In fact, because of the external kicking, they are not in equilibrium with the environment. Still, in the long-time limit we expect that a lot of energy is delivered to the system, so we can assume the infinite-temperature canonical ensemble as the equilibrium limit ensemble ρ_∞.

In the phase space of the CKT of Fig. 4.1(a), chaotic initial points explore much of the phase space, in comparison to regular initial points which explore a regular narrow band of the phase space; correspondingly chaotic regions are ergodic, whereas regular regions are not. Does this notion of chaos and ergodicity hold in the quantum case? To answer this question, we calculate the quantum ergodicity at points corresponding to chaotic and regular initial conditions.

We pick two representative initial conditions corresponding to regular and chaos points, and calculate their ergodicity in the QKT: $(\Phi, \Theta) = (2.20, 2.25)$ and $(3.57, 2.25)$, labelled respectively as T_1 and T_2 in Fig. 4.1. Fig. 4.2 plots the ergodicity of these two points: point T_2 is "quasi" ergodic, since our ergodicity measure is close to 1 (about 0.8), whereas point T_1 is far from ergodic. The reason why the chaotic regions are not fully ergodic is that there are regular regions which are not visited by initial conditions beginning in the chaotic regions. In other words, chaotic regions are ergodic and regular regions are not, in the corresponding quantum system. In the next section, we calculate the EE of these regions.

4.2.4 Top entanglement entropy

The QKT Hamiltonian acts collectively on all N spins, thereby preserving the symmetry of the N-spin state; this means that the spin expectation value of any single spin is

$$\langle s_\gamma \rangle = \frac{\langle J_\gamma \rangle}{2j} \,. \tag{4.17}$$

The reduced density matrix of a single spin is

$$\rho_{(1)} = \frac{1}{2} + \langle \boldsymbol{s} \rangle \cdot \boldsymbol{\sigma} \,. \tag{4.18}$$

In the context of quantum chaos and EE, the choice of bipartition is not well understood; different bipartition choice can lead to different results. In prior work, Ref. [Gho+08; LM11] bi-partitioned one-particle from the larger systems, Ref. [Wan+04] bi-partitioned two-particles from the larger system, and Ref. [Lak01] averages over-all possible partitions. However, only the one-particle bi-partition has been experimentally verified [Nei+16]. Here we have chosen the one-particle bi-partition, because it is the simplest to calculate. The role that the choice of bipartition plays in quantum chaos would make an interesting future study.

From the definition of linear entropy ($S = 1 - \mathrm{tr}\rho_{(1)}^2$), the EE of a single spin with the rest of the system is [Gho+08]

$$S = \frac{1}{2}\left(1 - \frac{\langle \boldsymbol{J} \rangle \cdot \langle \boldsymbol{J} \rangle}{j^2}\right) . \tag{4.19}$$

We define the time-averaged EE as $1/T \sum_n S(n)$, where $S(n)$ is the linear entropy after the n kicks and T is the final number of kicks. For finite systems, time-averaging is used to estimate the equilibrium value approached by larger systems [Nei+16]. It is worth noting that the time-average of S is different from applying the time-average of the density matrix to Eq. (4.19), which would not be a measure of EE.

We use the time-average EE to depict a quantum phase space: choosing the initial state to be spin coherent $|\Theta, \Phi\rangle$ with $0 \leq \Theta < \pi$ and $0 \leq \Phi < 2\pi$, Fig. 4.1(c) plots the time-averaged EE of the QKT for $\alpha = \pi/2, \beta = 3$. Remarkably there is an obvious correspondence between the time-averaged EE of the QKT and the classical phase space trajectories and KSE, as shown in Fig. 4.1(a) and (b). Regions of low EE correspond to regular trajectories (KSE = 0), and regions of high EE correspond to chaotic trajectories (KSE > 0).

An important difference between the KSE and EE of the kicked top however, is that in the classical case there is a well defined demarcation between chaotic and regular regions, whereas in the quantum case the transition from regions of low to high EE is smooth. The change in EE becomes greater with increasing number of spins, and therefore the transition from regions of high EE to low EE occurs more rapidly as shown in Fig. 4.1(d). From Fig. 4.1(d) one may conjecture that in the very large spin limit, classical chaotic regions correspond to maximum EE = $1/2$, and regular regions corresponds to minimum EE = 0, with a well defined demarcation between these two EE regions, in the QKT.

The surprising correspondence between EE and KSE is made more stark when one compares the vastly different forms of the KSE Eq. (4.12) and the EE Eq. (4.19). Underlying these very different equations however is a commonality in the information that they encapsulate; both are the rate of information production in their relative classical and quantum domains [ZS98].

In the kicked-top, chaotic regions are quasi-ergodic, and these regions are marked by high EE, and non-ergodic regions are marked by low EE. This however is not a general relation, and in the next section we show that non-ergodic regions can also exhibit high EE.

4.3 Quantum kicked rotor

Another well-known kicked system used in the study of chaos is the kicked rotor. The Hamiltonian of the QKR is

$$H_R = \frac{1}{2I} P^2 + K \cos\Phi \sum_{n=-\infty}^{\infty} \delta(t-n) \tag{4.20}$$

where Φ is the angle operator and P is the angular momentum, canonically conjugate to Φ. K is the kicking strength and I is the moment of inertia. The rotor operators obey the commutation relation

$$[P, \Phi] = -i\,. \tag{4.21}$$

The angular momentum and angle operator at each kick can be obtained from the discrete time evolution of the operators in the Heisenberg picture,

$$\begin{aligned} P_{n+1} &= U_R^\dagger P_n U_R \ , \\ \Phi_{n+1} &= U_R^\dagger \Phi_n U_R \ , \end{aligned} \tag{4.22}$$

where the Floquet operator U_R is

$$U_R = \exp(-i\frac{P^2}{2I}) \exp(-iK\cos\Phi) \ . \tag{4.23}$$

This produces the stroboscopic equations

$$\begin{aligned} P_{n+1} &= P_n + K\sin\Phi_n \ , \\ \Phi_{n+1} &= \Phi_n + P_{n+1}/I \ . \end{aligned} \tag{4.24}$$

As there are no products of P and Φ terms, this equation is also valid classically.

The phase space of the rotor is a cylinder, $-\infty < P < \infty$, $0 \leq \Phi < 2\pi$. This is topological different from the spherical phase space of the top. Although the rotor is unbounded in P, the stroboscopic equations show that the system is invariant under $2\pi I$ translations in P and 2π in Φ. Fig. 4.4(a) plots the classical rotor phase space for $K = 0.9, I = 1$.

4.3.1 Classical rotor-limit of the top

Rotor dynamics may be derived from the top if we confine the top to an equatorial waistband as depicted in Fig. 4.3 [HS88]. This is achieved by reducing the precession frequency about the x-axis and increasing the torsion strength about the z-axis through the rescaling

$$\alpha = K/j \ , \quad \beta = j/I \ , \tag{4.25}$$

where $j \to \infty$. We call this substitution the **rotor-limit of the top**, or simply the **rotor-limit**. If one begins in the equatorial waistband, this rescaling confines the angular momentum to (Fig. 4.3)

$$X = \cos\Phi \ , \quad Y = \sin\Phi \ , \quad Z = P/j \ . \tag{4.26}$$

Substitution of Eq. (4.25) and (4.26) into the kicked-top map of Eq. (4.11), takes one to the kicked-rotor map of Eq. (4.24).

The rotor may be approximated by the top even for relatively modest values of j. Fig. 4.4(c) plots the top phase space with the rescaled α and β for $j = 9$, in between $P = 0$ and 2π. A comparison with the rotor phase space of Fig. 4.4(a), shows that rotor characteristics are clearly seen in the rotor-limit of the top phase space of Fig. 4.4(c).

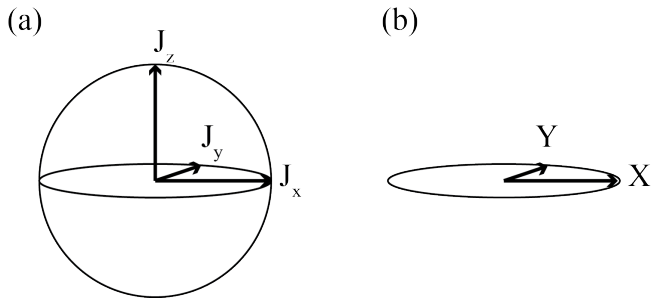

FIGURE 4.3: (a) The magnitude of the angular momentum $\boldsymbol{J}$ of the top is a conserved quantity, and therefore is represented on a sphere. (b) The rotor-limit is achieved with the rescaling $\alpha = K/j, \beta = j/I$, where $j \to \infty$. If one begins in the equatorial waistband, this rescaling confines the angular momentum to $X = \cos\Phi, Y = \sin\Phi, Z = P/j$.

4.3.2 Rotor Kolmogorov-Sinai entropy

To further quantity the similarities of the rotor and the rotor-limit, we compare the KSE of the two. From Eq. (4.24), the tangent map for the rotor is (see Appendix A.3 for derivation)

$$\delta P_{n+1} = \delta P_n + K\cos(\Phi_n)\delta\Phi_n \ , \tag{4.27}$$

$$\delta\Phi_{n+1} = \Big(1 + \frac{K}{I}\cos\Phi_n\Big)\delta\Phi_n + \frac{\delta P_n}{I}. \tag{4.28}$$

Using this tangent map, Fig. 4.4(b) plots h_{KS} for the rotor for $K = 0.9, I = 1$. Fig. 4.4(d) similarly plots h_{KS} for the rotor-limit. The two plots show a high level of similarities, but also differences, which we discuss below.

4.3.3 Quantum rotor-limit of the top

Let us define the following rescaled operators,

$$\hat{X} \equiv \hat{J}_x/j \ , \quad \hat{Y} \equiv \hat{J}_y/j \ , \quad \hat{P} \equiv \hat{J}_z \ . \tag{4.29}$$

Substitution of these operators into the commutation relations of Eq. (4.5), and taking $j \to \infty$ so that we may drop the $1/j^2$ terms, we get,

$$[\hat{X}, \hat{Y}] = 0, \quad [\hat{Y}, \hat{P}] = i\hat{X} \ , \quad [\hat{P}, \hat{X}] = i\hat{Y} \ . \tag{4.30}$$

These commutation relations are satisfied with

$$\hat{X} = \cos\Phi \ , \quad \hat{Y} = \sin\Phi \ , \quad \hat{P} = -i\frac{\partial}{\partial\Phi} \ . \tag{4.31}$$

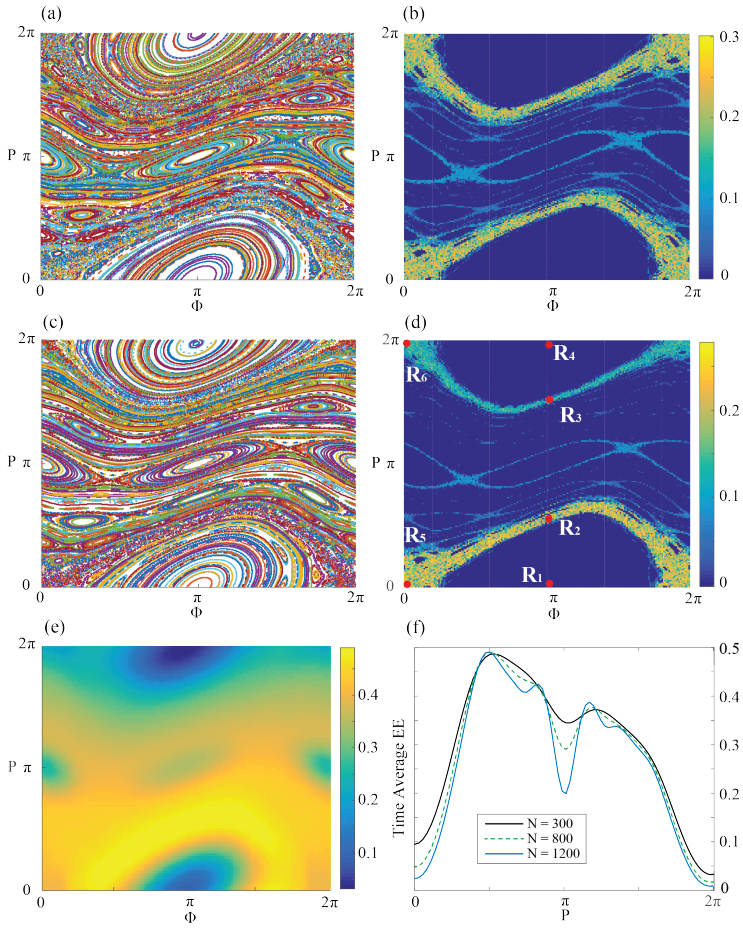

FIGURE 4.4: (a) and (c) show the classical phase space of the CKR and the CKR-limit ($j = 9$), with 500 random initial conditions for a duration of 500 kicks. (b) and (d) show the KSE of the CKR and CKR-limit ($j = 9$), calculated on a grid of 200×200 initial conditions, iterating the linear map for 10^4 steps. The points $R_1, R_2, R_3, R_4, R_5, R_6$ mark $(\Phi, \Theta) = (\pi, 0), (\pi, \pi/2), (\pi, 3\pi/4), (\pi, 2\pi), (0, 0), (0, 2\pi)$. (e) plots the time-averaged EE of the QKR-limit, for $N = 300$ spins and a duration of $T = 300$ kicks. (f) plots the time-averaged EE of the QKR-limit at $\Phi = \pi$ for various N; the transition from regions of low EE to high EE becomes more stark with increasing number of spins. Parameters: $K = 0.9, I = 1$.

Substituting Eq. (4.25), Eq. (4.29), and (4.30), into the top Hamiltonian of Eq. (4.4), one retrieves the rotor Hamiltonian of Eq. (4.20) [HS88].

4.3.4 Rotor ergodicity

The presence of KAM tori can separate regions of *local chaos*. This is clearly represented in the phase space of the CKR of Fig. 4.4(b), where islands of KSE > 0 are separated from each other. Trajectories whose initial conditions lie in this regions, are completely irregular (non-periodic) *i.e.* chaotic; nevertheless, they cannot invade other regions of the phase space. The KAM tori act as inpenetrable barriers which prevent the system from exploring the whole phase space; here the system is highly non-ergodic. These chaotic regions are localised, as opposed to the global chaos exhibited in the CKT.

We calculate the ergodicity corresponding to a point in one of these regular region and also in a local chaos region: $(\Theta, \Phi) = (\pi, 0)$ and $(\pi, \pi/2)$, respectively. These points are marked by R_1 and R_2 in Fig. 4.4(d). Fig. 4.2 shows that the ergodicity of the regular region is low, but that point R_2 is also highly non-ergodic. We would like to know, whether EE can still be a signature of quantum chaos in these highly non-ergodic regions.

4.3.5 Rotor entanglement entropy

As the classical rotor may be extracted from the top for modest values of j, quantum rotor physics may also be extracted from the quantum top. However in the quantum case we will need a large number of spins to identify the correspondence between EE and chaos in the rotor, as we will show.

We begin with the rotor-limit with $j = 9$, as with the classical example. For the range $0 \leq \langle \hat{P} \rangle < 2\pi$, Θ is restricted to $\arccos(2\pi/j) \leq \Theta < \pi/2$ or -$\pi/2 \leq \Theta < -\arccos(2\pi/j)$, since $P = Zj = j\cos\Theta$. We choose the latter range for Θ, as this will correspond to the rotor map of Eq. (4.24). For large j, this range is a small strip in the equatorial waistband of the top phase space.

Now unlike the classical case, where the demarcation between regular and chaotic regions are well defined, in the quantum regime the transition between corresponding regions of low and high EE is gradual. This means that deeper in the quantum regime, features corresponding to the classical features may be washed out. Fig. 4.6 plots the EE for 4 different points ($K = 0.9, I = 1$): $R_1 = (\Phi, P) = (\pi, 0)$, $R_2 = (\pi, \pi/2)$, $R_3 = (\pi, 3/4\pi)$, $R_4 = (\pi, 2\pi)$ for $N = 50$ and 500. From Fig. 4.4(b), we see that points R_1 and R_4 correspond to classical regular behavior, and points R_2 and R_3 correspond to chaos. A comparison of Fig 4.6(a) and (b) shows that as one increases the number of spins these regions become more distinguishable, in that there is less overlap of the EE marking each region. This is also reflected in Fig. 4.4(f) which plots the EE at $\Phi = \pi$ for various N, where the difference between EE of chaotic and regular regions becomes greater with increasing N.

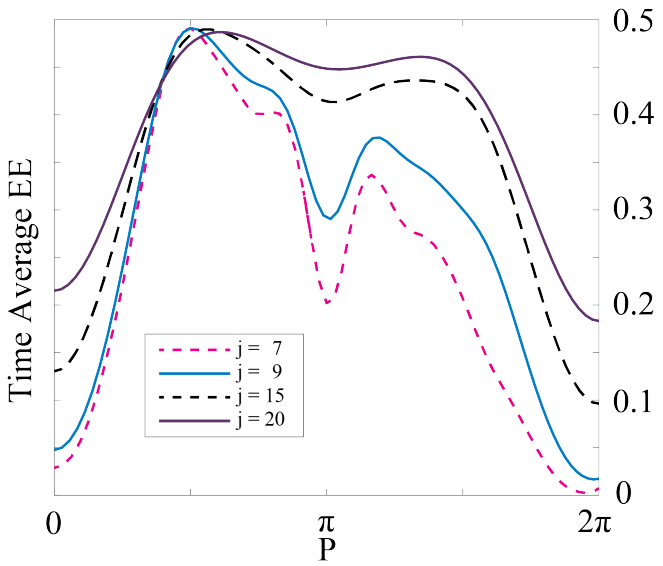

FIGURE 4.5: The time-averaged EE of the QKT-limit with $N = 600$ spins, at $\phi = \pi$ for various j. As j increases, the EE is more symmetric as it approaches the QKR.

Fig. 4.6 shows that points R_2 and R_3 are different, revealing an asymmetry in the rotor-limit, that is not present in the rotor phase space. This asymmetry is also clearly evident in Fig. 4.4(f). In the classical case, the KSE plot of the rotor-limit [Fig. 4.4(d)] is also asymmetric, whereas the KSE plot of the rotor is not [Fig. 4.4(b)]. The root of the asymmetry lies in the fact that we have used a finite value of j, whereas the rotor is reached from the top only in the limit of $j \to \infty$.

Fig. 4.5 plots the time-averaged EE at $\Phi = \pi$ for various j with constant $N = 500$. Now two operational properties of the rotor-limit are revealed here. Firstly, increasing j means that the behavior of the system approaches that of the quantum rotor, thereby reducing the aforementioned asymmetry. Secondly, increasing j for a constant N presents a trade-off: although the system approaches the quantum rotor, for larger values of j one requires more spins to achieve the correspondence between EE and the classical features of the phase space; *i.e.* the difference between the EE of chaotic and regular regions is reduced. The intuitive reason for this is that, larger j means that we are working in a narrower equatorial waistband. In the parameters of the top, this means that Θ is confined to the range $\{\pi/2, \arccos(2\pi/j)\}$. As we are working in an increasingly narrower region as j increases, one requires a larger number of spins to be able to distinguish the corresponding classical features, as exemplified in Fig. 4.6.

Finally we plot the EE corresponding to the entire classical phase space for the QKR-limit in Fig. 4.4(e). We see a qualitative correspondence with the KSE

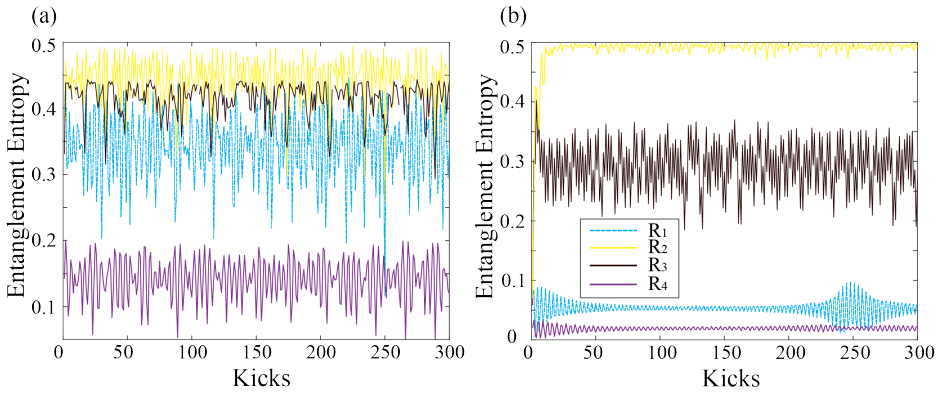

FIGURE 4.6: Plots of the EE for 4 different points [as marked in Fig. 4.4(d)]: $R_1 = (\Phi, P) = (\pi, 0)$, $R_2 = (\pi, \pi/2)$, $R_3 = (\pi, 3/4\pi)$, $R_4 = (\pi, 2\pi)$ for (a) $N = 50$ and (b) 500. Points R_1 and R_4 correspond to classical regular behavior, and points R_2 and R_3 corresponds to chaos. A comparison of (a) and (b) shows that as one increases the number of spins these regions become more distinguishable, in that there is less overlap of the EE marking each region. Parameters follow Fig. 4.4.

of the CKR-limit in Fig. 4.4(d). Importantly, in contrast to the kicked top, here the system is far from ergodic. *Therefore EE can be a signature of quantum chaos even in non-ergodic systems*.

To intuit how this is so, recall Eq. (4.19) which gives the EE of the one-spin bipartition. For maximally mixed states, the state space is explored uniformly, so that $\langle \boldsymbol{J} \rangle = 0$. One may roughly consider this to be the case for the quasi-ergodic QKT in Fig. 4.1. However, one should only consider this as an intuitive explanation, as our system is in fact not maximally mixed; it is the time-averaging that gives rise to these effects. In the rotor-limit however, exploration in the $\boldsymbol{J}_z$ direction is suppressed, so that $\boldsymbol{J}_z \to 0$, for states beginning in the equatorial waistband. This suppression means that not the entire space of states is uniformly explored, and therefore the system is far from being ergodic. This means that, $\langle \boldsymbol{J} \rangle = 0$ under the conditions that $\langle \boldsymbol{J} \rangle_x = \langle \boldsymbol{J} \rangle_y = 0$; under these conditions EE is maximised even though the system is non-ergodic conditions. In the next section, we provide an alternative explanation which is reminiscent of KAM theory.

4.4 Quantum Kolmogorov-Arnol'd-Moser theory

An integrable Hamiltonian H_0 in the presence of perturbation is written as

$$H = H_0(\boldsymbol{\kappa}) + \epsilon V(\boldsymbol{\kappa}, \boldsymbol{\lambda}) \tag{4.32}$$

where $\boldsymbol{\kappa}$ and $\boldsymbol{\lambda}$ are the action variables with total D dimension, and ϵ is a small perturbation parameter. Integrable H_0 generates periodic phase-space trajectories that lie on D-dimensional tori surfaces. The **KAM theorem** states that for sufficiently small ϵ, the tori of H_0 do not vanish but are deformed, so that the trajectories generated by H are conditionally periodic [Arn13]. *What is the quantum analogue of KAM theory?*

Understanding the crossover behavior arising from the integrability breaking in quantum systems have been pursued through indirect measures such as level statistics [BT77; BKM10; Rig09a; Rig09b] and in the quasi-classical limit of systems using semi-classical eigenfunction hypothesis [Per73; Ber77; Vor79]. In more direct analogy with KAM theory, an existence conditions for localisation in non-integrable quantum systems has also been developed [HT83]. We do not give a quantum KAM theory here, but simply show properties in our quantum system that are reminiscent of KAM theory. Our motivation is that this may lead to a robust quantum KAM theory in future work.

4.4.1 Entanglement entropy and quantum KAM tori

An alternative perspective on why regions with maximum EE may not be ergodic, can be found by considering the CKR in the context of KAM theory [Chi79; Gre79]. For very small kicking strength trajectories are regular, for very large kicking strength trajectories are chaotic. In between these two extremes, both types of trajectories exists in the phase space, with islands of chaotic regions separated by KAM tori. This means that these islands of chaotic trajectories are bounded and do not explore the whole phase space. The critical value of K where the last of the KAM tori disappears is $K_C \simeq 0.971635$ ($I = 1$) [Gre79].

A quantum analogue of this classical behavior can be qualitatively inspected by using the **Husimi distribution** [Hus40; TS85]. At each point (Φ, P) of the quantum phase space, the Husimi distribution gives the expectation value of the density matrix ρ_n (at time n) of the **spin coherent state** $|\Phi, P\rangle$,

$$\mathcal{P}_H(\Phi, P) = \frac{2j+1}{4\pi}\langle \Phi, P|\rho_n|\Phi, P\rangle. \tag{4.33}$$

In Fig. 4.7, we apply the Husimi distribution to the QKT for states initialised in the regular region (point T_1) and chaotic region (point T_2). Here the Husimi distribution floods the phase space for states initialised in the chaotic region [Fig. 4.7(a)], and is localised for states initialised in a regular region [Fig. 4.7(b)].

In Fig. 4.8(a), (c) and (e), we apply the Husimi distribution to the QKR-limit for states initialised in the chaotic region (point R_5) for increasing kicked strengths: $K = 0.9$ (below the classical critical point K_C), $K = 1.2$ (just above K_C) and $K = 2$ (well above K_C). We observe that although all the three cases correspond to chaos, it is only when K is well above K_C that Husimi distribution floods the phase space [Fig. 4.8(e)]; in comparison, for K near and below K_C, the Husimi distribution is confined to a much smaller fraction of the phase

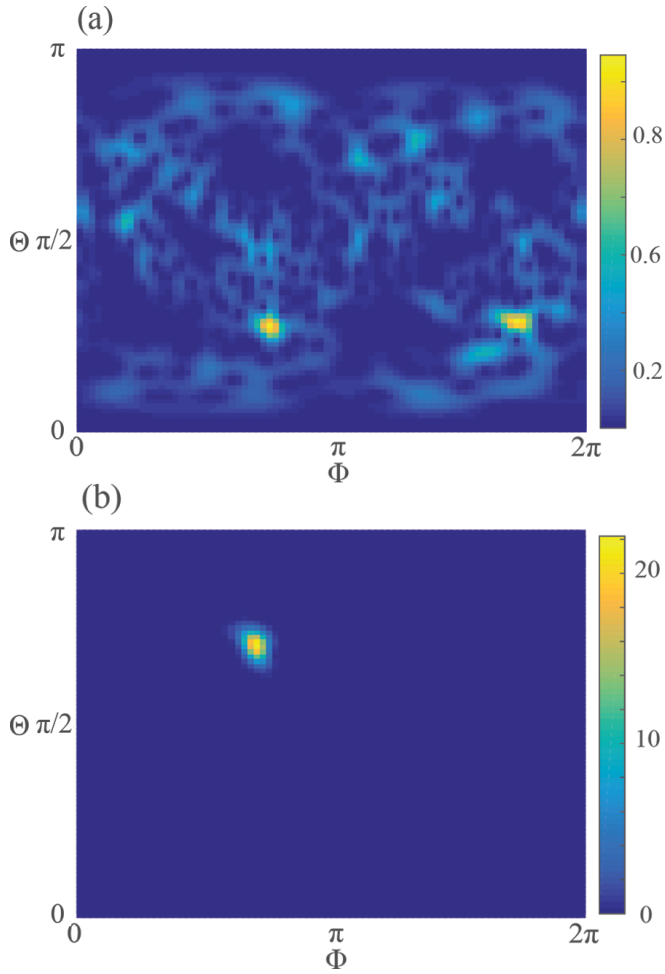

FIGURE 4.7: The Husimi distribution for the QKT after 500 kicks. (a) The initial state corresponds to chaotic point T_2 in Fig. 4.1. The resulting Husimi distribution spreads across the phase space. (b) The initial state corresponds to regular point T_1 in Fig. 4.1. The resulting Husimi distribution is highly confined. All the parameter of the QKT are the same as in Fig. 4.1(c).

space [Fig. 4.8(a) and (c)]. This is in constrast to the QKT, where chaos corresponds to a Husimi distribution which floods the phase space.

We compare the Husimi distribution of the QKR-limit with the classical trajectories of th CKR-limit. In Fig. 4.8(b), (c) and (d), we plot the trajectories of the CKR-limit for states initialised in the chaotic region (point R_5) for the same values of K as for the QKR-limit. When K is above the critical point the trajectory floods the phase space [Fig. 4.8(d) and (f)]; in comparison, when K is below the critical point, the trajectory is confined to a much smaller fraction of the phase space [Fig. 4.8(b)]. Classically, this confinement marks the boundary of the impenetrable regular KAM tori. A comparison of the Husimi distribution of the QKR-lmit with the classical trajectories of the CKR-limit for K well above and below K_C shows a clear qualitative resemblance. This behavior suggests the presence of a quantum analogue of the KAM tori and a phase transition. An important difference however occurs near K_C, which will discuss later in this section.

One may consider torus regions of low EE as the quantum counterpart of classical KAM tori, separating islands of high EE. By analogy to the classical case, we conjecture that the presence of torus regions of low EE indicate that states beginning in different islands of high EE will explore mutually exclusive states, *i.e.* low EE tori separate orthogonal states. This conjecture is numerically supported in Fig. 4.9(a)-(d) which shows the time-averaged density matrices of the full system with initial conditions marked by T_2 in Fig. 4.1(b), and initial conditions marked by R_5,R_2,R_3 in Fig. 4.4(b). Fig. 4.9 graphically depicts the magnitude of the elements of the time-averaged density matrices. Note that we use larger values of $j = 15$ and $N = 500$ than that used to generate Fig. 4.4(e), to be closer to the rotor-limit. The graphical representation clearly shows that T_2 explores the full Hilbert space, whilst R_2,R_3, R_5 only explore a subset of the Hilbert space, explaining why these latter systems are not ergodic. R_2 and R_5 explore the same subspace, whilst R_2 and R_3 explore different different subspaces. Inspection of the rotor phase space in Fig. 4.4(b) shows that R_2 and R_5 belong to the same chaotic island, whilst R_3 belongs to a different one, separated by KAM tori. This leads to the notion that evolution from initial conditions belonging to the same high EE island will explore the same subspace, but different islands explore different subspaces. It is surrounded by a sea of low EE tori that acts to prevent the subspace overlap between different islands.

Increasing the kicking strength above some critical point destroys the low EE tori, and the system is free to explore the full Hilbert space, as for example represented with point T_2; here the system uniformly explores the full Hilbert space and therefore has high fidelity with the infinite-temperature Gibbs-Boltzmann canonical ensemble, ρ_∞. Interestingly the critical point which sees the destruction of low EE tori and the onset of ergodicity, corresponds near to the classical K_C value. In the CKR, K_C marks the disappearance of the last KAM tori and the formation of **KAM cantori** (broken tori [MMP84; BK84]). In the classical case, KAM tori act as impenetrable barriers to the growth of the mean square

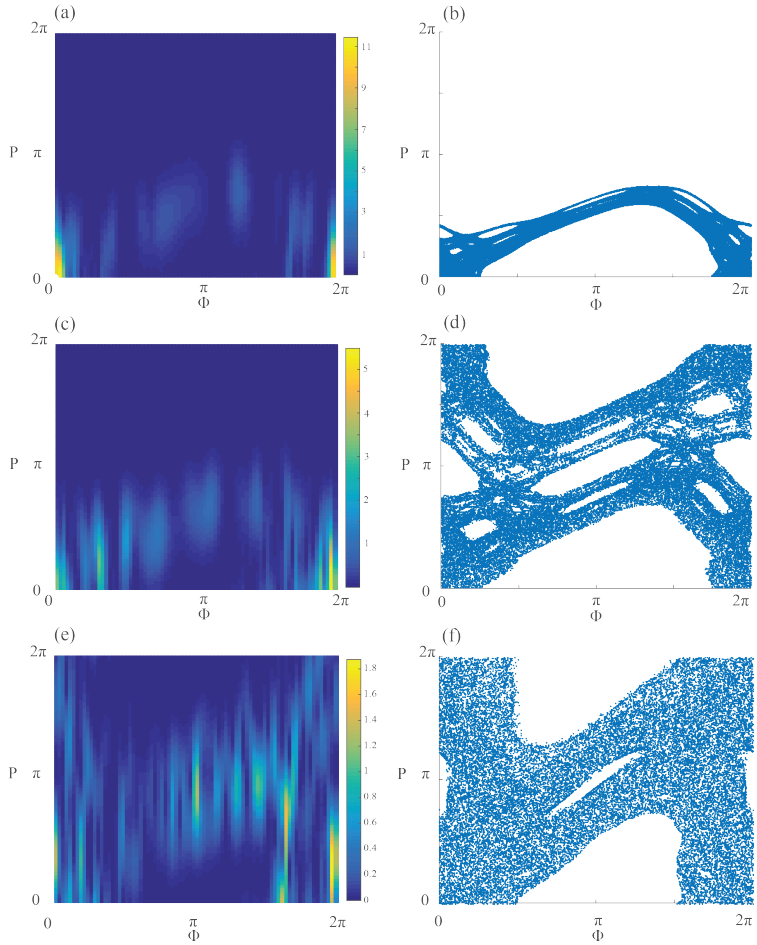

FIGURE 4.8: A comparison of the Husimi distributions [(a), (c) and (e)] for the QKR-limit and trajectories for the CKR [(b), (d) and (f)], for the initial state corresponding to point R_5 [in Fig. 4.4(d)], after 500 kicks, for $N = 500$. In (a) and (b) the kicked strength $K = 0.9$ is below the critical point K_C, and KAM tori confine the Husimi distribution and the classical trajectories. In (c) and (d), $K = 1.2$ is just above K_C: in the quantum case the Husimi distribution is confined (c), whereas the classical trejctory spreads across the phases space. Here the KAM cantori is impenetrable in the quantum case, but permeable in the classical case. Finally, in (e) and (f) the kicked strength $K = 2$ is well above the critical point K_C, and the absence of KAM tori and cantori means the Husimi distribution and the classical trajectory can flood the phase space.

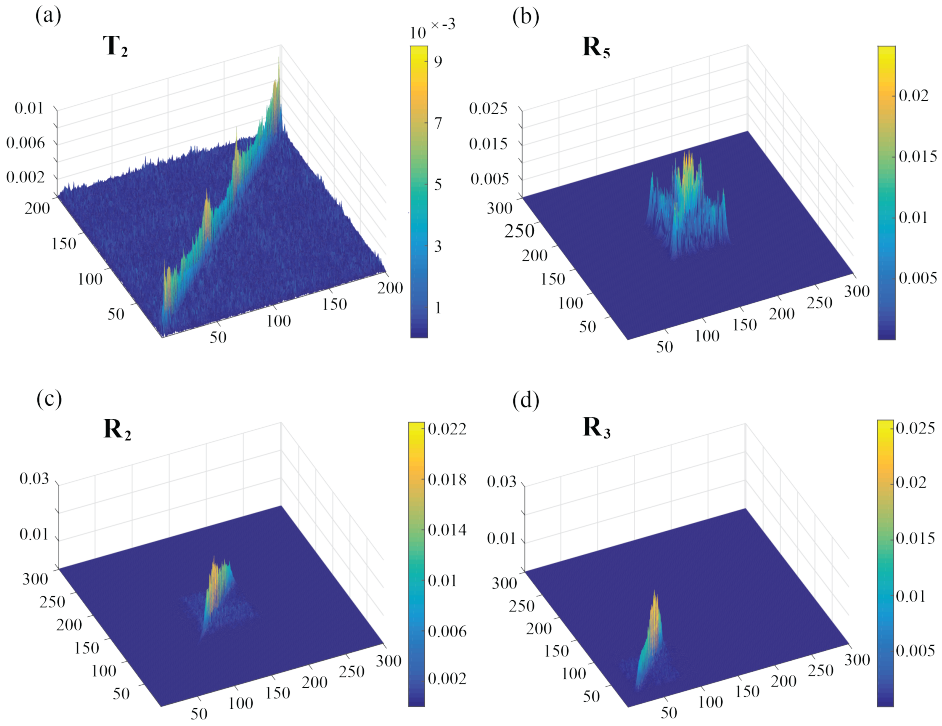

FIGURE 4.9: (a)-(d) shows the time-averaged density matrices for point T_2 in Fig. 4.1(c) and points R_5,R_2,R_3 in Fig. 4.4(d), respectively. R_2 and R_5 belong to the same island of high EE, whereas R_3 belongs to a different high EE island. T_2 uniformly explores the full Hilbert space and therefore is ergodic. R_2,R_3,R_5 explore a subset of the full Hilbert space, and therefore is not ergodic. R_2 and R_3 explore different regions of the subspace, whilst R_2 and R_5 explore the same subspace, leading to the notion that evolution from initial conditions belonging to the same island will explore the same subspace, but different islands explore different subspaces.

displacement, whereas KAM cantori are permeable barriers which only slow the diffusive growth. In contrast, Geisel *et al.* [GRR86] showed that in the quantum case, both KAM tori and cantori correspond to the prohibition of diffusive growth.

To locate the quantum critical point, corresponding to the breaking of the of quantum cantori, in Fig. 4.10, we plot the time averaged fidelity of points R_3 and R_5 [$F(\hat{\rho}_{R_3}, \hat{\rho}_{R_5})$] as a function of K for $N = 500, 1000, 2000, 3000$. Remarkably, the fidelity of points R_3 and R_5 begin to increase not at K_C, but just after, supporting the Giesel *et al.'s* result that cantori correspond to an impenetrable barrier in the quantum case. In other words, Fig. 4.10 suggests that between $K = 0.97$ and 1.3, there exists low EE cantori that prevents diffusive growth. This behavior is supported in the Husimi distribution of Fig. 4.8 (c): in the quantum case the Husimi distribution is localised (c), whereas the classical trajectory has spread across the phase space (d). This is because here, K is not too far above the critical point. Further increases in K sees the Husimi distribution spread across the phase space (e).

The behavior of the EE described here are highly reminiscent of the properties of classical KAM tori, supporting our conjecture that the quantum equivalent of KAM trajectories are tori regions of low EE. The Husimi distribution is a useful tool for locating the quantum cantori. These properties suggests that the methods used and quantum systems studied here, are a fruitful avenue to study quantum KAM theory.

4.5 Summary

In this chapter we have explored the correspondence of EE and chaos in the kicked top and kicked rotor. We have shown that high EE corresponds to global chaos in ergodic systems. The key ingredient throughout the analysis has been the careful use of the rotor-limit of the kicked top. We started from the popular and largely used representation of the QKT as a multi-qubit system, and then we extended it to the study of the QKR, take advantage of a correspondence existing between the two systems, pointed out by Haake and Shepelyansky in [HS88]. An important result is that in taking the rotor-limit of the kicked top, we have also shown that EE corresponds to local chaos in non-ergodic systems. We have shown that the behavior of EE tori resembles that of KAM tori, and therefore propose that entanglement should play an important role in any quantum KAM theory.

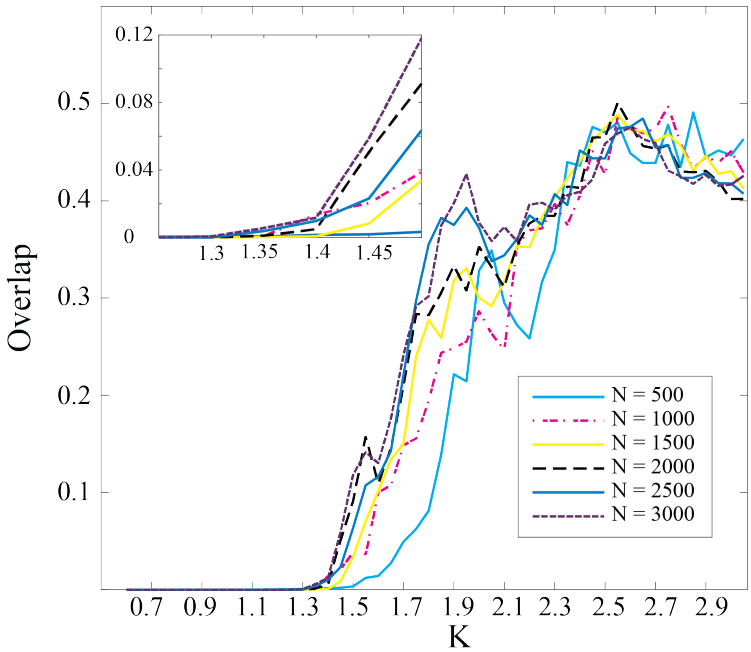

FIGURE 4.10: The time averaged fidelity of points $R_5 = (0, 0)$ and $R_6 = (0, 2\pi)$, $F(\hat{\rho}_{R_5}, \hat{\rho}_{R_6})$, as a function of K for $N = 500, 1500, 2000, 2500, 3000$. The fidelity of points R_5 and R_6 begin to increase not at $K_C \simeq 0.971635$, but just after, supporting the idea that cantori correspond to an impenetrable barrier in the quantum case.

5 Imbalanced Creutz-Hubbard model

In Chap. 2 the entanglement entropy (EE) was introduced as a characteristic quantum property very useful in the analysis of many-body quantum systems. The ground states of gapped-local Hamiltonians satisfy an area law for the entanglement entropy that allows their efficient simulation with only classical resources by using tensor network based numerical techniques introduced in Chap. 3. For one-dimensional ($1D$) systems the EE is bounded by a constant in the gapped phases, while in the proximity of a quantum phase transition (QPT) it diverges logarithmically, where the central charge of the underlying conformal field theory plays the role of universality-class scaling-factor.

In this chapter, we apply these concepts to a concrete interacting $1D$ fermionic system, the **imbalanced Creutz-Hubbard ladder**, to explore new physics. This system possesses a rich phase diagram and the interactions lead to very neat interplay of strongly-correlated and topological effects.

The original results of this chapter are based on the article *"Exploring interacting topological insulators with ultracold atoms: The synthetic Creutz-Hubbard model"* [Jün+17], where a complete theoretical and numerical analysis of the synthetic Creutz-Hubbard ladder is presented and where a possible experimental implementation with ultracold fermions in intensity-modulated optical lattices is also proposed. Here we mainly focus on the numerical matrix product state (MPS) simulations, in order to understand the model in all regimes and to locate exactly its critical lines and the underlying conformal field theories. Wherever possible (namely, in the limit of strong and weak interactions and in the intermediate regime) we compare these numerical results with analytical calculations, but we make reference to the original paper for the details of the derivations, which are beyond the scope of this thesis.

This chapter is organized as follows. Sec. 5.1 is devoted to a crash course on topological insulators, where the main ingredients and terminology used in the rest of the chapter are introduced. We conclude the section showing that for $1D$ spin-systems, MPSs play a crucial role not only in the numerical simulations, but also as a theoretical tool for the classification of the different possible topological nontrivial phases. In Sec. 5.2 the imbalanced Creutz-Hubbard ladder is introduced. In Sec. 5.2.1 the non-interacting limit is reviewed, showing

that this model leads to a topological insulator. In Sec. 5.2.2 the effects of Hubbard interactions are analyzed in the weak, strong and intermediate interacting limit respectively. In Sec. 5.2.3 we completely identify the different phases of the model, together with standard and topological QPT that connect them by numerical density matrix renormalization group (DMRG) simulations.

5.1 Topological phases of matter

Topological features of quantum many-body systems provide a new paradigm in our understanding of the phases of matter [Wen04] and give rise to a promising avenue towards fault-tolerant quantum computation [Kit03; Nay+08]. From a condensed-matter perspective, such features lead to exotic ground states beyond the conventional phases of matter, which are typically understood by the principle of symmetry breaking and the notion of a local order parameter. On the contrary, these exotic states can only be characterised by certain topological properties.

The *integer quantum Hall effect*, which is a paradigmatic example of such peculiar phases [KDP80], requires the introduction of a topological invariant to describe the different plateaus and their associated transverse conductivities [Tho+82]. Another interesting property of this state of matter is the *bulk-boundary correspondence*, which relates such a topological conductivity, a bulk property, to the existence of current-carrying edge states localized within the boundaries of the system [Hal84]. Although the bulk of an integer quantum Hall sample appears as a trivial band insulator, its boundary corresponds to a chiral liquid [KF04].

As realized in a series of seminal works [Hal88; Kit01; KM05], these remarkable properties are not unique to quantum Hall samples subjected to strong magnetic fields. Instead, they arise in various models with different symmetries and in different dimensions [AZ97; Sch+08; Kit09], the so-called **topological insulators and superconductors** [HK10; QZ11], which also lead to the notion of **symmetry-protected topological** (**SPT**) **phases** in the context of **topological order** [Wen04]. Remarkably enough, some of these models have turned out to be accurate descriptions of real insulating materials [Kön+07; Hsi+08; HK10; QZ11], and promising candidates to account for observations in proximitized superconducting materials [Mou+12].

In this section we review the main properties of topological insulators and some useful methods for their characterization. For non-interacting systems, a single particle description is possible and most of the topological features can be extracted by the topology of the bulk's bands (the so-called **bulk-boundary correspondence**). For free fermions, a complete classification of their phases is possible: there exist in fact only ten classes of symmetry for Hamiltonians, corresponding to ten possible combinations of **time-reversal**, **particle-hole** and **chiral** (or **sub-lattice**) symmetries.

Switching on interactions has a twofold effect. On one side they can destroy some topological phases, transforming the topological insulator in a trivial one. On the other side, new topological classes, eluding the non-interacting classification, may appear. From a practical point of view, in presence of interactions, the calculation of **Chern numbers**, **winding numbers**, and other quantities related to bands curvature can become hard, although recently some possible alternatives have been proposed. In the last decade, several works pointed out that bulk entanglement properties of the ground state provide signatures of the topological features for interacting systems. Here we focus on the **entanglement spectrum** (**ES**) already introduced in Sec. 2.1: even if a general theory still lacks, at least for spin chains the ES degeneracy is strictly related to the symmetries of Hamiltonians and it is a powerful tool to distinguish between topological and trivial phases.

5.1.1 Symmetry protected topological phases

In the traditional *Landau-Ginzburg* paradigm of QPT, some symmetries of the Hamiltonian are spontaneously broken by the ground state when a critical point is crossed. The symmetry-broken phase is always associated with a non-zero order parameter, which vanishes in the symmetric phase. An example is the spin-1/2 ferromagnetic Ising chain $H = -\sum_i \sigma_i^x \sigma_{i+1}^x - h\sigma_i^z$. The critical point is $h = 1$ [Pfe70]. For $h \to \infty$ the phase is paramagnetic, characterized by low entanglement and exponentially decaying correlation functions; all spins point along the z-direction and they are uncorrelated; the ground state is unique and shares the $\mathbf{Z}_2$ symmetry with the Hamiltonian, due to the equivalence under the exchange $\sigma^z \to -\sigma^z$. For $h \to 0$ the system is in a gapped ferromagnetic phase; correlation functions decay exponentially but there is a long-range order and nonzero entanglement; the magnetization is the order parameter and the ground state is doubly degenerate, breaking the $\mathbf{Z}_2$ symmetry (it "chooses" pointing up ($+x$) or down ($-x$)).

However, the Landau-Ginzburg paradigm fails in many interesting cases. To give an example, let us consider a modified spin-1 Heisenberg chain $H = \sum_i \vec{S}_i \vec{S}_{i+1} + D(S_i^z)^2$: for $D = 0$, it is the standard Heisenberg model. In the limit $D \to \infty$ the ground state is gapped, the energy is minimized by $S_i^z = 0$ and there is no long-range order. The ground state of the Heisenberg limit is also disordered (there is no local order parameter) and gapped (Haldane conjecture [Hal83], see also Sec. 3.2.1). Actually, the two limits correspond to different phases separated by a critical point at D_C (detectable from a gap closure [GS84] as well as a diverging entanglement entropy [Vid+03; Pol+10]).

The ground state for $D < D_C$ is a new kind of quantum phase, the Haldane phase. It turns out that also the ground state of the AKLT model [Aff+04] lies in such a phase (as addressed in Sec. 3.2.1). Exploiting such analogy, one can characterize the Haldane phase: (i) each spin-1 site is virtually splitted in two spin-1/2 which form valence bonds with neighbors spins; (ii) for open boundary

conditions and in the thermodynamic limit, two spins-$1/2$ at the extremes of the chain remain uncoupled, resulting in two independent *localized edge states*. The four possible ways to arrange the edge states (namely $++$, $-+$, $+-$ and $--$) turn out in a fourfold degeneracy of the ground state. The presence of edge states resemble the gapless modes inducing the boundary current in the *quantum Hall effect*. The Haldane phase is, in fact, an example of **symmetry protected topological (SPT) phase** in $1D$ [GW09]: the Heisenberg model has many symmetries (namely rotations, translation, time-reversal, inversion, etc.) and it is, in fact, possible to add the Hamiltonian many terms which explicitly break some symmetry, but the Haldane phase is preserved until the inversion symmetry $S_j^{x,y,z} \rightarrow S_{-j+1}^{x,y,z}$ is not broken [Pol+10]. In this sense, the phase is "symmetry protected".

From a quantum information perspective, the above-stated distinction can be reformulate more precisely in terms of ground-state entanglement in a way resulting useful in classifying phases in the interacting case [CGW10]. In this view, two gapped phases (ground states) belong to the same equivalent class if one can be transformed into the other by performing only *local unitary transformations*:

$$U = \mathcal{T}\left[e^{-i\int_0^\infty dg \tilde{H}(g)}\right], \tag{5.1}$$

where $\mathcal{T}$ denotes the time ordering and $\tilde{H}(g)$ is a sum of local Hermitian terms. Since local unitaries cannot create global (long-range) entanglement (LRE), *if no further symmetry constraints are present*, two states belong to the same phase only if they share the same LRE structure. Alternatively speaking, only states with long-range entanglement can be in distinct phases. State with only short-range entanglement (SRE) can be transformed in (*i.e.* are equivalent to) a product state. The presence of long-range entanglement is a requirement for having "genuine" **topological order**. In [CGW11a] is proved that in $1D$ and in absence of symmetries, all the gapped phases are actually equivalent to the trivial product state, which implies that there is no genuine topological order in $1D$. Instead, also in $1D$ many nonequivalent phases with only SRE exist if symmetries are imposed. In this case, transformation (5.1) must be modified in order to admit only symmetry-preserving local Hermitian terms. This approach gives back a more formal definition of symmetry protected topological phase. The previous example of the Haldane phase can be reformulated in this context. As a final remark, let us noted that in [CGW10; CGW11a] (as in many related works) it is crucial the use of MPSs and PEPS' as representatives of gapped ground states of local Hamiltonians.

5.1.2 Non-interacting fermionic topological insulators

A comprehensive classification exclusively based on the Hamiltonian symmetries exists for non-interacting systems [AZ97; Sch+08; Kit09]. According to the *Wigner theorem*, any quantum mechanical symmetry can be implemented by either a linear-unitary or an antilinear-antiunitary representation acting on the

Hilbert space. We limit the discussion to global symmetries, while gauge symmetries are excluded. Symmetries can be *spatial* (if they act on the spatial part of the Hamiltonian, *e.g.* rotations, reflections, translations) or *non-spatial* (time reversal, particle-hole, chiral). Firstly, we focus on the latter. We are interested on

System	Cartan nomenclature	TRS	PHS	SLS	$d=1$	$d=2$	$d=3$
standard (Wigner-Dyson)	A (unitary)	0	0	0	-	$\mathbf{Z}$	-
	AI (orthogonal)	$+1$	0	0	-	-	-
	AII (symplectic)	-1	0	0	-	$\mathbf{Z}_2$	$\mathbf{Z}_2$
chiral (sublattice)	AIII (chiral unit.)	0	0	1	$\mathbf{Z}$	-	$\mathbf{Z}$
	BDI (chiral orthog.)	$+1$	$+1$	1	$\mathbf{Z}$	-	-
	CII (chiral sympl.)	-1	-1	1	$\mathbf{Z}$	-	$\mathbf{Z}_2$
BdG	D	0	$+1$	0	$\mathbf{Z}_2$	$\mathbf{Z}$	-
	C	0	-1	0	-	$\mathbf{Z}$	-
	DIII	-1	$+1$	1	$\mathbf{Z}_2$	$\mathbf{Z}_2$	$\mathbf{Z}$
	CI	$+1$	-1	1	-	-	$\mathbf{Z}$

FIGURE 5.1: The ten symmetry classes of single particle Hamiltonians classified in terms of the presence or absence of time-reversal, particle-hole and chiral symmetry. The last three columns list all possible topologically nontrivial quantum phases as a function of symmetry class and spatial dimension d. For example, in $d = 1$ only five classes (AIII, BDI, CII D and DIII) can host a topological phase. The symbol $\mathbf{Z}$ ($\mathbf{Z}_2$) means that there is one phase for each integer (resp. for each integer modulo 2). Band insulators corresponding to different integers in the same symmetry class cannot be adiabatically deformed one into another without closing the gap, *i.e.* without crossing a phase transition. Reprinted from [Sch+08].

how symmetries are implemented on fermionic systems. Let $c^{(\dagger)}$ be the canonical fermionic annihilation (creation) operator. A **unitary symmetry** $\mathcal{U}$ acts on c as $c \to c' = \mathcal{U}c\mathcal{U}^{-1}$ and the system is invariant under $\mathcal{U}$ if the canonical anticommutations relations and the Hamiltonian are preserved: $\mathcal{U}\{c, c^\dagger\}\mathcal{U}^\dagger = \{c, c^\dagger\}$ and $\mathcal{U}H\mathcal{U}^{-1} = H$.

Time-reversal $\mathcal{T}$ is an antiunitary operator and therefore its matrix representation T can be always expressed as a combination of a unitary U_T and the complex conjugation K, *i.e.* $T = U_T K$. A system is $\mathcal{T}$-invariant if anticommutation relations are preserved and if $U_T^\dagger H^* U_T = H$. It turns on that $U_T^* U_T = \pm\mathbb{1}$, leading to two different possible implementations of the symmetry.

Another antiunitary symmetry is the **particle-hole** (or **charge conjugation**) $\mathcal{C}$. Besides the anticommutations rules preservation, a non-interacting Hamiltonian must satisfy $U_C^\dagger H^T U_C = -H$ in order to be $\mathcal{C}$-invariant. Also in this case, a further condition on U_C holds: $U_C^* U_C = \pm\mathbb{1}$.

Taking into account the last two symmetries $\mathcal{T}$ and $\mathcal{C}$, a system can be in 9 different classes, which correspond to all the possible combinations among the three occurrences of $\mathcal{T}$ via U_T (*i.e.* $+1$, -1 or no symmetry 0) and the analogous behaviors ($+1$, -1 or 0) for $\mathcal{C}$.

For 8 of these combinations, that is when at least one of $\mathcal{T}$ or $\mathcal{C}$ is different from zero, also the product $\mathcal{S} = \mathcal{T} \times \mathcal{C}$ is uniquely determined. $\mathcal{S}$ is a special unitary symmetry, called **chiral**. There can be a situation in which both $\mathcal{T}$ and $\mathcal{C}$ are broken but $\mathcal{S}$ is satisfied. $\mathcal{S}$ differentiates from a standard unitary since a Hamiltonian is $\mathcal{S}$-preserving if $U_S^\dagger H U_S = -H$.

Finally, the tenth possibility occurs when no one of the symmetries is satisfied, that is in the case where only trivial global unitary symmetries are possible. This **tenfold classification** is often called **Altland-Zirnbauer (AZ) classification** [AZ97; Sch+08; Kit09]. An exhaustive table summarizing the ten classes and their properties (if a class can host topological insulator, in which dimension etc.) is shown in Fig. 5.1. For example, the *quantum Hall insulator* belongs to class A (no symmetries at all). The *Creutz ladder* [Cre99] falls in the BDI class, where the three symmetries are satisfied and $\mathcal{T} = \mathcal{C} = \mathcal{S} = +1$. For experimental feasibility, in this chapter we will study a modified version of this ladder, the *imbalanced* Creutz ladder, which belongs to the AIII class, where only the chiral symmetry is satisfied (and it survives also in the presence of interactions).

Let us summarize how $\mathcal{T}$, $\mathcal{C}$ and $\mathcal{S}$ act on fermionic operators and Hamiltonians:

$$\begin{aligned} \mathcal{T} c_{j,\sigma} \mathcal{T}^{-1} &= U^*_{T\sigma,\sigma'} c_{j,\sigma'}, & \mathcal{T} c^\dagger_{j,\sigma} \mathcal{T}^{-1} &= c^\dagger_{j,\sigma'} U_{T\sigma,\sigma'}; \\ \mathcal{C} c_{j,\sigma} \mathcal{C}^{-1} &= U_{C\sigma,\sigma'} c^\dagger_{j,\sigma'}, & \mathcal{C} c^\dagger_{j,\sigma} \mathcal{C}^{-1} &= c_{j,\sigma'} U^*_{C\sigma,\sigma'}; \\ \mathcal{S} c_{j,\sigma} \mathcal{S}^{-1} &= U_{S\sigma,\sigma'} c^\dagger_{j,\sigma'}, & \mathcal{S} c^\dagger_{j,\sigma} \mathcal{S}^{-1} &= c_{j,\sigma'} U^*_{S\sigma,\sigma'}; \end{aligned} \tag{5.2}$$

where we have introduced the index j, defining the position of the fermionic operator on a lattice and the index σ stands for the internal degrees of freedom (*e.g.* $\uparrow, \downarrow$). For quadratic Hamiltonians on a periodic lattice it can be convenient working in momentum space: $H = \sum \Psi(q)^\dagger H(q) \Psi(q)$, where $\Psi = (c_\sigma(q), c^\dagger_\sigma(q))^t$ are spinors and $c^{(\dagger)}_\sigma(q)$ is the Fourier transform of $c_{j,\sigma}$ (resp. $c^\dagger_{j,\sigma}$). In this case, the required constraints for the Hamiltonian being symmetric are:

$$\begin{aligned} U_T H(q)^* U_T^{-1} &= H(-q); \\ U_C H(q)^* U_C^{-1} &= H(-q); \\ U_S H(q) U_S^{-1} &= -H(q). \end{aligned} \tag{5.3}$$

The previous relations imply several constraints on the form of the Hamiltonians. In the case of chiral symmetry, in the basis in which U_S is diagonal, H is block off-diagonal:

$$H = \begin{pmatrix} 0 & h(q) \\ h^\dagger(q) & 0 \end{pmatrix}, \tag{5.4}$$

where h is a $N_A \times N_B$ matrix, with $N_A + N_B = N$. Furthermore, chiral symmetry

gives rise to a symmetric spectrum with energy eigenvalues appearing in pairs: if $u(q)$ is an eigenstate with energy ϵ, $U_S u(q)$ is also an eigenstate but with energy $-\epsilon$.

In terms of bulk properties, several **topological invariants** can be calculated to characterize the phase. In lattice models, the **Chern number** [Tho+82] is broadly used:

$$C_\alpha = \frac{1}{2\pi}\int_{BZ} d^D q \mathcal{B}_\alpha(q). \tag{5.5}$$

Here D is the lattice dimension; α labels the band; q is the momentum, restricted to the first Brillouin zone; $\mathcal{B}_\alpha(q) = \nabla_q \times \mathcal{A}_\alpha(q)$ is the *Berry curvature* of the band, defined as the curl of the *Berry connection* $\mathcal{A}_\alpha(q) = i\sum_{b=1}^{\mathcal{N}} u_b^{\alpha *}(q)\nabla_q u_b^\alpha(q)$, where $u_b^\alpha(q)$ are Bloch wave functions and $b = 1, \dots \mathcal{N}$ labels different sites in the unit cell. The Chern number is an integer, which is nonzero if the sample is topologically nontrivial. Chern number is deeply connected with the quantized Hall conductance $\sigma_H = C_\alpha e^2/h$, where e is the electron charge and h the Plank's constant [KDP80]. The integer nature of the Chern number reflects the robustness of the phase against smooth deformations of the Hamiltonian parameters.

The Berry connection leads to the introduction of another relevant quantity, the **Berry-Zak phase** [Ber84; Zak89] which is the phase accumulated by an eigenstate of the Hamiltonian along a parallel transport across the Brillouin zone:

$$\phi_\alpha = \int_{BZ} d^D q \mathcal{A}_\alpha(q). \tag{5.6}$$

For chiral systems, the characteristic topological invariant is the **winding number** [AOP16]. In $1D$ it is defined, in the notation of Eq. (5.4), as

$$\mathcal{W} = \frac{1}{2\pi i}\int_{BZ} dq Tr\left[h^{-1}(q)\partial_q h(q)\right] \tag{5.7}$$

5.1.3 Topological insulators in presence of interactions

AZ classification ceases to work when interactions are added. For example, Fidkowski and Kitaev in [FK11] and independently Turner *et al.* in [TPB11], showed that for interacting fermions in $1D$, the BDI class collapses to only 8 phases (*i.e.* it is characterized by $\mathbf{Z}_8$ instead that $\mathbf{Z}$; the number of phases increases to 16 in the presence of translational symmetry). On the other side, some SPT phases exist only in presence of interactions (see *e.g* [LTH16] in $1D$, [WPS13] in $3D$). For interacting bosons, a complete classification for arbitrary dimensions exists [Che+12]. For interacting fermions, the classification is complete in $1D$ [FK11; CGW11a; CGW11b; SPGC11], while results are partial in higher dimensions (see [WG18] and references therein).

In $1D$, *Jordan-Wigner transformations* [JW28; Nie05]:

$$\begin{aligned} c_j^\dagger &\to \sigma^+ \prod_{k<j} \sigma_k^z, \qquad & c_j &\to \prod_{k<j} \sigma_k^z \sigma^-; \\ \sigma_j^+ &\to c_j^\dagger \prod_{k<j} \left(1 - 2c_k^\dagger c_k\right), \qquad & \sigma_j^- &\to \prod_{k<j} \left(1 - 2c_k^\dagger c_k\right) c_j; \end{aligned} \tag{5.8}$$

map fermionic chains in spin chains (and vice-versa) and the symmetries of the former can be more easily classified by studying the latter [CGW11b; SPGC11]. In particular, as an efficient representation of $1D$ gapped spin states, MPSs turn out to be very useful thanks to the possibility to easily implement symmetries and extract entanglement properties of the bulk, recovering the bulk-boundary correspondence. In fact, even if not impossible [Hat06], for interacting systems the calculation of topological invariants from bulk bands properties is not trivial [ZMP14; GC+19].

5.1.4 Entanglement spectrum degeneracy as signature of topological order

As shown in [CGW11b; SPGC11] each phase of a spin system can be classified according to all the inequivalent **projective representations** of the symmetry group of the Hamiltonian. An operator $u(g)$ is a projective representation of the group of symmetry G if it behaves under composition as

$$u(g_1)u(g_2) = \phi(g_1, g_2)u(g_1 g_2), \qquad g_1, g_2 \in G. \tag{5.9}$$

$\phi(g_1, g_2) \in \mathbb{C}$ is a phase, the *factor system* of the projective representation. If $\phi(g_1, g_2) = 1$ the representation reduces to the usual linear representation [1].

Here we show that the degeneracy of the ES is *even* when the ground state of a spin chain is in a nontrivial topological phase (namely, if the projective representation of the Hamiltonian symmetry group is nonlinear), whereas there are no constraints on the ES if the phase is non-topological and the representation acts linearly. We will explicitly prove this statement in the particular example of inversion symmetry, following the reasoning originally proposed in [Pol+10].

In [LH08], Li and Haldane introduced the ES in the context of the FQHE as a fingerprint of topological order. As mentioned in Sec. 2.1 the ES in nothing but the set of the Schmidt coefficient of a bipartition A/B of the system,

[1] More specifically, ϕ defines the class and satisfies $\phi(g_2, g_3)\phi(g_1, g_2 g_3) = \phi(g_1, g_2)\phi(g_1 g_2, g_3)$. If ϕ_1 and ϕ_2 are factor systems for two different classes (*i.e.* given $g \in G$, $u_1(g)$ is associated with $\phi_1(g_1, g_2)$ and $u_2(g)$ is associated with $\phi_2(g_1, g_2)$), the representation $u_1(g) \otimes u_2(g)$ is projective with factor group $\phi_1(g_1, g_2)\phi_2(g_1, g_2)$ and the corresponding class is $\phi = \phi_1 + \phi_2$. The equivalence class of the factor systems is abelian under such composition and forms the *second cohomology group* of G, $H^2(G, \mathbb{C})$; the identity in $H^2(G, \mathbb{C})$ is the class of the linear representations of G. A classical example is $G = SO(3)$, where $H^2(SO(3), \mathbb{C}) = \mathbf{Z}_2$ whose two elements ± 1 represent the integer (linear) and half-integer ($SU(2)$) representations.

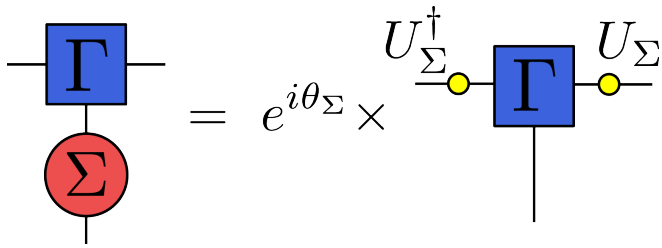

FIGURE 5.2: A symmetry Σ acting unitarily on the physical space (the physical index) can be equivalently considered as acting projectively on the bonds as in Eq. (5.10). U is a projective representation of dimension χ

now interpreted as the spectrum of an *"entanglement Hamiltonian"* H_A defined by the reduced density matrix $\rho^{(A)} = e^{-H_A}$. Consider a pure state $|\psi\rangle$ and its MPS representation $|\psi[\Gamma,\Lambda]\rangle$ in the canonical form [Eq. (3.5)], invariant under a local symmetry. In the context of MPS, it is a well-known result [PG+08] that a symmetry acting unitarily on the physical space (the physical index) can be equivalently considered as acting projectively on the bonds [Fig. 5.2]:

$$\sum_s \Sigma_{ss'}\Gamma^s = e^{i\theta_\Sigma} U_\Sigma^\dagger \Gamma^s U_\Sigma. \tag{5.10}$$

Here Σ and U_Σ are unitary matrices; in particular, U_Σ is a projective representation of dimension χ. For a time-reversal symmetry Γ_m is replaced by Γ_m^* on the lhs and by Γ_m^T for inversion symmetry.

Consider the inversion symmetry ($\mathcal{I}$) [2]:

$$\Gamma^{sT} = e^{i\theta_\mathcal{I}} U_\mathcal{I}^\dagger \Gamma^s U_\mathcal{I}. \tag{5.11}$$

Transposing both sides of the equation (iterating the transformation on the rhs), we obtain:

$$\Gamma^s = e^{i2\theta_\mathcal{I}} (U_\mathcal{I} U_\mathcal{I}^*)^\dagger \Gamma^s (U_\mathcal{I} U_\mathcal{I}^*). \tag{5.12}$$

Using the canonical conditions [Eq. (3.7)] and the fact $[U_\mathcal{I}, \Lambda] = 0$, we obtain:

$$\begin{aligned}\sum_s \Gamma^{s\dagger}\Lambda^2\Gamma^s &= \sum_s \Gamma^{s\dagger}\Lambda^2 e^{i2\theta_\mathcal{I}} (U_\mathcal{I} U_\mathcal{I}^*)^\dagger \Gamma^s (U_\mathcal{I} U_\mathcal{I}^*) \\ &= \sum_s \Gamma^{s\dagger}\Lambda (U_\mathcal{I} U_\mathcal{I}^*)^\dagger \Lambda \Gamma^s = e^{-i2\theta_\mathcal{I}} (U_\mathcal{I} U_\mathcal{I}^*)^{-1}.\end{aligned} \tag{5.13}$$

[2] $\mathcal{I}$ acts on the spins as $S_j^{x,y,z} \to S_{-j+1}^{x,y,z}$. The modified Heisenberg Hamiltonian introduced in Sec. 5.1.1 is invariant under $\mathcal{I}$

Inverting the last relation (taking the transposition and the complex conjugation) we finally get the crucial equation

$$e^{i2\theta_{\mathcal{I}}} U_{\mathcal{I}} U_{\mathcal{I}}^* = \sum_s \Gamma^{s\dagger} \Lambda U_{\mathcal{I}} U_{\mathcal{I}}^* \Lambda \Gamma^s, \tag{5.14}$$

which means that $U_{\mathcal{I}} U_{\mathcal{I}}^*$ is an eigenvector of the transfer matrix with eigenvalue $e^{i2\theta_{\mathcal{I}}}$. Since $|e^{i2\theta_{\mathcal{I}}}| = 1$, the canonical conditions and the assumption that the state is pure imply that

$$U_{\mathcal{I}} U_{\mathcal{I}}^* = e^{i\omega_{\mathcal{I}}} \mathbb{1} \tag{5.15}$$

(in fact the transfer matrix admits a unique eigenvector with unimodular eigenvalue, that is the identity). It follows that

$$(U_{\mathcal{I}} U_{\mathcal{I}}^*)^{-1} = U_{\mathcal{I}}^T U_{\mathcal{I}}^{-1} = e^{-i\omega_{\mathcal{I}}} \mathbb{1} \Rightarrow U_{\mathcal{I}}^T = e^{-i\omega_{\mathcal{I}}} U_{\mathcal{I}}. \tag{5.16}$$

Repeating this relation twice it also follows that $e^{-2i\omega_{\mathcal{I}}} = 1$ and then $\omega_{\mathcal{I}} = \{0, \pi\}$. It turns out that the phase $\omega_{\mathcal{I}}$ identifies the projective class. The nontrivial topological case is $\omega_{\mathcal{I}} = \pi$ where, from Eq. (5.16), one has $U_{\mathcal{I}}^T = -U_{\mathcal{I}}$, that is $U_{\mathcal{I}}$ is an antisymmetric unitary matrix. Since $[U_{\mathcal{I}}, \Lambda] = 0$, the eigenspaces of Λ (corresponding to the eigenvalues Λ_α of the ES) are invariant under the action of $U_{\mathcal{I}}$ and these eigenspaces have even dimension k_α (*i.e.* the multiplicity of the eigenvalues of the ES is even). This follows from the fact that $U_{\mathcal{I}}^\alpha$ (the projection of $U_{\mathcal{I}}$ onto the k_α-dimensional eigenspace) satisfies $\det U_{\mathcal{I}} = \det[-U_{\mathcal{I}}] = (-1)^{k_\alpha} \det U_{\mathcal{I}}$ ($U_{\mathcal{I}}$ is antisymmetric) and then k_α is even because $\det U_{\mathcal{I}} \neq 0$ ($U_{\mathcal{I}}$ is unitary).

The two discrete distinct values of ω correspond to two different phases and there is no way to change from one phase to the other by means of continuous transformations of the ground state, *i.e.* without crossing a QPT. However in both phases, the inversion symmetry is preserved, there is not a spontaneous symmetry breaking and hence such phase transition eludes the Landau-Ginzburg paradigm. This is, in fact, a topological QPT.

The $\omega = \pi$ phase is the Haldane phase of the spin-1 Heisenberg model, as it can be directly checked on the AKLT state. In canonical form, the AKLT state is defined by $\Gamma^s = \sigma^s$ and $\Lambda = 1/\sqrt{2}\mathbb{1}$. Under inversion $\sigma^s \to \sigma^{sT} = -\sigma^y \sigma^s \sigma^y$, that is $U_{\mathcal{I}} = \sigma^y$ and $\theta_{\mathcal{I}} = \pi$. Since $\sigma^y \sigma^{y*} = -\mathbb{1}$, from Eq. (5.15) follows $e^{i\omega_{\mathcal{I}}} = -1$ and a doubly degenerate ES.

Analogous results can be derived for many other symmetries as done in *e.g.* [Pol+10; TPB11; Pol+12; PT12].

5.2 Imbalanced Creutz-Hubbard model

The subject of topological insulators and superconductors is not only at the forefront of academic research, but also at the focus of technological applications [Kit03; Nay+08]. Despite the success, *(i)* there are still several paradigmatic

models of topological models whose connection to real materials still remains unknown, or even seems quite unlikely, as it occurs for the *Hofstadter model* with magnetic fluxes on the order of the flux quantum [Hof76], or the *Haldane model* [Hal88]. Moreover, *(ii)* most of the topological materials explored in the laboratory so far do not display important electronic *correlation effects* [HA13]. This is rather unfortunate in view of the richness of the *fractional quantum Hall effect* [Lau83], where such correlations are responsible for a plethora of exotic topological phases of matter.

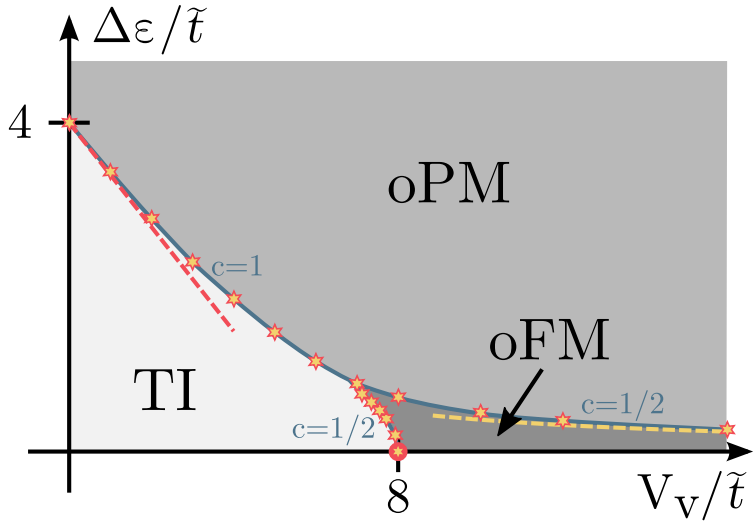

FIGURE 5.3: **Phase diagram of the imbalanced Creutz-Hubbard ladder:** Phase diagram displaying a topological insulator (TI) phase, and a pair of non-topological phases: an orbital phase with long-range ferromagnetic Ising order (OFM), and an orbital paramagnetic phase (OPM). The horizontal axis represents the ratio of the inter-particle interactions to the tunneling strength, whereas the vertical axis corresponds to the ratio of the energy imbalance to the tunneling strength. The dashed yellow line shows the transition points of the effective model in the strong-coupling effective (Ising) model. The dashed red line indicates the transition as obtained from the weak-coupling expansion. The red circle shows the transition point in the balanced model at intermediate interactions. Stars label numerical results, and the blue line is an extrapolation of the phase-boundaries. The labels of the critical lines give the central charge of their underlying conformal field theory.

In the present section we introduce a variant of the quasi-one-dimensional (quasi-1D) **Creutz topological insulator** [Cre99], and study the effect of repulsive Hubbard-type interactions on the topological phase. This model shall be

referred to as the **imbalanced Creutz-Hubbard ladder**. We argue that such a model has all the required ingredients to become a workhorse in the study of strongly-correlated topological phases in molecular and optical (AMO) platforms, more particularly with ultracold gases of neutral atoms trapped in periodic potentials made of light, *i.e.* optical lattices [BDZ08; LSA12; BDN12].

Starting from a *flat-band* regime, we show that the imbalance and the interactions lead to a competition between a topological phase and two different phases of orbital quantum magnetism. At large interaction strength, a long-range in-plane ferromagnetic order arises, related to the symmetry-broken phase of an orbital quantum Ising model; while the imbalance then drives a standard QPT in the Ising universality class towards a paramagnetic phase. The full phase diagram is shown in Fig. 5.3, where the yellow stars indicate the critical lines obtained with MPS simulations.

The **standard Creutz model** describes a system of spinless fermions on a two-leg ladder (see Fig. 5.4 (a)), which are created-annihilated by the fermionic operators $c^\dagger_{i,\ell}, c_{i,\ell}$, where $i \in \{1, \dots, N\}$ labels the lattice sites within each leg of the ladder $\ell \in \{\mathrm{u}, \mathrm{d}\}$. Fermions are allowed to hop vertically along the rungs of the ladder with tunnelling strength t_v, and horizontally along the legs of the ladder with a complex tunnelling $t_\ell = t_\mathrm{h}(\mathrm{e}^{\mathrm{i}\theta}\delta_{\ell,\mathrm{u}} + \mathrm{e}^{-\mathrm{i}\theta}\delta_{\ell,\mathrm{d}})$, where t_h is a tunnelling strength, and $\delta_{a,b}$ is the Kronecker delta. The arrangement of complex phases in the horizontal links leads to a net 2θ-flux gained by a fermion hopping around a square unit cell, playing thus the role of the so-called Peierls phases of a magnetic field piercing the ladder. In addition, the kinetic part of the Hamiltonian also includes a diagonal tunnelling of strength t_diag, yielding altogether

$$H_\mathrm{C} = -\sum_i \sum_\ell \left(t_\ell c^\dagger_{i+1,\ell} c_{i,\ell} + t_\mathrm{diag} c^\dagger_{i+1,\ell} c_{i,\bar{\ell}} + t_\mathrm{v} c^\dagger_{i,\ell} c_{i,\bar{\ell}} + \mathrm{H.c.} \right), \tag{5.17}$$

where we use the notation $\bar{\ell} = \mathrm{d}(\bar{\ell} = \mathrm{u})$ for $\ell = \mathrm{u}$ ($\ell = \mathrm{d}$).

This quadratic lattice model was put forth in Ref. [Cre99] as a simple toy model to understand some of the key properties of higher-dimensional domain-wall fermions [Kap92; CH94], which were introduced in the context of lattice gauge theories to bypass the fermion-doubling problem [NN81a; NN81b]. For periodic boundary conditions, this model leads to a couple of bands that display a pair of massive Dirac fermions with different Wilson masses m_0, m_π at momenta $k_\mathrm{D} \in \{0, \pi\}$ [Ber+10] [3]. For open boundary conditions, a pair of zero-energy modes exponentially localized to the left/right edges of the ladder appear as one of the Wilson masses gets inverted ($m_\pi < 0$) when $t_\mathrm{v} < 2t_\mathrm{diag}$. Considering the bulk-boundary correspondence discussed in the introduction, these edge states resemble the surface current of the higher-dimensional topological insulators. In fact, the change in polarisation of the system can be characterised by a Zak's phase (5.6), such that the appearance of these zero-energy modes coincides with a non-vanishing topological invariant, and the Creutz ladder yields

[3] Valid only for a flux $2\theta = \pi$, as we will assume.

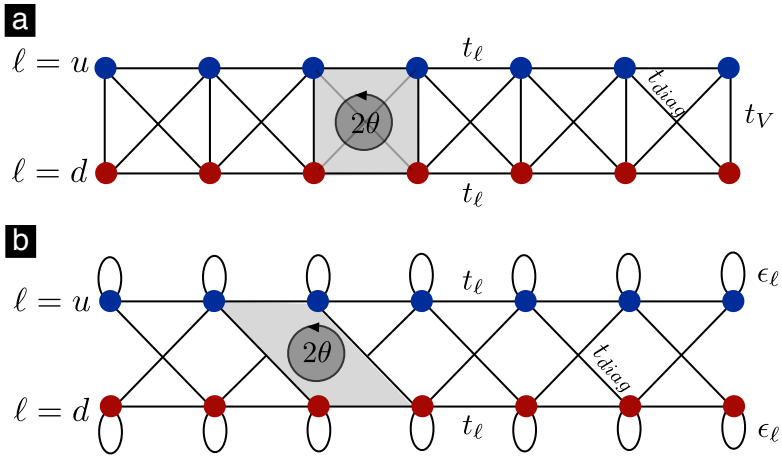

FIGURE 5.4: **Standard and imbalanced Creutz ladder:** Two-leg ladder where fermions tunnel along the black links enclosing a net flux 2θ along a closed plaquete: (a) standard Creutz ladder (5.17), and (b) imbalanced Creutz ladder, which leads to Eq. (5.20) in the π-flux limit.

a symmetry-protected topological phase in this regime. As discussed below, for $\theta = \pi/2$, this topological phase corresponds to a BDI topological insulator.

Since the objective of this work is to study correlation effects, we now consider the simplest possible **Hubbard interactions** between the **spinless fermions**

$$H_{\rm H} = \sum_i \sum_\ell \left(V_{\rm h} n_{i,\ell} n_{i+1,\ell} + \frac{V_{\rm v}}{2} n_{i,\ell} n_{i,\bar{\ell}} \right), \tag{5.18}$$

where $V_{\rm h}$ ($V_{\rm v}$) are the density-density interaction strengths between fermions residing in neighbouring sites along horizontal (vertical) bonds of the ladder, and we have introduced the fermion number operators $n_{i,\ell} = c^\dagger_{i,\ell} c_{i,\ell}$.

To make the system suitable for cold-atoms implementation, in the following we will deal with a variant of the Creutz Hamiltonian: *(i)* we shall substitute the vertical tunnelling by an energy imbalance between the legs of the ladder $\epsilon_{\rm u} = \Delta\epsilon/2 = -\epsilon_{\rm d}$, which changes the symmetry class of the topological insulator for $\theta = \pi/2$ from BDI to AIII; *(ii)* we limit the interaction terms (5.18) to the anisotropic regime $V_{\rm h} = 0$; *(iii)* we set the amplitude of the diagonal hopping equal to the one along the legs ($|t_{\rm diag}| = |t_\ell| = \tilde{t}$) and finally *(iv)* we fix the phases in order to get a net π-flux through the plaquettes. The resulting Hamiltonian (see Fig. 5.4 (b)), which we will refer to as the **imbalanced Creutz-Hubbard**

Hamiltonian, is

$$H_{\pi\mathrm{CH}} = H_{\pi\mathrm{C}} + V_{\mathrm{Hubb}}, \quad H_{\pi\mathrm{C}} = H_{\mathrm{FB}} + V_{\mathrm{imb}}, \tag{5.19}$$

where we have introduced the kinetic term

$$H_{\mathrm{FB}} = \sum_{i,\ell} \left(-\tilde{t} c^{\dagger}_{i+1,\ell} c_{i,\bar{\ell}} + \mathrm{i} s_{\ell} \tilde{t} c^{\dagger}_{i+1,\ell} c_{i,\ell} + \mathrm{H.c.} \right) \tag{5.20}$$

with $s_{u/d} = \pm 1$. This term leads to a pair of flat bands, and a couple of zero-energy topological edge states. The remaining terms

$$V_{\mathrm{imb}} = \sum_{i,\ell} \frac{\Delta\epsilon}{2} s_{\ell} n_{i,\ell}, \quad V_{\mathrm{Hubb}} = \sum_{i,\ell} \frac{V_{\mathrm{v}}}{2} n_{i,\ell} n_{i,\bar{\ell}}, \tag{5.21}$$

contain the Hubbard interactions and the energy imbalance, which can have nontrivial effects on the flat-band physics, and induce a phase transition to other non-topological phases of matter. In the following section, we present a new formalism to understand such transitions.

The following subsections are devoted to the construction of the phase diagram shown in Fig. 5.3. We start by discussing the solution of the non-interacting imbalanced Creutz ladder, and the appearance of flat bands and fully-localized edge states in the Hamiltonian (5.20) (see Sec. 5.2.1). This corresponds to the vertical axis of the phase diagram. In Sec. 5.2.2, we initially examine the weakly-interacting regime and show that the model maps onto a pair of weakly-coupled Ising chains, which can be studied through a mean-field analysis (*i.e.* the region in the vicinity of the vertical axis of Fig. 5.3). Then, we study the opposite limit of very strong interactions (*i.e.* rightmost region of Fig. 5.3), and discuss the possible non-topological orbital magnetic phases that can arise. Finally, we explore the intermediate regime. These different methods allow us to build an analytical prediction of the phase diagram of the model. Finally, in Sec. 5.2.3, we test numerically the above predictions, and provide a detailed study of the phase diagram by means of MPS numerical simulations.

5.2.1 Non-interacting limit: flat bands and edge states

We start by solving the kinetic part (5.20) of the π-flux Creutz-Hubbard Hamiltonian (5.19). For *periodic boundary conditions*, and after introducing the spinor $\Psi(q) = (c_{\mathrm{u}}(q), c_{\mathrm{d}}(q))^{\mathrm{t}}$ for the fermion operators in momentum space $c_{\ell}(q) = \sum_i \mathrm{e}^{-\mathrm{i}qai} c_{i,\ell}/\sqrt{N}$, one finds

$$H_{\mathrm{FB}} = \sum_{q \in \mathrm{BZ}} \Psi^{\dagger}(q) \boldsymbol{B}(q) \cdot \boldsymbol{\sigma} \Psi(q), \tag{5.22}$$

where $\boldsymbol{\sigma} = (\sigma_x, \sigma_y, \sigma_z)$ is the vector of Pauli matrices, and $\boldsymbol{B}(q) = 2\tilde{t}\,(-\cos(qa), 0, \sin(qa))$. By direct diagonalization, one finds that the system develops two *flat bands* $\epsilon_\pm := \epsilon_\pm(q) = \pm 2\tilde{t}$, where $q \in \mathrm{BZ} = [-\pi/a, \pi/a)$ is the quasi-momentum, and the lattice constant shall be set to $a = 1$ henceforth. The vanishing group velocity associated with these bands, $v_\mathrm{g} = \partial_q \epsilon_\pm(q) = 0$, indicates that the ground state must be insulating, regardless of the particular filling. This can be considered as a new type of insulator, namely a **flat-band insulator**, which corresponds neither to the usual band insulator, nor to the Mott insulators. It shares some properties with the former (*i.e.* no correlations), and with the latter (*i.e.* localized fermions), but it differs from both insulators in the large degeneracy of the ground state, except for half-filling conditions.

On top of this, the flat bands are also *topological*: the diagonalization of the discrete chiral symmetry σ_y (s.t. $\sigma_y H(q) \sigma_y = -H(q)$, with $H(q) = \boldsymbol{B}(q) \cdot \boldsymbol{\sigma}$) puts the Hamiltonian (5.22) in a purely off-diagonal form, with elements $B_x \pm iB_z$; its complex phase gets a nontrivial winding number $\mathcal{W} = \mathrm{sgn}(\tilde{t}) \neq 0$ [Maz+15]. Equivalently, we could consider the eigenvectors

$$q|\epsilon_\pm(q)\rangle \propto \left((B_x + iB_z)^{1/2}, \pm(B_x - iB_z)^{1/2}\right)^t \tag{5.23}$$

and realize that they exhibit a **uniform Berry connection** $\mathcal{A}_\pm(q) = \mathrm{i}\langle\epsilon_\pm(q)|\partial_q|\epsilon_\pm(q)\rangle = \frac{1}{2}$. The uniform Berry connection leads to a finite Zak's phase (5.6) $\varphi_{\mathrm{Zak},\pm} = \pi$ for our **topological flat bands**. This Zak's phase pinpoints the topological properties of the bands, and can be connected to a macroscopic observable: the polarization of the system [XCN10].

Interestingly enough, the Creutz ladder displays an infinite flatness parameter without requiring long-range tunnelings, as necessary in higher-dimensional models of topological flat bands [PRS13]. From this perspective, switching on the leg imbalance $\Delta\epsilon > 0$ in Eq. (5.21) leads to some curvature in the energy bands

$$\epsilon_\pm(q) = \pm\epsilon(q) = \pm 2\tilde{t}\sqrt{1 + \mathfrak{f}^{-2} + 2\mathfrak{f}^{-1}\sin q}, \tag{5.24}$$

where we have introduced the flatness parameter $\mathfrak{f} = 4\tilde{t}/\Delta\epsilon$, which becomes infinite for vanishing imbalance. The presence of the imbalance also drives the system out of the BDI class and into the AIII class [AZ97; Sch+08; Kit09], since $B_z(q) = \Delta\varepsilon/2 + 2\tilde{t}\sin q$ acquires a mixed parity under $k \leftrightarrow -k$ and therefore no effective time-reversal ($U_T H(-q)^* U_T^\dagger = +H(q)$) or particle-hole ($U_C H(-q)^* U_C^\dagger = -H(q)$) operators can be found. Anyway, the discrete chiral symmetry is still described by σ_y and the whole procedure described above can be employed. The Berry connection of the bands becomes non-uniform due to their **curvature**

$$\mathcal{A}_\pm(q) = \frac{1 + \mathfrak{f}^{-1}\sin q}{2(1 + \mathfrak{f}^{-2} + 2\mathfrak{f}^{-1}\sin q)}, \tag{5.25}$$

which leads to the following Zak's phase $\varphi_{\mathrm{Zak},\pm} = \pi\theta(\mathfrak{f} - 1)$, where $\theta(x)$ is the Heaviside step function. Hence, the Zak's phase yields topological effects

provided that the bands are sufficiently flat, *i.e.* $\mathfrak{f} > 1$. Conversely, when $\Delta\epsilon > 4\tilde{t}$, the curvature of the bands is large, *i.e.* $\mathfrak{f} < 1$, and no topological phenomenon occurs. This marks a quantum phase transition between the AIII topological insulator and a trivial band insulator, as shown in the vertical axis of Fig. 5.3.

To have an alternative view on these topological features, let us introduce the so-called **Aharonov-Bohm cages** [Vid+00] (**ABC**), which will also become very useful once interactions are switched on. In the π-flux Creutz ladder (5.20), the fermions cannot tunnel two sites apart due to the Aharonov-Bohm effect [Cre99] (see Fig. 5.5(a)). One can thus find single-particle eigenstates strictly localized in cages formed by simple square plaquettes (see Fig. 5.5(c)). In second quantisation, such ABC with energies $\epsilon_\pm = \pm 2\tilde{t}$ are

$$\begin{aligned} |+2\tilde{t}\rangle_i &= w^\dagger_{i,+}|0\rangle, \quad w^\dagger_{i,+} = \frac{1}{2}\left(\mathrm{i}c^\dagger_{i,\mathrm{u}} + c^\dagger_{i,\mathrm{d}} - c^\dagger_{i+1,\mathrm{u}} - \mathrm{i}c^\dagger_{i+1,\mathrm{d}}\right), \\ |-2\tilde{t}\rangle_i &= w^\dagger_{i,-}|0\rangle, \quad w^\dagger_{i,-} = \frac{1}{2}\left(\mathrm{i}c^\dagger_{i,\mathrm{u}} + c^\dagger_{i,\mathrm{d}} + c^\dagger_{i+1,\mathrm{u}} + \mathrm{i}c^\dagger_{i+1,\mathrm{d}}\right), \end{aligned} \tag{5.26}$$

with $i \in \{1, \dots N\}$ for periodic boundary conditions, where one identifies $c_{N+1,\ell} = c_{1,\ell}$. Conversely, for open boundary conditions, these squared ABC can only be defined for $i \in \{1, \dots, N-1\}$, and simple counting shows that there are only $2(N-1)$ possible states that can be accommodated in such flat bands. The two missing states are zero-energy modes, $\epsilon_l = \epsilon_r = 0$, fully localized at the boundaries

$$\begin{aligned} |0\rangle_{\mathrm{L}} &= l^\dagger|0\rangle, \quad l^\dagger = \frac{1}{\sqrt{2}}\left(c^\dagger_{1,\mathrm{u}} + \mathrm{i}c^\dagger_{1,\mathrm{d}}\right), \\ |0\rangle_{\mathrm{R}} &= r^\dagger|0\rangle, \quad r^\dagger = \frac{1}{\sqrt{2}}\left(c^\dagger_{N,\mathrm{u}} - \mathrm{i}c^\dagger_{N,\mathrm{d}}\right). \end{aligned} \tag{5.27}$$

For these particular weights, the fermions cannot tunnel one site apart due to the Aharonov-Bohm effect (see Fig. 5.5(a), and are thus localized within a boundary ABC (see Fig. 5.5(b), which corresponds to an edge state within the bulk-edge correspondence of the topological insulator.

We can finally express the π-flux Creutz Hamiltonian (5.19) for open boundary conditions as

$$H_{\mathrm{FB}} = \sum_{i=1}^{N-1} \sum_{\alpha=\pm} \epsilon_\alpha w^\dagger_{i,\alpha} w_{i,\alpha} + \sum_{\eta=l,r} \epsilon_\eta \eta^\dagger \eta \ . \tag{5.28}$$

Although generic fillings can lead to a variety of interesting phases in the presence of interactions [Bar+19], potentially connected to fractional topological insulators [PRS13], we shall only be concerned in this work with half-filling, *i.e.*

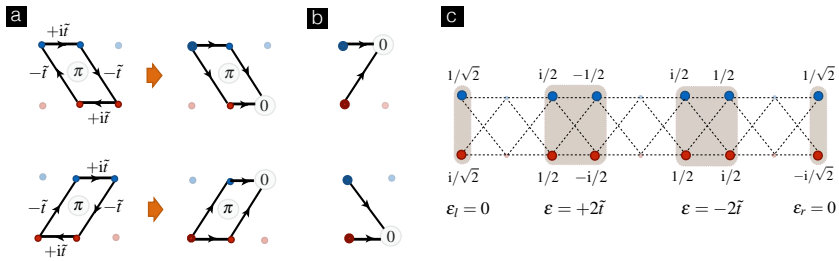

FIGURE 5.5: **Aharonov-Bohm cages in the Creutz ladder:** (a) Considering the tunnelling paths in the Creutz ladder (5.20), one can identify two type of rhombic plaquettes that enclose a synthetic π-flux (left). Therefore, a particle trying to tunnel two sites apart (middle) will be subjected to a destructive Aharonov-Bohm interference that forbids this process. Accordingly, particles are confined to the so-called Aharonov-Bohm cages and cannot spread through the entire lattice. These cages correspond to square plaquettes, except at the edges (b), where destructive interference can also be found for a particle trying to tunnel one site apart (right). (c) Aharonov Bohm cages with the relative amplitudes for a single-particle state in two possible flat bands, and in the two possible zero-energy edge modes.

N fermions, where the ground state of Eq. (5.28) is two-fold degenerate

$$\begin{aligned} |\epsilon_{\rm g},{\rm L}\rangle_{\rm NI} &= l^\dagger w^\dagger_{1,-} w^\dagger_{2,-} \cdots w^\dagger_{N-1,-}|0\rangle, \\ |\epsilon_{\rm g},{\rm R}\rangle_{\rm NI} &= r^\dagger w^\dagger_{1,-} w^\dagger_{2,-} \cdots w^\dagger_{N-1,-}|0\rangle, \end{aligned} \tag{5.29}$$

and the ground-state energy is

$$\epsilon_{\rm g,L} = \epsilon_{\rm g,R} = -2\tilde{t}(N-1). \tag{5.30}$$

We thus see that the ground-state degeneracy corresponds to the two possible choices in populating either of the zero-energy edge modes, and it is related to the topology of the ladder (*i.e.* ring versus line with open edges).

The effects of the leg imbalance $\Delta\epsilon > 0$ in (5.21) can be understood from this edge perspective by writing

$$\begin{aligned} V_{\rm imb} = &\sum_{i=2}^{N-1} t_{\rm imb}\left(w^\dagger_{i-1,+} - w^\dagger_{i-1,-}\right)\left(w_{i,+} + w_{i,-}\right) \\ &+ \sum_{\alpha=\pm} \sqrt{2} t_{\rm imb}\left(-l^\dagger w_{1,\alpha} - {\rm i}\alpha r^\dagger w_{N-1,\alpha}\right) + {\rm H.c.}, \end{aligned} \tag{5.31}$$

where $t_{\rm imb} = -{\rm i}\Delta\epsilon/4$ is an effective tunnelling induced by the imbalance, and

has two relevant effects. The first line describes the hopping of fermions in neighboring ABC, which leads to the aforementioned curvature of the bulk energy bands (5.24). The second line represents the hopping between the topological edge modes and the bulk ABC. As discussed in Sec. 5.2.2, both terms conspire to induce a broadening of the edge modes in the regime $4\tilde{t} \leq \Delta\epsilon$, which is the regime where the topological Zak's phase vanishes, signaling an *imbalance-induced topological phase transition*.

5.2.2 Effects of interactions

Let us now address the fate of this topological phase as the Hubbard repulsion is switched on, reporting only the those analytical results which are necessary for the following discussions. The details of the calculations can be found in the original paper [Jün+17].

Weak interactions: quantum Ising ladder. We start by exploring the weakly-interacting regime $\tilde{t} \gg V_{\mathrm{v}}$. Introducing the following rung operators

$$\begin{aligned} r_{j,1} &= \frac{\mathrm{i}^j}{\sqrt{2}} \left(\mathrm{i} c_{j,\mathrm{u}} + (-1)^j c_{j,\mathrm{d}}^\dagger \right), \\ r_{j,2} &= \frac{\mathrm{i}^j}{\sqrt{2}} \left(c_{j,\mathrm{u}} + \mathrm{i}(-1)^j c_{j,\mathrm{d}}^\dagger \right), \end{aligned} \tag{5.32}$$

an after a Jordan-Wigner transformation (5.8), it turns out that the non-interacting imbalanced model $H_{\pi\mathrm{C}} = H_{\pi\mathrm{C}}(\tilde{t}, \Delta\epsilon)$ (5.19) can be rewritten as a **two-leg quantum Ising ladder** [4]

$$H_{\pi\mathrm{C}} = \sum_j \sum_{n=1,2} \left(-\tilde{t} \sigma_{j,n}^x \sigma_{j+1,n}^x + \frac{\Delta\varepsilon}{4} \sigma_{j,n}^z \right). \tag{5.33}$$

The Hubbard repulsion are now expressed as a coupling between the two legs of the quantum Ising ladder

$$V_{\mathrm{Hubb}} = -\frac{V_{\mathrm{v}}}{4} \sum_j \sigma_{j,1}^z \sigma_{j,2}^z + \mathrm{const.} \tag{5.34}$$

[4] For open boundary conditions, this description allows an alternative interpretation of the edge-state behaviour by writing the Ising model as a Kitaev-Majorana chain [Kit01]. The ferromagnetic regime is associated with two uncoupled Majorana zero-energy modes on the opposing edges of the system for each of the legs of the Ising ladder. Combining the two free Majoranas on either edge of the Ising-ladder then yields the local fermionic edge modes defined in Eq. (5.27).

For weak interactions, $V_v \ll \Delta\varepsilon, \tilde{t}$, we can treat the influence of one Ising chain on the remaining one with a mean-field approximation

$$H_{\pi\mathrm{CH}} \approx \sum_{j,n} \left(-\tilde{t}\sigma^x_{j,n}\sigma^x_{j+1,n} + \frac{\Delta\varepsilon - V_\mathrm{v} m_{\bar{n}}(\Delta\varepsilon, V_\mathrm{v}, \tilde{t})}{4}\sigma^z_{j,n} \right), \tag{5.35}$$

where we have introduced the transverse magnetization $m_{\bar{n}}(\Delta\varepsilon, V_\mathrm{v}, \tilde{t}) = \langle\sigma^z_{j,\bar{n}}\rangle$ for each leg of the ladder, and $\bar{n} = \{2, 1\}$ for $n = \{1, 2\}$. We thus observe a renormalization of the imbalance parameter that controls the transverse field of the Ising model, and thus leads to a shift of the critical point as the interaction strength V_v increases. Accordingly, the topological phase of Sec. 5.2.1 survives in a finite region of parameter space as the interactions are switched on. The critical point $\Delta\epsilon/\tilde{t} = 4$ flows towards smaller values of the imbalance as the interactions increase

$$\frac{\Delta\epsilon}{\tilde{t}} = 4 - \frac{2}{\pi}\frac{V_v}{\tilde{t}} + \mathcal{O}\left(\frac{V_v^2}{\tilde{t}^2}\right). \tag{5.36}$$

This weak-coupling expansion defines a critical line in parameter space that separates the topological and non-topological phases, and agrees well with our numerical findings for the phase diagram of the model, as discussed below (see the red dashed line in Fig. 5.3).

Strong interactions: orbital Ising ferromagnet. Now we explore the opposite limit of the Creutz-Hubbard ladder (5.19), namely the strongly-interacting regime $\tilde{t} \ll V_\mathrm{v}$. In the limit $\tilde{t} = 0$, the ground state of the Creutz-Hubbard Hamiltonian corresponds to a Mott insulator where the N fermions are distributed in the ladder avoiding simultaneous occupancies of two sites within the same rung.

To second order of perturbation theory [MGY88], and considering the half-filling regime, the relevant Hamiltonian describing the low-energy physics corresponds to an **orbital quantum Ising model**, namely

$$\mathcal{P}_\mathrm{r} H_{\pi\mathrm{CH}} \mathcal{P}_\mathrm{r} = \tfrac{1}{4}JN + J\textstyle\sum_i T^y_i T^y_{i+1} + \Delta\epsilon \sum_i T^z_i, \tag{5.37}$$

where the coupling $J = -8\tilde{t}^2/V_\mathrm{v}$ and the leg imbalance $\Delta\epsilon$ plays the role of an effective transverse field. The above spin operators are defined as the orbital analogue of the usual spin operators for electrons

$$T^y_i = \frac{1}{2}\left(-\mathrm{i}c^\dagger_{i,\mathrm{u}}c_{i,\mathrm{d}} + \mathrm{i}c^\dagger_{i,\mathrm{d}}c_{i,\mathrm{u}}\right), \quad T^z_i = \frac{1}{2}\left(c^\dagger_{i,\mathrm{u}}c_{i,\mathrm{u}} - c^\dagger_{i,\mathrm{d}}c_{i,\mathrm{d}}\right). \tag{5.38}$$

Finally, $\mathcal{P}_\mathrm{r} = \Pi_i(1 - n_{i,\mathrm{u}}n_{i,\mathrm{d}})$ is a Gutzwiller projector onto the subspace of singly-occupied vertical rungs.

The $1D$ quantum Ising model can be exactly solved [Pfe70] by introducing a Jordan-Wigner transformation (5.8), followed by a fermionic Bogoliubov transformation [Bog59]. In comparison with the non-interacting ground state (5.29),

which displays a topological two-fold degeneracy, the strongly-interacting ground state for $\Delta\epsilon < |J|/2$ has a non-topological degeneracy related to the $\mathbf{Z}_2$ symmetry of the Ising model. In this regime, the ground state develops long-range order as a consequence of spontaneous symmetry breaking

$$\lim_{r\to\infty}\langle T^y_i T^y_{i+r}\rangle_{\rm SI} = \tfrac{1}{4}\left(1-h^2\right)^{\frac{1}{4}}, \tag{5.39}$$

where $h = 2\Delta\epsilon/|J| < 1$. This defines a critical line

$$\frac{\Delta\epsilon}{\tilde{t}} = \frac{4\tilde{t}}{V_{\rm v}}, \tag{5.40}$$

that separates the phase of long-range order, i.e. an **orbital ferromagnet** (**OFM**), from the disordered phase, i.e. an **orbital paramagnet** (**OPM**), and is depicted by a yellow dashed line in Fig. 5.3. As the leg imbalance is increased above a critical value $\frac{\Delta\epsilon}{\tilde{t}}|_{\rm c} = \frac{4\tilde{t}}{V_{\rm v}}$, a standard quantum phase transition occurs between the long-range ordered Ising ferromagnet and a disordered orbital paramagnet, where all fermions tend to occupy the lower leg of the ladder. We note that this transition is not of a topological origin, as it can be understood by a local order parameter: the orbital magnetisation $\langle T^y_i T^y_{i+r}\rangle_{\rm SI} \to m_y^2$.

Intermediate interactions: extended Hubbard models. The long-range ferromagnetic order is totally absent in the non-interacting topological ground-state (5.29), where one finds

$$\langle T^y_i T^y_{i+r}\rangle_{\rm NI} = 0. \tag{5.41}$$

Accordingly, it is clear that one cannot connect the non-interacting topological and strongly-interacting ferromagnetic phases adiabatically. Therefore, there should be an *interaction-induced topological quantum phase transition* between the symmetry-protected topological phase, and a state with magneto-orbital long-range order, for intermediate interactions $V_{\rm v}/\tilde{t}$.

To study intermediate interactions, it is convenient to rewrite the Hubbard-interactions as a sum of three contributions $V_{\rm Hubb} = V_{\rm nn} + V_{\rm pt} + V_{\rm dt}$, expressed in the ABC base (5.26)-(5.27). $V_{\rm nn}$ includes *nearest-neighbour interaction* between fermions confined in adjacent ABC

$$V_{\rm nn} = \frac{V_{\rm v}}{2}\sum_{\alpha=\pm}(n_l n_{1,\alpha} + n_r n_{N-1,\alpha}) + \frac{V_{\rm v}}{4}\sum_{i=2}^{N-1}\sum_{\alpha,\beta=\pm} n_{i-1,\alpha}n_{i,\beta}, \tag{5.42}$$

where the ABC number operators are $n_{i,\alpha} = w^\dagger_{i,\alpha}w_{i,\alpha}$ for $\alpha \in \{+,-\}$, and $n_\eta = \eta^\dagger\eta$ for $\eta \in \{\ell, r\}$.

$V_{\rm pt}$ and $V_{\rm dt}$ are *correlated tunnelling* processes of two types. A *pair-tunnelling* Hamiltonian

$$V_{\rm pt} = \tilde{J} \sum_{i=2}^{N-1} \left(w^\dagger_{i-1,+} w_{i-1,-} (w^\dagger_{i,-} w_{i,+} + w^\dagger_{i,+} w_{i,-}) \right) + \text{H.c.} \tag{5.43}$$

where $\tilde{J} = -V_{\rm v}/4$. In addition, we also obtain an inter-leg *density-dependent tunnelling*

$$\begin{aligned} V_{\rm dt} = T_{\rm d} \sum_{i=2}^{N-1} & \left(n_{i-1,+} + n_{i-1,-} - n_{i+1,+} - n_{i+1,-} \right) w^\dagger_{i,+} w_{i,-} \\ & + 2T_{\rm d} \left(n_l w^\dagger_{1,+} w_{1,-} - n_r w^\dagger_{N-1,+} w_{N-1,-} \right) + \text{H.c.}, \end{aligned} \tag{5.44}$$

where $T_{\rm d} = V_{\rm v}/4$ is the tunneling strength. The first line describes an inter-leg tunnelling within the bulk of the ladder that depends on the density difference of the neighbouring ABC, and will be negligible for a ground state with translationally-invariant bulk properties. On the other hand, the second line describes inter-leg tunnelings that occur at the boundaries of the Creutz-Hubbard ladder, and depend on the density of the edge ABC . These terms are not negligible for translational-invariant bulks, and will play a key role in the topological phase transitions of the model.

For the balanced interacting model ($\Delta\varepsilon = 0$) the Hamiltonian reads $H_{\pi\rm CH} = H_{\rm FB} + V_{\rm nn} + V_{\rm pt} + V_{\rm dt}$ and an effective boundary theory for intermediate interactions $V_{\rm v}/\tilde{t}$ can be derived.

Although the pair and density-dependent tunnellings in Eqs. (5.43)-(5.44) modify the distribution of particle-hole pairs in the rungs of the virtual ladder, the nearest-neighbour interactions (5.42) do not change, since the number of neighbouring ABC that are occupied is preserved under such processes. Therefore, in this limit, the nearest-neighbour interactions (5.42) can be substituted by a c-number, and only the flat-band (5.28) and the correlated-tunnelling terms (5.43)-(5.44) have an important effect on the non-interacting ground states (5.29). Moreover, as argued below Eq. (5.44), only the density-dependent tunnelling at the edges of the ladder will play a role to determine the order of the translationally-invariant ground states.

According to this discussion, we can rearrange these terms as $H_{\pi\rm CH} = H_{\rm edge} + H_{\rm bulk} + H_{\rm b-e}$, where

$$H_{\rm edge} = \epsilon_l l^\dagger l \ + \epsilon_r r^\dagger r \ , \tag{5.45}$$

stands for the Hamiltonian of the zero-energy edge modes. After introducing the two spinor-operators

$$\tilde{T}^x_i = \frac{1}{2} \left(w^\dagger_{i,+} w_{i,-} + w^\dagger_{i,-} w_{i,+} \right), \ \ \tilde{T}^z_i = \frac{1}{2} \left(w^\dagger_{i,+} w_{i,+} - w^\dagger_{i,-} w_{i,-} \right), \tag{5.46}$$

the bulk Hamiltonian becomes

$$H_{\text{bulk}} = \frac{V_{\text{v}}}{4} N + \sum_{i=1}^{N-1} 4\tilde{t}\tilde{T}_i^z + \sum_{i=2}^{N-1} 4\tilde{J}\tilde{T}_{i-1}^x \tilde{T}_i^x, \tag{5.47}$$

where $\tilde{J} = -V_{\text{v}}/4$, which corresponds to a ferromagnetic Ising model in a transverse field. This model can be solved exactly for periodic boundary conditions [Pfe70] by means of a Jordan-Wigner transformation [JW28] $\tilde{T}_i^z = f_i^\dagger f_i - \frac{1}{2}$ and $\tilde{T}_i^x = \frac{1}{2} f_i^\dagger \mathrm{e}^{\mathrm{i}\pi \sum_{j<i} f_j^\dagger f_j} + \text{H.c.}$, where $f_i^\dagger = (f_i)^\dagger$ are spinless fermionic operators. Considering periodic boundary conditions $f_N = f_1$, we would obtain the energy bands for single-particle excitations

$$\tilde{\epsilon}_\pm(q) = \pm\tilde{\epsilon}(q) = \pm 2|\tilde{J}|\sqrt{1 + \tilde{\mathfrak{f}}^2 - 2\tilde{\mathfrak{f}}\cos q}, \tag{5.48}$$

where we have introduced the flatness parameter $\tilde{\mathfrak{f}} = 8\tilde{t}/V_{\text{v}}$, such that we recover perfect flat bands in the non-interacting regime $V_{\text{v}} = 0$. Analogously to the non-interacting case, where the curvature $\mathfrak{f} < 1$ denoted the transition to the non-topological imbalanced regime, here we have that $\tilde{\mathfrak{f}} = 1$ locates the critical point of the interaction-induced quantum phase transition at $\frac{V_{\text{v}}}{t}|_{\text{c}} = 8$, which has been represented by a red circle in the phase diagram of Fig. 5.3.

5.2.3 Phase diagram of the Creutz-Hubbard ladder

Our considerations in the above sections already allowed us to determine the possible phases of the model and their phase boundaries in certain parameter regimes. In the following, we lay out the full phase-diagram of the model in the $(\frac{\Delta\epsilon}{t}, \frac{V_{\text{v}}}{t})$ plane using DMRG calculations. In Appendix B the matrix product operator used for these simulation is described.

The analytic and numerical results for the phase diagram, collected in Fig. 5.3, are described in the following subsections.

Topological insulator to orbital paramagnet phase transition. As shown in Sec. 5.2.2, the mapping of the Creutz ladder onto a quantum Ising ladder allows us to predict a critical line (5.36) separating the topological insulator (TI) and the orbital paramagnet (OPM) for sufficiently weak interactions. This critical line is represented by a red dashed line that starts form the point $\Delta\epsilon = 4\tilde{t}, V_{\text{v}} = 0$ in Fig. 5.3.

A good indicator for this quantum phase transition is the Ising transverse magnetization or equivalently the density imbalance between the legs of the Creutz ladder:

$$\Delta n = \frac{1}{N} \sum_i \left(c_{i,\text{u}}^\dagger c_{i,\text{u}} - c_{i,\text{d}}^\dagger c_{i,\text{d}} \right) = \frac{1}{2N} \sum_j \sum_n \sigma_{j,n}^z. \tag{5.49}$$

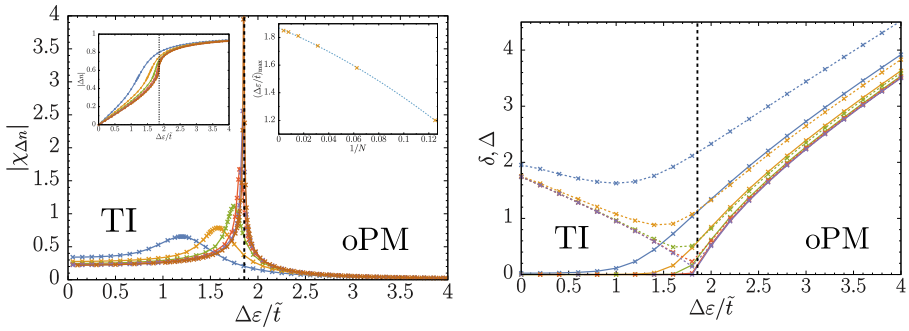

FIGURE 5.6: **Paramagnetic susceptibility and energy gaps along the TI-OPM-transition:** Left: The divergence of the magnetization susceptibility $\chi_{\Delta n}$ with growing system size indicates the critical point for a cut through the phase-diagram at $V_v = 4.0$ (left inset: occupation imbalance Δn, right inset: fitted finite-size scaling of the susceptibility maxima assuming up to second-order corrections, $\Delta\varepsilon_c(N) = \Delta\varepsilon_c(1 + aN^{-1} + bN^{-2})$). Right: The dashed lines show the finite size results for the energy gap Δ, which is non-zero in both the TI- and the OPM-phase. The quantity δ (solid lines), on the contrary, is zero in the TI-phase due to the presence of zero energy modes, but achieves a non-vanishing value in the OPM phase. Blue: $N = 8$, orange: $N = 16$, green: $N = 32$, red: $N = 64$, violet: $N = 128$, brown: $N = 256$. The vertical line (black) indicates the transition point ($\Delta\varepsilon_c = 1.857$).

Both can be easily calculated numerically using the DMRG code.

We can determine the critical line by studying the divergence of the imbalance susceptibility $\chi_{\Delta n} = \partial\langle\Delta n\rangle/\partial(\Delta\epsilon/\tilde{t})$ (Fig. 5.6 (left)).

As an alternative means of identifying the TI phase, we can study the behaviour of the ground-state degeneracy in the Creutz-Hubbard model with variable filling. We therefore introduce the **single- and two-particle energy gaps**

$$\Delta = \lim_{N\to\infty} \tfrac{1}{2}\left[E(N+2) + E(N-2) - 2E(N)\right], \tag{5.50}$$

$$\delta = \lim_{N\to\infty} \left[E(N+1) + E(N-1) - 2E(N)\right], \tag{5.51}$$

where $E(x)$ is the ground-state energy of a system with x particles. It can be shown that the two quantities coincide for gapless systems ($\Delta = \delta = 0$) and conventional insulators ($\Delta = \delta \neq 0$). In a topological insulator, however, $\delta = 0$ due to the presence of zero-energy edge modes while $\Delta \neq 0$ measures (half) the band-gap. In Fig. 5.6 (bottom), we show that the predicted behaviour is indeed observed.

The critical points obtained through these different observables are represented by yellow stars in the left part of Fig. 5.3. As can be seen from these results, the analytical prediction of the phase boundary (5.36) is reasonably accurate even for quite large interactions, where the exact critical line given by DMRG departs from a straight line, and bends up.

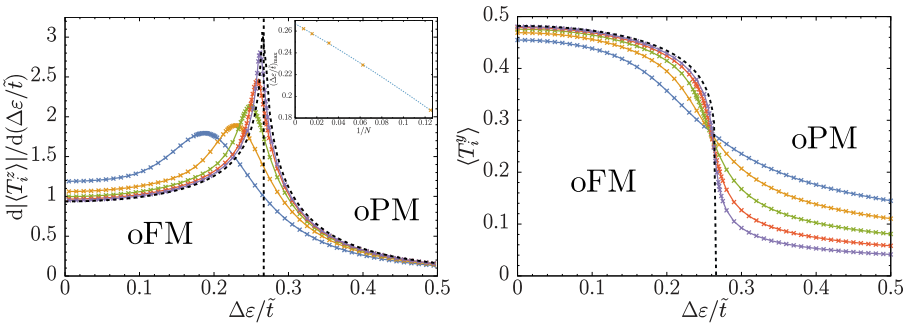

FIGURE 5.7: **Ferro- and paramagnetic magnetization along the OFM-OPM-transition:** Left: Paramagnetic magnetization susceptibility for a cut through the phase diagram at $V_v = 16\tilde{t}$ and different system sizes (inset: fitted finite-size scaling of the susceptibility maxima assuming up to second-order corrections, $\Delta\varepsilon_c(N) = \Delta\varepsilon_c(1+aN^{-1}+bN^{-2})$). Right: Ferromagnetic magnetization along the same line. Blue: $N = 8$, orange: $N = 16$, green: $N = 32$, red: $N = 64$, violet: $N = 128$. The light blue vertical line (dashed) in the top figure indicates the critical point (here: $\Delta\varepsilon_c/\tilde{t} = 0.266$). The black dashed curves indicate the analytical predictions of an Ising model with the same critical point (and a saturation of the ferromagnetic magnetization $\langle T_i^y\rangle_{\max} = 0.48$). The effective Ising model in Eq. (5.38) suggests $\Delta\varepsilon_c/\tilde{t} = 0.25$ and $\langle T_i^y\rangle_{\max} = 0.5$.

Orbital ferromagnet to orbital paramagnet phase transition. In Sec. 5.2.2, we introduced an effective orbital Ising model in the limit of very strong interactions, which allowed us to predict a critical line (5.40) separating the OFM and OPM. This critical line is represented by a yellow dashed line in Fig. 5.3.

Indeed by measuring the **paramagnetic and ferromagnetic magnetization** ($\langle T_i^z\rangle$ resp. $\langle T_i^y\rangle$ in Eq. (5.38)), we confirm that these quantities scale equally, and identify the phase-transition point also for finite interactions (Fig. 5.7) [5].

We observe for both quantities an Ising-like scaling, which differs from the strong-coupling prediction only by a renormalization of the critical point and of the maximum ferromagnetic magnetization (comp. Fig. 5.7).

[5]Technically, we determine the paramagnetic magnetization by measuring the fermionic observable that defines T_i^z, which is proportional to the leg density imbalance discussed above (see

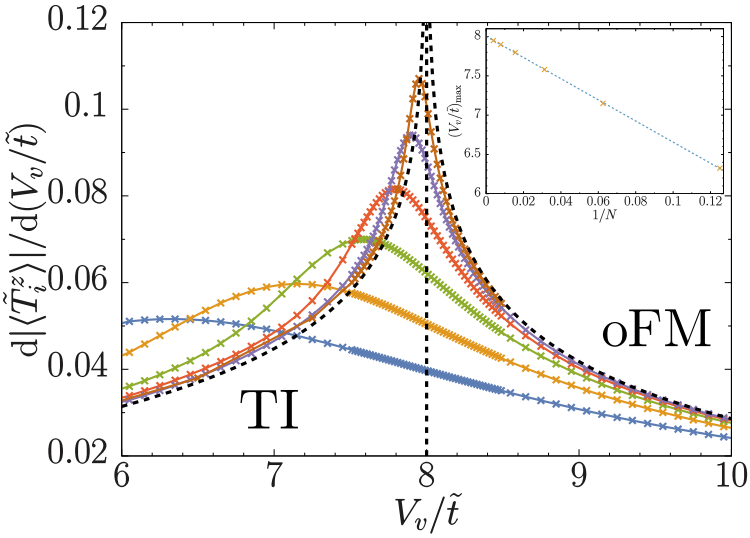

FIGURE 5.8: **Paramagnetic magnetization susceptibility along the TI-OFM-transition:** Blue: $N = 8$, orange: $N = 16$, green: $N = 32$, red: $N = 64$, violet: $N = 128$, brown: $N = 256$. The black dashed lines indicate the TD-result in a TFIM-model. Inset: The finite-size scaling of the maxima of the susceptibility yields $(V_v/\tilde{t})_{\mathrm{c,num}} = 8.003$ (here fitted via $V_{v,\mathrm{c,num}}(N) = V_{v,\mathrm{c,num}}(1 + aN^{-1})$), in good agreement with the analytical result $(V_v/\tilde{t})_{\mathrm{c}} = 8$.

The critical points obtained through these magnetizations are represented by yellow stars in the right part of Fig. 5.3. As can be seen from these results, the analytical prediction of the phase boundary (5.36) is reasonably accurate even for moderate interactions.

Topological insulator to orbital ferromagnet phase transition. For intermediate interactions we predicted the extension of the topological phase along the $(0, \frac{V_{\mathrm{v}}}{t})$ axis of the phase diagram until a critical point $\frac{V_{\mathrm{v}}}{t} = 8$. Beyond this point, the long-range ordered orbital Ising magnet sets in, and the topological edge

Eq. (5.38)). In order to avoid problems due to incomplete symmetry breaking when studying the ferromagnetic order-parameter $\langle T_i^y \rangle$ (i.e. between the possible alignments in the ferromagnetic phase), we determine instead the zero-momentum component of the orbital magnetic structure factor

$$S_{T_y T_y}(k) = \frac{1}{N^2} \sum_{i,j} \mathrm{e}^{\mathrm{i}k(i-j)} \left\langle T_i^y T_j^y \right\rangle , \tag{5.52}$$

which yields the desired ferromagnetic magnetization in the thermodynamic limit $\langle T_i^y \rangle = (S_{T_y T_y}(0))^{1/2}$.

modes disappear into the bulk. This critical point is represented by a red circle in Fig. 5.3.

The numerical analysis (Fig. 5.8) confirms the validity of the effective Ising-model derived in Eq. (5.47), and the exact location of this critical point. Moreover, in the case of finite imbalance ($\Delta\varepsilon \neq 0$), the divergence of the paramagnetic susceptibility serves as a criterion for the determination of the phase-boundary (see inset Fig. 5.8). The critical points obtained by these means are represented by yellow stars in the middle part of Fig. 5.3.

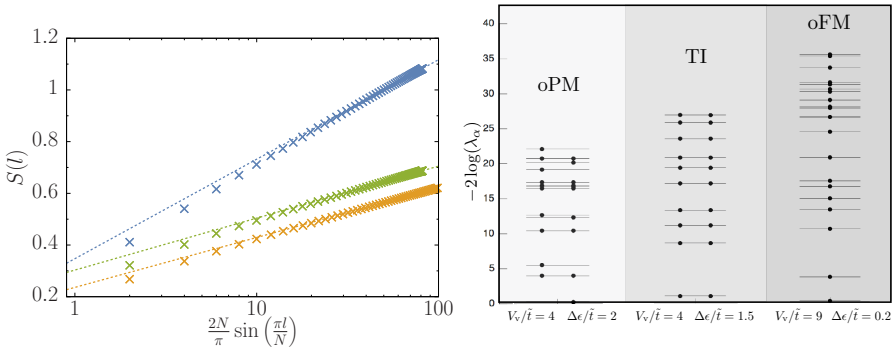

FIGURE 5.9: **(Left) Scaling of the entanglement entropy for critical points on the different transition lines.** The prefactor c in $S(l) = \frac{c}{6}\ln(\frac{2N}{\pi}\sin\frac{\pi l}{N}) + \text{const.}$ identifies the central charge of a critical phase. Here we show the entanglement entropy in systems with N sites and fit the data for $N/4 < l \leq N/2$. The fitting results for the TI-OPM transition yield $c = 1.003$ for $V_v/\tilde{t} = 4.0, \Delta\varepsilon/\tilde{t} = 1.857, N = 128$ (blue line), the OFM-OPM transition yield $c = 0.524$ for $V_v/\tilde{t} = 16, \Delta\varepsilon = 0.266, N = 128$ (green line), and the TI-OFM transition yield $c = 0.503$ for $V_v/\tilde{t} = 0, \Delta\varepsilon/\tilde{t} = 8, N = 256$ (yellow line). All these numerical fits agree considerably well with the model predictions $c \in \{1, 1/2, 1/2\}$. **(Right) Degeneracies of the entanglement spectrum for different phases.** For a ladder of length $L = 128$ and for a bipartition in the half chain, the twenty lower eigenvalues of the ES are depicted for the three different phases. The dots represent the degeneracy of the corresponding eigenvalue. In the TI phase, for $V_v/\tilde{t} = 4$ and $\Delta_\epsilon/\tilde{t} = 1.5$ the eigenvalues are all doubly degenerate. In the OPM phase, for $V_v/\tilde{t} = 4$ and $\Delta_\epsilon/\tilde{t} = 2$, and in the OFM phase for $V_v/\tilde{t} = 9$ and $\Delta_\epsilon/\tilde{t} = 0.2$ almost all the eigenvalues are not degenerate. Following the convention, the ES is defined as a logarithmic rescaling of the Schmidt values, $-2\log(\lambda_i)$. We found the same behaviour elsewhere in the phase space.

5.2.4 Entanglement analysis of phase transitions

So far, we have used a conventional condensed-matter approach to explore numerically the phase diagram of the model, which is based on exploiting energy gaps, susceptibilities, and correlation functions to identify phases with long-range order or symmetry-protected topological phases, and critical lines that separate them. Here we used the modern complementary approach, based on the ground-state entanglement, as introduced in details in previous chapters.

Conformal field theories for the critical lines. We argued above that the synthetic Creutz ladder for sufficiently weak interactions can be understood as a couple of Ising models of length $L = N$ with a renormalized transverse field. Accordingly, the corresponding CFT (see Sec. 2.2.2) should have **central charge** of $c = 1/2 + 1/2 = 1$, such that we would expect the scaling [Eq. (2.19)] $S(l) = \frac{1}{6} \ln \left(\frac{2N}{\pi} \sin \frac{\pi l}{N} \right) + a$.

For the strongly-interacting regime, we showed that the OFM-OPM quantum phase transition can be predicted in terms of a single Ising model of length $L = N$ in a transverse field. Accordingly, the corresponding CFT should have central charge of $c = 1/2$, and $S(l) = \frac{1}{12} \ln \left(\frac{2N}{\pi} \sin \frac{\pi l}{N} \right) + \tilde{a}$.

Finally, in the intermediate interacting regime of Sec. 5.2.2, we argued that the relevant physics to understand the TI-OFM phase transition is approximated by another Ising model and therefore $S(l) = \frac{1}{12} \ln \left(\frac{2N}{\pi} \sin \frac{\pi l}{N} \right) + a'$.

We confirm the above predictions through the numerical determination of the central charge along the critical lines in three representative cases (see Fig. 5.9 (left)). We find central charge values agreeing with $c = 1/2$ for the TI-OFM and the OFM-OPM-transition. The charge $c = 1$ along the TI-OPM-transition originates from the hybrid nature of the Ising-model describing it (see Eq. (5.33)). Building on these results, we depict the central charges of the three critical lines of our phase diagram in Fig. 5.3.

Entanglement spectrum characterization of the topological insulating phase. In the previous sections we provided many indicators that ensure the nontrivial topological nature of the TI phase, namely the presence of localized edge states and degenerate ground state. But, differently from non-interacting systems, for interacting systems, an invariant quantity which incontestably determines the topological class is not still available. However, as proven in detail in Sec. 5.1.4 a strong signature of the presence of topological order can be extracted from the study of the **entanglement spectrum** (**ES**). As shown in Fig. 5.9 (right) in the imbalanced Creutz-Hubbard model, the ES in the TI phase is not trivial, with *double degenerate eigenvalues*, whereas in the OPM and OFM phases the ES is trivial and almost completely not degenerate, supporting the presence of topological order.

5.3 Summary

In this chapter we applied a variety of analytical and numerical techniques on the study of a concrete fermionic model, the imbalanced Creutz-Hubbard ladder, which falls in the AIII topological class. By adding on-site repulsive interactions only, we can induce phase transitions of different universality classes into an orbital ferro- or para-magnetic phase. We then advance on the understanding of the competition between topological features and interaction effects in quantum many-body systems. The tensor network based methods introduced in Chap. 3 allowed to detailing study the phase diagram and the quantum phase transitions as well as a characterization of the topological insulating phase by the analysis of the entanglement spectrum.

6 Bell Correlations at Ising quantum critical points

This chapter is of crucial interest in this dissertation, since the role of entanglement entropy and nonlocality in characterizing quantum critical points (QCP) will be compared in a concrete foundamental many-body system, a long-range (power-law decaying $1/r^\alpha$ interactions) ferromagnetic Ising chain. We first establish spin squeezing as a necessary condition to violate the permutational invarinat Bell inequalities (PIBI) introduced in Sec. 2.3.4, in a Bell scenario involving identical measurement settings on all qubits. Based on numerical matrix product states (MPSs) adapted to long-range interactions and analytical linear spin-wave computations, we show that spin squeezing is a generic feature close to the QCP, leading to a maximal violation for $\alpha < d$ in the thermodynamic limit. Interestingly, the violation of the PIBI is maximal for all-to-all interactions, where the semi-classical spin-wave theory is exact. Bipartite entanglement entropy (EE), on the other hand, shows the opposite behavior, being maximal for nearest-neighbour interactions.

6.1 Introduction

Nonlocal correlations, witnessed by the violation of Bell inequalities (BIs), mark the strongest departure from classical physics that correlated quantum systems may exhibit [Bru+14]. To violate a BI, entanglement among the individual degrees of freedom is necessary (albeit not sufficient [Wer89]). Such quantum correlations are typically fragile against thermal effects, especially when considering many degrees of freedom. Nevertheless, thermalization is not always detrimental to entanglement: indeed, quantum critical points (QCPs) [Sac11] represent a special instance of equilibrium states, where multipartite entanglement is stabilized at *all* length scales [Hau+16]. Multipartite entanglement survives also at finite temperature in the quantum-critical regime, but thermal effects reduce the range of the correlations [Hau+16; GSP18; FR19]. In addition to entanglement, are there QCPs which stabilize also nonlocal correlations among the individual components of the system? An important result from quantum information theory shows that all non-product pure states, including those at QCPs,

possess bipartite nonlocal correlations [Gis91]. Demonstrating and quantifying the presence of nonlocal correlations among a macroscopic number of degrees of freedom is, in general, a very challenging task [Bru+14]. Nonetheless, a **permutationally invariant Bell inequality** (**PIBI**) involving only first and second moments of collective observables was derived recently [Tur+14; Tur+15b], which is especially revelant for a collection of N qubits. The preparation, in a *Bose-Einstein condensate* (BEC), of massively entangled states of two-level atoms violating this inequality, was subsequently reported [Sch+16].

In the BEC experiment, violatation of the PIBI was achieved through the dynamical generation of spin-squeezed states [Sch+16; Pez+18]. On the other hand, *spin squeezing* is known to be present at the QCP of the **transverse-field ferromagnetic** (**FM**) **Ising model** (**TFIM**), at least for a sufficiently large number d of spatial dimensions [FR18; GSP18]. Here, we investigate nonlocal correlations at the QCP of the TFIM with power-law decaying ($1/r^\alpha$) interactions, interpolating between infinite-range ($\alpha = 0$) and nearest-neighbour ($\alpha \to \infty$) interactions. Besides its fundamental interest as a paradigmatic model for quantum phase transitions, this model has been implemented in various quantum simulators [Ber+17; Zha+17; Cha+18].

6.2 Bell inequality violation and spin squeezing

We consider the Bell scenario $(N, 2, 2)$ faced in Sec. 2.3.4, here realized in a N-qubits quantum state, where every qubit (labelled by the index i) is subjected to two *local dichotomic projective measures* (already introduced in Eq. (2.46)):

$$\begin{aligned} \mathcal{M}_n^{(i)} &= \mathcal{M}_n = \cos\theta\sigma_z + \sin\theta\sigma_y, \\ \mathcal{M}_m^{(i)} &= \mathcal{M}_m = \cos\phi\sigma_z + \sin\phi\sigma_y, \end{aligned} \tag{6.1}$$

corresponding to two possible directions $\hat{n}$ and $\hat{m}$ defined by the angles ϕ and θ. Note that we dropped the index i since we restrict to the fully symmetric case, where the measures are the same for each qubit (see discussion below Eq. (2.46)).

We aim at certifying the nonlocal nature of the resulting correlations, relying on 1- and 2-body expectation values. More specifically, we consider BIs involving symmetric combinations of such correlators, *i.e.* the PIBI established in [Tur+14] (and discussed in this thesis in Sec. 2.3.4, Eq. (2.45)) which here we rewrite for the sake of readability:

$$W = 1 - \frac{1}{N}S_n + \frac{1}{4N}(S_{nn} - 2S_{nm} + S_{mm}) \geq 0, \tag{6.2}$$

where

$$\mathcal{S}_k := \sum_{k=1}^{N} \langle \mathcal{M}_k \rangle \qquad \mathcal{S}_{kw} := \sum_{\substack{k,w=1 \\ k \neq w}}^{N} \langle \mathcal{M}_k^{(i)} \mathcal{M}_w^{(j)} \rangle, \tag{6.3}$$

with $\hat{k}, \hat{w} \in \{\hat{n}, \hat{m}\}$. PIBI (6.2) must be fulfilled by any statistical model obeying Bell locality hypothesis. Given a quantum state, we look for optimal measurement directions $(\hat{n}, \hat{m})$ in order to maximally violate inequality (6.2). Note that we follow a different approach than in [Tur+14]: there (as explained below Eq. (2.46)) the authors fixed the Bell operator (the rhs of Eq. (6.2)) and hence calculated the quantum state which maximally violate the inequalities; here we are instead already provided with a given quantum state, the ground state of a concrete model, and look for the optimal measurements in order to violate the inequality. This optimization can be performed analytically where all observers measure the same observables. First, introducing $\hat{a} = (\hat{n} - \hat{m})/|\hat{n} - \hat{m}|$, defining the collective spin $\vec{J} = \sum_{i=1}^{N} \vec{\sigma}_i/2$, and using elementary spin algebra, Eq. (6.2) can be recast in the equivalent form [Sch+16]

$$W = 1 - |C_n| + (\hat{a} \cdot \hat{n})^2(\zeta_a^2 - 1) \geq 0 \,, \tag{6.4}$$

where $C_n = \langle J^n \rangle/(N/2) \equiv 1 - r < 1$ and $\zeta_a^2 = \langle (J^a)^2 \rangle/(N/4)$ are the first and second moments of the collective spin along, respectively, directions $\hat{n}$ and $\hat{a}$, scaled to the coherent spin state values. ζ_a^2 is the **squeezing parameter** already met in Sec. 2.1.4, Eq. (2.13).

Notice that measuring the collective spin projectively along $\hat{n}$ and $\hat{a}$ does not realize a Bell scenario, but witnesses the ability to prepare many-spin states exhibiting nonlocality if the spins are individually measured along $\hat{n}$ and $\hat{m}$ [Sch+16]. Indeed, Eqs. (6.2) and (6.4) have a different status. On the one hand, Eq. (6.2) allows for a device-independent test of nonlocality, valid even if individual measurement axes are not well-controlled, and even if the individual systems are actually not qubits but have an arbitrary physical structure. The only assumption leading to Eq. (6.2) – beyond Bell locality hypothesis – is that two possible measurement settings can be freely chosen on each party, each of which yielding two possible outcomes [Tur+14; Tur+15b]. On the other hand, Eq. (6.4) relies on extra physical assumptions: applicability of quantum-mechanical spin algebra and correct calibration of measurement axes [Sch+16].

We define $\hat{z}$ as the mean spin direction: $\langle \vec{J} \rangle \propto \hat{z}$. If $\hat{a} \cdot \hat{z} \neq 0$, then $\zeta_a^2 \propto N$, precluding violation of Eq. (6.4) for large N. Hence, axis $\hat{a}$ must be chosen perpendicular to $\hat{z}$. Then, the minimal value of W is obtained if $\hat{a}$ is along the direction of minimal variance $\vec{J}$. Violation of inequality (6.4) then requires $\zeta_a^2 < 1$ (namely, spin squeezing [KU93; Pez+18]), while maintaining the largest possible spin length ($r \ll 1$). Then, we choose $\hat{n} = \hat{z}\cos\phi + \hat{a}\sin\phi$, yielding $W = (1 - \zeta_a^2)\cos^2\phi - (1 - r)\cos\phi + \zeta_a^2$. The minimal W is

$$W_{\min} = \zeta_a^2 - \frac{(1-r)^2}{4(1-\zeta_a^2)} > -\frac{1}{4} \,, \tag{6.5}$$

achieved for $\cos\phi = (1 - r)/[2(1 - \zeta_a^2)]$. The second measurement direction is $\hat{m} = \hat{z}\cos\phi - \hat{a}\sin\phi$. Maximal violation of inequality (6.4) is achieved for perfect squeezed states ($\zeta_a^2 \to 0$ and $r \to 0$), possible only for $N \to \infty$.

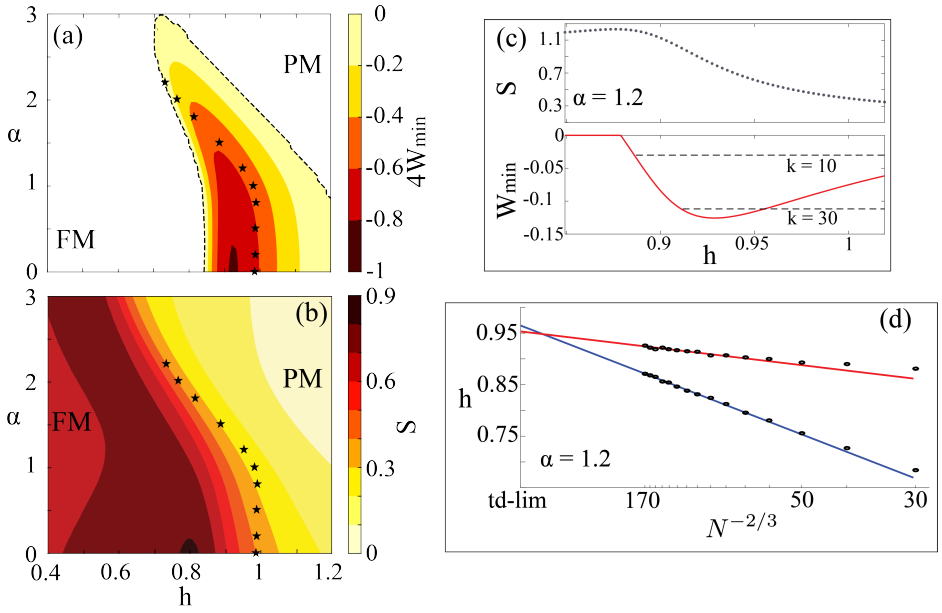

FIGURE 6.1: (a) BI violation and (b) bipartite EE (b) for the one-dimensional long-range TFIM ($N = 40$). Stars are extrapolations for $N \to \infty$ of the maximum of EE. (c): bipartite EE and maximal violation of BI Eq. (6.2) for $N = 170$ and $\alpha = 1.2$. Black dashed lines: k-producibility bounds [Tur+19] (see text) for $k = 10$ and $k = 30$. (d): for $\alpha = 1.2$, critical point extrapolated for $N \to \infty$. Both maximum of EE and maximal violation of the BI occur for the same transverse-field. The fit used for the the extrapolation $N \to \infty$ is of the form $h_c(N) = h_c(\infty) + aN^{-2/3}$. In fact, finite-size scaling theory predicts $h_c(N) - h_c(\infty) \sim L^{-1/\nu}$ with ν the exponent of the correlation length. For infinite-range interactions, L is replaced by N^{1/d_c} where $d_c = 3$ is the upper critical dimension of the quantum Ising model [BJP82]. Hence, taking the mean-field exponent $\nu = 1/2$ (expected for infinite-range interactions), we obtain $h_c(N) - h_c(\infty) \sim N^{-2/3}$.

6.3 Ferromagnetic Ising model

We investigate violation of Eqs. (6.2) and (6.4) at the QCP of the TFIM, with power-law FM interactions:

$$\mathcal{H} = -\frac{1}{\gamma_{\mathbf{0}}} \sum_{i \neq j} \gamma_{ij} S_i^x S_j^x - h \sum_i S_i^z \tag{6.6}$$

where $\gamma_{ij} = |\mathbf{l}_i - \mathbf{l}_j|^{-\alpha}$, and $S_i^a = x, y, z = \sigma_i^a/2$ are $s = 1/2$ spin operators. i and j run over the sites of a $d-$dimensional square lattice of size $N = L \times (L/2)^{d-1}$, and $\mathbf{l}_i$ denotes the position of spin i. We introduced $\gamma_{\mathbf{k}} = N^{-1} \sum_{i \neq j} \exp[-\mathbf{k} \cdot (\mathbf{l}_j - \mathbf{l}_i)]\gamma_{ij}$, and, to have a well-defined thermodynamic limit also for $\alpha < d$, we normalized the interaction term to $\gamma_{\mathbf{k}=\mathbf{0}}$. Mean-field theory predicts a QCP for $h = h_c = 1$, separating paramagnetic (PM) (for $h > h_c$) from FM phases ($h < h_c$). The exact QCP is in general at $1/2 \leq h_c \leq 1$; in the $d = 1$ nearest-neigbour limit, $h_c = 1/2$ [Sac11]. In the PM phase, spins are aligned along $\hat{z}$; in the FM phase, they sponteneously align along $\tilde{z} = \hat{z} \cos\theta \pm \hat{x} \sin\theta$, with $\cos\theta = h$ in mean-field theory.

At the QCP, fluctuations of the magnetization along $\hat{x}$ diverge as a power-law with the system size, namely $\langle (J^x)^2 \rangle / N \sim N^{\theta(\alpha)}$ with a critical exponent $\theta(\alpha)$. On the other hand, due to the presence of the transverse-field, the system maintains a finite magnetization along $\hat{z}$, so that $\langle J^z \rangle / N = O(1)$. In virtue of Heisenberg inequality for the collective spin, this opens the possibility for squeezing the fluctuations of J^y, as $\zeta_y = \langle (J^y)^2 \rangle / N \geq O(N^{-\theta(\alpha)})$. While quantum-critical spin squeezing is indeed present when $\alpha = 0$ [DV04; FR18], for nearest-neighbour interactions it is present for $d \geq 2$ but absent in $d = 1$ [LMW13; FR18]. FM power-law interactions increase the connectivity of the Ising model, and can be viewed as effectively increasing the physical dimension of the system. Hence, we may expect spin squeezing, as well as the resulting violation of inequality (6.2), to exhibit a nontrivial behavior when varying the power-law exponent α at the QCP. In particular, in $d = 1$, we may expect a violation for small values of α, but not in the nearest-neighbour limit $\alpha \to \infty$. This scenario is indeed confirmed by our numerical DMRG results, consistently with LSW analytical predictions.

6.4 DMRG results in one dimension

Our DMRG algorithm variationally finds the ground state of the model using an MPS ansatz with bond dimension $\chi = 100$. The long-range interactions are implemented on a matrix product operator (MPO) following the prescriptions in [CDV08; FND10b]. We can employ chains of length up to $N = 170$. The details about the construction of this MPO are illustrated in Appendix C. From the ground state in MPS representation, one can straightforwardly calculate the

two-body correlators. The optimization of the angles θ and ϕ in order to obtain the maximal violation of the PIBI is numerically performed following the algorithm presented in [Tur+19].

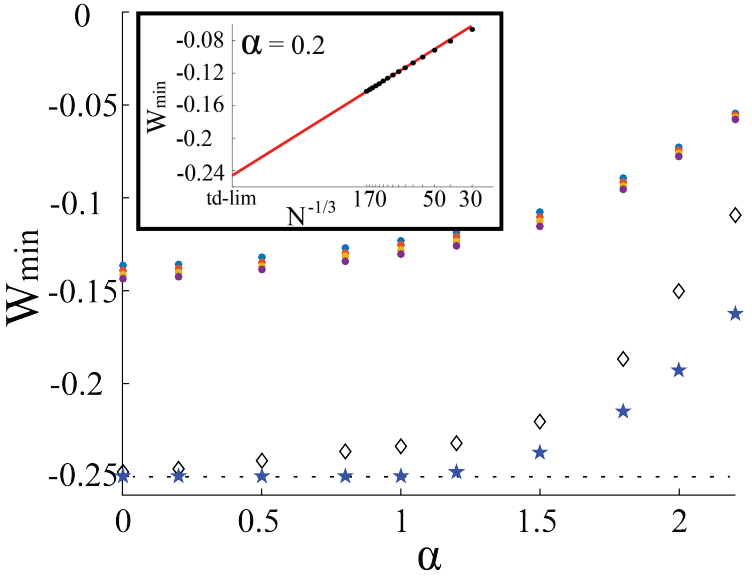

FIGURE 6.2: BI violation at the QCP of the $d = 1$ TFIM, for different values of α. Dots: finite size DMRG calculations ($N = 150, 160, 170$). Diamonds: extrapolations for $N \to \infty$ (using $N = 30, 40, \ldots, 170$). Stars: LSW results ($N = 10^5$). Inset: extrapolation for $\alpha = 0.2$, of the form $W_{\min}(N) = W_{\min}(\infty) + aN^{-1/3}$. Analytical results for $\alpha = 0$ [DV04] predict that $\langle J^{\mathbf{z}} \rangle \to N/2$ and $\langle (J^{\mathbf{y}})^2 \rangle \sim N^{2/3}$, and thus $W_{\min} = -1/4 + aN^{-1/3}$ from Eq. (6.5). As LSW theory predicts that for any $\alpha < 1$, the model is equivalent to the $\alpha = 0$ limit, it is natural to expect that a similar scaling law holds up to $\alpha = 1$. For $\alpha > 1$, there is no reason to expect the same exponent. However, for $\alpha \leq 2.2$, probably becaus of strong finite-size effects in numerical simulations, we could not observe deviations from the $\alpha = 0$ behavior and therefore we used the same fit.

On Fig. 6.1(a), we plot the maximal violation of the BI [Eq. (6.2)], as a function of the transverse-field h and of α. For values of $\alpha \lesssim 3$, nonlocal correlations are detected in the vicinity of the QCP, with maximal violation for $\alpha \to 0$. For $\alpha \gtrsim 3$, no violation is detected, consistently with the quasi-absence of spin squeezing at the nearest-neighbour QCP [LMW13; FR18]. Fig. 6.1(b) shows von Neumann half-chain EE. Regardless of α, for $N \to \infty$, EE is maximal at the QCP. The quantum-critical origin of the BI violation is demonstrated on Fig. 6.1(b), as

maximal EE and maximal violation of Eq. (6.2) occur for the same transverse-field in the thermodynamic limit. On Fig. 6.2, we plot, varying the power-law exponent α and system size N, the maximal violation of Eq. (6.2) obtained at the finite-size precursor $h_c(\alpha, N)$ of the QCP (defined as the value of h for which $W_{\min}$ is minimal). For $\alpha < d$ and $N \to \infty$, LSW theory (detailed below) predicts that $W_{\min} \to -1/4$. Due to strong finite-size effects, our extrapolation for $N \leq 170$ does not exactly match this prediction (see inset of Fig. 6.2). However, increasing α, we clearly see a weakening violation of Eq. (6.2), up to $\alpha \gtrsim 3$ where no violation is detected any more.

As show in [Tur+19], observing a violation exceeding the value of $\beta(k)$ given in Eq. (2.49), certifies an entanglement depth of at least $k+1$ [1]. Such bounds are indicated on Fig. 6.1(a, inset). In particular, a violation $W_{\min} \to -1/4$, as observed at the critical point for $\alpha < 1$, certifies a diverging entanglement depth [Tur+19]. Such bounds are indicated on Fig. 6.1(a, inset). In particular, a violation $W_{\min} \to -1/4$, as observed at the critical point for $\alpha < 1$, certifies a diverging entanglement depth [Alo+19], *genuine multipartite entanglement*.

6.5 Linear spin-wave theory

Linear spin-wave (**LSW**) theory is expected to give an accurate semi-classical description of the many-body state. Indeed, as FM long-range interactions harden quantum fluctuations about the mean-field ground state, it is especially accurate for small values of α. In fact, it will be shown that LSW theory even becomes exact in the thermodynamic limit for $\alpha < d$. In the following, we choose FM order along $+\mathbf{x}$. After a **Holstein-Primakoff** (**HP**) mapping of the spin operators to bosonic modes [2], we obtain the LSW Hamiltonian:

$$\mathcal{H}_{\mathrm{LSW}} = \frac{\max(1,h)}{2} \sum_{\mathbf{k}} (\hat{P}_{\mathbf{k}} \hat{P}_{-\mathbf{k}} + \omega_{\mathbf{k}}^2 \hat{X}_{\mathbf{k}} \hat{X}_{-\mathbf{k}}) \,, \tag{6.7}$$

which is valid up to second order in HP operators. We introduced $\omega_{\mathbf{k}} = \sqrt{1 - \frac{\gamma_{\mathbf{k}}}{h\gamma_{\mathbf{0}}}}$ in the PM phase, and $\omega_{\mathbf{k}} = \sqrt{1 - \frac{h^2\gamma_{\mathbf{k}}}{\gamma_{\mathbf{0}}}}$ in the FM phase. In terms of the HP bosonic operators $b_{\mathbf{k}}^{(\dagger)}$ at wave-vector $\mathbf{k}$, $\hat{X}_{\mathbf{k}}$ and $\hat{P}_{\mathbf{k}}$ are defined as

$$\hat{X}_{\mathbf{k}} = \frac{b_{\mathbf{k}} + b_{-\mathbf{k}}^\dagger}{\sqrt{2}} \;\; ; \;\; \hat{P}_{\mathbf{k}} = \frac{b_{-\mathbf{k}} - b_{\mathbf{k}}^\dagger}{i\sqrt{2}} \,, \tag{6.8}$$

[1] See Sec. 2.1.2: a state ρ is k-producible if it is a mixture of tensor products of states involving at most k spins [Tót12; Hyl+12]. The entanglement depth is the minimal value of k such that ρ is k-producible.

[2] The HP mapping takes the form: $S_j^z = (\cos\theta)(1/2 - b_j^\dagger b_j) - (\sin\theta)(b_j + b_j^\dagger)/2$; $S_j^x = (\sin\theta)(1/2 - b_j^\dagger b_j) + (\cos\theta)(b_j + b_j^\dagger)/2$; $S_j^y = (b_j - b_j^\dagger)/(2i)$, where all expressions are valid up to order $O(b_j^3)$. b_j are bosonic operators which, in Fourier space, read: $b_{\mathbf{k}} = N^{-1/2} \sum_j \exp(-i\mathbf{k}\cdot\mathbf{r}_j) b_j$.

such that $[\hat{X}_{\mathbf{k}}, \hat{P}_{\mathbf{k}'}] = i\delta_{\mathbf{k},\mathbf{k}'}$, and $[\hat{X}_{\mathbf{k}}, \hat{X}_{\mathbf{k}'}] = [\hat{P}_{\mathbf{k}}, \hat{P}_{\mathbf{k}'}] = 0$. The LSW Hamiltonian of Eq. (6.7) is diagonalized by the Bogoliubov rotation $\beta_{\mathbf{k}} = \hat{X}_{\mathbf{k}}\sqrt{\omega_{\mathbf{k}}/2} + i\hat{P}_{-\mathbf{k}}/\sqrt{2\omega_{\mathbf{k}}}$, such that $\mathcal{H}_{\rm LSW} = \max(1,h)\sum_{\mathbf{k}}\omega_{\mathbf{k}}(\beta^{\dagger}_{\mathbf{k}}\beta_{\mathbf{k}} + 1/2)$. Written in the form of Eq. (6.7), the physical meaning of the LSW mapping is especially transparent.

Indeed, the two quadratures $\hat{P}_{\mathbf{k}}$ and $\hat{X}_{\mathbf{k}}$ represent fluctuations of the collective spin in the two directions transverse to the mean spin orientation, namely (in the LSW approximation): $\hat{P}_{\mathbf{k}} = J^{\mathbf{y}}_{\mathbf{k}}/\sqrt{N/2}$ and $\hat{X}_{\mathbf{k}} = J^{\tilde{\mathbf{x}}}_{-\mathbf{k}}/\sqrt{N/2}$, with $\tilde{\mathbf{x}} = \mathbf{x}\cos\theta - \mathbf{z}\sin\theta$ and $J^{\mathbf{u}}_{\mathbf{k}} = \sum_j \exp(i\mathbf{k}\cdot\mathbf{r}_j)(\mathbf{u}\cdot\vec{S}_j)$. Within LSW theory, their fluctuations are simply harmonic, and the sectors corresponding to different wave-vectors $\mathbf{k}$ are decoupled from each other. Finally, Eq. (6.7) allows one to directly read the eigen-frequencies of the collective spin fluctuations, namely $E_{\mathbf{k}} = \max(1,h)\omega_{\mathbf{k}}$. Approching the critical point at $h = 1$, $\omega_{\mathbf{k}=\mathbf{0}}$ becomes gapless, implying a divergence of the fluctuations of the $\hat{X}_{\mathbf{0}}$ quadrature (and, correspondingly, squeezing of the $\hat{P}_{\mathbf{0}}$ quadrature). In terms of the collective spin degrees of freedom ($\vec{J} = \sum_i \vec{S}_i \equiv \vec{J}_{\mathbf{k}=\mathbf{0}}$), one indeed finds

$$\langle (J^{\tilde{\mathbf{x}}})^2\rangle = \frac{N}{4\omega_{\mathbf{0}}} \;\; ; \;\; \langle (J^{\mathbf{y}})^2\rangle = \frac{N\omega_{\mathbf{0}}}{4} \; . \tag{6.9}$$

The divergence of the fluctuations of the order parameter (here, $J^{\mathbf{x}} = J^{\tilde{\mathbf{x}}}\cos\theta$) is a generic signature of a critical phase transition (quantum or thermal). The squeezing of fluctuations transverse to the order parameter (namely of $J^{\mathbf{y}}$), on the other hand, is a *genuine signature of quantum criticality* which has no classical analog [FR18]. In the present case, it signals the presence of genuine multipartite entanglement at the QCP [PS09; FR18; GSP18], which translates into a maximal violation of the multipartite Bell inequality Eq. (6.2). LSW predicts a perfect squeezing of $J^{\mathbf{y}}$ fluctuations at the QCP ($\zeta_{\mathbf{y}} = \omega_{\mathbf{0}} = 0$), so that from Eq. (6.5), the minimal value of W is simply

$$W_{\rm min} = -\frac{(1-r)^2}{4} \;\; \text{[at the QCP]} \; . \tag{6.10}$$

At the LSW level of approximation, the Bell-inequality violation at the QCP has thus a very transparent interpretation, involving solely the reduction of the mean spin length by quantum fluctuations.

Predictions from LSW theory are reliable as long as the mean spin length,

$$1 - r = (2/N)\langle J^{\tilde{\mathbf{z}}}\rangle = 1 - (2/N)\sum_{\mathbf{k}}\langle b^{\dagger}_{\mathbf{k}} b_{\mathbf{k}}\rangle \; , \tag{6.11}$$

is moderately reduced by the occupation of HP bosonic modes, namely $r \ll 1$. We find that $r = (2N)^{-1}\sum_{\mathbf{k}}(1-\omega_{\mathbf{k}})^2/\omega_{\mathbf{k}}$. For $\alpha < d$, $\gamma_{\mathbf{k}\neq\mathbf{0}}/\gamma_{\mathbf{0}} \to 0$ for $N \to \infty$ [FNR17], so that $\omega_{\mathbf{k}\neq\mathbf{0}} \to 1$, and $r \sim (2N)^{-1}(1-\omega_{\mathbf{0}})^2/\omega_{\mathbf{0}}$. In other words, all quantum fluctuations apart from those of the collective spin are effectively

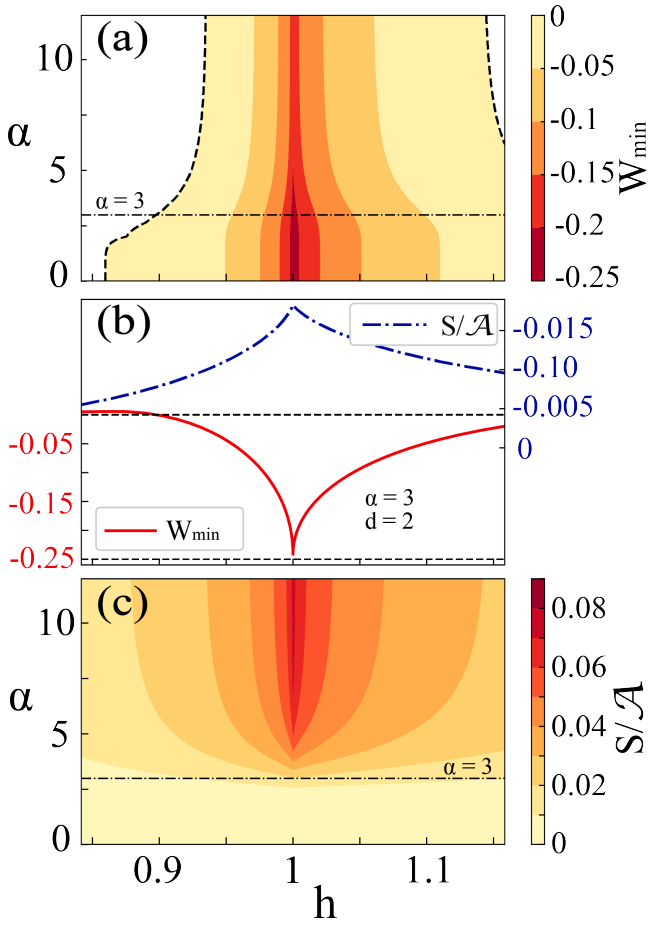

FIGURE 6.3: BI violation (a) and bipartite EE (c) for the $d = 2$ long-range TFIM calculated from LSW. (b) Cut across the line $\alpha = 3$ of the phase diagrams [dashed-dotted line on panels (a) and (c)]. Dashed lines: classical ($W_{\min} \geq 0$) and quantum ($W_{\min} \geq -1/4$) bounds of the PIBI. EE is computed for half a torus of size $L_x = 200$ times $L_y = 100$, and rescaled to the boundary area ($\mathcal{A} = 2L_y$).

frozen out. For any $h \neq 1$, we find that $r \to 0$: LSW theory is asymptotically exact at any finite detuning from the QCP. The situation is different for $\alpha > d$. On the one hand, away from the QCP, $\omega_{\mathbf{k}}$ is gapped, so that r is always finite. The only possible instance of (infrared) divergence for r is then at the QCP, where $\omega_{\mathbf{k}} \sim k^z$ with a dynamical exponent $z = \min[1, (\alpha - d)/2]$ [FNR17]. The condition for infrared divergence of r is then equivalent to the divergence of $\int dk k^{d-1}/k^z$ at low k, *i.e.* to the condition $z \geq d$. This condition is only met for $\alpha \geq 3$ ($z = 1$) in $d = 1$, where the divergence is logarithmic. Otherwise, r converges for $N \to \infty$ to a finite value, which must satisfy $r \ll 1$ for LSW theory to be reliable [3].

Remarkably, for $\alpha < d$, $W_{\min} \to -1/4$ in the thermodynamic limit, corresponding to the maximal possible violation of the considered BI [Tur+14]. This property is illustrated on Fig. 6.2 in $d = 1$, and on Fig. 6.3(a) in $d = 2$, where $W_{\min}$ is plotted across the phase diagram. It may seem surprising that the limit of infinite-range interactions, leading to a complete suppression of quantum fluctuations at $\mathbf{k} \neq 0$ in the ground state, is identified as maximally nonlocal. Indeed, in contrast, as shown on Fig. 6.3(c), in $d > 2$ bipartite EE is strongly suppressed for $\alpha \to 0$, obeying at most a $\log(N)$ scaling for $\alpha < d$ [Lat+05] instead of a L^{d-1} (area-law) scaling. This feature should be understood as a specificity of the (permutationally invariant) BI we have considered, rather than an intrinsic property of the many-body state. In general, for all α, we always find maximal violation of the PIBI at criticality, where bipartite EE is also maximal [Fig. 6.3(b)], demonstrating the quantum-critical origin of the correlations leading to nonlocality detection. Finally, we notice that for $d = 2$, in contrast to $d = 1$, nonlocal correlations are detected at the QCP for any value of α. This observation is consistent with the presence of spin-squeezing for nearest-neighbour interactions in $d = 2$ [FR18].

6.6 Summary

We investigated the violation of a permutationally invariant Bell inequality (PIBI, Eq. (6.2)) induced by a quantum critical point (QCP). We identified spin squeezing – in a general sense – as a necessary ingredient to violate the PIBI when identical measurements are performed on a collection of qubits. Focusing on the ground state of the ferromagnetic TFIM, we showed that power-law decaying interactions favor the development of spin squeezing at the QCP, leading to a maximal violation of the PIBI in the limit of infinite-range interactions. Our results are relevant to various experimental platforms implementing the quantum Ising model with power-law interactions, like trapped ions [Zha+17], Rydberg

[3] For $d = 3$, the maximal value for r is $r \approx 0.045$ for nearest-neighbour interactions at the QCP; for $d = 2$, we find $r \lesssim 0.122$. LSW theory is thus reliable all over the phase diagram for $d = 2, 3$. In $d = 1$, we find $r \approx 0.1$ for $\alpha \approx 2$ at the QCP, but already $r \approx 0.3$ for $\alpha = 2.4$, indicating a strong effect of quantum fluctuations for larger values of α. We thus complement our LSW approach by DMRG calculations in $d = 1$.

atoms [Ber+17] and nano-photonic structures [Cha+18] (the last only recently proposed, but not yet implemented). In particular, BI violation is expected to be robust against thermal noise [FR18; GSP18] and particle losses [Tur+14].

7 Tensor networks in higher dimensions

So far in this dissertation, we considered systems in one dimension ($1D$), as in the case of the long-range Ising chain in Chap. 6 or in quasi-$1D$, the Creutz-Hubbard ladder treated in Chap. 5. The quantum kicked top studied in Chap. 4 is instead invariant under permutation of any particle and because of that in treatable as a point-like adimensional system and its dynamical evolution is easily numerically followed with exact diagonalization routines. In Chap. 6 and Chap. 5 the density matrix renormalization group (DMRG) introduced in Sec. 3.3 was extensively used, as the most powerful algorithm to calculate the ground states of gapped $1D$ systems. In higher dimensions, an equally efficient algorithm is still missing. In this chapter, still in the framework of the tensor networks (TNs) [Chap. 3], we propose a few-body model algorithm that can be efficiently solved by classical simulations, to accurately capture the ground-state properties of the infinite many-body system in higher dimensions.

We start reviewing the state of the art of existing numerical algorithms used to simulate high dimensional quantum many-body systems. Our TN-based algorithm follows the tradition of those methods which map the full-body problem in few-body one where the rest of the system is approximated as a "bath" or "environment" (famous examples are the mean-field theory and the dynamical mean-field theory). The algorithm we propose is in fact a high-dimension extension of the "ab-initio optimization principle" introduced in [Ran16] and in detail reported in Sec. 7.2. In Sec. 7.3 we derive the algorithm for two- and three-dimensions. We benchmark it in Sec. 7.4: the $2D$ case is tested by calculating the ground-state energy of the Heisenberg model on honeycomb lattice; then we apply our approach to the $3D$ simple cubic lattice, where the ground-state properties of Heisenberg anti-ferromagnet and the quantum phase transition of transverse Ising model are investigated. In Sec. 7.5 possible connections with experiments are discussed. In Sec. 7.6 we summarize the results of the chapter.

7.1 Numerical algorithms for high dimensional quantum many-body problems

7.1.1 Quantum many-body systems in one, two and three dimensions

Technically, one-dimensional models are the simplest to solve, even for strong interactions among their components, although quantum fluctuations in $1D$ are particularly large [Gia03]. The $1D$ systems play important roles in *electronics and spintronics*, as they provide specific possibilities in controlling transport and reveal exotic excitations such as *Majorana fermions* [NP+10; Suo+17]. They can be naturally viewed as the edges of two-dimensional ($2D$) systems, which may appear as edge states [Wen04; QZ11]. $2D$ systems are obviously more demanding, whereas from a physical point of view they can be taken as playgrounds for novel concepts and exotic states such as *anyonic excitations* [Wen04; Yos13], *frustrated antiferromagnetism* [ML05; Sac11], *spin liquids* [SB16], *topological order and topological phase transitions*, and *graphene-like systems* [Net+09], etc.

In principle, the three-dimensional ($3D$) models are even more interesting, as they are much closer to reality of our daily things. Because of their extreme complexity, the adoption of various approximations to treat them is totally unavoidable. The three dimension is closer to the upper critical dimension, and one may expect that the mean-field theories would work well for them. A paradigmatic example is the *Bose-Hubbard model*, which can be nicely explored by bosonic *dynamic mean-field theory* (DMFT) [And+10]. Such few, but well-controlled systems can serve as validation, calibration and benchmark for various numerical and analytical methods. Still, there are also $3D$ models that are extremely demanding to be understood, such as, among others, the *spin ice* [NMS13] with *pyrochlore lattice* [GM14], that is a highly frustrated magnet; the *Fermi-Hubbard model*, which is usually invoked to describe *high temperature superconductivity* of cuprates that consist of strongly correlated $2D$ planes weakly coupled in the transverse direction ([Lee07], see also [Imr+14] for a quantum simulation with ultracold atoms). The $(3+1)D$ *lattice gauge theories* at high densities and temperature are also beyond the possibilities of the existing codes and machines. Generally, different approximate analytical methods might generate converse results, leading to unnecessary controversies in many cases. It turns out that finding reliable and efficient numerical methods to solve $3D$ quantum many-body problems is very desirable.

7.1.2 Tensor networks: state of the art

The DMRG [Whi92] is widely recognized as a major breakthrough in the calculations of the ground states in $1D$ systems and it has been extensively used in Chap. 5 and Chap 6. Originally proposed as a mere numerical tool, the reformulation of the DMRG as a variational algorithm in terms of matrix product

states (MPS) [Sch11] leads to the proposal of the more general formalism of tensor networks (TNs) [CV09; Orú14; VMC08; Ran+19] introduced it Chap. 3. TNs provide a very general ansatz for the wave functions and they have rapidly evolved into a promising powerful tool to study large or even infinite size systems in two dimensions. In contrast to *quantum Monte Carlo* (QMC), TNs do not suffer from the notorious "negative-sign" problem [TW05; Whi+89] and allow for a direct access to frustrated spin systems and fermionic models away from half-filling.

We introduced the basis of the TN formalism in Chap. 3, where we underlined that to what extent the TN is feasible depends on the amount of entanglement of the states to be simulated. The efficiency (computational memory and time) of the TN approaches is also determined by the capability of the current computers. In the standard formulations, TN works quite well for low-entangled states since they, by construction, satisfy an area law for the entanglement entropy [Sec. 2.2]. This fact explains the efficiency of the MPS-based algorithms in $1D$. For the same reason, the MPS-based algorithms (*e.g.* DMRG) work well for small $2D$ systems, but are strongly limited when the size grows [WS98; SW12; VMC08]. By acknowledging this, many different competing approaches have been developed. Among others, a purely $2D$ ground-state TN ansatz, the projected entangled pair state (PEPS), was proposed as a natural extension of MPS. PEPS fulfils the $2D$ area law of entanglement entropy [VMC08; CV09; Orú14; Ver+06], while the multiscale entanglement renormalization ansatz (MERA) [Vid07b] bears particular advantages for studying critical models.

Within the existing TN algorithms, a lot of works were done on $2D$ quantum as well as $3D$ classical models, where the simulations consist in the contractions of $3D$ TNs [Vid07a; Vid07b; VC04a; Jor+08; JWX08; LN07; GLW08; Xie+09; Xie+12; YGW17; NO96; OV09; Orú12; Nis+00; Cor16; Van+16; Phi+15; GSL13]. This well-known quantum-classical equivalence [Suz76] becomes very explicit in the TN terminology, and is utilized frequently in the TN approaches for ground-state [Vid07a; VC04a; Jor+08; JWX08] and thermodynamic [BXG96; Li+11; Ran+12; Ran+13; CCD12] studies on discrete and even continuous [VC10] systems. However, for $3D$ ground-state simulations, we are essentially facing the contractions of four-dimensional TNs [Ten17; BOWR15], which are hardly treatable even with small bond dimensions. Therefore, developing efficient $3D$ quantum algorithms is strongly desired, in particular for infinite quantum systems.

7.1.3 "Bath-stimulated" methods

For $3D$ quantum models, many interesting issues remain to be explored or even unsolved to a large extent [Bal10; GBH94; NMS13; MR06; Ram94]. They have been the subject of intensive studies in recent years and many numerical methods were developed to handle them. Several approaches were proposed beyond

the standard mean-field and renormalization group methods, such as the *linked cluster expansions* [OHZ06; Jos+15; Coe+16], and the functional renormalization group method [Met+12; Iqb+16]. On the other hand, the numerical simulations are extremely challenging and the finite-size algorithms, including exact diagonalization (ED) and DMRG, suffer severe finite-size effects, therefore they are quite consuming for large systems and can access infinite systems only by utilizing finite-size scaling. A separate discussion should be reserved for QMC. This is indeed a finite-size algorithm but, whenever applicable (namely for bosons or for fermions but only if the negative-sign problem is cured), the finite-size effects are strongly reduced thanks to the huge number of sites/particles one can reach in the simulations (of the order of thousands or hundreds of thousands).

To treat the correlations in many body systems, one usually starts by evoking the ideas of *"mean-field"*, *"bath"* or *boundary conditions*. Analytical methods such as the *Hartree-Fock mean-field theory* and the *saddle point approximation* in path integral are commonly used. In fact, for lattice models the mean-field idea goes back to the *single-site Weiss method*, applied first for classical magnetic models [Wei07]. Contemporary mean-field methods for lattice models include *Guztwiller ansatz* for bosons and/or fermions, or *pairing approaches* (Bogoliubov-like for bosons, or Bardeen-Cooper-Schrieffer-like for fermions) — for an overview of these and other methods see Ref. [LSA12] and references therein. In the context of the present work it is important to mention the *"cluster mean-field theory"* (CMFT), where the mean field à la Weiss is combined with exact diagonalization on clusters (for recent developments see [Yam09; RTX14] and references therein). It is also worth mentioning the *"entanglement mean-field theory"* (EMFT) [DS12a; DS12b], which for spin models is formulated on few spin clusters, demanding self-consistency of entanglement properties. Both CMFT and EMFT are close to the standard MFT that can give quite accurate description of standard Landau-Ginsburg ordered and disordered phases, but typically only far from criticality.

For thermal and open systems, one popular way is to introduce a *"heat bath"* to mimic the interactions between the system and the environment [Zur82]. Regarding numerical approaches, the *density functional theory* (DFT), also known as *ab-initio* first-principle calculations [She10], was built by extending the Thomas-Fermi approximation of homogeneous electron gas to the inhomogeneous electron system [Tho27]. Its huge success in condensed matter physics, quantum chemistry, and materials science largely relies on the simplicity and unification, *"using a popular code, a standard basis, and a standard functional approximation"* [She10].

In order to handle strong correlations, several schemes were developed in the spirit of DFT. The examples include the *dynamical mean-field theory* [MV89; GK92; Geo+96] that maps a lattice model (such as the Hubbard model) onto a quantum impurity model subject to self-consistent conditions, and the *density-matrix embedding theory* (DMET) [KC12] that was proposed aiming at a better consideration of the entanglement, thanks to the accompanying advances in

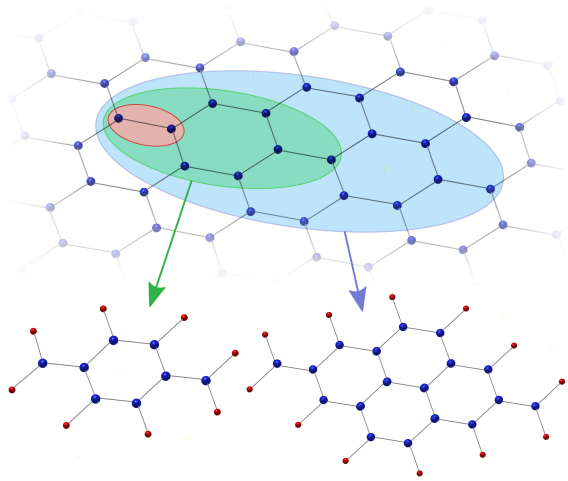

FIGURE 7.1: The system on an infinite lattice is transformed into one defined on finite clusters embedded in the entanglement bath. We take the $(8+8)$-site and $(18+12)$-site clusters for the simulations on honeycomb lattice, where the first contains 8 physical (blue balls) and 8 bath sites (red balls), and the second contains 18 physical and 12 bath sites. The entanglement bath is calculated by choosing two sites as the supercell (small circle). The legs stand for the interactions between the connecting sites.

both quantum information science [Hor+09] and condensed matter physics [Ami+08]. However, it is difficult to use these algorithms to study long-range ordered states or phase transitions. To probe the disordered ground-states (*e.g.* the spin liquids in the infinite frustrated systems), it was proposed to signal the disordered nature by simulating a finite system with random boundary conditions [YMCS17].

7.1.4 Our proposal: mimicking many-body systems by few-body ones

In general, as illustrated in Fig. 7.1, the central idea of our work is to optimally find the few-body Hamiltonian to mimic the infinite model, without any prior knowledge of the ground state. The few-body model contains the physical sites in a finite cluster and the "bath" sites around it. The few-body Hamiltonian consists of two parts: the interactions among the physical sites (blue balls) within the cluster, and those [Eq. (7.21)] between the boundary physical sites and the bath sites (red balls). The physical-bath interactions are represented by some local Hamiltonians, which reproduce the quantum entanglement between the cluster and the bath, in such a way that the many-body effects from the infinite

environment are well captured in the few-body simulations. Then the ground-state information of the infinite system is encoded in the reduced density matrix of the few-body ground state after tracing the bath degrees of freedom.

The theoretical scheme we propose is a higher-dimensional generalization of the ***ab-initio* optimization principle** (**AOP**) formulated with TN [Ran16], and originally developed for infinite $1D$ systems with translational invariance. The idea is to find the simplest eigenvalue equations that encodes the infinite TN contraction problem. For the purpose of the present work, the main advantage of the AOP is its flexibility and implications in high dimensions: without any substantial conceptual changes, the AOP can be readily extended to $2D$ and even $3D$ systems with high efficiency. Furthermore, the dynamic correlation length and the first excitation gap can be straightforwardly extracted (see Appendix D.5 for details).

Our scheme consists of **two stages**: (i) compute physical-bath Hamiltonian and (ii) solve the few-body Hamiltonian.

1. In the first stage, by choosing the dimension D of the bath site and a supercell that obeys the translational invariance, we start from the original Hamiltonian of the system and **construct a set of self-consistent eigenvalue equations**. Their solution gives the Hamiltonian $\hat{\mathcal{H}}^{\partial}$ [Eq. (7.21)] that describes the **interactions between a physical and a bath sites**. Such equations in fact encode an optimal zero-loop TN approximation of the state. This approximation directly enters the thermodynamic limit with a Bethe TN state ansatz [LCP00; NC13], and already gives us the first glance of the ground state with good accuracy especially for the gapped states [JWX08; Ran+12; Ran+13; BOWR15; LCP00; NC13].

2. The aim of the second stage is to **construct the few-body Hamiltonian** $\hat{\mathcal{H}}^{FB}$, and solve its ground state $|\tilde{\Phi}\rangle$ by *e.g.*, DMRG (with certain dimension cut-off's denoted by χ). $\hat{\mathcal{H}}^{FB}$ is formed by all the physical interactions inside a chosen cluster and several physical-bath interactions given by $\hat{\mathcal{H}}^{\partial}$. The choice of the cluster is very flexible. The ground-state properties of the infinite system is then encoded in the ground state $|\tilde{\Phi}\rangle$ of $\hat{\mathcal{H}}^{FB}$. In other words, quantities such as energy, magnetization and entanglement of the infinite ground state are obtained from the density matrix of $|\tilde{\Phi}\rangle$ by tracing all the bath degrees of freedom [Eq. (7.23)].

Our numerical results show, for instance, that the Heisenberg model on infinite honeycomb lattice is accurately simulated by a $\hat{\mathcal{H}}^{FB}$ that only contains $N_p = 18$ physical sites surrounded by $N_b = 12$ bath sites. For the $3D$ Heisenberg models on infinite simple cubic lattice, the ground-state properties including the critical behaviors near the quantum phase transition point are faithfully captured with only $N_p = 8$ physical and $N_b = 24$ bath sites. The discrepancy (such as energy) compared with the state-of-the-art TN algorithm is around $\mathcal{O}(10^{-3})$.

The algorithm built from our scheme possesses several advantages (see Appendix D.6). It can directly reach the thermodynamic limit by means of the

physical-bath interactions on the boundary, hence it has no conventional finite-size effects compared with the finite algorithms such as ED and DMRG. The strongly-correlated effects of the infinite models are accurately considered, and the many-body features, *e.g.*, entanglement and criticality, can be efficiently captured, thus our scheme goes beyond the mean-field-based methods such as DFT [She10] and DMFT [MV89; GK92; Geo+96]. Comparing with DMFT where the original model is approximated by an impurity model in a bath, we approximate the infinite-size system into a few-body model that contains its original interactions and the emergent physical-bath interactions. The accuracy is enhanced by fully considering all interactions in the cluster, thus outperforms the Bethe TN-based algorithms [JWX08; Ran+12; Ran+13; BOWR15; LCP00; NC13]. In higher dimensions, the computational cost of our scheme is much lower than, *e.g.*, the TN renormalization group algorithms [LN07; Vid07b; VC04a; VC04a; NO96; OV09; Orú12; Nis+00]. It has no sign problem [Whi+89] thus can be used to simulate frustrated and fermionic systems.

The construction of $\hat{\mathcal{H}}^{FB}$ makes it possible to investigate the many-body effects in experiments by designing the few-body models — quantum simulators described by the predicted Hamiltonians. The many-body behaviors are expected to be observed in the bulk of the few-body model. The feasibility of realizing $\hat{\mathcal{H}}^{FB}$ in cold atom experiments is supported by several facts observed in our numerical simulations: the few-body Hamiltonian has the same interaction length as the original Hamiltonian; with a proper tolerance of error, say $\mathcal{O}(10^{-2})$, the size of the few-body model can be very small. Especially for spin-$1/2$ models on simple cubic lattice, we show that it is sufficient to use only the spin-$1/2$'s as the bath sites. The few-body Hamiltonian then is just a small spin-$1/2$ system that includes some special interactions (given by $\hat{\mathcal{H}}^{\partial}$) on the boundary.

7.2 *Ab-initio* optimization principle approach in one dimension

Understanding the $1D$ AOP [Ran16; Tir+18a] will be a lot of help to understand the higher-dimensional version. The idea of AOP scheme [Ran16] is, without any previous knowledge of the ground state, to transfer the infinite system to a finite one embedded in an entanglement bath. In the language of TN, the idea is to encode the contraction of an infinite TN in a simplest-possible local function that can be exactly computed, with smallest-possible number of inputs. Let us take the following translationally invariant Hamiltonian as an example, which reads

$$\hat{H} = \sum_{n} \hat{H}_{n,n+1}, \tag{7.1}$$

with $\hat{H}_{n,n+1}$ the two-body interaction.

Stage One: calculate the entanglement bath. The first stage is to calculate the entanglement bath represented by a set of tensors dubbed as **boundary tensors**. They are obtained by solving a set of self-consistent eigenvalue equations [see Eqs. (7.4)-(7.6) below]. These equations are parametrized by the Hamiltonian as well as by the boundary tensors themselves, thus they can be solved in an alternative way: starting from an arbitrary guess, we update one boundary tensor by fixing all others as the parameters of the equations, and iterate such a procedure for every tensor until the fixed point is reached. Given the Hamiltonian, the next step is to prepare the **cell tensor** that parameterize the self-consistent equation. One firstly chooses a **supercell** that obeys the translational invariance, *e.g.* two adjacent sites. The bulk interaction is simply the coupling between these two spins, *i.e.* $\hat{H}^B(i,j) = \hat{H}(i,j)$. Then we define the **two-body operator** $\hat{F}^\partial(i,j) = I - \tau\hat{H}(i,j)$ (this shift does not change the ground state) as the shifted interaction on the boundary of the supercell and do the singular value decomposition as

$$\hat{F}^\partial(i,j) = \sum_a \hat{F}^L(i)_a \otimes \hat{F}^R(j)_a. \tag{7.2}$$

$\hat{F}^L(i)_a$ and $\hat{F}^R(j)_a$ are two sets of one-body operators (labeled by a) acting on the left and right spins of $\hat{F}^\partial(i,j)$, respectively. We dub a as the *boundary index*.

The **cell tensor** is defined as the product of the (shifted) bulk Hamiltonian with $\hat{F}^L_a$ and $\hat{F}^R_a$ as

$$\hat{\mathcal{F}}(i,j)_{a_1a_2} = \hat{F}^R(i)_{a_1}\tilde{H}^B(i,j)\hat{F}^L(j)_{a_2}, \tag{7.3}$$

with $\tilde{H}^B(i,j) = I - \tau\hat{H}^B(i,j)$.

Then, with two boundary tensors $|V^{[x]}\rangle$ (guessed or previously obtained in the last iteration) and the cell tensor $\hat{\mathcal{F}}(i,j)$, we define three **eigenvalue equations** [Fig. 7.2] as

$$\hat{\mathcal{H}}(i,j)_{\substack{\mu_1'\mu_2\\ \mu_1\mu_2}} = \sum_{a_1a_2} (V^{[1]}|_{a_1\mu_1\mu_1'}\hat{\mathcal{F}}(i,j)_{a_1a_2}|V^{[2]})_{a_2\mu_2\mu_2'}, \tag{7.4}$$

$$M^{[1]}_{\substack{a_1\mu_1\mu_1'\\ a_2\mu_2\mu_2'}} = \langle\tilde{A}^{[1]}(i,j)|_{\mu_1'\mu_2'}\hat{\mathcal{F}}(i,j)_{a_1a_2}|\tilde{A}^{[1]}(i,j)\rangle_{\mu_1\mu_2}, \tag{7.5}$$

$$M^{[2]}_{\substack{a_1\mu_1\mu_1'\\ a_2\mu_2\mu_2'}} = \langle\tilde{A}^{[2]}(i,j)|_{\mu_1'\mu_2'}\hat{\mathcal{F}}(i,j)_{a_1a_2}|\tilde{A}^{[2]}(i,j)\rangle_{\mu_1\mu_2}. \tag{7.6}$$

By solving the leading eigenvector of $\hat{\mathcal{H}}(i,j)$ given by Eq. (7.4), we obtain the **central tensor** $|A(i,j)\rangle_{\mu_1\mu_2\mu_3\mu_4}$. The central tensor can be considered as a state in the Hilbert space of the supercell labeled by two virtual indexes. Meanwhile, $|V^{[x]}\rangle$ is obtained as the (left) leading eigenvector of $M^{[x]}$ [Eqs. (7.5) and (7.6)]. $M^{[x]}$ is defined by the isometries $|\tilde{A}^{[x]}(i,j)\rangle$ that is obtained by the QR

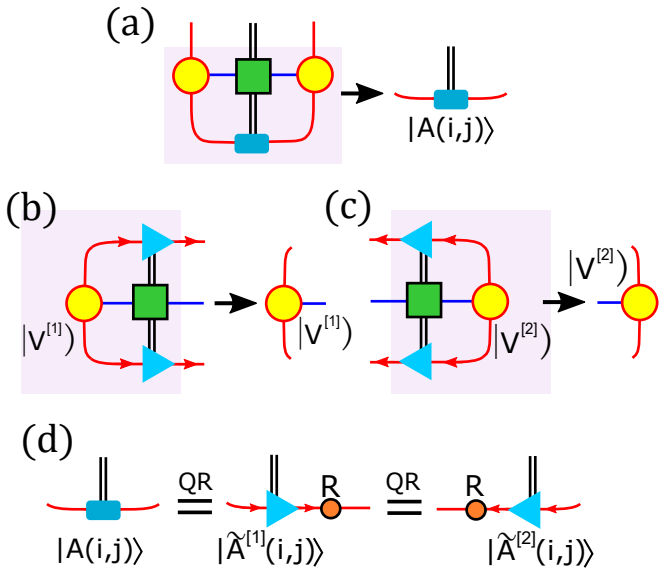

FIGURE 7.2: The illustration of the self-consistent eigenvalue equations [Eqs (7.4)-(7.5)] of $1D$ AOP approach.

decomposition of $|A(i,j)\rangle$. For example for $x=1$, we have

$$|A(i,j)\rangle_{\mu_1\mu_2} = \sum_{\nu} |\tilde{A}^{[1]}(i,j)\rangle_{\nu\mu_2} R^{[1]}_{\nu\mu_1}. \tag{7.7}$$

$|\tilde{A}^{[1]}(i,j)\rangle$ is orthogonal, satisfying

$$\sum_{\mu_2} \langle \tilde{A}^{[1]}(i,j)|_{\mu_1\mu_2} \tilde{A}^{[1]}(i,j)\rangle_{\mu_1'\mu_2} = I_{\mu_1\mu_1'}. \tag{7.8}$$

These isometries play the role of the renormalization group flow in the standard DMRG [Whi92]. Similarly, $|V^{[x]})_{a_x\mu_x\mu_x'}$ can be understood as a "state" defined in the space of the boundary index a_x labeled by μ_x and μ_x' [1]. One can see that these equations are parametrized by the solutions of others, and can be solved in an alternative way in practice.

In the language of TN, Eqs. (7.4)-(7.6) encode an infinite TN that represents the *imaginary time evolution for the ground state* [Fig. 7.3]. Defining the local scalar function shown in the top of Fig. 7.3 it is easy to see that this function is maximized at the *fixed point* of the self-consistent equations. Then, one can reconstruct an infinite MPO multiplied with an MPS and its conjugate by repetitively replacing $|V^{[x]})$ by $M^{[x]}|V^{[x]})$. Still, the scalar function is maximized, meaning

[1] To distinguish from the states in physical Hilbert space $|*\rangle$, the symbol $|*)$ is used to denote a state in the space of boundary indexes $\{a\}$.

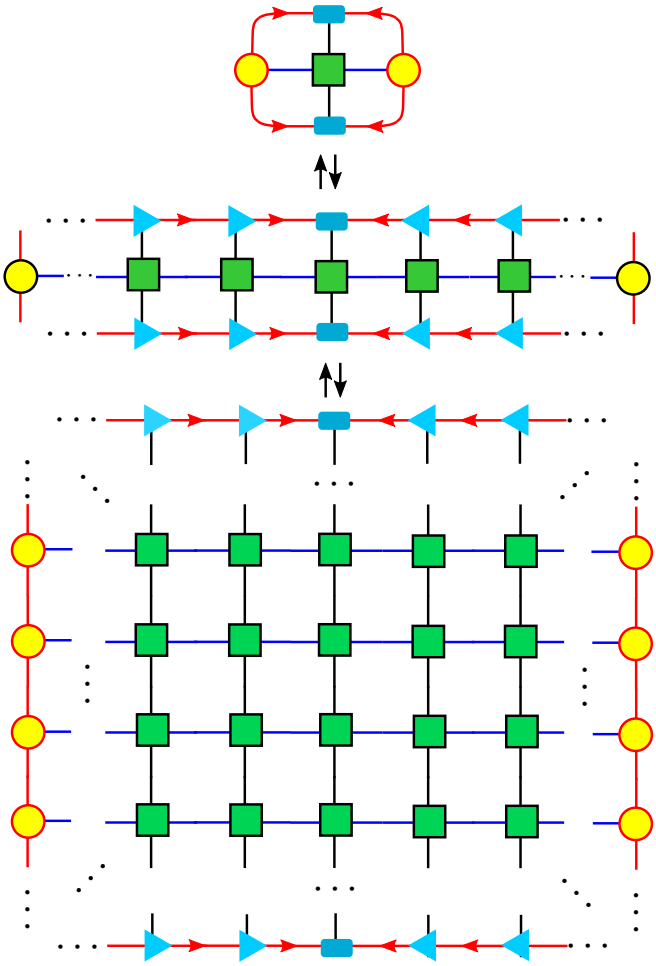

FIGURE 7.3: The illustration of the encoding scheme for a $2D$ TN. The infinite TN represents the imaginary time evolution of the ground state.

the MPS is the dominant eigenstate of the MPO. One can again iteratively replace one MPS by the product of the MPS and the MPO to reconstruct the whole infinite TN. Note such a reconstruction can be understood in an opposite order: by going from the bottom to the top of Fig. 7.3, it actually gives a contraction scheme of the TN [2].

There are two important constraints to realize such a reconstruction. In the step from the local scalar function to MPO, we have $(V^{[x]}|V^{[x]}) = 1$ since it should be the eigenstate of $M^{[x]}$. In the second step from the MPO to the whole TN, we require that the MPS is normalized, which is actually a non-local constraint. In the original proposal of the $1D$ AOP [Ran16], this constraint is turned to be local with some tricks under the assumption that all eigenvalue problems are Hermitian. In the generalized $1D$ version [Tir+18a] presented above, the MPS is normalized because of the orthogonality of $|\tilde{A}^{[x]}(i,j)\rangle\rangle$.

Stage two: construct the few-body Hamiltonian and solve it. Now we explain the **few-body Hamiltonian** that mimics the ground state of the infinite $1D$ chain. By reviewing Eq. (7.3), the matrix [Eq. (7.4)] whose eigenstate gives $|A(i,j)\rangle\rangle_{\mu_1\mu_2}$ can be written as the product of three parts: one bulk term and two boundary terms. The bulk term contains simply the physical interactions of the original model. The **boundary parts** are defined as

$$\hat{\mathcal{H}}^{\partial}(n,x)_{\mu_x\mu'_x} = \sum_{a_x} \hat{F}^{L(R)}(n)_{a_x} |V^{[x]}\rangle_{a_x\mu_x\mu'_x}. \tag{7.9}$$

The few-body Hamiltonian for the $1D$ simulator is obtained as

$$\hat{H}^{FB} = \sum_{\langle i,j\rangle\in cluster} \hat{H}(i,j) + \sum_{\langle x\in cluster, n\in bath\rangle} \hat{H}^{\partial}(n,x). \tag{7.10}$$

where $\hat{H}^{\partial}(n,x)$ satisfies $\hat{\mathcal{H}}^{\partial}(n,x) = I - \tau\hat{H}^{\partial}(n,x) + O(\tau^2)$.

7.3 Higher-dimensional *ab-initio* optimization principle approach

To present the approach in high dimensions, we take the $2D$ spin model with nearest-neighbor couplings on *honeycomb lattice* as an example. The implementation can be easily generalized to other models on $2D$ and $3D$ lattices.

[2] Formally these self-consistent equations have a unique fixed point, then the contraction scheme shown in 7.3 will be robust. In some cases, for example, when the TN represents the inner product of a topological iPEPS and its conjugate, a new and nontrivial degeneracy will emerge. Each equation, while seen solely, has unique dominant eigenvalue, but the equation set as a whole have more than one fixed points that are orthogonal to each other. It has been revealed that the number of the fixed points (named the ring degeneracy) can be used to detect the $\mathbf{Z}_n$ topological orders even with the noises that break the $\mathbf{Z}_n$ symmetries [Che+19].

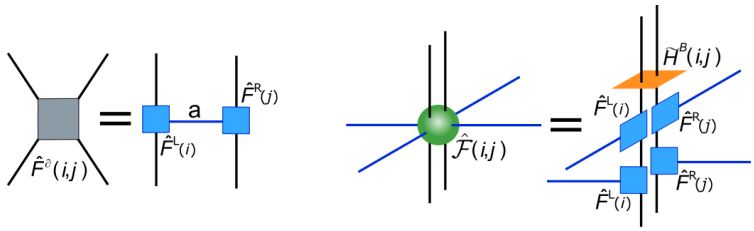

FIGURE 7.4: The left figure shows Eq. (7.11). The right one shows the construction of the cell tensor given by Eq. (7.12).

Stage One: calculate the entanglement bath. In a complete analogy to the $1D$ case, in the first stage consists in calculating the **boundary tensors** which mimic the entanglement bath. The resulting set of self-consistent eigenvalue equations is shown in Eqs. (7.13)-(7.17).

Though our method is based on the TN representation of the imaginary-time evolution with Trotter-Suzuki decomposition [SI87] like several existing methods [Vid07a; VC04a; Jor+08; NO96; OV09; Orú12], the idea here is to encode the TN in the eigenvalue equations instead of contracting the TN [3]. On the other hand, the implementation in this stage is borrowed from the generalization of DMRG on an infinite tree [LCP00; NC13], which can be easily extended to $3D$ models with high efficiency. In the DMRG language, the (convergent) boundary tensors can be understood as the infinite environment of the tree brunches.

To begin with, one chooses a **supercell** that obeys the translational invariance, *e.g.* two sites connected by a parallel bond (see the smallest shaded circle in Fig. 7.1), and construct the **cell tensor** that parametrizes the eigenvalue equations. The bulk interaction is simply the coupling between these two spins, *i.e.* $\hat{H}^B(i,j) = \hat{H}(i,j)$. For the interactions between two neighboring supercells, we define the two-body operator $\hat{F}^{\partial}(i,j) = I - \tau\hat{H}(i,j)$ and analogously to the $1D$ case [Eq. 7.2] do the singular value decomposition [Fig. 7.4] as

$$\hat{F}^{\partial}(i,j) = \sum_a \hat{F}^L(i)_a \otimes \hat{F}^R(j)_a. \tag{7.11}$$

To obtain the TN of the imaginary-time evolution, we define the cell tensor that is the product of the (shifted) bulk Hamiltonian with $\hat{F}^L_a$ and $\hat{F}^R_a$ [Fig. 7.4] as

$$\hat{\mathcal{F}}(i,j)_{a_1a_2a_3a_4} = \hat{F}^L(i)_{a_1}\hat{F}^L(i)_{a_2}\hat{F}^R(j)_{a_3}\hat{F}^R(j)_{a_4}\tilde{H}^B(i,j), \tag{7.12}$$

with $\tilde{H}^B(i,j) = I - \tau\hat{H}^B(i,j)$. Note that both $\hat{F}^{\partial}(i,j)$ and $\tilde{H}^B(i,j)$ can be different from the current choice. $\hat{F}^{\partial}(i,j)$ can be different when the model has

[3] The idea of utilizing eigenvalue equations for statistic or many-body systems has been used earlier by Baxter, Nishino, et al.. See for example [Bax78; NO95]

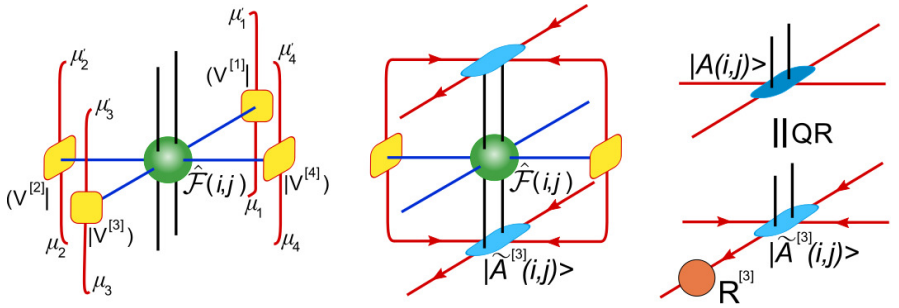

FIGURE 7.5: The graphic representations of $\hat{\mathcal{H}}(i,j)$ in Eq. (7.13) and $M^{[3]}$ in Eq. (7.16) are given in the left and middle figures, respectively. The QR decomposition [Eq. (7.18)] of the central tensor $|A(i,j)\rangle\rangle$ is shown in the right figure, where the arrows indicate the orthogonality of $|\tilde{A}^{[3]}(i,j)\rangle\rangle$ [Eq. (7.19)].

long-range interactions, and $\tilde{H}^B(i,j)$ can be different when choosing different subsystems to define the supercell. $\hat{\mathcal{F}}(i,j)$ [4] can be understood as a set of quantum operators defined in the Hilbert space of the supercell (spins i and j) labeled by the boundary indexes a_1, a_2, a_3 and a_4. Similar to $1D$ AOP [Ran16], τ is in fact the Trotter step, and $\hat{\mathcal{F}}(i,j)$ gives the TN representation of $I-\tau\hat{H}$ with an error $\mathcal{O}(\tau^2)$.

Then, with the boundary tensors $|V^{[x]})$ (guessed or previously obtained in the last iteration) and the cell tensor $\hat{\mathcal{F}}(i,j)$, we define five **eigenvalue equations** as

$$\hat{\mathcal{H}}(i,j)_{\substack{\mu_1'\mu_2'\mu_3'\mu_4'\\ \mu_1\mu_2\mu_3\mu_4}} = \sum_{\substack{a_1a_2\\ a_3a_4}} (V^{[1]}|_{a_1\mu_1\mu_1'}(V^{[2]}|_{a_2\mu_2\mu_2'}\hat{\mathcal{F}}(i,j)^{a_1a_2}_{a_3a_4}|V^{[3]})_{a_3\mu_3\mu_3'}|V^{[4]})_{a_4\mu_4\mu_4'}, \tag{7.13}$$

$$M^{[1]}_{\substack{a_1\mu_1\mu_1'\\ a_3\mu_3\mu_3'}} = \sum_{\substack{a_2a_4\mu_2\\ \mu_2'\mu_4\mu_4'}} (V^{[2]}|_{a_2\mu_2\mu_2'}\langle\tilde{A}^{[1]}(i,j)|_{\substack{\mu_1'\mu_2'\\ \mu_3'\mu_4'}}\hat{\mathcal{F}}(i,j)^{a_1a_2}_{a_3a_4}|\tilde{A}^{[1]}(i,j)\rangle\rangle^{\mu_1\mu_2}_{\mu_3\mu_4}|V^{[4]})_{a_4\mu_4\mu_4'}, \tag{7.14}$$

$$M^{[2]}_{\substack{a_2\mu_2\mu_2'\\ a_4\mu_4\mu_4'}} = \sum_{\substack{a_1a_3\mu_1\\ \mu_1'\mu_3\mu_3'}} (V^{[1]}|_{a_1\mu_1\mu_1'}\langle\tilde{A}^{[2]}(i,j)|_{\substack{\mu_1'\mu_2'\\ \mu_3'\mu_4'}}\hat{\mathcal{F}}(i,j)^{a_1a_2}_{a_3a_4}|\tilde{A}^{[2]}(i,j)\rangle\rangle^{\mu_1\mu_2}_{\mu_3\mu_4}|V^{[3]})_{a_3\mu_3\mu_3'}, \tag{7.15}$$

[4] In the following, we simplify the indexes when mentioning a tensor if it causes no confusion.

$$M^{[3]}_{\substack{a_1\mu_1\mu_1'\\ a_3\mu_3\mu_3'}} = \sum_{\substack{a_2a_4\mu_2\\ \mu_2'\mu_4\mu_4'}} (V^{[2]}|_{a_2\mu_2\mu_2'}\langle\tilde{A}^{[3]}(i,j)|_{\substack{\mu_1'\mu_2'\\ \mu_3'\mu_4'}}\hat{\mathcal{F}}(i,j)^{a_1a_2}_{a_3a_4}|\tilde{A}^{[3]}(i,j)\rangle^{\mu_1\mu_2}_{\mu_3\mu_4}|V^{[4]}\rangle_{a_4\mu_4\mu_4'}, \tag{7.16}$$

$$M^{[4]}_{\substack{a_2\mu_2\mu_2'\\ a_4\mu_4\mu_4'}} = \sum_{\substack{a_1a_3\mu_1\\ \mu_1'\mu_3\mu_3'}} (V^{[1]}|_{a_1\mu_1\mu_1'}\langle\tilde{A}^{[4]}(i,j)|_{\substack{\mu_1'\mu_2'\\ \mu_3'\mu_4'}}\hat{\mathcal{F}}(i,j)^{a_1a_2}_{a_3a_4}|\tilde{A}^{[4]}(i,j)\rangle^{\mu_1\mu_2}_{\mu_3\mu_4}|V^{[3]}\rangle_{a_3\mu_3\mu_3'}. \tag{7.17}$$

By finding the leading eigenvector of $\hat{\mathcal{H}}(i,j)$ given by Eq. (7.13), we obtain a tensor $|A(i,j)\rangle_{\mu_1\mu_2\mu_3\mu_4}$ dubbed as **central tensor** with μ_1, μ_2, μ_3 and μ_4 called **virtual indexes** according to the TN terminology. The central tensor can be considered as a state in the Hilbert space of the supercell labeled by four virtual indexes.

Meanwhile, $|V^{[x]}\rangle$ is obtained as the (left) leading eigenvector of $M^{[x]}$ [Eqs. (7.14)-(7.17)]. One can see that $M^{[x]}$ is defined by the isometries $|\tilde{A}^{[x]}(i,j)\rangle$ that is obtained by the QR decomposition of $|A(i,j)\rangle$ (referring to the x-th virtual bond μ_x) of the central tensor. For example for $x=3$, we have [Fig. 7.5]

$$|A(i,j)\rangle_{\mu_1\mu_2\mu_3\mu_4} = \sum_{\nu} |\tilde{A}^{[3]}(i,j)\rangle_{\mu_1\mu_2\nu\mu_4} R^{[3]}_{\nu\mu_3}. \tag{7.18}$$

$|\tilde{A}^{[3]}(i,j)\rangle$ is orthogonal, satisfying

$$\sum_{\mu_1\mu_2\mu_4} \langle\tilde{A}^{[3]}(i,j)|_{\mu_1\mu_2\mu_3\mu_4}|\tilde{A}^{[3]}(i,j)\rangle_{\mu_1\mu_2\mu_3'\mu_4} = I_{\mu_3\mu_3'}. \tag{7.19}$$

These isometries play the role of the renormalization group flow in the tree DMRG [LCP00; NC13]. Again, $|V^{[x]}\rangle_{a_x\mu_x\mu_x'}$ can be understood as a "state" defined in the space of the boundary index a_x labeled by μ_x and μ_x'. The graphic representations of $\hat{\mathcal{H}}(i,j)$ and $M^{[3]}$ are given in Fig. 7.5 as examples.

One can see that these equations are parametrized by the solutions of others, and can be solved in an alternative way in practice. One can start with four random $|V^{[x]}\rangle$'s and calculate $|A(i,j)\rangle$ by solving the leading eigenvector of Eq. (7.13). Then one obtains $|\tilde{A}^{[x]}(i,j)\rangle$'s using Eq. (7.18) and update the $|V^{[x]}\rangle$'s according to Eqs. (7.14)-(7.17). Repeat this process until the central tensor and all boundary tensors converge.

In fact, the ground-state properties can already be well extracted by the central tensor $|A(i,j)\rangle$. For example, the reduced **density matrix of the supercell** $\hat{\rho}(i,j) = \mathrm{Tr}_{/(i,j)}|\Psi\rangle\langle\Psi|$ (with $|\Psi\rangle$ denoting the ground state of the infinite model)

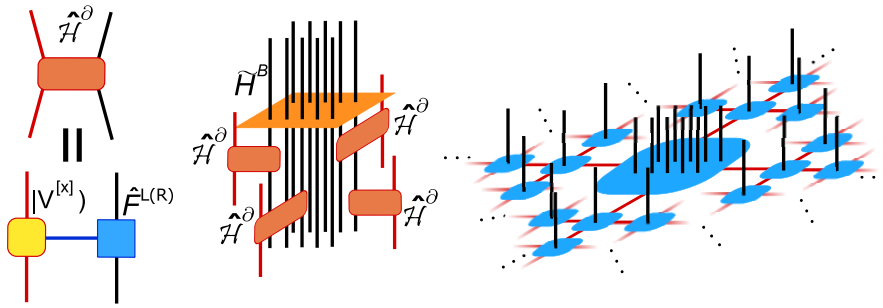

FIGURE 7.6: The left figure shows the bath Hamiltonian $\hat{\mathcal{H}}^{\partial}$ [Eq. (7.21)] that gives the interaction between the corresponding physical and bath site. The few-body Hamiltonian in Eq. (7.22) is formed by the shifted bulk Hamiltonian and $\hat{\mathcal{H}}^{\partial}$ between every physical site on the boundary and a neighboring bath site. For simplicity, the middle figure only illustrates four of the $\hat{\mathcal{H}}^{\partial}$'s. The right one shows the ground-state ansatz of AOP approach, which is the bulk state of the few-body Hamiltonian entangled with several branches of infinite tree PEPS. In fact, the number of tree branches should equal to the number of the physical sites on the boundary (*i.e.* the number of $\hat{\mathcal{H}}^{\partial}$). For conciseness, we only illustrate four of the tree branches.

is well approximated by the central tensor as

$$\hat{\rho}(i,j) \approx \sum_{\mu_1\mu_2\mu_3\mu_4} |A(i,j)\rangle_{\mu_1\mu_2\mu_3\mu_4}\langle A(i,j)|_{\mu_1\mu_2\mu_3\mu_4}. \tag{7.20}$$

Since each boundary tensor can be understood as the environment of an infinite tree branch, the original model is actually approximated at this stage by one defined on an infinite tree. Note that when only looking at the tree locally (from one site and its nearest neighbors), it looks the same to the original lattice. Thus, the loss of information is mainly long-range, *i.e.* from neglect loops. Though it has been shown numerically by many previous work that the tree approximation is very accurate especially for gapped systems [JWX08; Ran+12; Ran+13; BOWR15], we are still facing the difficulty of controlling the effects (errors) brought by such an approximation. More discussions about such a tree approximation are given in the Appendix D.1, starting from the state ansatz behind our approach. One can also find more details in the forth section of a recent review [Ran+19]. To further improve the precision in a systematic way, the next stage is to embed a much larger subsystem in the entanglement bath.

Stage two: construct the few-body Hamiltonian and solve it. The second stage is to choose a finite cluster and use the obtained boundary tensors to construct

a few-body Hamiltonian. All interactions inside the cluster will be fully considered to reduce the error from the tree approximation. The entanglement bath mimics the environment of the infinite tree branches, thus the algorithm directly accesses the thermodynamic limite and there is no conventional finite-size error that appears in, *e.g.* ED, DMRG or QMC.

The embedding is based on the generalizations of $\hat{\mathcal{H}}(i,j)$ [Eq. (7.13)] in stage one. From the formulation given above, one can see that $\hat{\mathcal{H}}(i,j)$ is actually the product of two parts. The first is the shifted Hamiltonian that contains all interactions inside the supercell (two neighboring sites in our example), and the second is in fact the physical-bath interactions [Fig. 7.6], whose Hamiltonian (Same to Eq. (7.9) in $1D$ AOP) is written as

$$\hat{\mathcal{H}}^{\partial}(n,x)_{\mu_x\mu'_x} = \sum_{a_x} \hat{F}^{L(R)}(n)_{a_x} |V^{[x]})_{a_x\mu_x\mu'_x}. \tag{7.21}$$

Now we extend the supercell to a chosen larger cluster, where the **few-body Hamiltonian** denoted by $\hat{\mathcal{H}}^{FB}$ is written as

$$\hat{\mathcal{H}}^{FB} = \prod_{\langle x\in cluster, n\in bath\rangle} \hat{\mathcal{H}}^{\partial}(n,x) \sum_{\langle i,j\rangle\in cluster} [I - \tau\hat{H}(i,j)]. \tag{7.22}$$

Same as $\hat{\mathcal{H}}(i,j)$, $\hat{\mathcal{H}}^{FB}$ is also formed by two terms [Fig. 7.6]. The first term is the product of several bath Hamiltonians that mimic the interactions between the cluster and the environment, and in the second term, the summation in Eq. (7.22) contains all couplings inside the cluster.

The entanglement bath only "interacts" with the physical sites nearby according to the coupling distance of the original Hamiltonian. In our example with nearest-neighbor couplings, every physical sites on the boundary interact with a bath site, and thus, the number of $\hat{\mathcal{H}}^{\partial}(n,x)$ in the product above scales with the length of the boundary of the cluster. For this reason, $\hat{\mathcal{H}}^{FB}$ is the product/summation of sparse or local matrices, and its ground state can be efficiently solved by using the finite-size approaches, such as ED or DMRG.

Note that if one takes the cluster as the supercell with two sites, Eq. (7.22) becomes exactly Eq. (7.13). The bath calculation itself can be considered as using ED to solve the $\hat{\mathcal{H}}^{FB}$ that contains only the supercell and the bath. The cluster can be arbitrarily chosen according to the computational capacity, and it does not have to obey the translational invariance of the model.

With the ground state $|\tilde{\Phi}(i,j,\cdots)\rangle_{\{\mu\}}$ of $\hat{\mathcal{H}}^{FB}$, the physical properties such as energy, magnetization, etc., can be obtained from the **density operator** $\tilde{\rho}$ by tracing all degrees of freedom of the bath sites as

$$\tilde{\rho}(i,j,\cdots) = \sum_{\{\mu\}} |\tilde{\Phi}(i,j,\cdots)\rangle_{\{\mu\}}\langle\tilde{\Phi}(i,j,\cdots)|_{\{\mu\}}. \tag{7.23}$$

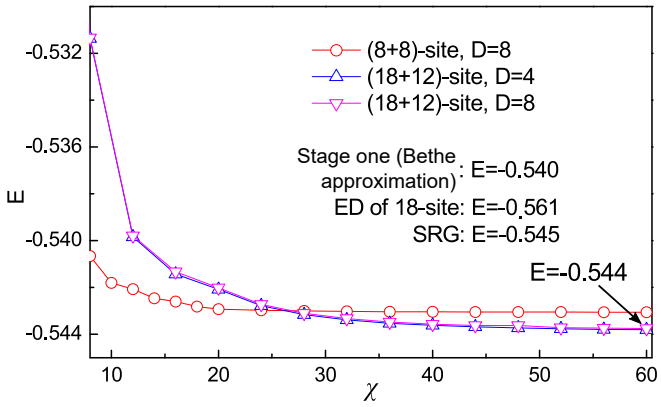

FIGURE 7.7: The ground-state energy E (per site) of the Heisenberg model on honeycomb lattice. The cluster we choose is $(N_p + N_b)$-site where N_p and N_b denote the number of physical and bath sites, respectively (see Fig. 7.1). The ED on the 18-site cluster with periodic boundary condition suffers severe finite-size effects, and the tree approximation (simply from the bath calculations) underestimates long-range correlations. Our results are consistent with second renormalization group (SRG) of TN, showing that both finite-size effects and the error from the tree approximation are largely reduced.

Again, this is a generalization of Eq. (7.20).

Comparing the $1D$ and higher-dimensional AOP versions, we can see many connections, including the idea of defining the eigenvalue equations, the constraints for the encoding/reconstruction process, and the emergence of the few-body Hamiltonians. The differences are also crucial. For $1D$ quantum systems, we can directly encode the imaginary-time-evolution TN. In higher dimensions, the tree approximation is introduced. The essential reason is to satisfy the second constraint, which is the normalization of the state ansatz (see Appendix D.1). The normalization of a standard TN state (*e.g.*, on square lattice) requires an extra loop of TN encoding or contraction. The AOP algorithm to directly encode the $(D+1)$-dimensional imaginary-time-evolution TN for D-dimensional quantum system ($D \geq 2$) is still an open issue. This will lead to a general form of the few-body Hamiltonians (see Appendix D.4).

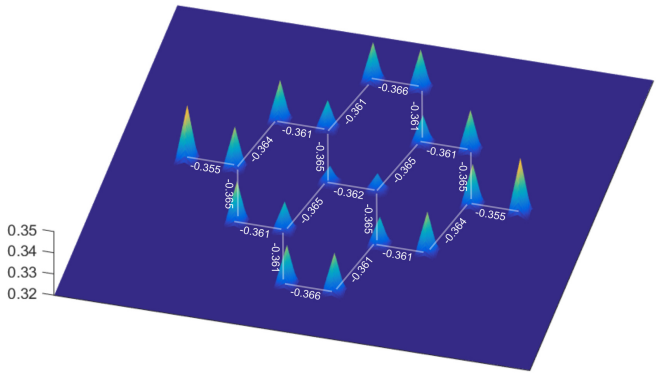

FIGURE 7.8: Finite-size effects of AOP from the ground-state magnetization (absolute value) and the bond energies $e = \langle \hat{S}_i \hat{S}_j \rangle$ of the Heisenberg model on honeycomb lattice. Here we choose a cluster with $N_p = 18$ physical and $N_b = 12$ bath sites. Each peak shows the absolute values of the local magnetization of the physical sites, which ranges from $M = 0.329$ (center) to 0.347 (boundary). We take $D = 8$ and $\chi = 60$. For comparison, the results from the tree approximation in the first stage are $e = -0.360$ and $M = 0.347$, and those from SRG are $e = -0.363$ and $M = 0.310$. QMC is supposed to give the most reliable result $M = 0.22$ [RRY89; Cas+06].

7.4 Numerical results

7.4.1 Heisenberg model on honeycomb lattice

We simulate the ground-state properties of the Heisenberg model on **honeycomb lattice**, which is on a gapless point and considered to be challenging to simulate. The Hamiltonian is the summation of the two-body interactions as

$$\hat{H} = \sum_{\langle i,j \rangle} \hat{H}(i,j). \tag{7.24}$$

For Heisenberg model, we have $\hat{H}(i,j) = J_x \hat{S}^x(i)\hat{S}^x(j) + J_y \hat{S}^y(i)\hat{S}^y(j) + J_z \hat{S}^z(i)\hat{S}^z(j)$, with $\hat{S}^\alpha(i)$ ($\alpha = x, y, z$) the α component of the spin-1/2 operators on the i-th site and J_α the coupling constants.

In stage one, the bath is calculated by choosing two neighboring sites as the supercell. It means $\hat{\mathcal{H}}^{FB}$ that appears in this stage contains $N_p = 2$ physical and $N_b = 4$ bath sites. For stage two, we choose two different clusters to construct $\hat{\mathcal{H}}^{FB}$, which contains $N_p = 8$ physical sites surrounded by $N_b = 8$ bath sites and $N_p = 18$ physical sites with $N_b = 12$ bath sites, respectively [Fig. 7.1]. We utilize finite DMRG [Whi92] to solve the ground state of $\hat{\mathcal{H}}^{FB}$.

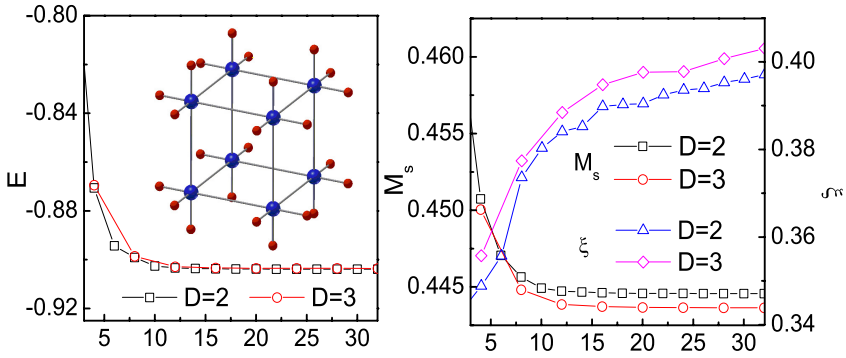

FIGURE 7.9: The ground-state energy E of the Heisenberg model on simple cubic lattice versus χ is shown in the left figure. The simulation by QMC on a $(10 \times 10 \times 10)$ lattice with periodic boundary condition gives $E = -0.902$. The inset shows the cluster with $N_p = 8$ physical (blue balls) and $N_b = 24$ bath sites (red balls) used in the second stage in our AOP approach for the simulations on cubic lattice. The legs stand for the interactions between the connecting sites. In the right one, we show the staggered magnetization M_s and correlation length ξ of the ground state (see Appendix D.5 for a definition). We take $D = 2$ and 3.

The **ground-state energy** E with different dimensions of the bath site $D = 4$ and 8 is shown in Fig. 7.7. One can see that E converges rapidly by increasing the dimension cut-off of DMRG χ to $E = -0.543$ and -0.544 for the two clusters, respectively. With larger D, the bath will be able to carry more entanglement and lead to a better accuracy. The accuracy will also be improved by increasing χ since the result will approach to the exact ground state of $\hat{\mathcal{H}}^{FB}$ with no DMRG error. When χ is sufficiently large, the errors inside the cluster due to the tree approximation, Trotter discretization and truncations will vanish.

For a comparison, the ground-state energy by ED on such a cluster of 18 spins [Fig. 7.1] with periodic boundary condition is $E = -0.561$, which suffers severe finite-size effects. The result solely by bath calculation (tree approximation) is $E = -0.540$, and by second renormalization group (SRG) [Xie+09] of TN is $E = -0.545$. SRG belongs to the state-of-the-art TN approaches for simulating $2D$ ground states with a high accuracy. The difference compared with our results are only $\mathcal{O}(10^{-3})$. QMC results for the model are [RRY89] $E = -0.5445(10)$, comparable with our results.

To further investigate the effects of the finiteness of the clusters, we calculate the **nearest-neighbor bond energies** $e = \langle \hat{S}_i \hat{S}_j \rangle$ and the **staggered magnetizations** with the cluster of $N_p = 18$ and $N_b = 12$ [Fig. 7.8]. The changes of both quantities in different positions of the cluster is mostly $\mathcal{O}(10^{-2})$. By comparing with the tree results in the bath calculation and SRG, we find that the

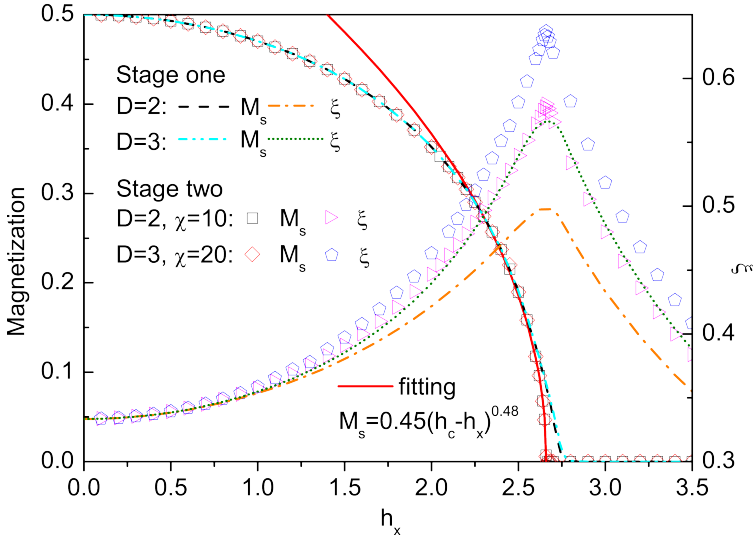

FIGURE 7.10: Staggered magnetization per site M_s and dynamic correlation length ξ of the ground state of the transverse Ising model on simple cubic lattice. The results obtained in Stage one (Bethe approximation) and Stage two are shown for comparison. We take $D = 2$, $\chi = 10$, and $D = 3$, $\chi = 20$. The quantum phase transition is found to occur at $h_c = 2.66$. The critical behavior of M_s is obtained by fitting the data from the results of Stage two near h_c, where we have $M_s \propto (h_c - h_x)^{0.48}$.

bond energies and magnetization on the boundary of the cluster are very close to the tree results, and in the middle where the "boundary effects" as well as the difference between our results and the SRG are minimal. Nevertheless, QMC simulations deviate from our results, giving a lower staggered magnetization ($M_{QMC} = 0,22 < 0.347$).

Our simulations show that without increasing the computational cost much, the finite-size effects are suppressed by introducing the entanglement bath, and at the same time the error from the tree approximation are reduced by choosing larger clusters.

7.4.2 Spin models on simple cubic lattice.

We investigate the ground-state properties and quantum phase transitions in the spin models on **simple cubic lattice**. For bath calculations, the supercell is chosen to be two neighboring sites, giving a $\hat{\mathcal{H}}^{FB}$ with $N_p = 2$ physical and $N_b = 10$ bath sites. In stage two, we choose a cubic with $N_p = 8$ physical and $N_b = 24$ bath sites to construct $\hat{\mathcal{H}}^{FB}$ (inset of Fig. 7.9).

Heisenberg model. The **ground-state energy** E, the **staggered magnetization** M_s and **dynamic correlation length** ξ of the antiferromagnetic Heisenberg model on simple cubic lattice are shown in Fig. 7.9. The energy converges to $E = -0.904$, while that from QMC [PST98; Hua+16] on a $(10 \times 10 \times 10)$ lattice with periodic boundary condition is $E = -0.902$ [5]. Note the result from the tree approximation in the first stage is $E = -0.892$, which is already quite accurate. For M_s and ξ, the finite-size effects are much stronger for our QMC calculations. The AOP simulations show that $M_u = 0$ (uniform magnetization), $M_s = 0.445$ and $\xi = 0.405$. Our results are consistent with the widely accepted consensus, that its ground state is an antiferromagnetic ordered (Néel) state with a short correlation length.

Ising model. The quantum phase transition of the anti-ferromagnetic quantum Ising model in a transverse field (IMTF) on simple cubic lattice [Fig. 7.10] is also analized. The Hamiltonian reads $\hat{H} = \sum_{<i,j>} \hat{S}^x(i)\hat{S}^x(j) + h\sum_i \hat{S}^z(i)$. For a comparison, we try different dimension cut-offs with $D = 2$, $\chi = 10$, and $D = 3$, $\chi = 20$. The critical field is found to be around $h_c = 2.66$, consistent with the results from other algorithms (Table 7.1).

Our results show that from the few-body Hamiltonian, the scaling behavior in the critical region can be faithfully captured and the **critical exponents** are consistent with the results obtained by other methods. Meanwhile, obvious improvement in Stage two is observed compared with Stage one (Bethe approximation with a small cluster). By fitting the data in Stage two of $D = 3$ and $\chi = 20$ near the critical point, we find

$$M_s \propto (h_c - h_x)^{\beta}, \tag{7.25}$$

with $\beta = 0.48$, in agreement with the exact result, that is the mean-field critical exponent $\beta = 0.5$. In fact the upper critical dimension for the quantum IMTF is 3. Note that the exponent from the fitting on the data of Stage one is not reliable, which gives $\beta = 1$.

Finally, we also calculate the dynamic correlation length ξ, which shows a peak at the critical point. Nevertheless, the critical exponents we found are not correct, for reason that are explained in Appendix D.5.

[5] We are indebted to Y.-Z. Huang for providing these QMC data, where the worm algorithm is used with the inverse temperature around 50

TABLE 7.1: The values of the critical field h_c with the cluster quantum Monte Carlo (cQMC) [BD02], linked-cluster expansions (LCE) [Coe+16], mean-field theory (MFT) [SIC12], and our AOP simulations in Stages one and two.

	QMC	LCE	MFT	Stage one	Stage two
h_c	2.57906(3)	2.65	3	2.8	2.66

7.5 Discussions about experimental realizations

Our work provides a way of using few-body experiments to mimic many-body features of infinite systems. Since the few-body Hamiltonian only contains a handful of sites with local interactions, one could design cold-atom experiments to realize it in a lab. Specifically speaking in our examples, $\hat{\mathcal{H}}^{\partial}$ is the interaction between a physical spin and an artificial spin with D (bath) degrees of freedom. Here, we assume that $\hat{\mathcal{H}}^{\partial}$ is Hermitian, which should be true due to the structure of the eigenvalue equations [Eqs. (7.14)-(7.17)] of the boundary tensors, where we have $|V^{[x]}\rangle_{a\mu\mu'} = |V^{[x]}\rangle^*_{a\mu'\mu}$. The task here is to get the coupling constants explicitly for implementing experiments.

To this end, let us transform $\hat{\mathcal{H}}^{\partial}$ to the standard summation form. We define $\hat{H}^{\partial}$ that satisfies

$$\hat{\mathcal{H}}^{\partial}(n,x) = I - \tau \hat{H}^{\partial}(n,x) + O(\tau^2). \tag{7.26}$$

It means to the first order of τ, $\hat{\mathcal{H}}^{\partial}$ is the evolution operator of a Hamiltonian $\hat{H}^{\partial}$ for an infinitesimal imaginary time, similar to the $1D$ case [Eq. (7.10)]. This relation is true because in Eq. (7.21), $\hat{F}^{L(R)}$ is obtained by the decomposition of $I - \tau \hat{H}^{B}$, and the boundary tensor $|V^{[x]}\rangle$ has the similar structure since it forms an continuous MPS [Tir+18a; VC10] in the imaginary time direction.

Then, similar to Eq. (7.10), the few-body Hamiltonian in Eq. (7.22) can be rewritten in a standard summation form as $\hat{\mathcal{H}}^{FB} = I - \tau \hat{H}^{FB} + O(\tau^2)$ with

$$\hat{H}^{FB} = \sum_{\langle i,j\rangle \in cluster} \hat{H}(i,j) + \sum_{\langle x \in cluster, n \in bath\rangle} \hat{H}^{\partial}(n,x). \tag{7.27}$$

The two summations contain the physical and physical-bath interactions, respectively, and all terms are local as discussed above. Again, $\hat{\mathcal{H}}^{FB}$ is the evolution operator of $\hat{H}^{FB}$ for an infinitesimal imaginary time to the first order of τ, *i.e.* $\hat{\mathcal{H}}^{FB} \approx e^{-\tau \hat{H}^{FB}}$.

The coupling constants of the physical-bath interactions can be calculated by expanding $\hat{H}^{\partial}$ as

$$\hat{H}^{\partial}(n,x) = \sum_{\alpha\alpha'} J_{\alpha\alpha'}(n,x)\hat{\mathcal{S}}^{\alpha'}(n)\hat{S}^{\alpha}(x). \tag{7.28}$$

with $J_{\alpha\alpha'}(n,x)$ the physical-bath coupling constants and $\{\hat{S}^{\alpha}\}$ and $\{\hat{\mathcal{S}}^{\alpha'}\}$ the corresponding spin operators (including identity) that give the complete basis for the Hermitian matrices. $\{\hat{S}^{\alpha}\}$ is in fact the physical spin operators. For $\{\hat{\mathcal{S}}^{\alpha'}\}$, one can generally choose the generators of $SU(N)$ groups, which give a complete basis for an N-by-N Hermitian matrix. Then the bath spins should be $SU(N)$ spins. If a symmetry [MG02; Wei12] is used in the tensors, for example $SU(2)$ symmetry for spin models, the bath spins are SU(2) spins with higher total momentum, and one will explicitly have the coefficients from the elements of $\hat{H}^{FB}$. Moreover, it is possible to translate the whole few-body Hamiltonian into the second-quantized picture, by expanding it with the bosonic or fermionic operators. The key is that the chosen operator basis have to completely expand the physical-bath Hamiltonian.

From our numerical results, we can see that the properties of the infinite model can be accurately mimicked by very small bath dimension D and cluster size. Suppose we set the tolerance of the experimental error as $\mathcal{O}(10^{-2})$. In this case, the cluster can be chosen as two sites. Then we have $N_p = 2$, with $N_b = 4$ for honeycomb lattice and $N_b = 10$ for simple cubic lattice. For the spin-$1/2$ models on simple cubic lattice, the dimension of the bath sites can be chosen as $D = 2$. This means the bath spins are simply spin-$1/2$, same as the physical ones, which makes it easy to implement in experiments.

In short, the steps to mimic an infinite many-body system with a few-body model are the following:

- Starting from the Hamiltonian of the target model [*e.g.* Eq. (7.24)], compute the physical-bath Hamiltonian $\hat{\mathcal{H}}^{\partial}$ [Eq. (7.21)] by our AOP algorithm.
- Write $\hat{\mathcal{H}}^{\partial}$ into $\hat{H}^{\partial}$ by Eq. (7.26), so that the total Hamiltonian of the few-body model is in a standard summation form [Eq. (7.27)].
- According to the symmetry of the system, choose a set of matrix basis to expand $\hat{H}^{\partial}$ [Eq. (7.28)]. The basis will determine which kind of spins will be used as the bath sites, and the expansion coefficients will be the coupling constants.
- Build the few-body experiment with several physical sites in the bulk and bath sites on the boundary (*e.g.*, Fig. 7.1 or the inset of Fig. 7.9). The coupling constants in the bulk are the same as the target model, and the coupling constants on the boundary are given by the expansion coefficients of $\hat{H}^{\partial}$.

- Observe the properties of the bulk, which mimics the ground state of the infinite system.

7.6 Summary

We propose an *ab-initio* TN approach that allows for accurate survey of the ground states of infinite many-body systems in higher dimensions by an effective few-body models embedded in an "entanglement bath". On one hand, our scheme gives to birth to a flexible and efficient numeric algorithm for quantum lattice models. Our approach can directly access the thermodynamic limit by introducing the physical-bath interactions, which outperforms the finite-size methods such as ED and DMRG. The embedding idea allows for efficient and accurate simulations of infinite $3D$ quantum models, surpassing the existing TN methods. It is free from the "negative-sign" problem and can access to frustrated spin and fermionic models. It can accurately capture many-body features including entanglement, phase transitions and critical behaviors, thus it goes beyond the DFT-based approaches. It could be readily applied to other $(d \leq 3)$-dimensional systems and could be generalized to $(d \geq 4)$-dimensional models.

8 Conclusions and perspectives

In this thesis - mainly using a numerical approach and assisted, whenever possible, by some analytical calculations - several open problems in the realm of the strongly correlated many-body quantum systems (MBQS) have been approached from the point of view of entanglement and nonlocality, the most paradigmatic phenomena that depart from a classical description of nature and characterize the quantum realm.

In the first of two preliminary chapters [(Chap. 2)], we formally reviewed part of the (huge) literature concerning respectively entanglement and Bell nonlocality, limiting to those concepts useful in the rest of the dissertation and therefore paying special attention to the recent advances concerning the results in lattice many-body systems. The Von Neumann entanglement entropy (EE) is defined as the unique entropy measure for bipartite pure states and particularly the area law for the EE has been illustrated for systems in different dimensions. Such a law states that for the ground states of gapped-local Hamiltonians the EE grows proportionally with the surface of the bipartition, instead than with the volume, as occurs for a generic state. Importantly, in one-dimension ($1D$), a logarithmic violation of the area-law at criticality gives insights about the universality class of the quantum phase transition (QPT), described by the characteristic central charge of the underlying conformal field theory.

Entanglement area-law is crucial in the success of tensor-network (TN) techniques, which Chap. 3 is dedicated. TNs provide an ansatz to represent quantum states and operators as a contraction of small tensors. In their $1D$ version "matrix product states" (MPS) or higher-dimensional "projected entanglement pair state" (PEPS), TNs by construction satisfy the area law. Several algorithms in such formalism - the most famous, in $1D$ being the "density matrix renormalization group" (DMRG) - are available to efficiently simulate the ground state of gapped Hamiltonians and we have made extensive use of them in chapters 5, 6 and 7.

In Chap. 4 we studied in detail two simple but paradigmatic dynamical systems, the quantum kicked top (QKT) and the quantum kicked rotor (QKR), which both have chaotic behavior in their classical version. We showed that

bipartite entanglement entropy is a good signature of quantum chaos in this systems. While such correspondence was already well know in the case of the QKT, we extended it to the QKR, which differently from the former is a non-ergodic system. The steps towards these results can be summarized as follows:

- the classical kicked top can be obtained as the thermodynamic limit of a multi-qubit fully interacting quantum system. To connect the quantum description to the classical one, we choose the initial state to be the spin-coherent state. The EE is calculated taking a bipartition between one qubit and the rest of the system. After a Floquet unitary evolution, one consider the time-averaged EE.

- The entanglement-chaos correspondence is defined by the strong correspondence between the time-averaged EE quantum phase diagram and the classical Poincaré map. A high EE production corresponds to global chaos in this ergodic system. A low EE conversely corresponds to periodic classical orbits.

- The main advantage of this approach is that it can be realized in experiments with superconducting qubits.

- The QKR was then analized in a similarly, exploiting the "rotor-limit of the kicked top" for the first time pointed out by Haake and Shepelyansky in [HS88]. An important result is that in taking this limit we have also shown that EE corresponds to local chaos in non-ergodic systems.

- An important feature of the classical kicked rotor is the presence of a Kolmogorov-Arnol'd-Moser (KAM) phase transition driven by the kicking strength and distinguishing two regimes: for lower kicks extendend regular periodic orbits (KAM tori) isolate different sectors of the Poincaré map, preventing global chaos. At the KAM transition, the last tori is broken and trajectories can spread across the whole phase space. We have shown that the behavior of EE tori resembles that of KAM tori, and therefore conjectured that entanglement should play an important role in any quantum KAM theory.

An interesting avenue of future investigation would be to formally understand what the role of bi-partition choice plays in quantum chaos. Furthermore, it would be interesting to understand the role of the entanglement in the well known mapping between the QKR and the Anderson localization of a particle in a $1D$ lattice as established by Fishman, Grempel and Prange in [FGP82].

In Chap 5, a complete theoretical and numerical analysis of the imbalanced Creutz-Hubbard ladder is presented. This model is a quasi-$1D$ interacting fermionic system, which schematically can be viewed as two $1D$ lattices with inter- and intra-leg hopping and an energy imbalance between the two ladders. In its non-interacting regime, the Creutz ladder hosts a topological insulating phase. The

survival of topological effects when interactions are added is still broadly unexplored and the Creutz-Hubbard model is a nontrivial model where these problems can be studied, with the advantage of being able to be tested in laboratory with ultracold atoms experiments. In order to understand the model in all regimes and to locate exactly its critical lines and the underlying conformal field theories, numerical DMRG and MPS simulations were performed. Wherever possible (namely, in the limit of strong and weak interactions and in the intermediate regime) we compared these numerical results with analytical calculations. The main novel results we found in this study can be summarized as follows:

- In absence of interactions, the imbalance Creutz ladder hosts a symmetry protected topological insulator (TI) in the symmetry class AIII (chiral class), characterized by flat bands and fully-localised edge states.
- The TI is not directly destroyed by adding Hubbard interactions and indeed spreads across a relevant sector of the parameter space. Such a phase is still physically characterized by a degenerate ground state because of the presence of localized zero-energy edge-modes and by a doubly degenerate entanglement spectrum.
- For sufficiently weak interactions, the physics is approximated by a couple of Ising models with a renormalized transverse field connecting them. According to this, the TI and the orbital paramagnet (OPM) are separated by a QPT whose central charge is $c = 1$, *i.e.* double the central charge of a single Ising model.
- At large interaction strength, a long-range in-plane ferromagnetic order arises, related to the symmetry-broken phase of an orbital quantum Ising model, while the imbalance then drives a standard QPT in the Ising universality class (central charge $c = 1/2$) towards the OPM phase.
- For intermediate interaction strength, another Ising model describes the physics and the TI-OFM QPT is characterized by central charge $c = 1/2$.

It would be very interesting to study the imbalanced Creutz-Hubbard model at different fillings and to explore the possibility of finding topological phases of matter that disappear for vanishing interactions. In this respect, the analytic and numerical methods hereby presented may be generalized to other fillings, allowing to go beyond mean-field arguments that support the existence of such interesting ground states.

Chap. 6 contains important results that are crucial to shed light on the role of nonlocality in MBQS. We considered a ferromagnetic spin-half Ising model in a transverse-field with power-law ($1/r^\alpha$) ferromagnetic interactions, studying its ground-state phase diagram and QPT for α varying from $\alpha = 0$ to $\alpha \to \infty$, with a complementary analysis of EE and nonlocality, the latter measured via the

violation of the permutationally invariant BI with one- and two-body correlators (PIBI) derived in [Tur+14].

- We exactly locate the QPT by comparing the divergence of the EE with the maximal violation of the PIBI. This observation, obtained via analytical spin-wave calculations and numerical DMRG computations, is traced back to the squeezing of collective-spin fluctuations generated by quantum-critical correlations.

- We observe a maximal violation for infinite-range interactions ($\alpha = 0$), namely when interactions and correlations are themselves permutationally invariant.

Beyond the Ising model considered in this paper, we expect our results to hold for critical points corresponding to the spontaneous breaking of an Ising $\mathbf{Z}_2$ symmetry – for any range of interactions in $d > 1$, and for sufficiently long-range power-law interactions in $d = 1$. Extending our study to higher-order symmetries [$U(1)$, $SU(2)$, etc.] is, however, a nontrivial task, which may require the derivation of novel BIs.

Being invariant under the permutation of any of the N parties involved in the Bell scenario, the BI we have considered is especially suited to investigate nonlocal correlations in N-body states themselves permutationally invariant. This absence of spatial structure was indeed realized in the BEC experiment, where N atoms share one spatial mode, as well as in the ground-state of all-to-all interacting models. However, general quantum-critical states, like conventional many-body states, do usually have a nontrivial spatial structure. As the PIBI only depends on the two-body reduced density-matrix averaged over all pairs, the possibility to capture nonlocal features of QCPs is thus not obvious. The spatial structure of entanglement, on the other hand, is rather revealed through bipartite Schmidt decomposition, capturing entanglement at a many-body level. Developing further conceptual and technical tools to investigate nonlocal correlations in spatially structured many-body states is an important challenge for ongoing studies [WSN17].

In Chap. 7 we proposed a new TN-based scheme of constructing the few-body models that can be easily accessed by theoretical or experimental means, to accurately capture the ground-state properties of infinite MBQS in higher dimensions. The general idea is to embed a small bulk of the infinite model in an "entanglement bath" so that the many-body effects can be faithfully mimicked. The approach we proposed is efficient, simple, flexible, sign-problem free, and it directly accesses the thermodynamic limit.

In practice, our numerical simulations show that with only a handful of sites, the few-body models can accurately capture the many-body features of the infinite systems. With less than 18 physical and 12 bath sites, the difference between our results and the state-of-the-art TN methods is less than $\mathcal{O}(10^{-3})$. For the spin models on a simple cubic lattice, the properties of the quantum phase transitions

in a magnetic field, including the phase transition point and critical exponents, are faithful captured by the few-body model containing only 8 physical and 24 bath sites.

On the other hand, the few-body Hamiltonian only contains local interactions among a handful of sites, it can be realized by, *e.g.*, cold atoms or ions. It is possible to further improve the experiments by using the trick of synthetic gauge fields, where the higher spins, for instance, can be extended to lower spins in a synthetic dimension [Cel+14]. We suggest investigating infinite many-body systems by realizing the predicted few-body Hamiltonian with cold atoms or ions.

A Appendix to Chap. 4

A.1 Proof that ergodic system maximise entanglement entropy

The linear entanglement entropy defined as $S = 1 - \mathrm{tr}\rho^2$ is maximized when $\mathrm{tr}\rho^2$ is minimized. The density matrix ρ, is an Hermitian operator of unitary trace. We want to prove that $\mathrm{tr}\rho^2$ is minimised if all the diagonal elements $\rho_{11} = \rho_{11} = \cdots = \rho_{NN} = 1/N$, i.e. if the system is ergodic. This is a constrained optimization problem, solvable with the Lagrange multipliers method. The constraint is $\mathrm{tr}\rho = 1$. The quantity to minimize is $\mathrm{tr}\rho^2 = \rho_{11}^2 + \rho_{11}^2 + \cdots + \rho_{NN}^2$. We define the Lagrangian as:

$$\mathcal{L} = \rho_{11}^2 + \rho_{22}^2 + \cdots + \rho_{NN}^2 - \lambda\big(\rho_{11} + \rho_{22} + \cdots + \rho_{NN} - 1\big). \tag{A.1}$$

We want to minimize $\mathcal{L}$ with respect to ρ_{ii} and λ, $\frac{\partial \mathcal{L}}{\rho_{ii}} = \frac{\partial \mathcal{L}}{\lambda} = 0$. The system to solve is:

$$\begin{cases} 2\rho_{11} - \lambda = 0; \\ 2\rho_{22} - \lambda = 0; \\ \cdots \\ 2\rho_{NN} - \lambda = 0; \\ \rho_{11} + \rho_{22} + \cdots + \rho_{NN} - 1 = 0. \end{cases} \tag{A.2}$$

The solution of this system is $\rho_{11} = \rho_{11} = \cdots = \rho_{NN} = 1/N$.

A.2 Derivation of tangent space of CKT

The generalised iterative map $\boldsymbol{x}_{n+1} = f(\boldsymbol{x}_n)$ of Eq. (4.11), is linearised to give its associated tangent map $\delta\boldsymbol{x}_{n+1} = f(\boldsymbol{x}_n + \delta\boldsymbol{x}_n) - f(\boldsymbol{x}_n)$, where $\boldsymbol{x}_n = (X_n, Y_n, Z_n)$. We explicitly do the calculation in detail for the coordinate X (Y and Z follow

in a similar fashion).

$$\begin{aligned} dX_{n+1} &= f(X_n + \delta X_n) - f(X_n) \\ &= (X_n + dX_n)\cos\left\{\beta\left[(Y_n + dY_n)\sin\alpha + (Z_n + dZ_n)\cos\alpha\right]\right\} \\ &- \left[(Y_n + dY_n)\cos\alpha - (Z_n + dZ_n)\sin\alpha\right]\sin\left\{\beta\left[(Y_n + dY_n)\sin\alpha\right.\right. \\ &\left.\left. + (Z_n + dZ_n)\cos\alpha\right]\right\} - X_n\cos[\beta(Y_n\sin\alpha + Z_n\cos\alpha)] \\ &+ (Y_n\cos\alpha - Z_n\sin\alpha)\sin[\beta(Y_n\sin\alpha + Z_n\cos\alpha)]. \end{aligned} \tag{A.3}$$

Expanding the expression and keeping only the terms up to the first order in dX_n, dY_n and dZ_n, we obtain,

$$\begin{aligned} dX_{n+1} &= X_n\cos\left[(\beta Y_n\sin\alpha + \beta Z_n\cos\alpha) + (\beta dY_n\sin\alpha + \beta dZ_n\cos\alpha)\right] \\ &+ dX_n\cos\left[\beta Y_n\sin\alpha + \beta Z_n\cos\alpha\right] \\ &- Y_n\cos\alpha\sin\left[(\beta Y_n\sin\alpha + \beta Z_n\cos\alpha) + (\beta dY_n\sin\alpha + \beta dZ_n\cos\alpha)\right] \\ &- dY_n\cos\alpha\sin\left[\beta Y_n\sin\alpha + \beta Z_n\cos\alpha\right] \\ &+ Z_n\sin\alpha\sin\left[(\beta Y_n\sin\alpha + \beta Z_n\cos\alpha) + (\beta dY_n\sin\alpha + \beta dZ_n\cos\alpha)\right] \\ &+ dZ_n\sin\alpha\sin\left[\beta Y_n\sin\alpha + \beta Z_n\cos\alpha\right] \\ &- X_n\cos\left[\beta Y_n\sin\alpha + \beta Z_n\cos\alpha\right] \\ &+ Y_n\cos\alpha\sin\left[\beta Y_n\sin\alpha + \beta Z_n\cos\alpha\right] \\ &- Z_n\sin\alpha\sin\left[\beta Y_n\sin\alpha + \beta Z_n\cos\alpha\right]. \end{aligned} \tag{A.4}$$

Using the relation $\cos(x + dx) - \cos(dx) = -\sin(x)dx$ we get

$$\begin{aligned} dX_{n+1} &= -X_n\sin\left(\beta Y_n\sin\alpha + \beta Z_n\cos\alpha\right)d(\beta Y_n\sin\alpha + \beta Z_n\cos\alpha) \\ &- Y_n\cos\alpha\cos\left(\beta Y_n\sin\alpha + \beta Z_n\cos\alpha\right)d(\beta Y_n\sin\alpha + \beta Z_n\cos\alpha) \\ &+ Z_n\sin\alpha\cos\left(\beta Y_n\sin\alpha + \beta Z_n\cos\alpha\right)d(\beta Y_n\sin\alpha + \beta Z_n\cos\alpha) \\ &+ dX_n\cos\left[\beta Y_n\sin\alpha + \beta Z_n\cos\alpha\right] \\ &- dY_n\cos\alpha\sin\left[\beta Y_n\sin\alpha + \beta Z_n\cos\alpha\right] \\ &+ dZ_n\sin\alpha\sin\left[\beta Y_n\sin\alpha + \beta Z_n\cos\alpha\right]. \end{aligned} \tag{A.5}$$

Finally, grouping the dX_n, dY_n and dZ_n terms, we write down the tangent map in its standard linear form $dx_{n+1} = L(x_n)dx_n$ in Eq. (4.13).

A.3 Derivation of the tangent space of the CKR

The generalised iterative map $\boldsymbol{x}_{n+1} = f(\boldsymbol{x}_n)$ of Eq. (4.24), is linearised to give its associated tangent map $\delta\boldsymbol{x}_{n+1} = f(\boldsymbol{x}_n + \delta\boldsymbol{x}_n) - f(\boldsymbol{x}_n)$, where $\boldsymbol{x}_n = (\Phi_n, P_n)$.

$$\begin{aligned} \delta P_{n+1} &= P_n + \delta P_n + K\sin(\Phi_n + \delta\Phi_n) - \big(P_n + K\sin\Phi_n\big) \\ &= \delta P_n + K\cos(\Phi_n)\delta\Phi_n. \end{aligned} \tag{A.6}$$

$$\begin{aligned} \delta\Phi_{n+1} &= \Phi_n + \delta\Phi_n + \frac{P_{n+1} + \delta P_{n+1}}{I} - \Phi_n - \frac{P_{n+1}}{I} \\ &= \delta\Phi_n + \frac{\delta P_{n+1}}{I} = \delta\Phi_n + \frac{\delta P_n + K\cos(\Phi_n)\delta\Phi_n}{I} \\ &= \big(1 + \frac{K}{I}\cos\Phi_n\big)\delta\Phi_n + \frac{\delta P_n}{I}. \end{aligned} \tag{A.7}$$

B Appendix to Chap. 5

B.1 MPO for the imbalanced Creutz-Hubbard model

In this appendix we derive the matrix product operator (MPO) for the imbalanced Creutz-Hubbard Hamiltonian studied in Chap. 5 which we rewrite here for the sake of readability:

$$H_{\pi CH} = \sum_{i,\ell} \left(-\tilde{t} c^{\dagger}_{i+1,\ell} c_{i,\bar{\ell}} + \mathrm{i} s_{\ell} \tilde{t} c^{\dagger}_{i+1,\ell} c_{i,\ell} + \mathrm{H.c.} \right) + \sum_{i,\ell} \frac{\Delta\epsilon}{2} s_{\ell} n_{i,\ell} + \frac{V_{\mathrm{v}}}{2} n_{i,\ell} n_{i,\bar{\ell}}, \tag{B.1}$$

The interactions are schematically shown in the top of Fig. B.1, for a ladder of $N = 4$ fermionic sites. We label the down(up) rung-sites with odd(even) numbers for reasons that will be clear in the following.

To encode the Hamiltonian in an MPO, we need to express it in terms of local spin operators in a one-dimensional ($1D$) chain. After a Jordan-Wigner transformation (5.8), the fermionic Hamiltonian is in fact mapped in the following spin Hamiltonian

$$H^{spin}_{\pi CH} = \tilde{t} \sum_{j=1}^{L-1} \left(\sigma^{+}_{2j+1} \sigma^{-}_{2j} + \sigma^{+}_{2j} \sigma^{-}_{2j+1} \right) \tag{B.2}$$

$$+ \left(\sigma^{+}_{2j+2} \sigma^{z}_{2j+1} \sigma^{z}_{2j} \sigma^{-}_{2j-1} + \sigma^{+}_{2j-1} \sigma^{z}_{2j} \sigma^{z}_{2j+1} \sigma^{-}_{2j+2} \right) \tag{B.3}$$

$$+ \left(-i\sigma^{+}_{2j+2} \sigma^{z}_{2j+1} \sigma^{-}_{2j} + i\sigma^{+}_{2j} \sigma^{z}_{2j+1} \sigma^{-}_{2j+2} \right) \tag{B.4}$$

$$+ \left(i\sigma^{+}_{2j+1} \sigma^{z}_{2j} \sigma^{-}_{2j-1} - i\sigma^{+}_{2j-1} \sigma^{z}_{2j} \sigma^{-}_{2j+1} \right) \tag{B.5}$$

$$+ \sum_{j=1}^{L} \frac{\Delta}{2} \left(n_{2j} - n_{2j-1} \right) \tag{B.6}$$

$$+ V_V \left(n_{2j} n_{2j-1} \right). \tag{B.7}$$

where $L = 2N$. Each row of the previous equation corresponds to a different kind of interaction in the $1D$ mapping:

- (B.2) the diagonal/nearest-neighbor (solid green lines in Fig. B.1);
- (B.3) the diagonal/third-nearest-neighbor (dashed green lines in Fig. B.1);

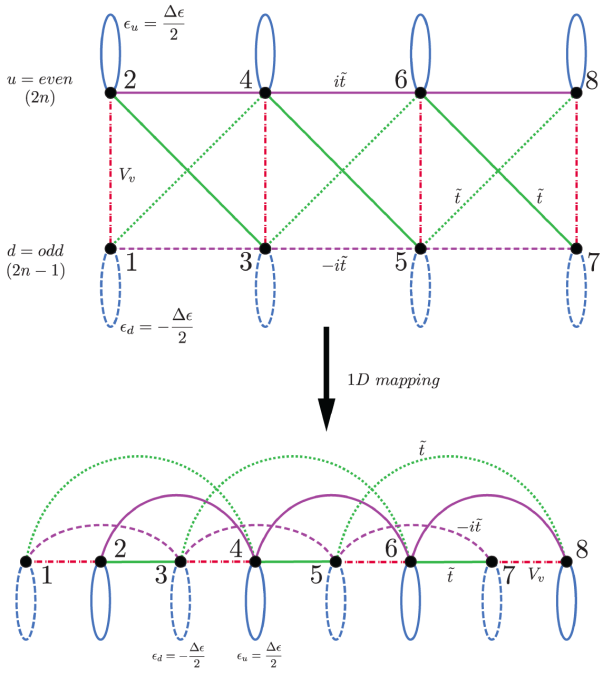

FIGURE B.1

- (B.4) the horizontal-down/odd-next-nearest-neighbor (dashed purple lines in Fig. B.1);
- (B.5) the horizontal-up/even-next-nearest neighbor (solid purple lines in Fig. B.1);
- (B.6) the imbalances. They pick a minus for the odd sites (dashed blue lines in Fig. B.1) and a plus for odd sites (solid blue lines in Fig. B.1);
- (B.7) the Hubbard interactions.

To write down the MPO, we take advantage of the method of the "finite states automata" [CDV08; FND10a] explained in Sec. 3.2.3. To give an example, let us consider the Hamiltonian's terms (B.2) between the sites $2j$ and $2j+1$, which read:

$$\mathbb{1} \otimes \mathbb{1} \otimes \cdots \tilde{t}\sigma^-_{2j} \otimes \sigma^+_{2j+1} \otimes \mathbb{1} \otimes \cdots \otimes \mathbb{1}. \tag{B.8}$$

The Hermitian conjugate must be also considered. Note that these terms appear in the Hamiltonian with the first operator σ^+_{2j} lying always in an even site and the second in the next (odd) one. To translate this interaction in the language of the automata, we enter in the automaton in the state 1, then we go in the state 2 (5 for the Hermitian conjugate) applying σ^+ and finally we exit after applying a

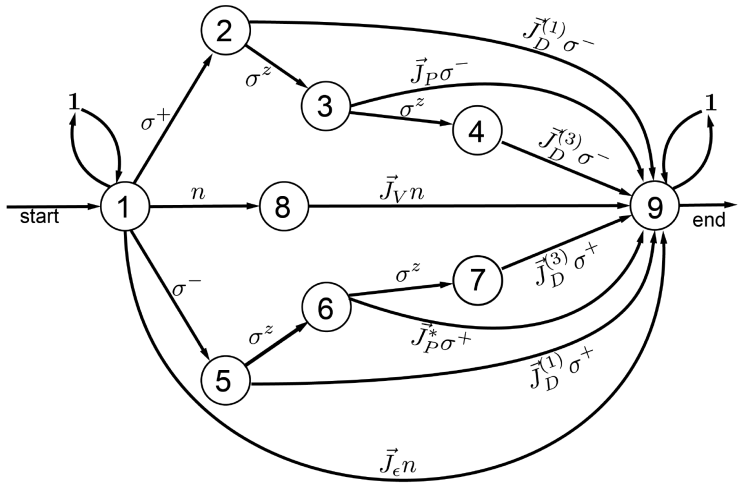

FIGURE B.2: Finite state automaton for the imbalanced Creutz-Hubbard MPO.

$\tilde{t}\sigma^-$. To take into account the fact that such interactions involve only alternated couples of sites where the first site is even-labeled (*i.e.* there are no terms of the form $\mathbb{1}\cdots\tilde{t}\sigma^-_{2j-1}\sigma^+_{2j}\cdots\mathbb{1}$), we introduce a two-dimensional vector of coupling constants $\vec{J}_D^{(1)}$ which picks the value $\tilde{t}$ if the second σ operator is in an odd position and the value zero otherwise. Similar arguments are considered for the remaining interactions. It results that we need an automaton of 9 internal states, which is depicted in Fig. B.2, where the following vectors of couplings are introduced:

$$\begin{aligned} \vec{J}_D^{(1)} &= \begin{pmatrix} 0 \\ \tilde{t} \end{pmatrix}, \qquad \vec{J}_D^{(3)} = \begin{pmatrix} \tilde{t} \\ 0 \end{pmatrix}, \qquad \vec{J}_\epsilon = \begin{pmatrix} \frac{\Delta_\epsilon}{2} \\ \frac{\Delta_\epsilon}{2} \end{pmatrix}, \\ \vec{J}_V &= \begin{pmatrix} V \\ 0 \end{pmatrix}, \qquad \vec{J}_P = \begin{pmatrix} -i\tilde{t} \\ +i\tilde{t} \end{pmatrix}, \qquad \vec{J}_P^* = \begin{pmatrix} +i\tilde{t} \\ -i\tilde{t} \end{pmatrix}. \end{aligned} \tag{B.9}$$

The resulting MPO has a two-site translation invariance and is composed by

the following tensors:

$$W^{[i]} = \begin{pmatrix} \mathbb{1} & \sigma^+ & 0 & 0 & \sigma^- & 0 & 0 & n & \vec{J}_\epsilon n \\ 0 & 0 & \sigma^z & 0 & 0 & 0 & 0 & 0 & \vec{J}_D^{(1)}\sigma^- \\ 0 & 0 & 0 & \sigma^z & 0 & 0 & 0 & 0 & \vec{J}_P\sigma^- \\ 0 & 0 & 0 & 0 & 0 & 0 & 0 & 0 & \vec{J}_D^{(3)}\sigma^- \\ 0 & 0 & 0 & 0 & 0 & \sigma^z & 0 & 0 & \vec{J}_D^{(1)}\sigma^+ \\ 0 & 0 & 0 & 0 & \sigma^z & 0 & \sigma^z & 0 & \vec{J}_P^{*}\sigma^+ \\ 0 & 0 & 0 & 0 & 0 & 0 & 0 & 0 & \vec{J}_D^{(3)}\sigma^+ \\ 0 & 0 & 0 & 0 & 0 & 0 & 0 & 0 & \vec{J}_V n \\ 0 & 0 & 0 & 0 & 0 & 0 & 0 & 0 & \mathbb{1} \end{pmatrix}. \tag{B.10}$$

for $i = 2, \ldots, L-1$, and

$$W^{[1]} = \begin{pmatrix} \mathbb{1} & \sigma^+ & 0 & 0 & \sigma^- & 0 & 0 & n & \vec{J}_\epsilon n \end{pmatrix},$$
$$W^{[L]\dagger} = \begin{pmatrix} \vec{J}_\epsilon n & \vec{J}_D^{(1)}\sigma^- & \vec{J}_P\sigma^- & \vec{J}_D^{(3)}\sigma^- & \vec{J}_D^{(1)}\sigma^+ & \vec{J}_P^{*}\sigma^+ & \vec{J}_D^{(3)}\sigma^+ & \vec{J}_V n & \mathbb{1} \end{pmatrix}. \tag{B.11}$$

Furthermore, it is necessary to fix the number of particles to half-filling. Since we are interested in the ground state of $H_{\pi CH}$, this can be done adding an extra term in the Hamiltonian that gives an extra positive energy (a penalty with respect to the ground state) if the system is outside of the half-filling.

$$H_{\pi CH}^{spin} \to H_{\pi CH}^{spin} + H_{hf} = H_{\pi CH}^{spin} + C\left(\hat{N} - \frac{N}{2}\mathbb{1},\right)^2 \tag{B.12}$$

where $\hat{N} = \sum_{i,\ell} n_{i,\ell}$ is the (total) number-of-particle operator For C large enough, the energies of all the eigenstates with a wrong number of particle are positively shifted and the true ground state will be the one with the lowest energy. In spin representation H_{hf} reads

$$H_{hf} = C\left(\hat{N} - \frac{N}{2}\mathbb{1}\right)^2 = C\sum_i \left(n_i - \frac{1}{2}\mathbb{1}\right)\sum_j \left(n_j - \frac{1}{2}\mathbb{1}\right) = \frac{C}{4}\sum_{i\neq j}\sigma_i^z\sigma_j^z + \frac{C}{4}N\mathbb{1}, \tag{B.13}$$

which translates in the following MPO tensors

$$W^{[i]} = \begin{pmatrix} \mathbb{1} & \frac{C}{4}\sigma^z & \frac{C}{4}\mathbb{1} \\ 0 & \mathbb{1} & \sigma^z \\ 0 & 0 & \mathbb{1} \end{pmatrix}. \tag{B.14}$$

Adding this contribute to the MPO, we finally obtain

$$W^{[i]} = \begin{pmatrix} \mathbb{1} & \sigma^+ & 0 & 0 & \sigma^- & 0 & 0 & n & \frac{C}{4}\sigma^z & \vec{J}_\epsilon n + \frac{C}{4}\mathbb{1} \\ 0 & 0 & \sigma^z & 0 & 0 & 0 & 0 & 0 & 0 & \vec{J}_D^{(1)}\sigma^- \\ 0 & 0 & 0 & \sigma^z & 0 & 0 & 0 & 0 & 0 & \vec{J}_P\sigma^- \\ 0 & 0 & 0 & 0 & 0 & 0 & 0 & 0 & 0 & \vec{J}_D^{(3)}\sigma^- \\ 0 & 0 & 0 & 0 & 0 & \sigma^z & 0 & 0 & 0 & \vec{J}_D^{(1)}\sigma^+ \\ 0 & 0 & 0 & 0 & \sigma^z & 0 & \sigma^z & 0 & 0 & \vec{J}_P^*\sigma^+ \\ 0 & 0 & 0 & 0 & 0 & 0 & 0 & 0 & 0 & \vec{J}_D^{(3)}\sigma^+ \\ 0 & 0 & 0 & 0 & 0 & 0 & 0 & 0 & 0 & \vec{J}_V n \\ 0 & 0 & 0 & 0 & 0 & 0 & 0 & 0 & \mathbb{1} & \sigma^z \\ 0 & 0 & 0 & 0 & 0 & 0 & 0 & 0 & 0 & \mathbb{1} \end{pmatrix}, \tag{B.15}$$

$$W^{[1]} = \begin{pmatrix} \mathbb{1} & \sigma^+ & 0 & 0 & \sigma^- & 0 & 0 & n & \frac{C}{4}\sigma^z & \vec{J}_\epsilon n + \frac{C}{4}\mathbb{1} \end{pmatrix},$$

$$W^{[L]\dagger} = \begin{pmatrix} \frac{C}{4}\mathbb{1}n & \vec{J}_D^{(1)}\sigma^- & \vec{J}_P\sigma^- & \vec{J}_D^{(3)}\sigma^- & \vec{J}_D^{(1)}\sigma^+ & \vec{J}_P^*\sigma^+ & \vec{J}_D^{(3)}\sigma^+ & \vec{J}_V n & \sigma^z & \mathbb{1} \end{pmatrix}. \tag{B.16}$$

C Appendix to Chap. 6

C.1 MPO for long-range Ising chain

In the following we derived the matrix product operator (MPO) used to simulate the one-dimensional long-range ferromagnetic Ising Hamiltonian in a transverse field studied in Chap. 6. Apart from a renormalization factor, the Hamiltonian (6.6) for a $1D$ chain with open boundary conditions reads

$$\mathcal{H} = -\sum_{i \neq j} \frac{1}{r^{\alpha}} \sigma_i^x \sigma_j^x - h \sum_i \sigma_i^z, \tag{C.1}$$

where $r = |i - j|$. While for finite-range Hamiltonians with some translation-invariance, the MPO is an exact tensor network representation of the original Hamiltonian, for generic interactions some approximation is required. Hamiltonians with exponential or power law decaying interactions can be efficiently encoded in a translational invariant MPO. Following the original idea in [CDV08; FND10a] one starts from considering the series expansion of the interaction-function

$$\frac{1}{r^{\alpha}} = \sum_i^K a_i b_i^{r-1} \tag{C.2}$$

where a_i and b_i are parameters founded by a non-linear least square minimization of the function

$$f(a_1, \ldots, a_K, b_1, \ldots, b_K) = \sum_{i=1}^{N} \sum_r^{r_c} \left(a_i b_i^{r-1} - \frac{1}{r^{\alpha}} \right)^2 \tag{C.3}$$

N being the length of the chain. The upper cutoff indicates the integration domain (chain's length) and was set to $r_c = 10000$. f is reduced increasing the number K of the coefficients used in the approximation. For our simulations, where we used chains of length up to $N = 200$, $K = 9$ is enough to well approximate the interaction strengths as shown in Fig. C.1(a).

Once the number of coefficients is fixed, the form of the MPO can be derived using the method of the "finite states automata" explained in Sec. 3.2.3, following the prescriptions in [CDV08; FND10a]. For our Ising model the scheme of the automaton is depicted in Fig. C.1(b), which results in the following local

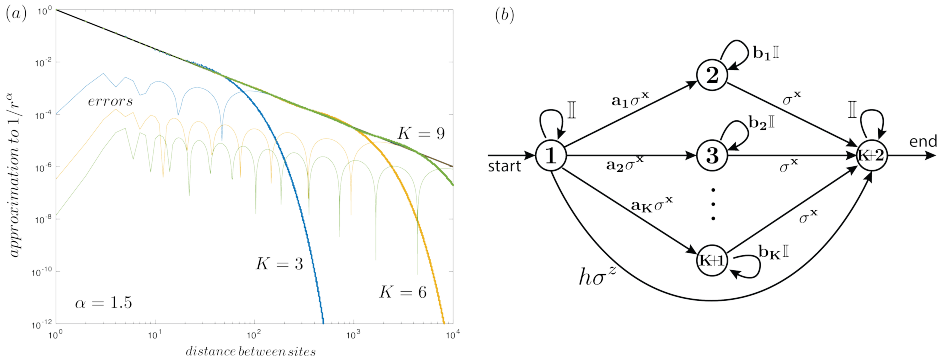

FIGURE C.1: (a) Approximation of the power-law decaying interactions $1/r^\alpha$ (the black solid line is the exact function) by the function (C.2) (dotted lines) and relative errors (solid lines) [Eq. (C.3)], as function of the number of coefficients K for $\alpha = 1.5$. (b) finite state automaton for the Hamiltonian (C.1).

tensors for the MPO:

$$W^{[i]} = \begin{pmatrix} \mathbb{1} & a_1\sigma^x & \cdots & \cdots & a_K\sigma^x & h\sigma^z \\ 0 & b_1\mathbb{1} & \cdots & \cdots & & \sigma^x \\ \vdots & \ddots & b_2\mathbb{1} & \ddots & & \sigma^x \\ \vdots & & & \ddots & & \vdots \\ & & & & b_K\mathbb{1} & \\ 0 & \cdots & \cdots & & 0 & \mathbb{1} \end{pmatrix}. \tag{C.4}$$

for $i = 2, \ldots, N-1$. The initial and final sites are

$$W^{[1]} = \begin{pmatrix} \mathbb{1} & a_1\sigma^x & \cdots & a_K\sigma^x & h\sigma^z \end{pmatrix}; \qquad W^{[N]} = \begin{pmatrix} h\sigma^z \\ \sigma^x \\ \vdots \\ \mathbb{1} \end{pmatrix}. \tag{C.5}$$

Note that the auxiliary dimension of the MPO is $c = K + 2$.

D Appendix to Chap. 7

D.1 State ansatz behind our approach in higher dimensions

At the first stage, the ansatz is an infinite tree PEPS that optimally approximates the ground state in the *rank-1* sense [DLDMV00; Ran+13]. This can be seen from the tensor network (TN) encoded in the self-consistent eigenvalue equations. Starting from Eq. (7.13), one can substitute each of the boundary tensors $|V^{[x]})$'s by the contraction of the other three $|V^{[x]})$'s, $|\tilde{A}^{[x]})$, $(\tilde{A}^{[x]}|$ and the cell tensor $\hat{\mathcal{F}}$ according to Eqs. (7.14)-(7.17). We are using the fact that $|V^{[x]})$ is the eigenvector of $M^{[x]}$. By doing so repetitively, an infinite tree PEPS formed by $|A\rangle$ and $|\tilde{A}^{[x]})$'s can be grown to reach the thermodynamic limit. At the same time, the TN that gives $(I-\tau\hat{H}_{tree})$ appears, where $\hat{H}_{tree}$ is the Hamiltonian defined on the tree. The local interactions of $\hat{H}_{tree}$ are exactly the same with the original model as long as one only looks at a loop-free subsystem, thus $\hat{H}_{tree}$ provides a reasonable approximation. Such a tree PEPS minimizes the energy of $\hat{H}_{tree}$.

For better understanding the approximation of the state on, e.g., an infinite square lattice, we could "grow" the tree in such a way that it fills the whole square lattice. Inevitably, some $|V^{[x]})$'s on the boundary of the tree will gather at the same site. The tensor product of these $|V^{[x]})$'s in fact gives the optimal rank-1 approximation [DLDMV00] of the tensor that forms the bulk of tree TN (translational invariant). Now, if one uses the full-rank tensor to replace its rank-1 version (the tensor product of four $|V^{[x]})$'s), one will have the TN of $I-\tau\hat{H}$ (with H the target Hamiltonian on square lattice) instead of $I-\tau\hat{H}_{tree}$, and the tree PEPS becomes the one defined on the square lattice. Such a picture can be understood in the opposite manner: imaging that one has the "correct" TN defined on the square lattice, what we do is to replace certain tensors by its rank-1 approximations to destruct all the loops of the TN. In this sense, the tree PEPS defined on the original lattice (not actually a Cayley tree or Bethe lattice [Cay78; Bet35]) in stage one provides the optimal loop-free approximation of the ground state, where the loops are destructed by the rank-1 tensors. It would be very helpful to refer to the figures and the discussions in Ref. [[Ran+13]] that are given considering TN contractions.

There are several issues we shall stress. Firstly, one will actually *not* do the above substitutions to reconstruct the tree PEPS. It is automatically encoded

in the self-consistent equations. The "reconstruction picture" is proposed only to understand the ansatz behind the approach. Secondly, one may notice that the self-consistent equations proposed here are slightly different from those for the rank-1 decomposition of a single tensor [DLDMV00]. The reason is that in our case, the normalization of the PEPS should be considered when doing the rank-1 approximation. We here borrow the idea of iDMRG on the tree PEPS [LCP00; NC13] to satisfy this constraint. The third issue is about the uniqueness of the reconstruction of the tree PEPS. Indeed, the contraction of three $|V^{[x]}\rangle$'s, $|\tilde{A}^{[x]}\rangle$, $(\tilde{A}^{[x]}|$ and $\hat{\mathcal{F}}$ to substitute $|V^{[x]}\rangle$ is not unique. However, it is unique when we require the presence of $|\tilde{A}^{[x]}\rangle$, $(\tilde{A}^{[x]}|$ and $\hat{\mathcal{F}}$, in order to recover the TN's of $I - \tau\hat{H}$ as well as the tree PEPS. This is due to the uniqueness of the rank-1 decomposition, which is argued to be a concave problem [DLDMV00].

Such a tree approximation is also closely related to the iPEPS algorithms called simple update [JWX08; Ran+12; BOWR15], where the infinite PEPS is updated by considering the local environment. After reaching the fixed point, the PEPS satisfies a set of self-consistent equations, which lead to a similar tree structure [Ran+12]. Even some long-rang effects are ignored, simple update are still quite accurate especially for gapped states.

Aimed at reducing the error of the tree approximation, the second stage of our approach is to construct the few-body Hamiltonian $\hat{\mathcal{H}}^{FB}$ on a larger cluster by reusing the bath obtained in the first stage, and then calculate the ground state of $\hat{\mathcal{H}}^{FB}$ with a finite-size algorithm. The ansatz behind can be considered as a generalized tree PEPS. In the center of the PEPS, the tensor contains all the physical sites inside the cluster, connected with several infinite tree brunches that are the same to those appearing in stage one. The bath sites carry the entanglement between the physical sites in the cluster and these infinite tree brunches.

D.2 "Finite-loop" effects

Thanks to the infinite tree brunches in the PEPS ansatz, our algorithm does not suffer the conventional finite-size effect in the algorithms such as ED, QMC or DMRG. Thus, the effects from the finiteness of the cluster in the second stage are essentially different. In the first stage, the system size is already infinite because the bath encodes the information of an infinite tree in the eigenvalue equations. Only the loops beyond the supercell are destroyed in an optimal manner (rank-1 approximation of the tensors) [Ran+13]. In stage two, there will be no tree error inside the cluster since all interactions there are fully considered. If the cluster contains larger loops than the cell tensor used in stage one, the precision will be improved. On the other hand, there will be no improvement if one increases the size of the cluster without having larger loops. For this reason, the "finite-size effects" of AOP mean the errors caused by the finiteness of the considered loops.

D.3 Computational cost

The motivation to use the tree approximation is its efficiency especially for 3D quantum models. The computational cost of the first stage is that of the generalized DMRG on an infinite tree PEPS [LCP00; NC13], which roughly scales as $\mathcal{O}(d^{2N_0}D^{3z})$ with d the dimension of the physical Hilbert space on one site, N_0 the number of physical sites in the supercell, D the dimension of a virtual index and z the coordination number of the lattice [1].

To solve the few-body Hamiltonian, the computational cost (leading term) with ED scales as $\mathcal{O}(d^N D^{N^\partial})$ (N and N^∂ the number of physical and bath sites, respectively), and that with DMRG scales as $\mathcal{O}[(N+N^\partial)\max(d,D)^3\chi^6]$ (χ the bond dimension cut-off of DMRG). The cost is similar to solving a nearest-neighbor finite-size system that contains two kinds of sites, whose local Hilbert space is of dimension d (physical) and D (bath), respectively. Surely one can choose other algorithms to solve the few-body Hamiltonian in the second stage, such as QMC or finite PEPS algorithms [LCB14a; Zha+16]. Benefits from the fact that the few-body Hamiltonian is the product (or summation) of local couplings, the efficiency will be similar to that when applying to the standard (short-range) Hamiltonians. In addition, it is possible to update the bath simultaneously in stage two, and the computational cost would be approximately identical to the cluster update schemes of TN.

D.4 General forms of few-body Hamiltonian

As discussed above, the dominant error comes from the destruction of the loops. As a consequence, the interactions between the bath and the physical sites are the tensor product of local terms

$$\hat{\mathcal{H}}^{FB} = \prod_{\langle x,n\rangle} \hat{\mathcal{H}}^{\partial}(n,x). \tag{D.1}$$

It means that in the standard summation form, there are no bath-bath interactions (Fig. D.1). The tree branches in the ground-state ansatz are not connected to each other from anywhere else than the central part.

One can adopt other TN algorithms such as the cluster or full update schemes [VC04a; Jor+08; WV11; LCB14b; NO96; OV09; Orú12; Cor16; Van+16; Xie+09; Xie+12] to obtain the physical-bath interactions. Then the Hamiltonian will not simply be the tensor product, but generally given by

$$\hat{\mathcal{H}}^{FB} = \sum_{\{\alpha\}} \prod_{\langle x,n\rangle} \hat{\mathcal{H}}^{\partial}(n,x)^{\alpha_{x,n}}. \tag{D.2}$$

[1] This is actually the leading term of the cost without using any tricks, such as taking advantage of the sparse property.

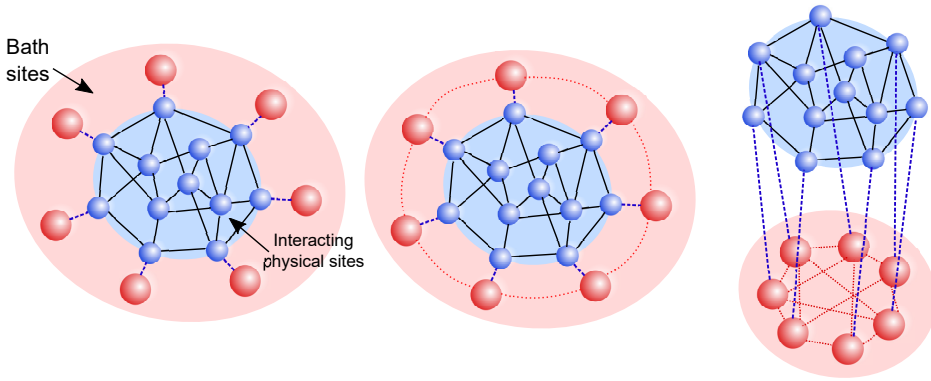

FIGURE D.1: (Color online) The illustrations of three kinds of possible few-body Hamiltonians that contain several interacting physical and bath sites. All the physical interactions (black lines) inside the chosen cluster should be fully considered. The left figure illustrates the one by using the tree DMRG for the physical-bath interactions $\hat{\mathcal{H}}^{\partial}$ (blue dashes), where there are no bath-bath interactions. By choosing other algorithms (e.g., SRG or CTMRG) to calculate $\hat{\mathcal{H}}^{\partial}$, it is possible to also have nearest-neighbor (middle figure) or even long-range (right figure) bath-bath interactions (red dots).

Then the bath-bath interactions will appear in the standard summation form. See the illustrations of three possible situations in Fig. D.1. The extra summations will lead to another (similar) PEPS ansatz beyond the one with tree branches, which should better mimics the infinite environment. However, the computational cost with the currently known methods will become much more sensitive to the coordination number and the dimensionality of the model, making the 3D ground states extremely difficult to access.

D.5 Discussions about imaginary-time evolution picture and criticality in higher dimensions

The idea of approximating an infinite Hamiltonian with a finite effective one has been proposed for the time evolution of $1D$ quantum systems [PVM12]. An important difference in our work is that the "evolution" of the finite effective model is constructed not from a new $\hat{H}$ but with a shift $(I - \tau\hat{H})$ that is in fact the imaginary-time evolution operator. It brings several operational advantages for simulating the ground states, in particular, of higher-dimensional systems. The triangular structure of the Hamiltonian is avoided here, thus the eigenvalue equations for the boundary tensors have stable solutions and the

entanglement bath is well-defined. The few-body Hamiltonians with the bath of higher-dimensional systems can be easily constructed as the summations of local terms.

Our scheme makes it possible to adopt the $(1+1)$-D scaling theories for characterizing criticality [Vid+03] to higher-dimensional models. It is known that any TN algorithms, essentially, cannot give directly a divergent correlation length at the critical point. For 1D quantum systems, it has been shown that at the critical point, any MPS with a finite bond dimension is gapped and possesses a finite correlation length ξ [Vid+03] satisfying

$$\xi \sim \mathcal{D}^{\kappa}, \tag{D.3}$$

with $\mathcal{D}$ the bond dimension of the MPS and κ its scaling exponent. One can see that with a finite $\mathcal{D}$, ξ is always finite, and the information of the criticality is in hidden the algebraical scaling behavior when $\mathcal{D}$ increases. For the scaling of magnetic field h near the critical point, the algebraic behavior of ξ versus h can still survive, however, the value of the exponent might be inaccurate.

For a 2D PEPS, one has to compute the contraction of a 2D TN (e.g., by iTEBD with MPS) to get its correlations using finite dimension cut-offs, and thus the results will still be finite [Pen+17]. To tackle this difficulty, it has been proposed that the divergence of the correlations can be studied by the scaling of the bond dimension of the MPS, from which the central charge of the conformal field theory to characterize the criticality can be accurately obtained [Vid+03; Pen+17].

In our approach, the dynamic correlation length of the ground state ξ is given by the correlation length of an infinite MPS formed by $|V^{[x]}\rangle$ in the imaginary time direction, written as $|\tilde{\psi}\rangle = \sum_{\{\mu\}} \prod |V^{[x]}\rangle_{a_x \mu_x \mu'_x}$. Such an MPS (dubbed as time MPS) is quasi-continuous (discretized up to the Trotter step $\tau \to 0$). Let us explain how to get ξ in the AOP approach. In higher dimensions, the scheme is similar.

The dynamic correlation function of the ground state is defined as $\langle\Phi|\hat{S}e^{-\beta\hat{H}}\hat{S}|\Phi\rangle/e^{-\beta E} - \langle\Phi|\hat{S}|\Phi\rangle^2$ with $|\Phi\rangle$ the ground state and E the ground-state energy. In our framework, it is the contraction of a TN, where the two operators are put in the same column. Thanks to the encoding scheme, such a contraction becomes the contraction of a tensor stripe (Fig. D.2). This stripe is the product of $\hat{\mathcal{H}}^{FB}$'s [Eq. (7.22), also called the transfer matrix] with the two operators in between. The dynamic correlation length is defined as [Tir+18b]:

$$\xi = \frac{\tau}{\log \Lambda_0 - \log \Lambda_1}, \tag{D.4}$$

with Λ_0 and Λ_1 the two largest eigenvalues of $\hat{\mathcal{H}}^{FB}$ (equivalently of the transfer matrix in the imaginary-time direction)

An advantage of the dynamic correlation properties is that we find much less finite-loop or finite-dimension-cutoff effects than the spatial correlations. This is also supported by a recent DMRG work [Pen+17], where the finite-size

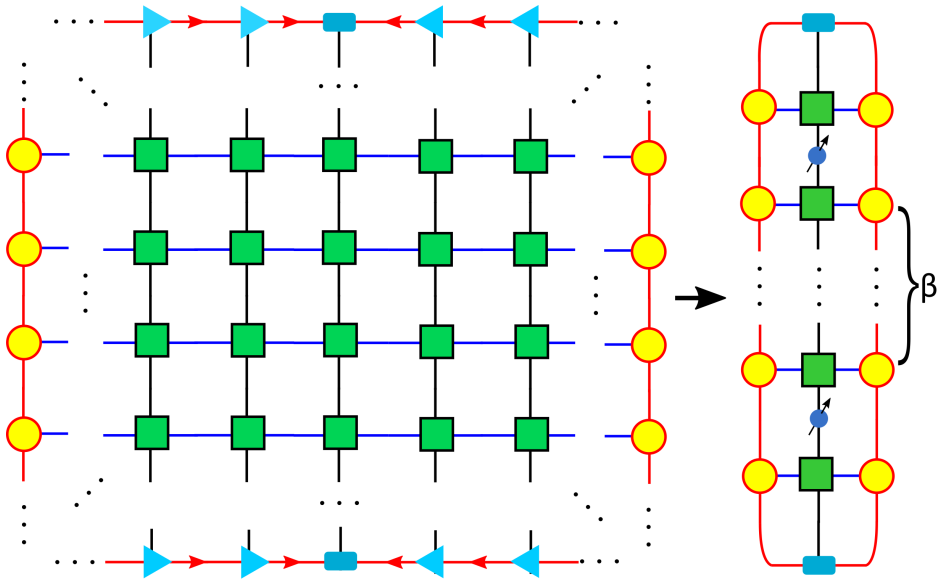

FIGURE D.2: (Color online) The illustrations of the computation of the correlation functions in 1D AOP.

effects are found to be much smaller for the dynamic correlations. Meanwhile, a finite dimensional matrix cannot give a critical spectrum. It means one cannot directly obtain a divergent correlation length at the critical point, and a scaling of the dimension would be necessary to identify the criticality. How to do such kind of scalings for 2D and 3D states is still an open question.

For the Ising model on the cubic lattice studied, we have tried to extract the critical exponent of the dynamical correlation function as

$$\xi \propto (h_c - h_x)^{-\sigma}, \tag{D.5}$$

with $\sigma = 0.25$ near the critical point in Stage two. In Stage one, we have $\sigma = 0.23$. The exact mean-field exponent of the (spatial) correlation length is $\sigma = 0.5$. The discrepancy might be have several reasons: the correlation length in the critical region will diverge with the scaling of the bath dimension D as well as the DMRG dimension cut-off χ (unlike M_s which converges to zero). Thus, it is difficult to directly extract the exponent of ξ with fixed dimensions. The good thing is that the algebraic behavior of ξ is clearly observed. What is open is how to get an accurate value of σ by the scaling factors versus not only h_x but also χ and D. However, recently in [Tir+18b], the relation between dynamic and spatial correlation length in TNs, at least for $1D$ systems, has been studied more in details, which could eventually be extended to higher dimensional systems.

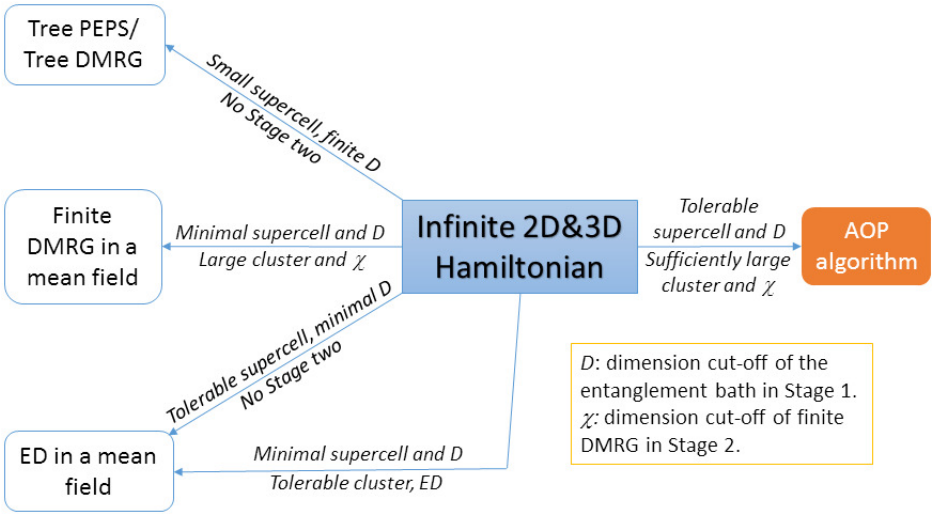

FIGURE D.3: (Color online) Relations between AOP and several existing algorithms (PEPS, DMRG and ED) for the ground-state simulations of 2D and 3D Hamiltonian. The corresponding computational set-ups in the first (bath calculation) and second (solving the few-body Hamiltonian) stages of AOP algorithm are given above and under the arrows, respectively.

D.6 Relations to other algorithms

By taking certain limits of the computational parameters, the relations among our approach and other algorithms are illustrated in Fig. D.3. The simplest situation is to take the dimension of the bath sites $\dim(\mu_{\mathrm{x}}) = \dim(\mu'_{\mathrm{x}}) = 1$, and then $\hat{\mathcal{H}}^{\partial}$ can be written as a linear combination of spin operators (and identity). Thus in this case, $|V^{[x]}\rangle$ simply plays the role of a mean field. If one only uses the bath calculation of the first stage to obtain the ground-state properties, the algorithm will be reduced to the tree DMRG [LCP00; NC13]. If one takes the minimal supercell with $D = 1$ in stage one, the entanglement bath will be reduced to a magnetic mean field. By choosing a large cluster, the DMRG [Whi92] simulation in stage two becomes equivalent to the standard DMRG for solving the cluster in a mean field. If one uses $D = 1$ and chooses a supercell of a tolerably large size in the first stage without entering stage two, or if one chooses a small cluster with $D = 1$ in stage one and uses ED in stage two to solve the few-body Hamiltonian with a tolerably large cluster, our approach will become the ED on the corresponding finite system in a mean field. By taking proper supercell, cluster, algorithms and computational parameters, our approach outperforms others.

D.7 Generalization to ($d \geq 4$) dimensions

Benefiting from its flexibility, it is possible to generalize our approach to even ($d \geq 4$)-dimensional quantum models. The main problem to be tackled is the computational cost. In the second stage by using DMRG for example, the cost increases polynomially with the size of the cluster, thus also polynomially with the dimensionality d. In the first stage with tree DMRG, the cost increase exponentially with d, which makes the simulations for higher-dimensional models extremely expensive. Luckily, the main task here is to solve $(2d + 1)$ number of self-consistent eigenvalue equations, say five [Eq. (7.13)-(7.17)] for 2D, seven for 3D and nine for 4D quantum systems. One way to lower the cost from exponential to polynomial expenses is to use a finite algorithm such as DMRG to solve each eigenvalue problem. It is certain that the stability and efficiency have to be tested.

D.8 Open issues

Several following-up issues are to be further investigated. The flexibility allows for possible incorporating with other methods. For example, the TN techniques with symmetries [MG02; Wei12] can be introduced to lower the computational cost so that much larger clusters can be reached in the second stage. Besides the tree DMRG [LCP00; NC13], the other TN optimization schemes such as TN variational techniques [Phi+15; Van+16; Cor16] and tensor renormalization group algorithms [LN07; OV09; Orú12; Xie+09; Xie+12; YGW17] can be adapted when the cost is tolerable. The finite-size scaling of the cluster should be explored. Our approach could also be readily generalized to higher-dimensional bosonic and fermionic lattice models. The entanglement embedding idea with the physical-bath Hamiltonian proposed here can be adopted to develop novel algorithms for infinite systems by hybridizing with other methods such as QMC, finite or tree PEPS algorithms [LDX12; LCB14a; Zha+16], or the approaches in material sciences and quantum chemistry, such as DFT [She10] and DMET [KC12].

Bibliography

[Ací+07] Antonio Acín et al. "Device-Independent Security of Quantum Cryptography against Collective Attacks". In: *Physical Review Letters* 98.23 (June 2007), p. 230501.

[ADR82] Alain Aspect, Jean Dalibard, and Gérard Roger. "Experimental test of Bell's inequalities using time-varying analyzers". In: *Physical Review Letters* 49.25 (1982), p. 1804.

[Aff+04] Ian Affleck et al. "Rigorous results on valence-bond ground states in antiferromagnets". In: *Condensed Matter Physics and Exactly Soluble Models*. Springer, 2004, pp. 249–252.

[AGR81] Alain Aspect, Philippe Grangier, and Gérard Roger. "Experimental tests of realistic local theories via Bell's theorem". In: *Physical Review Letters* 47.7 (1981), p. 460.

[Alo+19] Albert Aloy et al. "Device-independent witnesses of entanglement depth from two-body correlators". In: *Physical Review Letters* 123.10 (2019), p. 100507.

[Ami+08] Luigi Amico et al. "Entanglement in many-body systems". In: *Reviews of Modern Physics* 80.2 (2008), p. 517.

[And+10] Peter Anders et al. "Dynamical mean field solution of the Bose-Hubbard model". In: *Physical review letters* 105.9 (2010), p. 096402.

[AOP16] János K Asbóth, László Oroszlány, and András Pályi. "A short course on topological insulators". In: *Lecture notes in physics* 919 (2016).

[Arn13] V. I Arnol'd. *Mathematical methods of classical mechanics*. Vol. 60. Springer Science & Business Media, 2013.

[AZ97] Alexander Altland and Martin R Zirnbauer. "Nonstandard symmetry classes in mesoscopic normal-superconducting hybrid structures". In: *Physical Review B* 55.2 (1997), p. 1142.

[Bak+09] Waseem S Bakr et al. "A quantum gas microscope for detecting single atoms in a Hubbard-regime optical lattice". In: *Nature* 462.7269 (2009), p. 74.

[Bal10] Leon Balents. "Spin liquids in frustrated magnets". In: *Nature* 464.7286 (2010), p. 199.

[Bar+19] S Barbarino et al. "Topological Devil's staircase in atomic two-leg ladders". In: *New Journal of Physics* 21.4 (2019), p. 043048.

[Bax78] Rodney J Baxter. "Variational approximations for square lattice models in statistical mechanics". In: *Journal of Statistical Physics* 19.5 (1978), pp. 461–478.

[BB84] Charles H Bennett and Gilles Brassard. *Proceedings of the IEEE International Conference on Computers, Systems and Signal Processing*. 1984.

[BCK15] G. P. Brandino, J.-S. Caux, and R. M. Konik. "Glimmers of a quantum KAM theorem: insights from quantum quenches in one-dimensional Bose gases". In: *Physical Review X* 5 (4 2015), p. 041043.

[BD02] Henk WJ Blöte and Youjin Deng. "Cluster Monte Carlo simulation of the transverse Ising model". In: *Physical Review E* 66.6 (2002), p. 066110.

[BDN12] Immanuel Bloch, Jean Dalibard, and Sylvain Nascimbene. "Quantum simulations with ultracold quantum gases". In: *Nature Physics* 8.4 (2012), p. 267.

[BDZ08] Immanuel Bloch, Jean Dalibard, and Wilhelm Zwerger. "Many-body physics with ultracold gases". In: *Reviews of Modern Physics* 80.3 (2008), p. 885.

[Bel04] John Stewart Bell. *Speakable and unspeakable in quantum mechanics: Collected papers on quantum philosophy*. Cambridge University Press, 2004.

[Bel64] John S Bell. "On the einstein podolsky rosen paradox". In: *Physics Physique Fizika* 1.3 (1964), p. 195.

[Bel66] John S Bell. "On the problem of hidden variables in quantum mechanics". In: *Reviews of Modern Physics* 38.3 (1966), p. 447.

[Ben+93] Charles H Bennett et al. "Teleporting an unknown quantum state via dual classical and Einstein-Podolsky-Rosen channels". In: *Physical Review Letters* 70.13 (1993), p. 1895.

[Ben+96] Charles H Bennett et al. "Mixed-state entanglement and quantum error correction". In: *Physical Review A* 54.5 (1996), p. 3824.

[Ber+10] Alejandro Bermudez et al. "Wilson fermions and axion electrodynamics in optical lattices". In: *Physical review letters* 105.19 (2010), p. 190404.

[Ber+17] Hannes Bernien et al. "Probing many-body dynamics on a 51-atom quantum simulator". In: *Nature* 551.7682 (2017), p. 579.

[Ber77] M. V. Berry. "Regular and irregular semiclassical wavefunctions". In: *Journal of Physics A: Mathematical and General* 10.12 (1977), p. 2083.

[Ber84] Michael Victor Berry. "Quantal phase factors accompanying adiabatic changes". In: *Proceedings of the Royal Society of London. A. Mathematical and Physical Sciences* 392.1802 (1984), pp. 45–57.

[Bet35] Hans A Bethe. "Statistical theory of superlattices". In: *Proceedings of the Royal Society of London. Series A-Mathematical and Physical Sciences* 150.871 (1935), pp. 552–575.

[BGP10] Jean-Daniel Bancal, Nicolas Gisin, and Stefano Pironio. "Looking for symmetric Bell inequalities". In: *Journal of Physics A: Mathematical and Theoretical* 43.38 (2010), p. 385303.

[BJP82] R. Botet, R. Jullien, and P. Pfeuty. "Size Scaling for Infinitely Coordinated Systems". In: *Physical Review Letters* 49 (7 1982), pp. 478–481.

[BK84] D. Bensimon and L. P. Kadanoff. "Extended chaos and disappearance of KAM trajectories". In: *Physica D: Nonlinear Phenomena* 13.1 (1984), pp. 82 –89. ISSN: 0167-2789.

[BKM10] G. P. Brandino, R. M. Konik, and G. Mussardo. "Energy level distribution of perturbed conformal field theories". In: *Journal of Statistical Mechanics: Theory and Experiment* 2010.07 (2010), P07013.

[Bog59] Nikolaj Nikolaevič Bogolûbov. *A new method in the theory of superconductivity*. Chapman & Hall, 1959.

[Boh51] David Bohm. *Quantum theory*. Prentice Hall, 1951.

[BOWR15] Briiissuurs Braiorr-Orrs, Michael Weyrauch, and Mykhailo V Rakov. "Phase diagram of one-, two-, and three-dimensional quantum spin systems derived from entanglement properties". In: *arXiv preprint arXiv:1508.06508* (2015).

[Bru+14] Nicolas Brunner et al. "Bell nonlocality". In: *Reviews of Modern Physics* 86.2 (Apr. 2014), pp. 419–478.

[BT77] M. V. Berry and M. Tabor. "Level clustering in the regular spectrum". In: 356.1686 (1977), pp. 375–394.

[BXG96] RJ Bursill, Tao Xiang, and GA Gehring. "The density matrix renormalization group for a quantum spin chain at non-zero temperature". In: *Journal of Physics: Condensed Matter* 8.40 (1996), p. L583.

[Cam+14] Alessandro Campa et al. *Physics of long-range interacting systems*. OUP Oxford, 2014.

[Cap+01] Luca Capriotti et al. "Resonating valence bond wave functions for strongly frustrated spin systems". In: *Physical Review Letters* 87.9 (2001), p. 097201.

[Car10] Lincoln Carr. *Understanding quantum phase transitions*. CRC press, 2010.

[Cas+06] Eduardo V Castro et al. "Site dilution of quantum spins in the honeycomb lattice". In: *Physical Review B* 73.5 (2006), p. 054422.

[Cay78] Professor Cayley. "Desiderata and suggestions: No. 2. The Theory of groups: graphical representation". In: *American Journal of Mathematics* 1.2 (1878), pp. 174–176.

[CB08] Gregory M Crosswhite and Dave Bacon. "Finite automata for caching in matrix product algorithms". In: *Physical Review A* 78.1 (2008), p. 012356.

[CC04] Pasquale Calabrese and John Cardy. "Entanglement entropy and quantum field theory". In: *Journal of Statistical Mechanics: Theory and Experiment* 2004.06 (2004), P06002.

[CC09] Pasquale Calabrese and John Cardy. "Entanglement entropy and conformal field theory". In: *Journal of Physics A: Mathematical and Theoretical* 42.50 (2009), p. 504005.

[CCD12] Piotr Czarnik, Lukasz Cincio, and Jacek Dziarmaga. "Projected entangled pair states at finite temperature: Imaginary time evolution with ancillas". In: *Physical Review B* 86.24 (2012), p. 245101.

[CDV08] Gregory M Crosswhite, Andrew C Doherty, and Guifré Vidal. "Applying matrix product operators to model systems with long-range interactions". In: *Physical Review B* 78.3 (2008), p. 035116.

[Cel+14] Alessio Celi et al. "Synthetic gauge fields in synthetic dimensions". In: *Physical review letters* 112.4 (2014), p. 043001.

[CGW10] Xie Chen, Zheng-Cheng Gu, and Xiao-Gang Wen. "Local unitary transformation, long-range quantum entanglement, wave function renormalization, and topological order". In: *Physical Review B* 82.15 (2010), p. 155138.

[CGW11a] Xie Chen, Zheng-Cheng Gu, and Xiao-Gang Wen. "Classification of gapped symmetric phases in one-dimensional spin systems". In: *Physical Review B* 83.3 (2011), p. 035107.

[CGW11b] Xie Chen, Zheng-Cheng Gu, and Xiao-Gang Wen. "Complete classification of one-dimensional gapped quantum phases in interacting spin systems". In: *Physical Review B* 84 (23 2011), p. 235128.

[CH94] Michael Creutz and Ivan Horvath. "Surface states and chiral symmetry on the lattice". In: *Physical Review D* 50.3 (1994), p. 2297.

[Cha+18] D. E. Chang et al. "Colloquium: Quantum matter built from nanoscopic lattices of atoms and photons". In: *Reviews of Modern Physics* 90 (3 2018), p. 031002.

[Che+12] Xie Chen et al. "Symmetry-protected topological orders in interacting bosonic systems". In: *Science* 338.6114 (2012), pp. 1604–1606.

[Che+19] Xi Chen et al. "Noise-tolerant signature of Z N topological order in quantum many-body states". In: *Physical Review B* 99.19 (2019), p. 195101.

[Chi79] B. V. Chirikov. "A universal instability of many-dimensional oscillator systems". In: *Physics Reports* 52.5 (1979), pp. 263 –379. ISSN: 0370-1573.

[Cir80] Boris S Cirel'son. "Quantum generalizations of Bell's inequality". In: *Letters in Mathematical Physics* 4.2 (1980), pp. 93–100.

[Cla+69] John F Clauser et al. "Proposed experiment to test local hidden-variable theories". In: *Physical Review Letters* 23.15 (1969), p. 880.

[Coe+16] Kris Coester et al. "Linked-cluster expansions for quantum magnets on the hypercubic lattice". In: *Physical Review B* 94.12 (2016), p. 125109.

[Cor16] Philippe Corboz. "Variational optimization with infinite projected entangled-pair states". In: *Physical Review B* 94.3 (2016), p. 035133.

[Cre83] Michael Creutz. *Quarks, gluons and lattices*. Cambridge University Press, 1983.

[Cre99] Michael Creutz. "End states, ladder compounds, and domain-wall fermions". In: *Physical Review Letters* 83.13 (1999), p. 2636.

[CT17] Giuseppe Carleo and Matthias Troyer. "Solving the quantum many-body problem with artificial neural networks". In: *Science* 355.6325 (2017), pp. 602–606.

[CV09] J Ignacio Cirac and Frank Verstraete. "Renormalization and tensor product states in spin chains and lattices". In: *Journal of Physics A: Mathematical and Theoretical* 42.50 (2009), p. 504004.

[DCLS11] G De Chiara, M Lewenstein, and A Sanpera. "Bilinear-biquadratic spin-1 chain undergoing quadratic Zeeman effect". In: *Physical Review B* 84.5 (2011), p. 054451.

[Deu85] David Deutsch. "Quantum theory, the Church–Turing principle and the universal quantum computer". In: *Proceedings of the Royal Society of London. A. Mathematical and Physical Sciences* 400.1818 (1985), pp. 97–117.

[DLDMV00] Lieven De Lathauwer, Bart De Moor, and Joos Vandewalle. "A multilinear singular value decomposition". In: *SIAM journal on Matrix Analysis and Applications* 21.4 (2000), pp. 1253–1278.

[DN91] John Dewey and Ernest Nagel. *Logic, the theory of inquiry, 1938*. Southern University Press, 1991.

[Dou+15] James S Douglas et al. "Quantum many-body models with cold atoms coupled to photonic crystals". In: *Nature Photonics* 9.5 (2015), pp. 326–331.

[DS12a] Aditi Sen De and Ujjwal Sen. "Entanglement mean-field theory and the Curie-Weiss law". In: *EPL (Europhysics Letters)* 99.2 (2012), p. 20011.

[DS12b] Aditi Sen De and Ujjwal Sen. "Entanglement mean field theory: Lipkin–Meshkov–Glick Model". In: *Quantum Information Processing* 11.3 (2012), pp. 675–683.

[DV04] Sébastien Dusuel and Julien Vidal. "Finite-Size Scaling Exponents of the Lipkin-Meshkov-Glick Model". In: *Physical Review Letters* 93 (23 2004), p. 237204.

[ECP10] Jens Eisert, Marcus Cramer, and Martin B Plenio. "Colloquium: Area laws for the entanglement entropy". In: *Reviews of Modern Physics* 82.1 (2010), p. 277.

[Eis13] Jens Eisert. "Entanglement and tensor network states". In: *arXiv preprint arXiv:1308.3318* (2013).

[EPR35] Albert Einstein, Boris Podolsky, and Nathan Rosen. "Can quantum-mechanical description of physical reality be considered complete?" In: *Physical review* 47.10 (1935), p. 777.

[Eva04] L. C. Evans. "Towards a quantum analog of weak KAM theory". In: *Communications in Mathematical Physics* 244.2 (2004), pp. 311–334.

[Eve18] Glen Evenbly. "Gauge fixing, canonical forms, and optimal truncations in tensor networks with closed loops". In: *Physical Review B* 98.8 (2018), p. 085155.

[Fey82] Richard P Feynman. "Simulating physics with computers". In: *International journal of theoretical physics* 21.6 (1982), pp. 467–488.

[FGP82] Shmuel Fishman, DR Grempel, and RE Prange. "Chaos, quantum recurrences, and Anderson localization". In: *Physical Review Letters* 49.8 (1982), p. 509.

[Fin82] Arthur Fine. "Hidden variables, joint probability, and the Bell inequalities". In: *Physical Review Letters* 48.5 (1982), p. 291.

[Fis+89] Matthew PA Fisher et al. "Boson localization and the superfluid-insulator transition". In: *Physical Review B* 40.1 (1989), p. 546.

[FK11] Lukasz Fidkowski and Alexei Kitaev. "Topological phases of fermions in one dimension". In: *Physical Review B* 83.7 (2011), p. 075103.

[FMR91] J. Ford, G. Mantica, and G. H. Ristow. "The Arnol'd cat: Failure of the correspondence principle". In: *Physica D: Nonlinear Phenomena* 50.3 (1991), pp. 493 –520. ISSN: 0167-2789.

[FND10a] F Fröwis, V Nebendahl, and W Dür. "Tensor operators: Constructions and applications for long-range interaction systems". In: *Physical Review A* 81.6 (2010), p. 062337.

[FND10b] Florian Fröwis, Volckmar Nebendahl, and Wolfgang Dür. "Tensor operators: Constructions and applications for long-range interaction systems". In: *Physical Review A* 81.6 (2010), p. 062337.

[FNP98] K. Furuya, M. C. Nemes, and G. Q. Pellegrino. "Quantum dynamical manifestation of chaotic behavior in the process of entanglement". In: *Physical Review Letters* 80 (25 1998), pp. 5524–5527.

[FNR17] Irénée Frérot, Piero Naldesi, and Tommaso Roscilde. "Entanglement and fluctuations in the XXZ model with power-law interactions". In: *Physical Review B* 95.24 (June 2017), p. 245111.

[FNW92] Mark Fannes, Bruno Nachtergaele, and Reinhard F Werner. "Finitely correlated states on quantum spin chains". In: *Communications in mathematical physics* 144.3 (1992), pp. 443–490.

[Fou+01] WMC Foulkes et al. "Quantum Monte Carlo simulations of solids". In: *Reviews of Modern Physics* 73.1 (2001), p. 33.

[FR18] Irénée Frérot and Tommaso Roscilde. "Quantum Critical Metrology". In: *Physical Review Letters* 121.2 (July 2018), p. 020402.

[FR19] Irénée Frérot and Tommaso Roscilde. "Reconstructing the quantum critical fan of strongly correlated systems using quantum correlations". En. In: *Nature Communications* 10.1 (Feb. 2019), p. 577.

[Fro81] Marcel Froissart. "Constructive generalization of Bell's inequalities". In: *Il Nuovo Cimento B (1971-1996)* 64.2 (1981), pp. 241–251.

[FW12] Alexander L Fetter and John Dirk Walecka. *Quantum theory of many-particle systems*. Courier Corporation, 2012.

[GBH94] Muyu Guo, Ravindra N Bhatt, and David A Huse. "Quantum critical behavior of a three-dimensional Ising spin glass in a transverse magnetic field". In: *Physical review letters* 72.26 (1994), p. 4137.

[GC+02] Elise Gambetti-Césare et al. "Disorder-induced enhancement of the persistent current for strongly interacting electrons in one-dimensional rings". In: *EPL (Europhysics Letters)* 60.1 (2002), p. 120.

[GC+19] Daniel González-Cuadra et al. "Intertwined topological phases induced by emergent symmetry protection". In: *Nature communications* 10.1 (2019), p. 2694.

[Geo+96] Antoine Georges et al. "Dynamical mean-field theory of strongly correlated fermion systems and the limit of infinite dimensions". In: *Reviews of Modern Physics* 68.1 (1996), p. 13.

[GG17] Mariami Gachechiladze and Otfried Gühne. "Completing the proof of "Generic quantum nonlocality"". In: *Physics Letters A* 381.15 (2017), pp. 1281–1285.

[Gho+08] S. Ghose et al. "Chaos, entanglement, and decoherence in the quantum kicked top". In: *Physical Review A* 78 (4 2008), p. 042318.

[GHZ89] Daniel M Greenberger, Michael A Horne, and Anton Zeilinger. *Bell's theorem, quantum theory and conceptions of the universe*. Ed. by Menas Kafatos. Academic, Dordrecht, Holland, 1989, p. 69.

[Gia03] Thierry Giamarchi. *Quantum physics in one dimension*. Vol. 121. Clarendon press, 2003.

[Gis91] Nicolas Gisin. "Bell's inequality holds for all non-product states". In: *Physics Letters A* 154.5 (Apr. 1991), pp. 201–202.

[Giu+15] Marissa Giustina et al. "Significant-Loophole-Free Test of Bell's Theorem with Entangled Photons". In: *Physical Review Letters* 115 (25 2015), p. 250401.

[GK92] Antoine Georges and Gabriel Kotliar. "Hubbard model in infinite dimensions". In: *Physical Review B* 45.12 (1992), p. 6479.

[GLW08] Zheng-Cheng Gu, Michael Levin, and Xiao-Gang Wen. "Tensor-entanglement renormalization group approach as a unified method for symmetry breaking and topological phase transitions". In: *Physical Review B* 78.20 (2008), p. 205116.

[GM14] Michel JP Gingras and Paul A McClarty. "Quantum spin ice: a search for gapless quantum spin liquids in pyrochlore magnets". In: *Reports on Progress in Physics* 77.5 (2014), p. 056501.

[Gon+17] Zhe-Xuan Gong et al. "Entanglement Area Laws for Long-Range Interacting Systems". In: *Physical Review Letters* 119 (5 2017), p. 050501.

[GR07] V Gurarie and L Radzihovsky. "Resonantly paired fermionic superfluids". In: *Annals of Physics* 322.1 (2007), pp. 2–119.

[Gre79] J. M. Greene. "A method for determining a stochastic transition". In: *Journal of Mathematical Physics* 20.6 (1979), pp. 1183–1201.

[GRR86] T. Geisel, G. Radons, and J. Rubner. "Kolmogorov-Arnol'd-Moser barriers in the quantum dynamics of chaotic systems". In: *Physical Review Letters* 57 (23 1986), pp. 2883–2886.

[GS84] U. Glaus and T. Schneider. "Critical properties of the spin-1 Heisenberg chain with uniaxial anisotropy". In: *Physical Review B* 30.1 (1984), p. 215.

[GSL13] Artur García-Sáez and José I Latorre. "Renormalization group contraction of tensor networks in three dimensions". In: *Physical Review B* 87.8 (2013), p. 085130.

[GSP18] Marco Gabbrielli, Augusto Smerzi, and Luca Pezzè. "Multipartite Entanglement at Finite Temperature". En. In: *Scientific Reports* 8.1 (Oct. 2018), p. 15663.

[GSS96] Allan Griffin, David W Snoke, and Sandro Stringari. *Bose-einstein condensation*. Cambridge University Press, 1996.

[GT09] Otfried Gühne and Géza Tóth. "Entanglement detection". In: *Physics Reports* 474.1-6 (2009), pp. 1–75.

[Gur03] Leonid Gurvits. "Classical deterministic complexity of Edmonds' Problem and quantum entanglement". In: *Proceedings of the thirty-fifth annual ACM symposium on Theory of computing*. ACM. 2003, pp. 10–19.

[Gut90] M. C. Gutzwiller. *Chaos in classical and quantum mechanics, volume 1 of interdisciplinary applied mathematics*. Springer-Verlag, New York, 1990.

[GW09] Zheng-Cheng Gu and Xiao-Gang Wen. "Tensor-entanglement-filtering renormalization approach and symmetry-protected topological order". In: *Physical Review B* 80.15 (2009), p. 155131.

[HA13] M Hohenadler and F F Assaad. "Correlation effects in two-dimensional topological insulators". In: *Journal of Physics: Condensed Matter* 25.14 (2013), p. 143201.

[Haa13] F. Haake. *Quantum signatures of chaos*. Vol. 54. Springer Science & Business Media, 2013.

[Hae+11] Jutho Haegeman et al. "Time-dependent variational principle for quantum lattices". In: *Physical Review Letters* 107.7 (2011), p. 070601.

[Hae11] Jutho Haegeman. "Variational renormalization group methods for extended quantum systems". PhD thesis. Ghent University, 2011.

[Hal83] F Duncan M Haldane. "Nonlinear field theory of large-spin Heisenberg antiferromagnets: semiclassically quantized solitons of the one-dimensional easy-axis Néel state". In: *Physical Review Letters* 50.15 (1983), p. 1153.

[Hal84] B. I. Halperin. "Statistics of Quasiparticles and the Hierarchy of Fractional Quantized Hall States". In: *Physical Review Letters* 52 (18 1984), pp. 1583–1586.

[Hal88] F. D. M. Haldane. "Model for a Quantum Hall Effect without Landau Levels: Condensed-Matter Realization of the "Parity Anomaly"". In: *Physical Review Letters* 61 (18 1988), pp. 2015–2018.

[Has07] Matthew B Hastings. "An area law for one-dimensional quantum systems". In: *Journal of Statistical Mechanics: Theory and Experiment* 2007.08 (2007), P08024.

[Hat06] Yasuhiro Hatsugai. "Quantized Berry phases as a local order parameter of a quantum liquid". In: *Journal of the Physical Society of Japan* 75.12 (2006), pp. 123601–123601.

[Hau+16] Philipp Hauke et al. "Measuring multipartite entanglement through dynamic susceptibilities". en. In: *Nature Physics* 12.8 (Aug. 2016), pp. 778–782.

[Hen+15] Bas Hensen et al. “Loophole-free Bell inequality violation using electron spins separated by 1.3 kilometres”. In: *Nature* 526.7575 (2015), p. 682.

[Her82] Nick Herbert. “FLASH—A superluminal communicator based upon a new kind of quantum measurement”. In: *Foundations of Physics* 12.12 (1982), pp. 1171–1179.

[HK10] M Zahid Hasan and Charles L Kane. “Colloquium: topological insulators”. In: *Reviews of modern physics* 82.4 (2010), p. 3045.

[HKS87] F Haake, M. Kuś, and R. Scharf. “Classical and quantum chaos for a kicked top”. In: *Zeitschrift für Physik B Condensed Matter* 65.3 (1987), pp. 381–395. ISSN: 1431-584X.

[Hof76] Douglas R. Hofstadter. “Energy levels and wave functions of Bloch electrons in rational and irrational magnetic fields”. In: *Physical Review B* 14 (6 1976), pp. 2239–2249.

[Hor+09] Ryszard Horodecki et al. “Quantum entanglement”. In: *Reviews of Modern Physics* 81.2 (2009), p. 865.

[HS88] F. Haake and D. L. Shepelyansky. “The kicked rotator as a limit of the kicked top”. In: *EPL (Europhysics Letters)* 5.8 (1988), p. 671.

[Hsi+08] David Hsieh et al. “A topological Dirac insulator in a quantum spin Hall phase”. In: *Nature* 452.7190 (2008), p. 970.

[HT83] G. Hose and H. S. Taylor. “Quantum Kolmogorov-Arnol’d-Moser-like theorem: fundamentals of localization in quantum theory”. In: *Physical Review Letters* 51 (11 1983), pp. 947–950.

[HTT84] G. Hose, H. S. Taylor, and A. Tip. “A quantum KAM-like theorem. II. Fundamentals of localisation in quantum theory for resonance states”. In: *Journal of Physics A: Mathematical and General* 17.6 (1984), p. 1203.

[Hua+16] Yi-Zhen Huang et al. “Quantum phase transition, universality, and scaling behaviors in the spin-1/2 Heisenberg model with ferromagnetic and antiferromagnetic competing interactions on a honeycomb lattice”. In: *Physical Review E* 93.6 (2016), p. 062110.

[Hus40] K. Husimi. “Some formal properties of the density matrix”. In: *Proceedings of the Physico-Mathematical Society of Japan. 3rd Series* 22.4 (1940), pp. 264–314.

[Hyl+12] Philipp Hyllus et al. “Fisher information and multiparticle entanglement”. In: *Physical Review A* 85.2 (2012), p. 022321.

[Imr+14] Jakub Imriška et al. “Thermodynamics and magnetic properties of the anisotropic 3D Hubbard model”. In: *Physical review letters* 112.11 (2014), p. 115301.

[Iqb+16] Yasir Iqbal et al. "Functional renormalization group for three-dimensional quantum magnetism". In: *Physical Review B* 94.14 (2016), p. 140408.

[Jor+08] Jacob Jordan et al. "Classical simulation of infinite-size quantum lattice systems in two spatial dimensions". In: *Physical review letters* 101.25 (2008), p. 250602.

[Jos+15] Darshan G Joshi et al. "Nonlinear bond-operator theory and 1/d expansion for coupled-dimer magnets. I. Paramagnetic phase". In: *Physical Review B* 91.9 (2015), p. 094404.

[Joz94] Richard Jozsa. "Fidelity for mixed quantum states". In: *Journal of modern optics* 41.12 (1994), pp. 2315–2323.

[Joz98] Richard Jozsa. "Quantum effects in algorithms". In: *NASA International Conference on Quantum Computing and Quantum Communications*. Springer. 1998, pp. 103–112.

[JW28] Pascual Jordan and Eugene P. Wigner. "About the Pauli exclusion principle". In: *Z. Phys.* 47 (1928), pp. 631–651.

[JWX08] Hong-Chen Jiang, Zheng-Yu Weng, and Tao Xiang. "Accurate determination of tensor network state of quantum lattice models in two dimensions". In: *Physical review letters* 101.9 (2008), p. 090603.

[Jün+17] J Jünemann et al. "Exploring interacting topological insulators with ultracold atoms: The synthetic Creutz-Hubbard model". In: *Physical Review X* 7.3 (2017), p. 031057.

[Kai11] David Kaiser. *How the hippies saved physics: science, counterculture, and the quantum revival*. WW Norton & Company, 2011.

[Kap92] David B Kaplan. "A Method for simulating chiral fermions on the lattice". In: *Physics Letters B* 288.3-4 (1992), pp. 342–347.

[Kas+08] Dagomir Kaszlikowski et al. "Quantum correlation without classical correlations". In: *Physical Review Letters* 101.7 (2008), p. 070502.

[KC12] Gerald Knizia and Garnet Kin-Lic Chan. "Density matrix embedding: A simple alternative to dynamical mean-field theory". In: *Physical Review Letters* 109.18 (2012), p. 186404.

[KDP80] Klaus v. Klitzing, Gerhard Dorda, and Michael Pepper. "New method for high-accuracy determination of the fine-structure constant based on quantized Hall resistance". In: *Physical Review Letters* 45.6 (1980), p. 494.

[Kei+15] B Keimer et al. "From quantum matter to high-temperature superconductivity in copper oxides". In: *Nature* 518.7538 (2015), pp. 179–186.

[KF04] C. L. Kane and M. P. A. Fisher. *Perspectives in Quantum Hall Effects: Novel Quantum Liquids in Low-Dimensional Semiconductor Structures*. S. Das Sarma, and A. Pinczuk (Wiley-VCH Verlag, Weinheim), 2004.

[KG18a] M. Kumari and S. Ghose. "Quantum-classical correspondence in the vicinity of periodic orbits". In: *Physical Review E* 97.5 (2018), p. 052209.

[KG18b] M. Kumari and S. Ghose. "Untangling entanglement and chaos". In: *arXiv preprint arXiv:1806.10545* (2018).

[Kit01] A Yu Kitaev. "Unpaired Majorana fermions in quantum wires". In: *Physics-Uspekhi* 44.10S (2001), pp. 131–136.

[Kit03] Alexei Y. Kitaev. "Fault-tolerant quantum computation by anyons". In: *Annals of Physics* 303.1 (2003), pp. 2–30.

[Kit09] Alexei Kitaev. "Periodic table for topological insulators and superconductors". In: *AIP conference proceedings*. Vol. 1134. 1. AIP. 2009, pp. 22–30.

[KLT12] Thomas Koffel, M Lewenstein, and Luca Tagliacozzo. "Entanglement entropy for the long-range Ising chain in a transverse field". In: *Physical review letters* 109.26 (2012), p. 267203.

[KM05] C. L. Kane and E. J. Mele. "Z_2 Topological Order and the Quantum Spin Hall Effect". In: *Physical Review Letters* 95 (14 2005), p. 146802.

[Kol58] A. N. Kolmogorov. "A new metric invariant of transient dynamical systems and automorphisms in lebesgue spaces". In: *Doklady Akademii Nauk SSSR*. Vol. 119. 5. Russian Academy of Sciences. 1958, pp. 861–864.

[Kol59] A. N. Kolmogorov. "Entropy per unit time as a metric invariant of automorphisms". In: *Doklady Akademii Nauk SSSR*. Vol. 124. 4. Russian Academy of Sciences. 1959, pp. 754–755.

[KP06] Alexei Kitaev and John Preskill. "Topological entanglement entropy". In: *Physical Review Letters* 96.11 (2006), p. 110404.

[KU93] Masahiro Kitagawa and Masahito Ueda. "Squeezed spin states". In: *Physical Review A* 47.6 (June 1993), pp. 5138–5143.

[Kön+07] Markus König et al. "Quantum Spin Hall Insulator State in HgTe Quantum Wells". In: 318.5851 (2007), pp. 766–770.

[Lah+09] Thierry Lahaye et al. "The physics of dipolar bosonic quantum gases". In: *Reports on Progress in Physics* 72.12 (2009), p. 126401.

[Lak01] A. Lakshminarayan. "Entangling power of quantized chaotic systems". In: *Physical Review E* 64 (3 2001), p. 036207.

[Lat+05] José I Latorre et al. "Entanglement entropy in the Lipkin-Meshkov-Glick model". In: *Physical Review A* 71.6 (2005), p. 064101.

[Lau83] Robert B Laughlin. "Anomalous quantum Hall effect: an incompressible quantum fluid with fractionally charged excitations". In: *Physical Review Letters* 50.18 (1983), p. 1395.

[LCB14a] Michael Lubasch, J Ignacio Cirac, and Mari-Carmen Banuls. "Algorithms for finite projected entangled pair states". In: *Physical Review B* 90.6 (2014), p. 064425.

[LCB14b] Michael Lubasch, J Ignacio Cirac, and Mari-Carmen Banuls. "Unifying projected entangled pair state contractions". In: *New Journal of Physics* 16.3 (2014), p. 033014.

[LCP00] M-B Lepetit, Maixent Cousy, and Gustavo M Pastor. "Density-matrix renormalization study of the Hubbard model [4] on a Bethe lattice". In: *The European Physical Journal B-Condensed Matter and Complex Systems* 13.3 (2000), pp. 421–427.

[LDX12] Wei Li, Jan von Delft, and Tao Xiang. "Efficient simulation of infinite tree tensor network states on the Bethe lattice". In: *Physical Review B* 86.19 (2012), p. 195137.

[Lee07] Patrick A Lee. "From high temperature superconductivity to quantum spin liquid: progress in strong correlation physics". In: *Reports on Progress in Physics* 71.1 (2007), p. 012501.

[LH08] Hui Li and F Duncan M Haldane. "Entanglement spectrum as a generalization of entanglement entropy: Identification of topological order in non-abelian fractional quantum hall effect states". In: *Physical Review Letters* 101.1 (2008), p. 010504.

[Li+11] Wei Li et al. "Linearized tensor renormalization group algorithm for the calculation of thermodynamic properties of quantum lattice models". In: *Physical review letters* 106.12 (2011), p. 127202.

[LM11] M. Lombardi and A. Matzkin. "Entanglement and chaos in the kicked top". In: *Physical Review E* 83 (1 2011), p. 016207.

[LM15] M. Lombardi and A. Matzkin. "Reply to "Comment on 'Entanglement and chaos in the kicked top' "". In: *Physical Review E* 92 (3 2015), p. 036902.

[LMG65] Harry J Lipkin, N Meshkov, and AJ Glick. "Validity of many-body approximation methods for a solvable model:(I). Exact solutions and perturbation theory". In: *Nuclear Physics* 62.2 (1965), pp. 188–198.

[LMW13] Wan-Fang Liu, Jian Ma, and Xiaoguang Wang. "Quantum Fisher information and spin squeezing in the ground state of the XY model". In: *Journal of Physics A: Mathematical and Theoretical* 46.4 (2013), p. 045302.

[LN07] Michael Levin and Cody P Nave. "Tensor renormalization group approach to two-dimensional classical lattice models". In: *Physical review letters* 99.12 (2007), p. 120601.

[LR72] Elliott H Lieb and Derek W Robinson. "The Finite Group Velocity of Quantum Spin Systems". In: *Commun. Math. Phys.* 28 (1972), p. 251.

[LSA12] Maciej Lewenstein, Anna Sanpera, and Verònica Ahufinger. *Ultracold Atoms in Optical Lattices: Simulating quantum many-body systems*. OUP Oxford, 2012.

[LTH16] Matthew F. Lapa, Jeffrey C. Y. Teo, and Taylor L. Hughes. "Interaction-enabled topological crystalline phases". In: *Physical Review B* 93 (11 2016), p. 115131.

[LW06] Michael Levin and Xiao-Gang Wen. "Detecting topological order in a ground state wave function". In: *Physical Review Letters* 96.11 (2006), p. 110405.

[Mad15] V. Madhok. "Comment on "Entanglement and chaos in the kicked top"". In: *Physical Review E* 92 (3 2015), p. 036901.

[Mas09] Lluís Masanes. "Area law for the entropy of low-energy states". In: *Physical Review A* 80.5 (2009), p. 052104.

[Maz+15] Leonardo Mazza et al. "Methods for detecting charge fractionalization and winding numbers in an interacting fermionic ladder". In: *New journal of physics* 17.10 (2015), p. 105001.

[Mer04] N David Mermin. "Could Feynman have said this". In: *Physics Today* 57.5 (2004), p. 10.

[Met+12] Walter Metzner et al. "Functional renormalization group approach to correlated fermion systems". In: *Reviews of Modern Physics* 84.1 (2012), p. 299.

[Mez+09] Fabio Mezzacapo et al. "Ground-state properties of quantum many-body systems: entangled-plaquette states and variational Monte Carlo". In: *New Journal of Physics* 11.8 (2009), p. 083026.

[MG02] Ian P McCulloch and Miklós Gulácsi. "The non-Abelian density matrix renormalization group algorithm". In: *EPL (Europhysics Letters)* 57.6 (2002), p. 852.

[MGY88] Allan H MacDonald, SM Girvin, and D t Yoshioka. "t U expansion for the Hubbard model". In: *Physical Review B* 37.16 (1988), p. 9753.

[ML05] G Misguich and C Lhuillier. "Frustrated Spin Systems". In: *H. T. Diep (World Science, Singapore, 2005) ed.* 229 (2005).

[MM97] István Montvay and Gernot Münster. *Quantum fields on a lattice*. Cambridge University Press, 1997.

[MMP84] R.S. Mackay, J.D. Meiss, and I.C. Percival. "Transport in Hamiltonian systems". In: *Physica D: Nonlinear Phenomena* 13.1 (1984), pp. 55 –81. ISSN: 0167-2789.

[Mot49] Nevill F Mott. "The basis of the electron theory of metals, with special reference to the transition metals". In: *Proceedings of the Physical Society. Section A* 62.7 (1949), p. 416.

[Mou+12] V. Mourik et al. "Signatures of Majorana Fermions in Hybrid Superconductor-Semiconductor Nanowire Devices". In: 336.6084 (2012), pp. 1003–1007.

[MR06] Roderich Moessner and Arthur P Ramirez. "Geometrical frustration". In: *Phys. Today* 59.2 (2006), p. 24.

[MS06] André Allan Méthot and Valerio Scarani. "An anomaly of non-locality". In: *arXiv preprint quant-ph/0601210* (2006).

[MS98] P. A. Miller and S. Sarkar. "Fingerprints of classical instability in open quantum dynamics". In: *Physical Review E* 58.4 (1998), p. 4217.

[Mus10] Giuseppe Mussardo. *Statistical field theory: an introduction to exactly solved models in statistical physics*. Oxford University Press, 2010.

[MV89] Walter Metzner and Dieter Vollhardt. "Correlated lattice fermions in $d = \infty$ dimensions". In: *Physical review letters* 62.3 (1989), p. 324.

[Nay+08] Chetan Nayak et al. "Non-Abelian anyons and topological quantum computation". In: *Reviews of Modern Physics* 80.3 (2008), p. 1083.

[NC02] Michael A Nielsen and Isaac Chuang. *Quantum computation and quantum information*. AAPT, 2002.

[NC13] Naoki Nakatani and Garnet Kin-Lic Chan. "Efficient tree tensor network states (TTNS) for quantum chemistry: Generalizations of the density matrix renormalization group algorithm". In: *The Journal of chemical physics* 138.13 (2013), p. 134113.

[Nei+16] C. Neill et al. "Ergodic dynamics and thermalization in an isolated quantum system". In: *Nature Physics* 12.11 (2016), p. 1037.

[Net+09] AH Castro Neto et al. "The electronic properties of graphene". In: *Reviews of modern physics* 81.1 (2009), p. 109.

[Nie05] Michael A. Nielsen. "The Fermionic canonical commutation relations and the Jordan-Wigner transform". In: *School of Physical Sciences The University of Queensland* (2005).

[Nis+00] Tomotoshi Nishino et al. "Self-consistent tensor product variational approximation for 3D classical models". In: *Nuclear Physics B* 575.3 (2000), pp. 504–512.

[nK04] R. Demkowicz-Dobrza ński and M. Kuś. "Global entangling properties of the coupled kicked tops". In: *Physical Review E* 70 (6 2004), p. 066216.

[NM05] Reinhard M Noack and Salvatore R Manmana. "Diagonalization- and numerical renormalization-group-based methods for interacting quantum systems". In: *arXiv preprint cond-mat/0510321* (2005).

[NMS13] Cristiano Nisoli, Roderich Moessner, and Peter Schiffer. "Colloquium: Artificial spin ice: Designing and imaging magnetic frustration". In: *Reviews of Modern Physics* 85.4 (2013), p. 1473.

[NN81a] Holger Bech Nielsen and Masao Ninomiya. "Absence of neutrinos on a lattice:(I). Proof by homotopy theory". In: *Nuclear Physics B* 185.1 (1981), pp. 20–40.

[NN81b] Holger Bech Nielsen and Masao Ninomiya. "Absence of neutrinos on a lattice:(II). Intuitive topological proof". In: *Nuclear Physics B* 193.1 (1981), pp. 173–194.

[NO95] Tomotoshi Nishino and Kouichi Okunishi. "Product wave function renormalization group". In: *Journal of the Physical Society of Japan* 64.11 (1995), pp. 4084–4087.

[NO96] Tomotoshi Nishino and Kouichi Okunishi. "Corner transfer matrix renormalization group method". In: *Journal of the Physical Society of Japan* 65.4 (1996), pp. 891–894.

[NP+10] S Nadj-Perge et al. "Spin–orbit qubit in a semiconductor nanowire". In: *Nature* 468.7327 (2010), p. 1084.

[OHZ06] Jaan Oitmaa, Chris Hamer, and Weihong Zheng. *Series expansion methods for strongly interacting lattice models*. Cambridge University Press, 2006.

[ON02] Tobias J. Osborne and Michael A. Nielsen. "Entanglement in a simple quantum phase transition". In: *Physical Review A* 66 (3 2002), p. 032110.

[Orú12] Román Orús. "Exploring corner transfer matrices and corner tensors for the classical simulation of quantum lattice systems". In: *Physical Review B* 85.20 (2012), p. 205117.

[Orú14] Román Orús. "A practical introduction to tensor networks: Matrix product states and projected entangled pair states". In: *Annals of Physics* 349 (2014), pp. 117–158.

[Ost+02] Andreas Osterloh et al. "Scaling of entanglement close to a quantum phase transition". In: *Nature* 416.6881 (2002), p. 608.

[OV08] Roman Orus and Guifre Vidal. "Infinite time-evolving block decimation algorithm beyond unitary evolution". In: *Physical Review B* 78.15 (2008), p. 155117.

[OV09] Román Orús and Guifré Vidal. "Simulation of two-dimensional quantum systems on an infinite lattice revisited: Corner transfer matrix for tensor contraction". In: *Physical Review B* 80.9 (2009), p. 094403.

[PC04] Diego Porras and J Ignacio Cirac. "Effective quantum spin systems with trapped ions". In: *Physical Review Letters* 92.20 (2004), p. 207901.

[Pen+17] Cheng Peng et al. "Identifying Criticality in Higher Dimensions by Time Matrix Product State". In: *arXiv preprint arXiv:1708.07288* (2017).

[Per73] I. C. Percival. "Regular and irregular spectra". In: *Journal of Physics B: Atomic and Molecular Physics* 6.9 (1973), p. L229.

[Pes77] Y. B. Pesin. "Characteristic lyapunov exponents and smooth ergodic theory". In: *Russian Mathematical Surveys* 32.4 (1977), p. 55.

[Pez+18] Luca Pezzè et al. "Quantum metrology with nonclassical states of atomic ensembles". In: *Reviews of Modern Physics* 90.3 (Sept. 2018), p. 035005.

[Pfe70] Pierre Pfeuty. "The one-dimensional Ising model with a transverse field". In: *ANNALS of Physics* 57.1 (1970), pp. 79–90.

[Pfl05] C Pfleiderer. "Why first order quantum phase transitions are interesting". In: *Journal of Physics: Condensed Matter* 17.11 (2005), S987.

[PG+06] David Perez-Garcia et al. "Matrix product state representations". In: *arXiv preprint quant-ph/0608197* (2006).

[PG+08] David Pérez-García et al. "String order and symmetries in quantum spin lattices". In: *Physical review letters* 100.16 (2008), p. 167202.

[Phi+15] Ho N Phien et al. "Infinite projected entangled pair states algorithm improved: Fast full update and gauge fixing". In: *Physical Review B* 92.3 (2015), p. 035142.

[Pig+19] Angelo Piga et al. "Bell correlations at Ising quantum critical points". In: *Physical Review Letters* 123.17 (2019), p. 170604.

[Pir+10] Bogdan Pirvu et al. "Matrix product operator representations". In: *New Journal of Physics* 12.2 (2010), p. 025012.

[Pit86] Itamar Pitowsky. "The range of quantum probability". In: *Journal of Mathematical Physics* 27.6 (1986), pp. 1556–1565.

[PLQ19] Angelo Piga, Maciej Lewenstein, and James Q Quach. "Quantum chaos and entanglement in ergodic and nonergodic systems". In: *Physical Review E* 99.3 (2019), p. 032213.

[Pol+10] Frank Pollmann et al. "Entanglement spectrum of a topological phase in one dimension". In: *Physical Review B* 81.6 (2010), p. 064439.

[Pol+12] Frank Pollmann et al. “Symmetry protection of topological phases in one-dimensional quantum spin systems”. In: *Physical review b* 85.7 (2012), p. 075125.

[PR92] Sandu Popescu and Daniel Rohrlich. “Generic quantum nonlocality”. In: *Physics Letters A* 166.5-6 (1992), pp. 293–297.

[PRS13] Siddharth A Parameswaran, Rahul Roy, and Shivaji L Sondhi. “Fractional quantum Hall physics in topological flat bands”. In: *Comptes Rendus Physique* 14.9 (2013), pp. 816–839.

[PS09] Luca Pezzé and Augusto Smerzi. “Entanglement, Nonlinear Dynamics, and the Heisenberg Limit”. In: *Physical Review Letters* 102.10 (Mar. 2009), p. 100401.

[PST98] NV Prokof’Ev, BV Svistunov, and IS Tupitsyn. “Exact, complete, and universal continuous-time worldline Monte Carlo approach to the statistics of discrete quantum systems”. In: *Journal of Experimental and Theoretical Physics* 87.2 (1998), pp. 310–321.

[PT12] Frank Pollmann and Ari M Turner. “Detection of symmetry-protected topological phases in one dimension”. In: *Physical review b* 86.12 (2012), p. 125441.

[PV14] Martin B Plenio and Shashank S Virmani. “An introduction to entanglement theory”. In: *Quantum Information and Coherence*. Springer, 2014, pp. 173–209.

[PVM12] Ho N Phien, Guifré Vidal, and Ian P McCulloch. “Infinite boundary conditions for matrix product state calculations”. In: *Physical Review B* 86.24 (2012), p. 245107.

[QZ11] Xiao-Liang Qi and Shou-Cheng Zhang. “Topological insulators and superconductors”. In: *Reviews of Modern Physics* 83 (4 2011), pp. 1057–1110.

[Ram94] A P Ramirez. “Strongly Geometrically Frustrated Magnets”. In: *Annual Review of Materials Science* 24.1 (1994), pp. 453–480.

[Ran+12] Shi-Ju Ran et al. “Optimized decimation of tensor networks with super-orthogonalization for two-dimensional quantum lattice models”. In: *Physical Review B* 86.13 (2012), p. 134429.

[Ran+13] Shi-Ju Ran et al. “Theory of network contractor dynamics for exploring thermodynamic properties of two-dimensional quantum lattice models”. In: *Physical Review B* 88.6 (2013), p. 064407.

[Ran+17] Shi-Ju Ran et al. “Few-body systems capture many-body physics: Tensor network approach”. In: *Physical Review B* 96.15 (2017), p. 155120.

[Ran+19] Shi-Ju Ran et al. *Tensor Network Contractions. Methods and Applications to Quantum Many-Body Systems*. Springer International Publishing, 2019.

[Ran16] Shi-Ju Ran. "Ab initio optimization principle for the ground states of translationally invariant strongly correlated quantum lattice models". In: *Physical Review E* 93.5 (2016), p. 053310.

[Rav+17] David Raventós et al. "Cold bosons in optical lattices: a tutorial for exact diagonalization". In: *Journal of Physics B: Atomic, Molecular and Optical Physics* 50.11 (2017), p. 113001.

[Rei13] L. Reichl. *The transition to chaos: conservative classical systems and quantum manifestations*. Springer Science & Business Media, 2013.

[Ric+14] Philip Richerme et al. "Non-local propagation of correlations in quantum systems with long-range interactions". In: *Nature* 511.7508 (2014), p. 198.

[Rig09a] M. Rigol. "Breakdown of thermalization in finite one-dimensional systems". In: *Physical Review Letters* 103 (10 2009), p. 100403.

[Rig09b] M. Rigol. "Quantum quenches and thermalization in one-dimensional fermionic systems". In: *Physical Review A* 80 (5 2009), p. 053607.

[Riz+05] Matteo Rizzi et al. "Phase diagram of spin-1 bosons on one-dimensional lattices". In: *Physical Review Letters* 95.24 (2005), p. 240404.

[RLP17] J. B. Ruebeck, J. Lin, and A. K. Pattanayak. "Entanglement and its relationship to classical dynamics". In: *Physical Review E* 95.6 (2017), p. 062222.

[RRY89] JD Reger, JA Riera, and AP Young. "Monte Carlo simulations of the spin-1/2 Heisenberg antiferromagnet in two dimensions". In: *Journal of Physics: Condensed Matter* 1.10 (1989), p. 1855.

[RTX14] Yong-Zhi Ren, Ning-Hua Tong, and Xin-Cheng Xie. "Cluster mean-field theory study of J1- J2 Heisenberg model on a square lattice". In: *Journal of Physics: Condensed Matter* 26.11 (2014), p. 115601.

[Sac11] S. Sachdev. *Quantum Phase Transitions*. Cambridge: Cambridge Univ. Press, 2011.

[SB16] Lucile Savary and Leon Balents. "Quantum spin liquids: a review". In: *Reports on Progress in Physics* 80.1 (2016), p. 016502.

[SC96a] R. Schack and C. M. Caves. "Chaos for Liouville probability densities". In: *Physical Review E* 53 (4 1996), pp. 3387–3401.

[SC96b] R. Schack and C. M. Caves. "Information-theoretic characterization of quantum chaos". In: *Physical Review E* 53 (4 1996), pp. 3257–3270.

[Sch+08] Andreas P Schnyder et al. "Classification of topological insulators and superconductors in three spatial dimensions". In: *Physical Review B* 78.19 (2008), p. 195125.

[Sch+16] Roman Schmied et al. "Bell correlations in a Bose-Einstein condensate". en. In: *Science* 352.6284 (Apr. 2016), pp. 441–444.

[Sch+98] Peter Schmitteckert et al. “From the Fermi glass towards the Mott insulator in one dimension: Delocalization and strongly enhanced persistent currents”. In: *Physical Review Letters* 81.11 (1998), p. 2308.

[Sch11] Ulrich Schollwöck. “The density-matrix renormalization group in the age of matrix product states”. In: *Annals of Physics* 326.1 (2011), pp. 96–192.

[SDV06] Y-Y Shi, L-M Duan, and Guifre Vidal. “Classical simulation of quantum many-body systems with a tree tensor network”. In: *Physical Review A* 74.2 (2006), p. 022320.

[Sen96] Siddhartha Sen. “Average entropy of a quantum subsystem”. In: *Physical Review Letters* 77.1 (1996), p. 1.

[SH08] Lee Smolin and John Harnad. “The trouble with physics: the rise of string theory, the fall of a science, and what comes next”. In: *The Mathematical Intelligencer* 30.3 (2008), pp. 66–69.

[She+08] DN Sheng et al. “Strong-coupling phases of frustrated bosons on a two-leg ladder with ring exchange”. In: *Physical Review B* 78.5 (2008), p. 054520.

[She+10] Jacob F Sherson et al. “Single-atom-resolved fluorescence imaging of an atomic Mott insulator”. In: *Nature* 467.7311 (2010), p. 68.

[She10] C David Sherrill. “Frontiers in electronic structure theory”. In: *The Journal of chemical physics* 132.11 (2010), p. 110902.

[Sho94] Peter W Shor. “Algorithms for quantum computation: Discrete logarithms and factoring”. In: *Proceedings 35th annual symposium on foundations of computer science*. Ieee. 1994, pp. 124–134.

[SI87] Masuo Suzuki and Makoto Inoue. “The ST-transformation approach to analytic solutions of quantum systems. I: General formulations and basic limit theorems”. In: *Progress of Theoretical Physics* 78.4 (1987), pp. 787–799.

[SIC12] Sei Suzuki, Jun-ichi Inoue, and Bikas K Chakrabarti. *Quantum Ising phases and transitions in transverse Ising models*. Vol. 862. Springer, 2012.

[SPGC11] Norbert Schuch, David Pérez-García, and Ignacio Cirac. “Classifying quantum phases using matrix product states and projected entangled pair states”. In: *Physical Review B* 84.16 (2011), p. 165139.

[SR06] Daniel E Sheehy and Leo Radzihovsky. “BEC-BCS crossover in “magnetized” Feshbach-resonantly paired superfluids”. In: *Physical Review Letters* 96.6 (2006), p. 060401.

[Suo+17] HJ Suominen et al. “Scalable Majorana Devices”. In: *arXiv preprint arXiv:1703.03699* (2017).

[Suz76] Masuo Suzuki. "Relationship between d-dimensional quantal spin systems and (d+ 1)-dimensional Ising systems: Equivalence, critical exponents and systematic approximants of the partition function and spin correlations". In: *Progress of theoretical physics* 56.5 (1976), pp. 1454–1469.

[SW12] Edwin M Stoudenmire and Steven R White. "Studying two-dimensional systems with the density matrix renormalization group". In: *Annu. Rev. Condens. Matter Phys.* 3.1 (2012), pp. 111–128.

[SŻ94] W. Slomczyński and K. Życzkowski. "Quantum chaos: an entropy approach". In: *Journal of Mathematical Physics* 35.11 (1994), pp. 5674–5700.

[Tab89] M. Tabor. *Chaos and integrability in nonlinear dynamics: an introduction*. Wiley, 1989.

[Tak05] Minoru Takahashi. *Thermodynamics of one-dimensional solvable models*. Cambridge University Press, 2005.

[Ten17] Peiyuan Teng. "Generalization of the tensor renormalization group approach to 3-D or higher dimensions". In: *Physica A: Statistical Mechanics and its Applications* 472 (2017), pp. 117–135.

[TEV09] Luca Tagliacozzo, Glen Evenbly, and Guifré Vidal. "Simulation of two-dimensional quantum systems using a tree tensor network that exploits the entropic area law". In: *Physical Review B* 80.23 (2009), p. 235127.

[Tho+82] David J. Thouless et al. "Quantized Hall conductance in a two-dimensional periodic potential". In: *Physical Review Letters* 49.6 (1982), p. 405.

[Tho27] Llewellyn H Thomas. "The calculation of atomic fields". In: *Mathematical Proceedings of the Cambridge Philosophical Society*. Vol. 23. 5. Cambridge University Press. 1927, pp. 542–548.

[Tir+18a] Emanuele Tirrito et al. "Characterizing the quantum field theory vacuum using temporal Matrix Product states". In: *arXiv preprint arXiv:1810.08050* (2018).

[Tir+18b] Emanuele Tirrito et al. "Characterizing the quantum field theory vacuum using temporal Matrix Product states". In: *arXiv preprint arXiv:1810.08050* (2018).

[TPB11] Ari M Turner, Frank Pollmann, and Erez Berg. "Topological phases of one-dimensional fermions: An entanglement point of view". In: *Physical Review B* 83.7 (2011), p. 075102.

[TS85] K. Takahashi and N. Saitôn. "Chaos and Husimi distribution function in quantum mechanics". In: *Physical Review Letters* 55.7 (1985), p. 645.

[Tur+14] J. Tura et al. “Detecting nonlocality in many-body quantum states”. en. In: *Science* 344.6189 (June 2014), pp. 1256–1258.

[Tur+15a] J Tura et al. “Entanglement and nonlocality in many-body systems: a primer”. In: *arXiv preprint arXiv:1501.02733* (2015).

[Tur+15b] J. Tura et al. “Nonlocality in many-body quantum systems detected with two-body correlators”. In: *Annals of Physics* 362 (Nov. 2015), pp. 370–423.

[Tur+19] Jordi Tura et al. “Optimization of device-independent witnesses of entanglement depth from two-body correlators”. In: *Physical Review A* 100.3 (2019), p. 032307.

[TV06] Benjamin Toner and Frank Verstraete. “Monogamy of Bell correlations and Tsirelson’s bound”. In: *arXiv preprint quant-ph/0611001* (2006).

[TW05] Matthias Troyer and Uwe-Jens Wiese. “Computational complexity and fundamental limitations to fermionic quantum Monte Carlo simulations”. In: *Physical Review Letters* 94.17 (2005), p. 170201.

[Tót12] Géza Tóth. “Multipartite entanglement and high-precision metrology”. In: *Physical Review A* 85.2 (2012), p. 022322.

[Umr+07] CJ Umrigar et al. “Alleviation of the fermion-sign problem by optimization of many-body wave functions”. In: *Physical review letters* 98.11 (2007), p. 110201.

[Van+16] Laurens Vanderstraeten et al. “Gradient methods for variational optimization of projected entangled-pair states”. In: *Physical Review B* 94.15 (2016), p. 155123.

[VC04a] Frank Verstraete and J Ignacio Cirac. “Renormalization algorithms for quantum-many body systems in two and higher dimensions”. In: *arXiv preprint cond-mat/0407066* (2004).

[VC04b] Frank Verstraete and J Ignacio Cirac. “Valence-bond states for quantum computation”. In: *Physical Review A* 70.6 (2004), p. 060302.

[VC10] Frank Verstraete and J Ignacio Cirac. “Continuous matrix product states for quantum fields”. In: *Physical review letters* 104.19 (2010), p. 190405.

[Ver+06] Frank Verstraete et al. “Criticality, the area law, and the computational power of projected entangled pair states”. In: *Physical review letters* 96.22 (2006), p. 220601.

[VGRC04] Frank Verstraete, Juan J Garcia-Ripoll, and Juan Ignacio Cirac. “Matrix product density operators: simulation of finite-temperature and dissipative systems”. In: *Physical Review Letters* 93.20 (2004), p. 207204.

[Vid+00] Julien Vidal et al. "Interaction induced delocalization for two particles in a periodic potential". In: *Physical review letters* 85.18 (2000), p. 3906.

[Vid+03] Guifre Vidal et al. "Entanglement in quantum critical phenomena". In: *Physical Review Letters* 90.22 (2003), p. 227902.

[Vid03] Guifré Vidal. "Efficient classical simulation of slightly entangled quantum computations". In: *Physical Review Letters* 91.14 (2003), p. 147902.

[Vid04] Guifré Vidal. "Efficient simulation of one-dimensional quantum many-body systems". In: *Physical Review Letters* 93.4 (2004), p. 040502.

[Vid07a] Guifre Vidal. "Classical simulation of infinite-size quantum lattice systems in one spatial dimension". In: *Physical Review Letters* 98.7 (2007), p. 070201.

[Vid07b] Guifre Vidal. "Entanglement renormalization". In: *Physical review letters* 99.22 (2007), p. 220405.

[Vid08] Guifré Vidal. "Class of quantum many-body states that can be efficiently simulated". In: *Physical Review Letters* 101.11 (2008), p. 110501.

[VMC08] Frank Verstraete, Valentin Murg, and J Ignacio Cirac. "Matrix product states, projected entangled pair states, and variational renormalization group methods for quantum spin systems". In: *Advances in Physics* 57.2 (2008), pp. 143–224.

[VMDC04] Frank Verstraete, Miguel A Martin-Delgado, and J Ignacio Cirac. "Diverging entanglement length in gapped quantum spin systems". In: *Physical Review Letters* 92.8 (2004), p. 087201.

[Vod+15] Davide Vodola et al. "Long-range Ising and Kitaev models: phases, correlations and edge modes". In: *New Journal of Physics* 18.1 (2015), p. 015001.

[Vor79] A. Voros. *Semi-classical ergodicity of quantum eigenstates in the Wigner representation*. Ed. by G. Casati and J. Ford. Berlin, Heidelberg: Springer Berlin Heidelberg, 1979, pp. 326–333. ISBN: 978-3-540-35510-6.

[VPC04a] Frank Verstraete, Markus Popp, and J Ignacio Cirac. "Entanglement versus correlations in spin systems". In: *Physical Review Letters* 92.2 (2004), p. 027901.

[VPC04b] Frank Verstraete, Diego Porras, and J Ignacio Cirac. "Density matrix renormalization group and periodic boundary conditions: a quantum information perspective". In: *Physical Review Letters* 93.22 (2004), p. 227205.

[Wan+04] X. Wang et al. "Entanglement as a signature of quantum chaos". In: *Physical Review E* 70 (1 2004), p. 016217.

[Wei07] Pierre Weiss. "L'hypothèse du champ moléculaire et la propriété ferromagnétique". In: *J. Phys. Theor. Appl.* 6.1 (1907), pp. 661–690.

[Wei12] Andreas Weichselbaum. "Non-abelian symmetries in tensor networks: A quantum symmetry space approach". In: *Annals of Physics* 327.12 (2012), pp. 2972–3047.

[Wen04] Xiao-Gang Wen. *Quantum field theory of many-body systems: from the origin of sound to an origin of light and electrons*. Oxford University Press on Demand, 2004.

[Wer89] Reinhard F. Werner. "Quantum states with Einstein-Podolsky-Rosen correlations admitting a hidden-variable model". In: *Physical Review A* 40.8 (1989), pp. 4277–4281.

[WG18] Qing-Rui Wang and Zheng-Cheng Gu. "Towards a complete classification of symmetry-protected topological phases for interacting fermions in three dimensions and a general group supercohomology theory". In: *Physical Review X* 8.1 (2018), p. 011055.

[Whi+89] Steven R White et al. "Numerical study of the two-dimensional Hubbard model". In: *Physical Review B* 40.1 (1989), p. 506.

[Whi92] Steven R White. "Density matrix formulation for quantum renormalization groups". In: *Physical Review Letters* 69.19 (1992), p. 2863.

[Wil75] Kenneth G Wilson. "The renormalization group: Critical phenomena and the Kondo problem". In: *Reviews of Modern Physics* 47.4 (1975), p. 773.

[WN92] Steven R White and RM Noack. "Real-space quantum renormalization groups". In: *Physical Review Letters* 68.24 (1992), p. 3487.

[WNZ12] Marcin Wiesniak, Mohamed Nawareg, and Marek Zukowski. "N-particle nonclassicality without N-particle correlations". In: *Physical Review A* 86.4 (2012).

[WPS13] Chong Wang, Andrew C. Potter, and T. Senthil. "Gapped symmetry preserving surface state for the electron topological insulator". In: *Physical Review B* 88 (11 2013), p. 115137.

[WS98] Steven R White and Douglas J Scalapino. "Density matrix renormalization group study of the striped phase in the 2D t- J model". In: *Physical review letters* 80.6 (1998), p. 1272.

[WS99] Steven R White and DJ Scalapino. "Competition between stripes and pairing in a t- t- J model". In: *Physical Review B* 60.2 (1999), R753.

[WSN17] Zizhu Wang, Sukhwinder Singh, and Miguel Navascués. "Entanglement and Nonlocality in Infinite 1D Systems". In: *Physical Review Letters* 118.23 (June 2017), p. 230401.

[WV11] Ling Wang and Frank Verstraete. "Cluster update for tensor network states". In: *arXiv preprint arXiv:1110.4362* (2011).

[WZ82] William K Wootters and Wojciech H Zurek. "A single quantum cannot be cloned". In: *Nature* 299.5886 (1982), p. 802.

[Wür+12] Lars Erik Würflinger et al. "Nonlocal multipartite correlations from local marginal probabilities". In: *Physical Review A* 86.3 (2012), p. 032117.

[XCN10] Di Xiao, Ming-Che Chang, and Qian Niu. "Berry phase effects on electronic properties". In: *Reviews of modern physics* 82.3 (2010), p. 1959.

[Xie+09] Zhi-Yuan Xie et al. "Second renormalization of tensor-network states". In: *Physical review letters* 103.16 (2009), p. 160601.

[Xie+12] Zhi-Yuan Xie et al. "Coarse-graining renormalization by higher-order singular value decomposition". In: *Physical Review B* 86.4 (2012), p. 045139.

[Yam09] Daisuke Yamamoto. "Correlated cluster mean-field theory for spin systems". In: *Physical Review B* 79.14 (2009), p. 144427.

[YGW17] Shuo Yang, Zheng-Cheng Gu, and Xiao-Gang Wen. "Loop optimization for tensor network renormalization". In: *Physical review letters* 118.11 (2017), p. 110504.

[YHW11] Simeng Yan, David A Huse, and Steven R White. "Spin-liquid ground state of the S= 1/2 Kagome Heisenberg antiferromagnet". In: *Science* 332.6034 (2011), pp. 1173–1176.

[YMCS17] A Yuste, M Moreno-Cardoner, and A Sanpera. "Using random boundary conditions to simulate disordered quantum spin models in two-dimensional systems". In: *Physical Review B* 95.19 (2017), p. 195167.

[Yos13] Daijiro Yoshioka. *The quantum Hall effect*. Vol. 133. Springer Science & Business Media, 2013.

[Zak89] J Zak. "Berry's phase for energy bands in solids". In: *Physical review letters* 62.23 (1989), p. 2747.

[Zha+16] Hui-Hai Zhao et al. "Tensor network algorithm by coarse-graining tensor renormalization on finite periodic lattices". In: *Physical Review B* 93.12 (2016), p. 125115.

[Zha+17] J. Zhang et al. "Observation of a many-body dynamical phase transition with a 53-qubit quantum simulator". en. In: *Nature* 551.7682 (Nov. 2017), pp. 601–604. ISSN: 1476-4687.

[ZMP14] Michael P Zaletel, Roger SK Mong, and Frank Pollmann. "Flux insertion, entanglement, and quantized responses". In: *Journal of Statistical Mechanics: Theory and Experiment* 2014.10 (2014), P10007.

[ZP94] W. H. Zurek and J. P. Paz. "Decoherence, chaos, and the second law". In: *Physical Review Letters* 72 (16 1994), pp. 2508–2511.

[ZP95] W. H. Zurek and J. P. Paz. "Quantum chaos: a decoherent definition". In: *Physica D: Nonlinear Phenomena* 83.1 (1995). Quantum Complexity in Mesoscopic Systems, pp. 300 –308. ISSN: 0167-2789.

[ZS98] R. Zarum and S. Sarkar. "Quantum-classical correspondence of entropy contours in the transition to chaos". In: *Physical Review E* 57 (5 1998), pp. 5467–5471.

[Zur82] Wojciech H Zurek. "Environment-induced superselection rules". In: *Physical review D* 26.8 (1982), p. 1862.

[ZV04] Michael Zwolak and Guifré Vidal. "Mixed-state dynamics in one-dimensional quantum lattice systems: a time-dependent superoperator renormalization algorithm". In: *Physical Review Letters* 93.20 (2004), p. 207205.

[Zyc90] K. Zyczkowski. "Indicators of quantum chaos based on eigenvector statistics". In: *Journal of Physics A: Mathematical and General* 23.20 (1990), p. 4427.

[ÖR95] Stellan Östlund and Stefan Rommer. "Thermodynamic limit of density matrix renormalization". In: *Physical Review Letters* 75.19 (1995), p. 3537.

Acknowledgements

AP acknowledge the Spanish Ministry MINECO (National Plan 15 Grant: FISICATEAMO No. FIS2016-79508-P, FPI), European Social Fund, Fundació Cellex, Generalitat de Catalunya (AGAUR Grant No. 2017 SGR 1341 and CERCA/Program), ERC AdG OSYRIS and NOQIA, EU FETPRO QUIC, and the National Science Centre, Poland-Symfonia Grant No. 2016/20/W/ST4/00314, beca "la Caixa" de mobilitat internacional.